# Elaboration and characterization of CCM based on cross-linked hybrid nanocomposite membranes for PEM water electrolysis

Ali Abdelmotagali

THÈSE DE DOCTORAT

NNT : 2023UPASF022

université PARIS-SACLAY

# Elaboration and characterization of CCM based on cross-linked hybrid nanocomposite membranes for PEM water electrolysis

*Elaboration et caractérisation de CCM à base de membranes nanocomposites hybrides réticulées pour l'électrolyse de l'eau PEM*

**Thèse de doctorat de l'université Paris-Saclay**

École doctorale n°571 Sciences Chimiques : Molécules, Matériaux, Instrumentation et Biosystèmes (2MIB)
Spécialité de doctorat : Chimie
Graduate School : Chimie. Référent : Faculté des Sciences d'Orsay

Thèse préparée à l'**Institut de chimie moléculaire et des matériaux d'Orsay** (Université Paris-Saclay, CNRS), sous la direction de **Pierre MILLET**, Professeur

**Thèse soutenue à Paris-Saclay, le 20 mars 2023, par**

**Ali ABDELMOTAGALI**

## Composition du Jury

Membres du jury avec voix délibérative

| | |
|---|---|
| **Johnny DESCHAMPS**<br>Professeur, ENSTA | Président |
| **Gaël MARANZANA**<br>Professeur, Université Nancy-Lorraine | Rapporteur & Examinateur |
| **Stéphane MARAIS**<br>Professeur, Université de Rouen | Rapporteur & Examinateur |
| **Jennifer PERON**<br>Maître de Conférences, Université de Paris | Examinatrice |

université PARIS-SACLAY
ÉCOLE DOCTORALE
Sciences Chimiques : Molécules, Matériaux, Instrumentation et Biosystèmes (2MIB)

**Titre :** Elaboration et caractérisation de CCM à base de membranes nanocomposites hybrides réticulées pour l'électrolyse de l'eau PEM

**Mots clés :** électrolyse de l'eau PEM, électrolyte polymère, membranes nanocomposites, $SiO_2$, hydrogène, oxygène.

**Résumé :** L'hydrogène est un vecteur énergétique chimique permettant le stockage des énergies primaires renouvelables et le rendu de services énergétiques décarbonés en temps différé. L'électrolyse de l'eau est appelée à jouer un rôle central dans le cadre de la transition énergétique. La technologie d'électrolyse de l'eau à électrolyte polymère à conduction protonique possède un ensemble de caractéristiques clés qui la rende particulièrement attrayante. Cependant les matériaux polymères usuels (acides perfluorosulfonés), bien que très performants, restent chers, ce qui nécessite la recherche d'alternatives. Ce travail de thèse porte sur la mesure du niveau de performances (conductivité, stabilité) de membranes nanocomposites hybrides réticulées en électrolyse de l'eau PEM. Ces membranes, développées dans le cadre de travaux précédents, sont constituées de groupement PSS (acide polystyrène sulfonique) greffés de manière covalente sur des nanoparticules de $SiO_2$. Ces groupements qui apportent la conductivité protonique sont ensuite dispersés dans une matrice PVDF qui apporte le squelette membranaire et réticulés grâce à des agents pontant spécifiques.

Le premier chapitre présente l'état de l'art dans le domaine. Les différentes techniques utilisées pour la fabrication et la caractérisation multiphysique des assemblages membrane-électrodes (CCM) sont décrites dans le second chapitre. Dans le troisième et le quatrième chapitres sont regroupés les résultats obtenus avec des CCM de référence, commerciaux et fabriqués au laboratoire. Dans le cinquième chapitre, nous présentons les résultats obtenus avec des CCM de laboratoire intégrant les membranes hybrides nanocomposites. Les performances mesurées ont été comparées aux références. Dans le sixième chapitre, nous présentons les résultats obtenus à l'aide d'un stack industriel de 5 cellules. L'un des défis a consisté à fabriquer des CCM intégrant les membranes hybrides nanocomposites et à optimiser les conditions de fabrication pour obtenir des niveaux de performances comparables aux références et répétables. Nous avons également été confrontés au manque de stabilité chimique de ces matériaux et nous avons déterminé les mécanismes de dégradation.

**Title:** Elaboration and characterization of CCM based on cross-linked hybrid nanocomposite membranes for PEM water electrolysis

**Keywords:** PEM water electrolysis, polymer electrolyte, nanocomposite membranes, $SiO_2$, hydrogen, oxygen.

**Abstract:** Hydrogen is a chemical energy vector allowing the storage of renewable primary energy and the rendering of carbon-free energy services in deferred time. Water electrolysis is expected to play a central role in the energy transition. Proton-conducting polymer electrolyte water electrolysis technology has a set of key features that make it particularly attractive. However, the usual polymer materials (perfluorosulfonated acids), although very efficient, remain expensive, which requires the search for alternatives. This thesis work focuses on measuring the level of performance (conductivity, stability) of cross-linked hybrid nanocomposite membranes in PEM water electrolysis. These membranes, developed in the context of previous work, consist of PSS (polystyrene sulfonic acid) groups covalently grafted onto $SiO_2$ nanoparticles. These groups which provide proton conductivity are then dispersed in a PVDF matrix which provides the membrane skeleton and cross-linked using specific bridging agents.

The first chapter presents the state of the art in the field. The different techniques used for the fabrication and multi-physical characterization of membrane-electrode assemblies (MCCs) are described in the second chapter. In the third and fourth chapters are grouped the results obtained with reference, commercial and laboratory-made, CCMs. In the fifth chapter, we present the results obtained with laboratory CCMs integrating hybrid nanocomposite membranes. The measured performances were compared to the references. In the sixth chapter, we present the results obtained using a 5-cell industrial short stack. One of the challenges was to manufacture CCMs integrating nanocomposite hybrid membranes and to optimize the manufacturing conditions to obtain performance levels comparable to references and repeatable. We were also confronted with the lack of chemical stability of these materials and we determined the mechanisms of degradation.

*Dedication …*

*I dedicate this work to:*

*My loving Parents;*

*My darling wife has always made sacrifices to help me;*

*My adorable brothers and sisters;*

*And all my family;*

*May they find here the remembrance of my gratitude, which, however great it may be, will never match their sacrifice and commitment.*

*No dedication could adequately express my feelings.*

# Acknowledgements

This dissertation research was conducted at the Institute of Molecular Chemistry and Materials of Orsay (**ICMMO**) as part of the "Research and Innovation Team in Electrochemistry for Energy (**ERIEE**)" under the supervision of **Prof. Pierre Millet**.

I would like to thank **Prof. David Aitken**, Professor at Paris-Saclay University and **Director of ICMMO**, for welcoming me to the Institute (ICMMO) which he directs.

I would like to thank my **thesis supervisor**, **Professor Pierre Millet** of the University of Paris-Saclay, for agreeing to direct this project. His counsel, accessibility, and encouragement made it possible for me to complete this task under optimal circumstances. I am highly grateful to him for the confidence and compassion he has shown me over the past three years and his efforts in the final stretch. Thank you for always being available and enthusiastic, with great patience and a constant supply of fresh ideas. Thank you for introducing and converting me into an electrochemist and drawing me to the field of research. It was a beautiful, intense, and rich experience.

I would like to thank **Storengy** for the financial support during the preparation of this thesis work. In particular, I would like to thank **M. Rostand Ngameni** (former Hydrogen Technical Support Manager) who initiated this work, **Mrs. Diane Defrenne** (EISE - Projets Industriels), **Mr. Frédéric Ghys** (Project Manager, H2 P2G), and **Mrs. Imane Oudghiri** (Ingénieur Projets & Procédés Energies renouvelables) who accepted to participate to the jury.

I would like to thank **Prof. Gaël Maranzana** and **Prof. Stéphane Marais** for accepting to evaluate this work as **reviewers,** and **Prof. Johnny Deschamps** and **Dr. Jennifer Péron**, for serving as a member of my **thesis committee**, providing advice, and agreeing to participate in the thesis jury as an **examiner**.

I also would like to thank **Dr. Janick Bigarre,** Research Engineer at CEA Le Ripault, for agreeing to participate in the evaluation of my thesis as invited jury members.

My sincere thanks and appreciation go to the **permanent staff of the "ERIEE**" team, whose advice and scientific expertise greatly benefited me : **Dr. Loic Assaud**, for his enlightening scientific discussions in various electrochemistry-related fields and **Prof. Sylvain Franger**, for his insightful comments.

I would also like to thank **Dr. Waleed El-Rouby** for his assistance, scientific advice, and investment in the experiments' problem-solving. I'd also like to express my gratitude to **Dr. Joumada Al Cheikh**, for her advice and assistance with CCM production and analysis.

I warmly thank **Dr. Serge Albacha**, for his help, time, and always fascinating scientific advices. With him, I never felt alone in the laboratory.

Within ICMMO, I would like to thank **Dr. Hafsa Korri-Youssoufi**, for all of her enlightening scientific discussions in the field of FT-IR spectroscopy. I would also like to express my gratitude to the technical platform members, particularly **Dr. Francois Brisset, research engineer** at ICMMO, for his assistance and time with SEM and EDS measurements.

In conclusion, I would like to thank the **entire ERIEE team**, **Mr. Alain Goussian, Mr. Benjamin Rondeau, Dr. Arun Meena, Mr Julius Akinribido, and Ms Maria El Khoueiry** for their assistance and social presence in the laboratory.

I would also like to thank **Mrs Annie Millet** for her kindness and constant availability and for arranging a fantastic party for the whole ICMMO, and **Mrs Nelly Lecoeur** for her consistent assistance with administrative work.

I would like to thank the fantastic team of Elogen, **Dr. Raphael Faure, Dr. Angel Villagra and Mr. Olivier Debellemaniere** for their great help in working with the industrial PEM test benches at Elogen.

My gratitude also extends to all the former and current post-docs, PhD students, and interns with whom I have collaborated in the laboratory. Last but not least, I would like to thank the permanent and temporary staff of the **ERIEE** Laboratory, as well as all those who have contributed remotely to the completion of this thesis, for all the good times spent together: coffee breaks, conversations, and especially their availability for scientific discussions.

Having always been motivated and enthusiastic, I would like to express my gratitude to each **family** member, particularly my parents, my wife, and my brothers and sisters, for their unwavering support and selfless sacrifice. They have always been there to support, assist, and encourage me throughout the execution of this project.

Finally, I'd like to express my sincere gratitude to my **friends** for their support; I'd like to thank Abdelrahman Behiry, Ahmed Anwer, Omar El Najar, Imran Khan, and Yahya Khwaira. When times are difficult, especially when you are away from your family and nothing goes right, you recognize your true friends. These people are there to help you through difficult times and make you laugh when things improve.

# Summary

# Abbreviations

| | |
|---|---|
| ADEME | French Agency for Ecological Transition |
| AEL | Alkaline electrolysis |
| APTES | 3-Aminopropyl)triethoxysilane |
| AST | Accelerated stress test |
| ATR | attenuated total reflectance |
| BoT | Beginning of Test |
| BPP | Bipolar plate |
| CAPEX | Capital expenditures |
| CCM | Catalyst-coated membrane |
| CEVE | 2-chloroethyl vinyl ether |
| CL | Catalyst layer |
| CNC | Computer numerical control |
| CPE | Constant phase element |
| Cs | Specific areal capacitance |
| CTFE | Chlorotrifluoroethylene |
| CV | Cyclic voltammograms |
| DEVEP | Diethyl vinyl ether phosphonated |
| EDLC | Electric double layer capacitor |
| EDS | Energy dispersive X-ray analysis |
| EF | Fermi levels |
| EIS | Electrochemical impedance spectroscopy |
| EoT | End-of-test |
| ESC | Electrolyte supported cells |
| EW | Equivalent weight |
| FCH-JU | Fuel Cells and Hydrogen Joint Undertaking |
| FTIR | Fourier-transform infrared spectroscopy |
| GHGs | Greenhouse gases |
| HER | Hydrogen evolution reaction |
| HF | High frequency |
| HFR | High frequency resistance |
| High HNC | CCM contains N212/HNC/N212 membranes + high catalyst loading |
| HNC Membrane | Hybrid NanoComposite Membrane |
| HT | High temperature |
| HNC-180-2 | HNC membrane treated at 180 °C for 2 h |
| HNC-180-6 | HNC membrane treated at 180 °C for 6 h |
| HNC-inhomogeneous | Inhomogeneous HNC membrane |
| HNC-low | HNC membrane treated at low temperature |
| IEA | International Energy Agency |
| IEC | Ion exchange capacity |
| IPCC | Intergovernmental Panel on Climate Change |

| | |
|---|---|
| IPN | Semi-interpenetrated networks |
| $IrO_2$ | Iridium dioxide |
| L | Inductor |
| LF | low frequency |
| low HNC | CCM contains N212/HNC/N212 membranes + low catalyst loading |
| LSCF | lanthanum strontium cobaltite ferrite |
| LSV | Linear Sweep Voltammetry |
| MAF | α-trifluoromethacrylic acid |
| meq/g | Milliequivalents per gram |
| moderate HNC | CCM contains N212/HNC/N212 membranes and moderate catalyst Loading |
| MPa | Mega Pascal |
| MPTES | Mercaptopropyltriethoxysilane |
| Mtoe | Million Tonnes of oil equivalent |
| N1110, N117 | Nafion 1110, Nafion 117 |
| N113, N115, N212 | Nafion 113, Nafion 115, Nafion 212 |
| Ni/GDC | Nickel/gadolinia-doped ceria |
| OER | Oxygen evolution reaction |
| OPEX | Operating expenses |
| P | Pressure |
| PDMOS | Polydimethoxysiloxane |
| PEEK | Polyether ether ketone |
| PEM | Proton exchange membrane |
| PEM2G | Power supply to PEM electrolysis to gas |
| PEMFC | Proton exchange membrane fuel cell |
| PEMWE | Proteon exchange membrane water electrolysis |
| PET | Polyethylene terephthalate |
| PFSA | Perfluorinated sulfonic acid |
| poly(CTFEalt-DEVEP) | (poly(chlorotrifluoro ethylene-alt diethyl vinyl ether phosphonated) |
| poly(VDF-co-CTFE) | Poly(vinylidene fluoride-co-chlorotrifluoroethylene) |
| poly(VDF-co-HFP)-g-MA | Poly(vinylidene fluoride-co-hexafluoropropylene) grafted Maleic acid |
| poly(VDF-co-MAF) | Poly[vinylidene fluoride-co-2-(trifluoromethyl) acrylic acid copolymers |
| PPS | Polypheneylene sulfide |
| PSSA | Polystyrene sulfonic acid |
| Pt | Platinum |
| Pt/C | Carbon-supported platinum |
| PTFE | Polytetrafluoroethylene |
| PTL | Felt porous transport layer |
| PTL-L | PTL of Large Ti particles and larger porosity |
| PTL-S | PTL of Small Ti particles and reduced porosity |
| PVDF | Polyvinylidene fluoride |

| | |
|---|---|
| PVDF-HFP | Poly(vinylidene fluoride-co-hexafluoropropylene) |
| R | resistance |
| Ref-commercial | Commercial Nafion-based CCM |
| Ref-lab | Reference CCM with only two Nafion 212 membranes |
| $R_{HER}$ | Charge transfer resistance of HER |
| $R_{OER}$ | Charge transfer resistance of OER |
| Rpm | Rounds per minute |
| SOEL | Solid oxide electrolysis |
| SR | Swelling ratios |
| SWOT | Strengths, weaknesses, opportunities, and threats |
| T | Temperature (°C, K) |
| THDA | 2,2,4-trimethyl-1,6-hexanediamine |
| Ti | Titanium |
| TOC | Total organic carbon |
| VBMS | 4-(vinyloxy) butyl methanesulfonate |
| WEC | World Energy Council |
| WETO | World Energy Technology Outlook |
| WU | Water uptake |
| YSZ | Yttria stabilized zirconia |

# General introduction

This doctoral thesis concerns the production of hydrogen by water electrolysis using the so-called PEM technology (proton exchange membrane or polymer electrolyte membrane). Developed in the 1970s, following the discovery and marketing of proton-conducting PFSA (perfluoro sulfonic acid ionomers) by the US company Dupont de Nemours under the trade name of Nafion®[1], this particular electrolysis technique which operates under temperature conditions close to ambient (0-100°C) was first used for military and space applications, in particular for the production of oxygen in an anaerobic environment. Indeed, the high ionic conductivity of the polymer electrolyte allows operation at high current density (several $A/cm^2$), under high service pressure (50 bars) and under high $\Delta P$ (integral $\Delta P$). This results in a small footprint, a highly desirable feature in spatially confined environments. Since the end of the $20^{th}$ century and the need for energy transition, technology has found civilian applications. Despite some gloomy spirits who believe that the over-capex resulting from the use of PFSAs and PGMs represents a crippling handicap, spectacular progress in terms of performance (OPEX) and cost reduction (CAPEX) has been achieved. The arrival on the market of thin reinforced membranes, in the wake of developments in the field of PEM fuel cells, offers the prospect of electrolysers that can operate up to 5 $A/cm^2$ with iso-energy efficiency and iso-capex, a characteristic making it possible to compensate for any over-capex and therefore making the technology completely competitive from an economic point of view. This satisfactory state of the art does not prevent further research in materials science. The main objective is to discover/develop alternative membranes containing little or no fluorine and catalysts containing little or no precious metals (Pt at the cathode and Ir at the anode are commonly used in PEM technology). And this is not motivated only for cost reasons. Regarding PFSA membranes, the problem stems from environmental concerns. PFSAs contain fluorocarbon backbones; fluorine is used for a dual purpose: (i) to provide high chemical stability allowing operation in the presence of native oxygen at a high anodic potential; (ii) to allow the deprotonation of the sulphonic acid groups, which provide proton conduction. The strength of the C-F bond is such that these compounds are very (too) stable and non-biodegradable. But the problem is more general. PFSAs are part of a much larger family of fluorocarbon compounds, the PFAs (perfluoroalkyl chemicals), some of which are in direct contact with the general public. Discussions are currently taking place at European level under the aegis of REACH to determine which PFA should be banned, and which can continue to be used. REACH is a European Regulation and stands for Registration, Evaluation, Authorization and Restriction of Chemicals. The objectives of REACH are "to provide a high level of protection of human health and the environment from the use of chemicals, and to allow the free movement of substances on the EU market". Even if PFSAs are not chemical compounds in direct contact with populations, the risks of leakage into the environment and contamination of food chains must be managed with care. This general context alone justifies the need to develop alternative membranes containing little or no fluorine. The CEA (Commissariat à l'Energie Atomique et aux Energies Alternatives) has developed a new family of hybrid nanocomposite (HNC) membranes, less fluorinated than PFSAs, for PEM fuel cell applications. Our thesis work consisted in using them to manufacture catalyst-coated membranes (CCM) and studying their electrochemical behavior in PEM water electrolysers.

[1] Nafion is a registered trade name of Chemours Co. Nafion® is replaced by Nafion thoughout this thesis.

# Chapter 1. State of knowledge

## 1.1. Context

One of the great challenges of our century is to meet the ever-increasing energy needs of the world's population, while preserving the environment. This question is currently at the center of societal and scientific issues and debates, in the context of the energy transition. Developed countries have acquired a high level of comfort and hygiene through the use of previously abundant energy resources. Population growth and the development of emerging countries such as India, China and Brazil are leading to a spectacular increase in energy needs. To meet this growing need for energy, Man constantly draws on the various primary energy sources available on Earth. A 2015 report by the International Energy Agency (IEA) shows that global energy consumption nearly doubled (**Figure 1.1**), from 4,661 to nearly 9,384 Mtoe (million tons of oil equivalent) per year between 1973 and 2015. Similarly, the study report "World Energy Technology Outlook" (WETO-$H_2$) predicts that this consumption will reach 22,000 Mtoe in 2050.

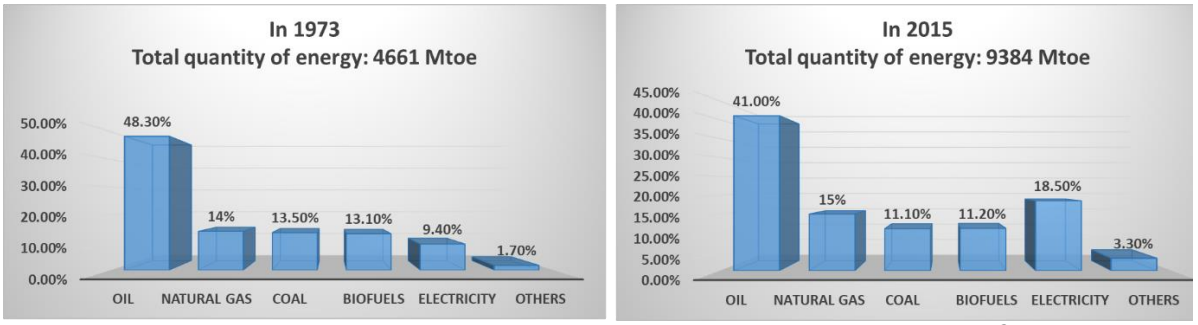


**Figure 1.1.** World energy consumption (left) in 1973; (right) in 2015[2].

Almost 80% of our energy consumption is based on fossil fuels (oil, coal, natural gas) (**Figure 1.1-right**). However, these fossil fuels are non-renewable resources, and the available reserves are not inexhaustible. According to the World Energy Council (WEC), the known coal reserves at the end of 2010 would cover 120 years of consumption at the current rate of extraction, 40 years for oil, and 65 years for natural gas[3]. New deposits are and will undoubtedly be discovered, but they are becoming increasingly limited and difficult to exploit. These resources are no longer sufficient to meet the next decades' energy needs. In addition, their massive use has raised questions about the environmental impact of greenhouse gases (GHG) emitted during their combustion. The main GHGs in the Earth's atmosphere are water vapour, carbon dioxide, and methane. Their role is essential for maintaining life on Earth. The greenhouse effect is a natural mechanism: trapping part of the infrared rays from the sun makes it possible to keep the earth's average surface temperature at + 15 ° C (instead of –18 ° C if this greenhouse mechanism did not work). However, anthropogenic GHGs artificially increase this effect. The Intergovernmental Panel on Climate Change (IPCC) has carried out numerous studies demonstrating the role of these anthropogenic GHGs in the variation of temperatures at the globe's surface, participating in the rise in the sea level and other extreme weather events. The following points reported in their fifth climate change assessment report[4] conducted in 2014 are particularly striking:

[2] International Energy Agency Report, 2017.
[3] World Energy Council Report, 2010.
[4] Fifth report of the Intergovernmental Panel on Climate Change, 2015.

- $CO_2$ from the combustion of fossil fuels plays a significant role in greenhouse gas emissions.
- It is still possible to limit the rise in global average temperature to + 2 ° C compared to the start of the industrial revolution if global greenhouse gas emissions are (reduced by 40 to 70% between 2010 and 2050).
- If humanity fully uses the available fossil fuel reserves, the planet earth would reach a warming of +4 to + 5 °C in 2100, which would lead to a continuation of this warming in the following century up to +7 or even + 8 °C.
- An essential result of the report is to show that the increase in fossil fuel reserves with the exploitation of unconventional oil and natural gas resources negates the hope that a rapid depletion of fossils could avoid the climate problem.

Indeed, the global average temperature is an excellent indicator of climate change as it synthetically reflects the climate's response to various factors, whether of natural or human origin. **Figure 1.2** shows the planet's average temperature evolution from 1850 to 2015[5]. The global average temperature is simulated by two climate models taking into account: the only natural external factors (solar variability and volcanism) (curve in blue), and the external biological factors added are those of human origin (orange curve).

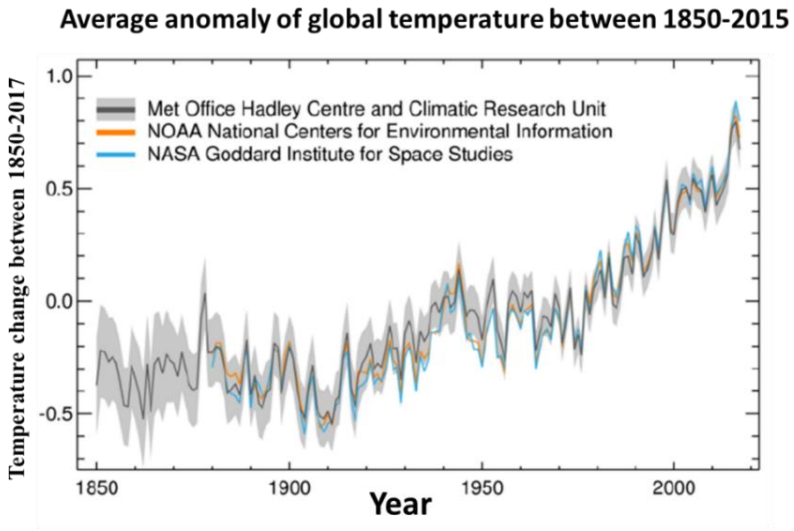


**Figure 1.2.** Evolution of the average temperature measured at the surface of the Earth (black curve).

In addition, numerous studies show that many physical and biological systems suffer from profound disturbances: the observed trends align with predictions linked to climate warming. Many models of climate change produced by the IPCC have been tested using increasingly powerful computers. Only those considering human activity can follow the evolution observed on our planet. However, a marked increase in $CO_2$, a potent GHG, began at the start of the industrial era and is estimated to be of anthropogenic origin. Over the past ten years, several modelling studies have shown 'the existence of a potentially significant positive feedback' (reaction amplifying the phenomenon) between climate change and the carbon cycle. The amount of anthropogenic $CO_2$ absorbed by natural carbon sinks (ocean and continental biosphere) depends on the climate. When the weather warms, the sinks are less and less efficient at absorbing carbon. Therefore, we can no longer simulate temperature and atmospheric $CO_2$ changes independently.

[5] Climate change: new French simulations for the next IPCC report, 2012.

Thus, some simulations consider this new exercise's coupling between the climate and the carbon cycle. **Figure 1.3**. shows the evolution of $CO_2$ emissions from fossil fuel resources (coal, oil, and gas) and industries (especially the cement industry) since 1850. They increased sharply during the period 1950-2020.

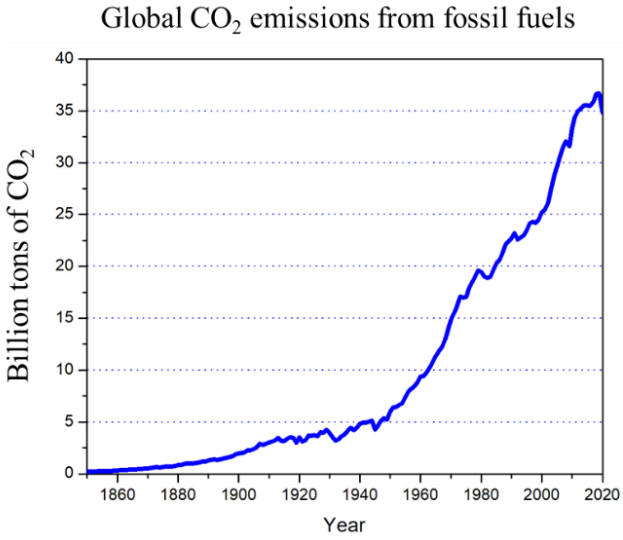


**Figure 1.3.** World annular $CO_2$ emissions from fossil fuels and industry[6].

Many efforts are being made to find alternatives to limit their harmful effects and especially to preserve the fossil resources of our planet, which is part of the energy transition context based on implementing sustainable and renewable energies. These are inexhaustible primary energies in the long term because they arise directly from natural phenomena (regular or constant) linked to the significance of the Sun or Earth. They are also clean energies that emit little or no GHGs and therefore have no environmental impact. The primary renewable energy sources currently in use are hydroelectric power, wind power, energy from biomass, solar energy (thermal and photovoltaic), geothermal energy, and marine energy.

It should be noted that the energy received by the Earth from the Sun's radiation in one hour would be sufficient to meet the global energy demand over a year[7]. However, if these energies are readily convertible into electricity, their large-scale distribution is still challenging to implement due to a lack of storage means and adequate transport solutions. Indeed, their production occurs intermittently and is unevenly distributed geographically. One solution would be to use chemical energy carriers such as molecular hydrogen, allowing energy to be easily transported to its final place of use.

Reducing $CO_2$ emissions within the European Union must be achieved, at least in part, by switching from fossil fuels to more environmentally friendly technologies. Global warming[8], which can be attributed to a rise in $CO_2$ levels emitted into the atmosphere[9,10], is a significant worry in today's world.

[6] Andrew, Robbie M., & Peters, Glen P. (2021). *The Global Carbon Project's fossil CO2 emissions dataset*. Zenodo.
[7] N. S. Lewis, D. G. Nocera, *Powering the planet: Chemical challenges in solar energy utilization*, Proc. Nat. Ac. Sc. USA 2006, 103, 15729-15735.
[8] Mann, Bradley, Hughes. *Northern hemisphere temperatures during the past millennium inferences, uncertainties, and limitations*. Geophys. Res. Lett. 1999;26:759-62.
[9] Cao L, Bala G, Caldeira K, Nemani R, Ban-Weiss G. *Importance of carbon dioxide physiological forcing to future climate change*. Proc. Natl. Acad. Sci. U. S. A. 2010;107:9513-8.
[10] Princiotta F. *Global climate change and the mitigation challenge*. Journal of the Air and Waste Management Association 2009;59:1194-211.

$CO_2$ levels have continued to rise[11] in recent decades as the world's population has grown and the demand for energy and material commodities has increased to record levels[12,13]. It is anticipated that society needs to be more electrified; in this sense, the hydrogen society fits in perfectly. During periods of low electrical demand, electricity from ecologically friendly sources (such as hydropower, wind turbines, and solar panels) can be stored as hydrogen and released during periods of high demand. A safe and environmentally friendly method of producing hydrogen is required to implement a 'Hydrogen Society.' Electrolysis is one method of producing clean hydrogen. The hydrogen produced is pure and environmentally benign if the electrical energy used to split the water originates from renewable sources.

Hydrogen is anticipated to play a central role in the energy transition from fossil fuels to renewable sources. It can reduce carbon emissions in industry, transportation, buildings, and power generation. In addition, hydrogen can store the excess solar and wind energy projected to reach 250–300 TWh by 2030. Thus, it is anticipated that by 2050, this versatile energy carrier will achieve the neutral climate objective ratified by several countries during the 21st conference of the parties that led to the Paris Climate Agreement. To achieve such widespread use of hydrogen, the annual demand for hydrogen must increase from 8 EJ today to approximately 80 EJ by 2050. 1 EJ equals 278 TWh of electricity, roughly one day's worth of global energy demand[14]. Consequently, a GW-scale increase in hydrogen production is required for the energy transition. Hydrogen is produced from various hydrogen-containing sources, including fossil fuels, water, and biomass[15].

The dissociation of water into molecular hydrogen and oxygen is an endergonic transformation ($\Delta G>0$). The following equations are the key thermodynamic characteristics of water dissociation:

$$H_2O\ (l) \rightarrow H_2\ (g) + ½\ O_2\ (g)$$

$$\Delta H^o = +\ 286\ kJ/mol\ ;\ \Delta S^o = +\ 0.163\ kJ/mol;\ T.\Delta S^o = +\ 49\ kJ/mol;\ \Delta G^o = +\ 237\ kJ/mol$$

These values of the thermodynamic quantities of reactions are at standard conditions. The dissociation of one mole of water requires 286 kJ or 237 kJ of electricity and 49 kJ of heat to accompany the entropy increase at constant temperature and pressure. The diagram in **Figure 1.4** shows a sectional view of a water electrolysis cell with the position of the Fermi levels ($E_F$) of the anode and of the cathode under current flow. The reaction starts when the cell voltage becomes equal to or greater than the thermodynamic dissociation voltage of water[16].

[11] Dufresne JL, Friedlingstein P, Berthelot M, Bopp L, Ciais P, Fairhead L, et al. *The magnitude of positive feedback between future climate change and the carbon cycle*. Geophys. Res. Lett. 2002;29:43-1-4.
[12] Siegenthaler U, Stocker TF, Monnin E, Luthi D, Schwander J, Stauffer B, et al. *Stable carbon cycle-climate relationship during the late Pleistocene*. Science (Washington DC) 2005;310:1313-7.
[13] Harris DC. *Charles David Keeling and the Story of Atmospheric CO2 Measurements*. Anal. Chem. 2010;82:7865-70.
[14] Hydrogen Council, November 2017, Hydrogen scaling-up.
[15] Nikolaidis P, Poullikkas A. *A comparative overview of hydrogen production processes*. Renew Sustain Energy Rev 2017;67:597–611. https://doi.org/10.1016/j.rser.2016.09.044.
[16] D. Bessarabov and P. Millet, PEM water electrolysis, "*Hydrogen and Fuel Cells Primers*", B.G. Pollet Editor, 1st Edition, Elsevier (2018).

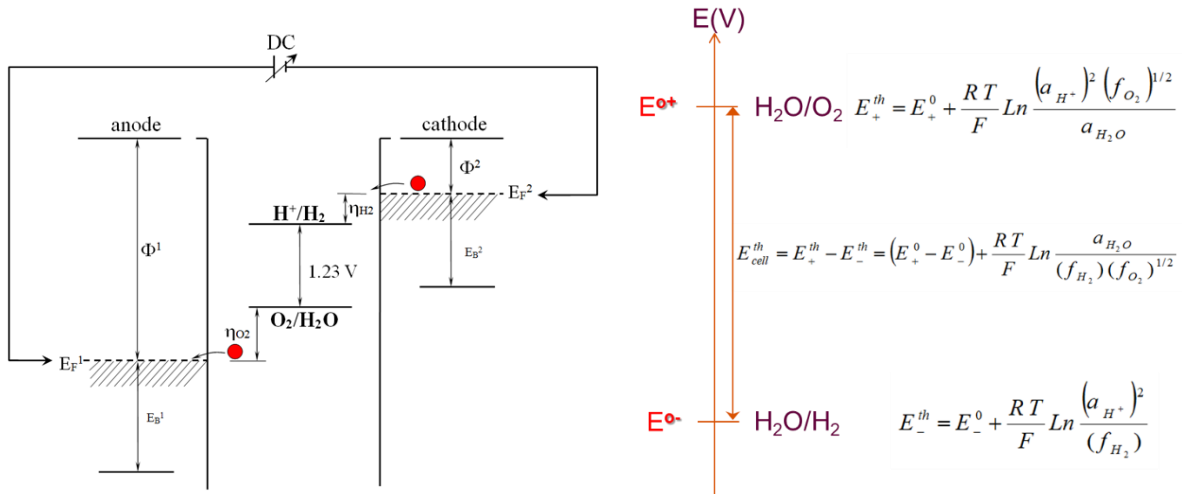


$$E_{+}^{th} = E_{+}^{0} + \frac{RT}{F} Ln \frac{(a_{H^+})^2 (f_{O_2})^{1/2}}{a_{H_2O}}$$

$$E_{cell}^{th} = E_{+}^{th} - E_{-}^{th} = (E_{+}^{0} - E_{-}^{0}) + \frac{RT}{F} Ln \frac{a_{H_2O}}{(f_{H_2})(f_{O_2})^{1/2}}$$

$$E_{-}^{th} = E_{-}^{0} + \frac{RT}{F} Ln \frac{(a_{H^+})^2}{(f_{H_2})}$$

**Figure 1.4.** (left) Schematic drawing showing the Fermi levels in a water electrolysis cell during operation; (right) expression of half-cell potentials.

## 1.2. Water electrolysis technologies

Water can be electrolyzed using a variety of methods, the three most common of which are: proton exchange membrane (PEM) electrolysis, alkaline electrolysis (AEL), and solid oxide electrolysis (SOEL)[17]. The alkaline technique is by far the most mature of these technologies, while SOEL is still in its early stages of development. **Figure 1.5** shows the block diagram of the three main water electrolysis technologies.

[17] Jensen JO, Bandur V, Bjerrum NJ, Jensen SH, Ebbesen S, Mogensen M, et al., *Pre-investigation of water electrolysis*. 2008: Lyngby. p. 195.

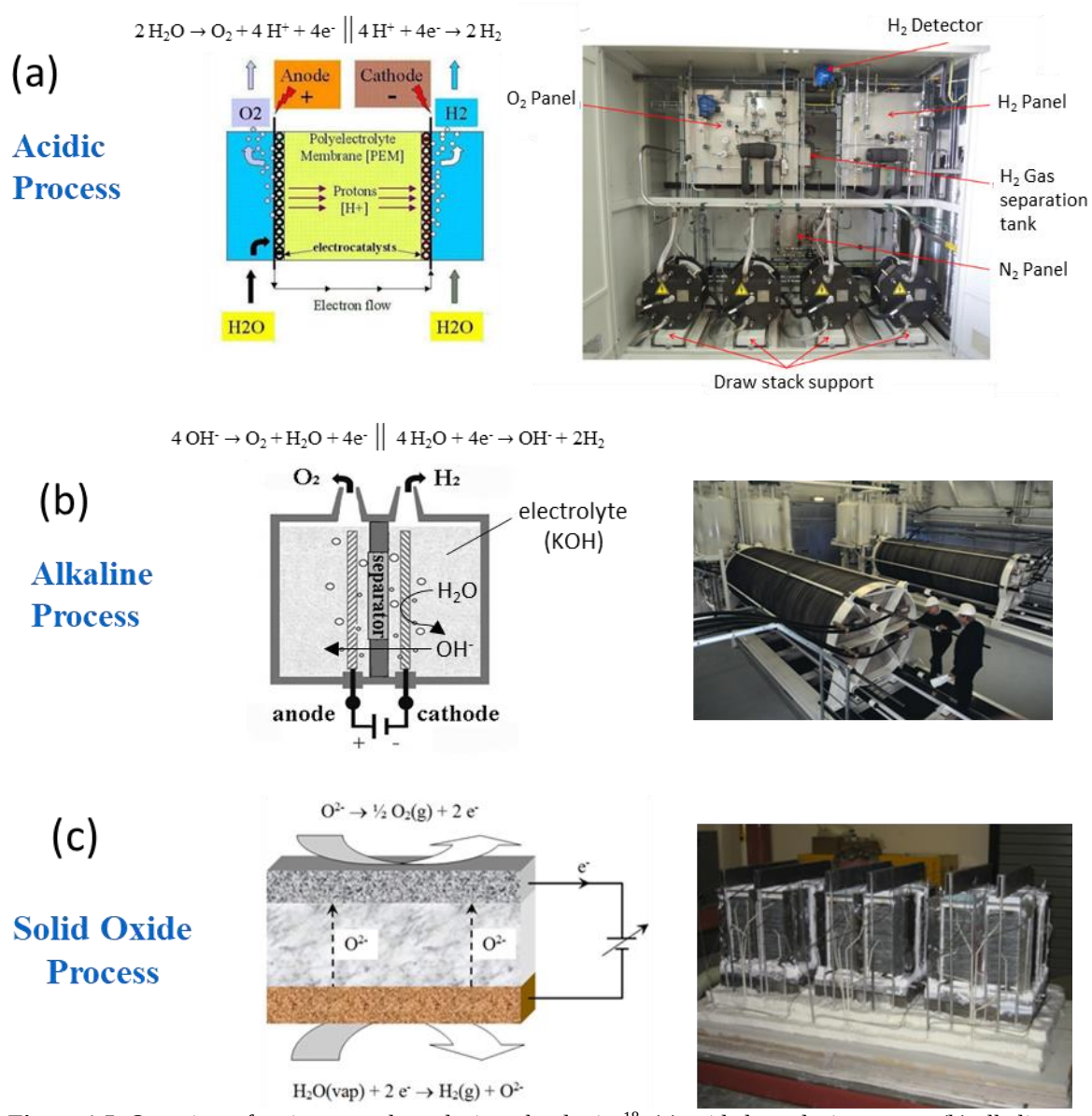


**Figure 1.5.** Overview of main water electrolysis technologies[18], (a) acid electrolysis process, (b) alkaline electrolysis process, and (c) solid oxide electrolysis process**.**

The potentials of the two half-reactions strongly depend on the pH of the electrolysis and the operating temperature. **Figure 1.6** shows the situation in strongly acidic conditions (PEM electrolysis) and in strongly alkaline conditions (alkaline electrolysis). The basification of the pH shifts the potentials towards less oxidizing, more protective values in the field of passivation of common metals. This is one of the strengths of alkaline water electrolysis compared to PEM, which requires precious metal-based electrocatalysts. **Figure 1.7** shows the effect of temperature on the iV curves of the water electrolysis reaction at two different operating temperatures. The iV curves of the $H_2/O_2$ fuel cell reactions are also plotted for direct comparison. PEM and alkaline water electrolysis operate under near-ambient temperature and pressure conditions. The oxygen/water redox system is significantly irreversible, and a significant oxygen-evolving overvoltage is required in both cases.

[18] P. Millet, *'Electrochemical Technologies for Energy Storage and Conversion',* chapter 9, Water electrolysis for hydrogen generation. R-S. Liu, X. Sun, H. Liu, L. Zhang and J. Zhang Editors, J. Wiley & Sons (2011).

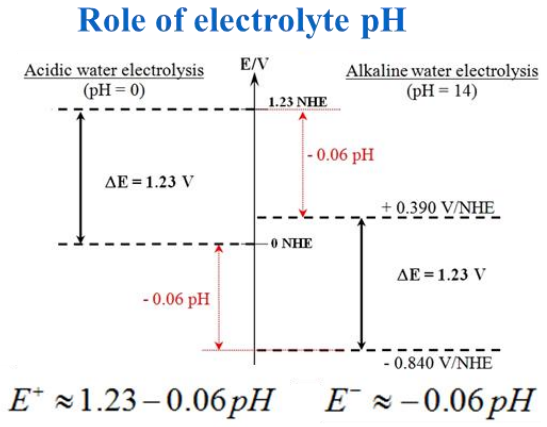


**Figure 1.6.** Anode and cathode potential levels as a function of electrolyte pH.

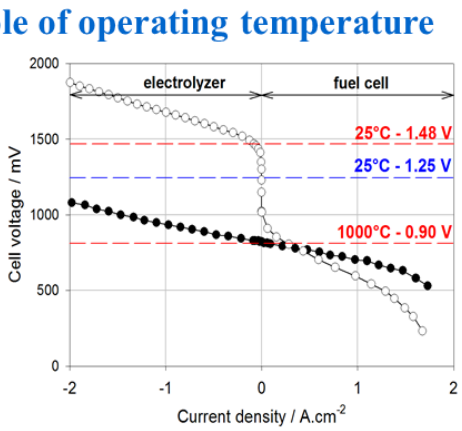


**Figure 1.7.** Typical iV curves were measured at ambient and elevated (1,000 °C) temperatures.

The following **Figure 1.8** provides a comparison of the three main water electrolysis technologies. This comparison is based on a set of performance indicators. At the European level, the interested reader is invited to learn about the work of the Fuel Cells and Hydrogen Joint Undertaking (FCH-JU), which publishes roadmaps taking into account the rapid evolution of performance in the field. It is interesting to note on the graph a certain complementarity between these technologies, even if they are in competition with each other.

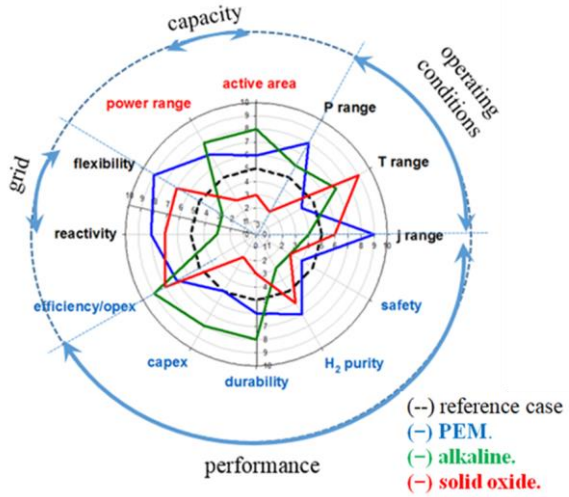


The reference case is the following:

- j range: 0 – 2.0 A.cm$^{-2}$.
- T range : 0-60ºC. P range : 0 – 35 bars.
- cell active area: 600 cm$^2$.
- power range : 0 – 1 MW.
- Flexibility: full flexibility between zero and peak power.
- Reactivity: zero -> nominal power < 30 sec.
- efficiency: < 50 kWh.kg$_{H2}^{-1}$ @ 2 A.cm$^{-2}$.
- capex: 1,500 €/kW @ 1 MW-scale.
- durability: 2% efficiency loss/year.
- $H_2$ purity at delivery : 4 N.
  Safety: %$H_2$ in $O_2$ < 25% ILE @ anytime

**Figure 1.8.** Comparison of the three main water electrolysis technologies[19].

### 1.2.1. PEM water electrolysis

PEM water electrolysis is distinguished from alkaline technology by the use of a solid electrolyte consisting of a protonically conductive perfluorinated sulfonic acid (PFSA) polymer membrane (**Figure 1.9**). This technology's advantages include the absence of liquid electrolytes, compactness, ease of manufacture, simplicity of design and operation, limitation of corrosion issues, significantly higher performance, and reduced sensitivity to environmental variations—input (interesting for operation with intermittent renewable sources). However, the cost of the polymer membrane and the use of electro-catalysts based on noble metals have made equipment more expensive than alkaline electrolysers of the same capacity.

[19] L. Allidières, A. Brisse, P. Millet, S. Valentin, M. Zeller, *On the ability of PEM water electrolyzers to provide power grid-services*, Int. J. Hydrogen Energy, 44(20) (**2019**) 9690-9700. DOI: https://doi.org/10.1016/j.ijhydene.2018.11.186

Polymer membrane electrolysis is nevertheless regarded as an already competitive technology due to the numerous advancements in fuel cells of comparable technology (PEM) and the resulting cost reduction. Small-capacity polymer membrane electrolysis is a mature technology utilized for decades in subsea applications (oxygen generation aboard nuclear submarines) and space (for the generation of oxygen in living compartments). These units can operate at atmospheric pressure, or at several tens of bars, or even several hundred bars. This type of electrolyzer is ideally suited for coupling with a renewable energy source because it can easily accommodate fluctuations in available electrical power. Furthermore, due to the improved performance of available electrolyzers, this acid electrolysis yields 5 to 10 percentage points higher efficiency than alkaline electrolysis. PEM electrolysers which were initially developed and used for oxygen generation in anaerobic conditions (space and underwater), are now widely used for hydrogen generation and mature enough to compete with AEL. **Figure 1.9** depicts the cross-section of a conventional PEM water electrolysis cell.

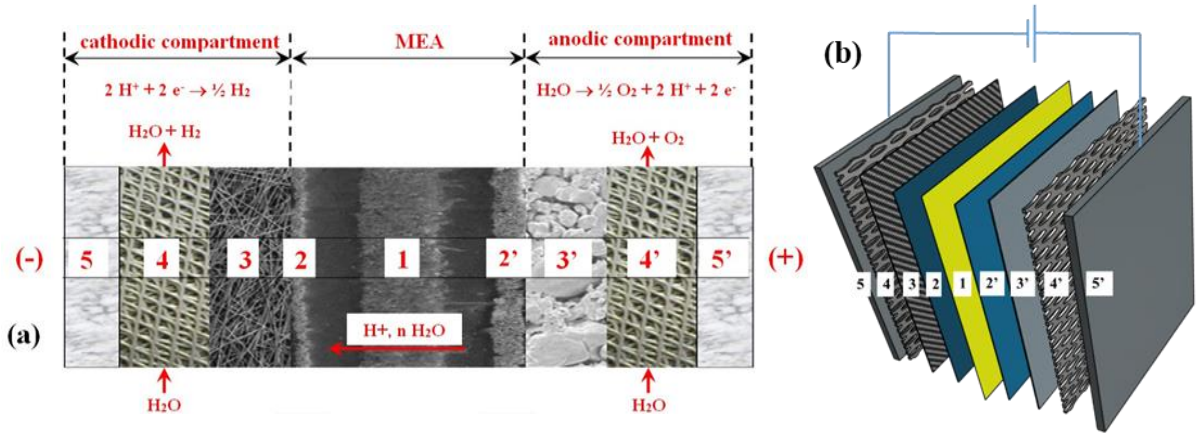


**Figure 1.9.** Schematic diagrams showing (a) the cross-section[20], and (b) the 3D structure of a conventional PEM water electrolysis cell. 1- polymer electrolyte; Cathodic compartments: 2- Pt/C Catalyst layer (CL), 3- Carbon felt porous transport layer (PTL), 4- a flowfield grid, and 5- a bipolar plate (negative pole). Anodic compartments: 2'- $IrO_2$ CL, 3'- Ti sintered particles PTL, 4'- a flowfield grid, and 5'- a bipolar plate (positive pole)[21].

The primary advantages of a "zero-gap" cell are its small thickness (5-7 mm on average). Its compactness (which makes dissipation less pronounced than conventional gap cells and favours operation at current densities up to 5 A/cm$^2$) and its longevity (up to 70,000 h) are typical good desires. Such characteristics explain why the technology has been used for oxygen generation in locations (underwater and in space) where compactness trumps efficiency and cost. Two titanium (Ti) endplates delimit the unit cell (5,5')[21]. The catalyst-coated membrane (CCM) is the heart of the cell (1, 2, 2'), where liquid water molecules transferred from the anodic chamber (4') are converted into oxygen gas (2') and hydrogen gas (2). A thin (50-200 µm thick) proton-conducting perfluorosulfonic acid (PFSA) polymer membrane fills the distance between the anode and cathode. The two catalytic layers (2- 2') contain a mixture of catalyst particles embedded in a PFSA matrix (in electrical contact). Electrochemical engineers use this concept of the so-called "3-D electrode" to increase the overall roughness of catalyst/electrolyte interfaces to reduce over-voltages by improving the value of apparent exchange current densities. Platinum (Pt) is the most effective and stable metal for the hydrogen evolution reaction (HER) (2) in acidic aqueous environments.

[20] Rozain C, Millet P. *Electrochemical characterization of Polymer Electrolyte Membrane Water Electrolysis Cells.* Electrochim Acta 2014;131:160–7. https://doi.org/10.1016/j.electacta.2014.01.099.
[21] Villagra A, Millet P. *An analysis of PEM water electrolysis cells operating at elevated current densities*. Int J Hydrogen Energy 2019;44:9708–17. https://doi.org/10.1016/j.ijhydene.2018.11.179.

Following trends in fuel cell technology, carbon-supported platinum nanoparticles (Pt/C) are now used at the cathode (2) of PEM water electrolysis. Unsupported iridium dioxide ($IrO_2$) particles are used at the anode (2') to promote oxygen evolution rection (OER) despite their low bulk electronic conductivity. Liquid water is pumped across the cells to feed the reaction and cool the cells. Various cell designs provide the necessary voids for pumping water across the cells: this can be a titanium grid (**Figure 1.9**, 4-4'). A porous transport layer (PTL) (3,3') is positioned between the CCM and the two cell spacers to enable water and gas flow through the cell.

When compared to alkaline electrolysers, PEM electrolysers have various advantages. PEM electrolysers are safer than alkaline electrolysers because they use a solid electrolyte rather than circulating a highly alkaline electrolyte[22], and they produce higher-purity hydrogen (99.99 %)[23]. Finally, it is possible to produce pressurized gases directly at 70 bar. Even differential pressurization (systems with approximately 20 bar pressure difference between the anode and cathode (high-pressure side)) due to better gas separation, and they can be made more compact because high current densities (between 1-2 A/cm$^2$) are possible[24]. The following equations explain the electrochemical process of water splitting at the anode and the cathode in an acidic medium:

| | |
|---|---|
| Anode: | $2\ H_2O \rightarrow O_2 + 4\ H^+ + 4e^-$ |
| Cathode: | $4\ H^+ + 4e^- \rightarrow 2\ H_2$ |
| Total: | $2\ H_2O \rightarrow O_2 + 2\ H_2$ |

On the one hand, a water electrolyser contains an electrochemical reactor (generally a stack of cells) and a set of ancillary functions forming part of the balance-of-plant (**Figure 1.10**). The main functions are the AC/DC transformer and rectifier, the water purification unit; the liquid/gas separation units; the water cooling unit; the hydrogen purification and drying unit[25]. The main difference is that in PEM, water is required on the oxygen side, whereas in alkaline, water is necessary on the hydrogen side.

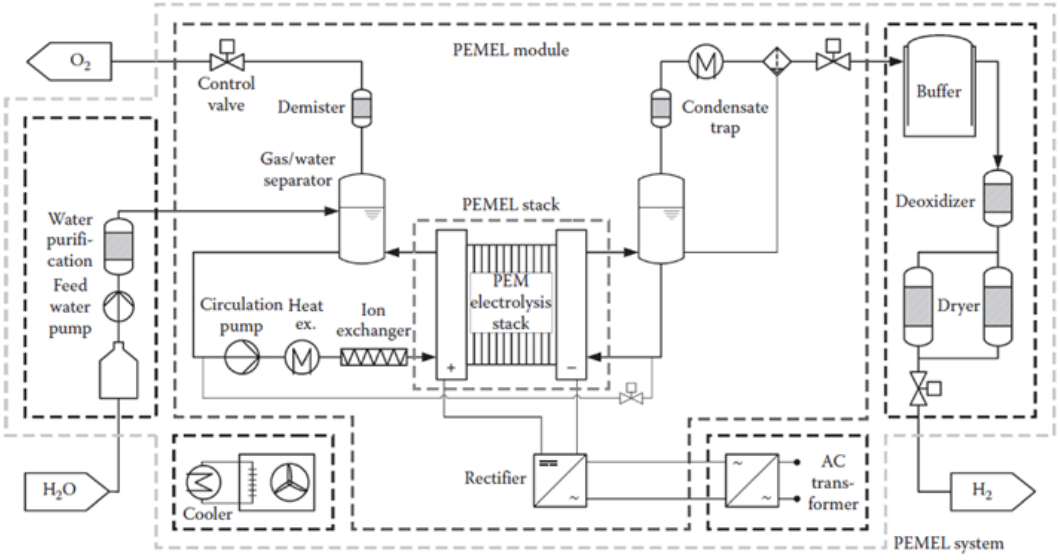


**Figure 1.10.** Balance of plant of PEM electrolyzer[25].

[22] Millet P. *Design and performance of a solid polymer electrolyte water electrolyzer*. Int J Hydrogen Energy 1996;21:87–93. https://doi.org/10.1016/0360-3199(95)00005-4.
[23] Grigoriev SA, Millet P, Volobuev SA, Fateev VN. *Optimization of porous current collectors for PEM water electrolysers*. Int J Hydrogen Energy 2009;34:4968–73. https://doi.org/10.1016/j.ijhydene.2008.11.056.
[24] Rasten E, Hagen G, Tunold R. *Electrocatalysis in water electrolysis with solid polymer electrolyte*. Electrochim Acta 2003;48:3945–52. https://doi.org/10.1016/j.electacta.2003.04.001.
[25] T. Smolinka, Water Electrolysis, Fuels – Hydrogen Production | Water Electrolysis, Elsevier (2009).

Some key advantages and limitations of PEM water electrolysis technology are:

Advantages

- Operation at high current density and small footprint
- Elevated operating pressure (60-80 bars $H_2$)
- The technology can operate under large DP
- Excellent flexibility and reactivity
- Lifespan: 50 – 70 khrs

Limitations

- Less mature and track record than alkaline
- CAPEX much larger than alkaline
- Capacity of commercial systems still limited

An essential comparison criterion is the specific cost of the hydrogen produced, expressed in euros per unit of mass or volume of hydrogen. The two main cost items are Capital expenditures (CAPEX) and operating expenses (OPEX) (**Figure 1.11**). The value of CAPEX reduced to kg of hydrogen takes into account the investment cost and the lifetime of the investment. The value of the OPEX reduced to kilograms of hydrogen depends essentially on the price of the electric kWh. Therefore, the total cost of the hydrogen produced includes a CAPEX component and an OPEX component. It is necessary to increase the current density to reduce the relative weight of the CAPEX and decrease the current density to reduce the relative importance of the OPEX[21]. PEM technology has a higher CAPEX but can operate at higher current densities, which allows it to be competitive.

$$CAPEX\ (€/kg_{H_2}) = \left(\frac{2F(C.mol^{-1}).IC(€)}{T(s).S(cm^2).M_{H_2}(kg_{H_2}.mol^{-1})}\right).\frac{1}{j(A.cm^{-2})}$$

$$OPEX\ (€/kg_{H_2}) = \left(\frac{U_{cell}(V).F(C.mol^{-1})}{3600(J.kg.kWh^{-1}.mol^{-1})}\right).EC(€/kWh)$$

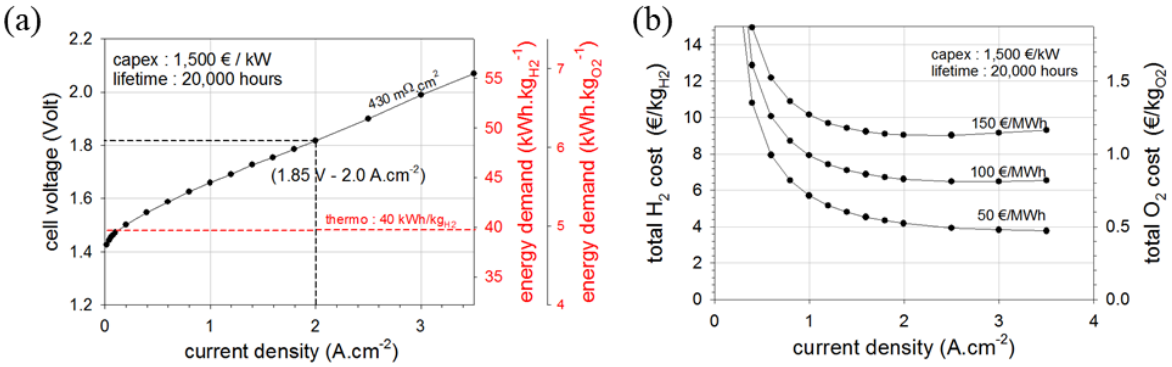


**Figure 1.11.** (a) typical iV curves of PEM water electrolysis cells; (b) total hydrogen cost as a function of operating current density for PEM water electrolysis[21].

The price of hydrogen produced by the electrolysis of water is set at 80% by that of the electric kWh[26]. The eruption of intermittent in the energy mix brings new regulatory needs and financial opportunities to light. Therefore, the idea is to operate the electrolysers at nominal power and devote resources that can go up to twice the nominal current density for network regulation. The associated remuneration makes it possible to make hydrogen more competitive for electric mobility applications. The reserve mechanisms managed by the network operators reveal the need for more or less dynamic regulation, and more or less remunerative. The difficulty lies in manufacturing electrolysers that are flexible and responsive enough to position themselves in this type of market. **Figure 1.12** shows an industrial PEM plant with stacks and balance of plant.

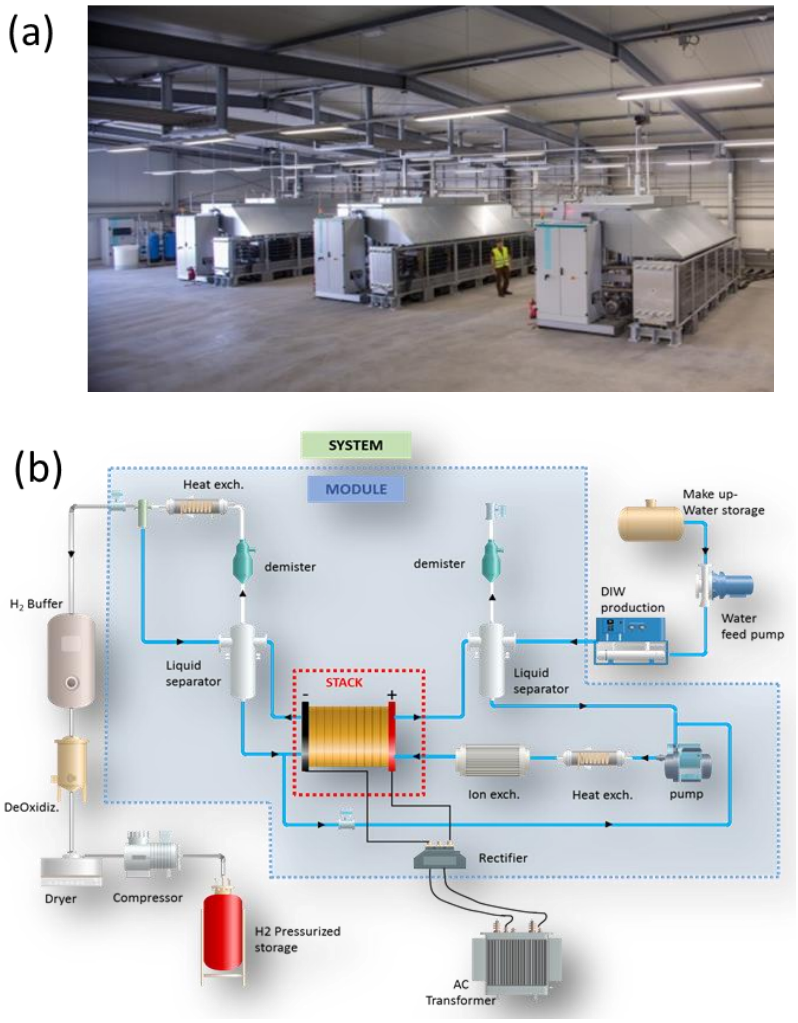


**Figure 1.12.** (a) PEM water electrolysis plant at Mainz (Germany, courtesy Siemens Co.) (b) balance-of-plant of a PEM water electrolysis unit.

The characteristics of PEM electrolysis vis-a-vis the electricity grid regulation market are summarized in **Figure 1.13**. The measurements were made on MW-scale systems, but the cell's results are expressed per $cm^2$. This technology is known to be flexible and responsive enough to produce by following the instructions given by the operator of the primary and secondary reserves[27].

[26] G. Tsotridis, A. Pilonga, *Low Temperature Water Electrolysis Terminology*, JRC (2017).
[27] Allidières L, Brisse A, Millet P, Valentin S, Zeller M. *On the ability of pem water electrolysers to provide power grid services*. Int J Hydrogen Energy 2019;44:9690–700. https://doi.org/10.1016/j.ijhydene.2018.11.186.

The onset of fluctuating power setpoints can lead to efficiency losses, usually for limited periods. There is, however, a double difficulty: correct management of set point overruns during cold starts and power stability during stationary phases. The substantial variation in the impedance of the stacks as a function of the operating temperature makes these problems difficult to resolve.

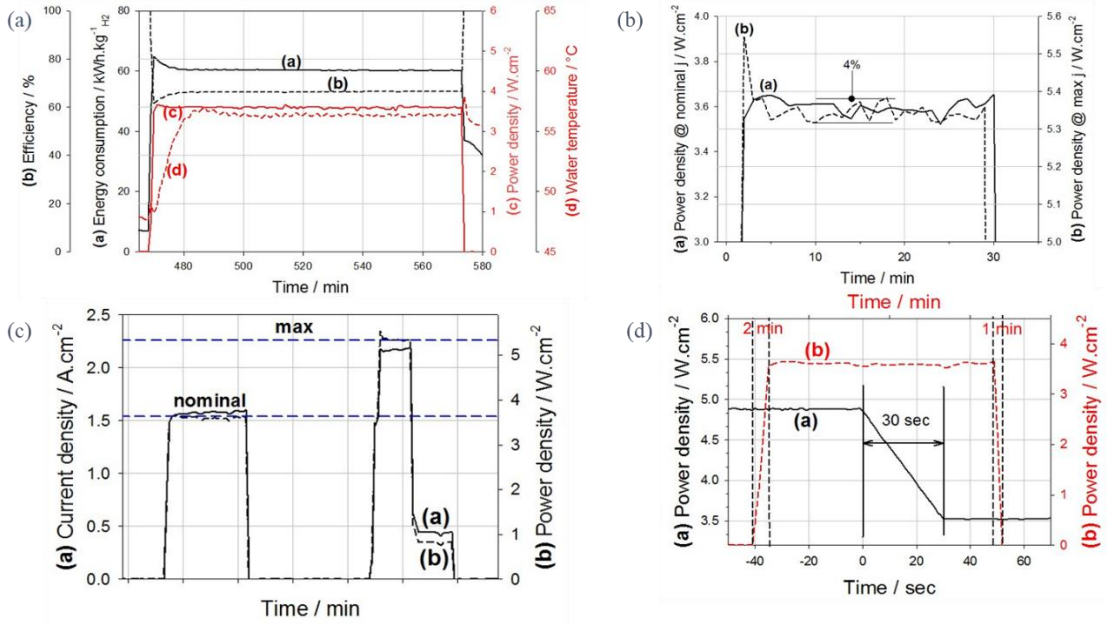


**Figure 1.13.** Dynamic characteristics of a MW-size PEM water electrolyser. (a) efficiency at the onset of a power request; (b) power fluctuations on a power plateau; (c) process flexibility; (d) ramp-down power setpoint.

### 1.2.2. Alkaline water electrolysis

The history of alkaline water electrolysis has been covered in detail previously[28]. Before Volta 1800 created the first powerful battery and the voltaic column, electrolysis could not be used in a targeted manner[29]. In his scientific works, which he did not publish until 1834, Faraday mentioned electrolysis for the first time in 1820[30] when discussing water splitting. From 1920 to 1930, the electrolysis industry flourished due to the high demand for ammonia. In Canada and Norway, plants with an installed capacity of 100 MW were primarily powered by hydroelectricity[31].

In 1925, an American engineer, Murray Raney, developed a highly active nickel catalyst that bears his name[32]. He investigated the activity of the electrode catalysts using finely-grained nickel (Raney nickel). He created a concrete surface of active catalyst by combining metallic nickel with silicone and then leaching the silicone with NaOH. Two years later, a patent describes the substitution of aluminium for silicon. Ni-based electrodes remain the most critical catalyst for alkaline electrolysis (AEL). In 1939, a single electrolyzer, for the first time, achieved a production rate of 10,000 $Nm^3/h$. 1948 introduced the first high-pressure industrial electrolyzer (Lonza) by E.A. Zdansky[33].

[28] D. Stolten, *Hydrogen and Fuel Cells: Fundamentals, Technologies and Applications*, 1st ed., Wiley-VCH, Weinheim, 2010. n.d.
[29] A. Volta. XVII. *On the electricity excited by the mere contact of conducting substances of different kinds*. In a letter from Mr. Alexander Volta, F. R. S. Professor of Natural Philosophy in the University of Pavia, to the Rt. Hon. Sir Joseph Banks, Bart. K.B. P. R. Philos Trans R Soc London 1800;90:403–31. https://doi.org/10.1098/rstl.1800.0018.
[30] K.J. Laidler, The chemical history of a current, Can. J. Chem. 75 (1997) 1552–1565. n.d.
[31] LEROY R. *Industrial water electrolysis: Present and future*, Int J Hydro. En. 1983;8:401–17. https://doi.org/10.1016/0360-3199(83)90162-3.
[32] M. Raney, *Method of producing finely-divided nickel*, US Patent 1563587 (1925), US Patent 1628190 (1927).
[33] KREUTER W. Electrolysis: *The important energy transformer in a world of sustainable energy*. Int J Hydrogen Energy 1998;23:661–6. https://doi.org/10.1016/S0360-3199(97)00109-2.

Since the efficiency of a system is strongly influenced by its operating temperature, corrosion-resistant materials were developed and tested successfully in AEL at 120°C in 1950. A year later, Lurgi utilized Lonza's technology and, for the first time, designed a pressure electrolyzer at 30 bar (Stat Oil- Hydro). After Winsel and Justi submitted their patent for Raney nickel in 1954, it was recognized for use in AELs[34] in 1957 Raney nickel is encased in a metal matrix, improving its electrical conductivity and mechanical stability. In 1967, Costa and Grimes introduced the zero-gap geometry for the electrode arrangement to decrease cell resistance by reducing the distance between the electrodes[35].

In alkaline electrolysis, oxygen and hydrogen are consequently released on the anode and cathode. In industrial electrolyzers, 20–40 wt % sodium or potassium hydroxide solution is used as the electrolyte to provide the necessary ionic conductivity. The porous or punched metal electrodes are positioned close to the anion-conducting diaphragm and electrically connected to the contact plates that separate each cell in the stack. The equilibrium voltage $U_{rev}$ for water splitting can be calculated using the equation. Half-cell reactions are [36]:

| | |
|---|---|
| Anode: | $4\ OH^- \rightarrow O_2 + 2\ H_2O + 4e^-$ |
| Cathode: | $4\ H_2O + 4e^- \rightarrow 4\ OH^- + 2H_2$ |
| Total: | $4\ H_2O \rightarrow 2\ O_2 + 4\ H_2$ |

In operational systems, electrolyte circuit cooling must be efficient. Between 50 and 80 °C is the current operating temperature of the AEL. A rise in operating temperature above 80 °C would result in greater efficiency. At higher temperatures, however, increased corrosion and consequently accelerated degradation rates of the cells and the material must also be accounted for. The advantages of alkaline electrolysis, in general, include durability, low costs, and operation under up to 30 bar pressures. Alkaline electrolysis, which is susceptible to corrosion, has disadvantages, including restricted load operation, high maintenance costs, and low achievable current densities compared to proton exchange membrane water electrolysis (PEMWE).

AELs with a so-called unipolar design (conventional configuration) are the most dependable and straightforward (**Figure 1.14 a**). Each cell comprises two electrodes, a separator, and an alkaline solution. By externally connecting multiple compartments, the cell can be assembled into stacks. The disadvantages of this design principle include energy losses, a heavy system weight, and large dimensions. Today's advanced systems are based on the so-called "zero-gap" bipolar configuration (**Figure 1.14 b**). In the bipolar cell, the metallic plate's one side serves as an anode, and on the other, as a cathode. Stacks comprised of bipolar cells are more compact, lighter, and require less wiring. In addition, bipolar cells can be operated under pressure, unlike unipolar cells

In the bipolar cell configuration, perforated electrodes are pressed against the separator to reduce resistance between the electrodes and prevent gas formation between the electrodes, increasing resistance. Too small holes would inhibit the formation of large bubbles, preventing them from reaching the detachment phase. The bubbles would obstruct the surface of the electrode, thereby decreasing the system's efficiency. Since the average bubble size for oxygen was 500 µm and 20–30 µm for hydrogen, the optimum hole size of 1.2 mm was suggested for the anode (oxygen side) and 0.3 mm for the cathode (hydrogen side)[36]. The separator is a 3D spacer that allows liquid electrolyte transport and prevents gases from crossover.

[34] E. Justi, W. Scheible and A. Winsel, German Patent 1019361 (1954).

[35] R.L. Costa, P.G. Grimes, *Electrolysis as a Source of Hydrogen and Oxygen*, Chem. Eng. Prog. 63 (4) (1967) 56–58.

[36] Ansar AS, Gago AS, Razmjooei F, Reißner R, Xu Z, Friedrich KA. *Alkaline electrolysis—status and prospects*. Electrochem. Power Sources Fundam. Syst. Appl., Elsevier; 2022, p. 165–98. https://doi.org/10.1016/B978-0-12-819424-9.00004-5.

The most common separator is Zirfon Perl, which is an alkaline-resistant polymer (polysulfone) matrix coated with hydrophilic zirconia particles[37].

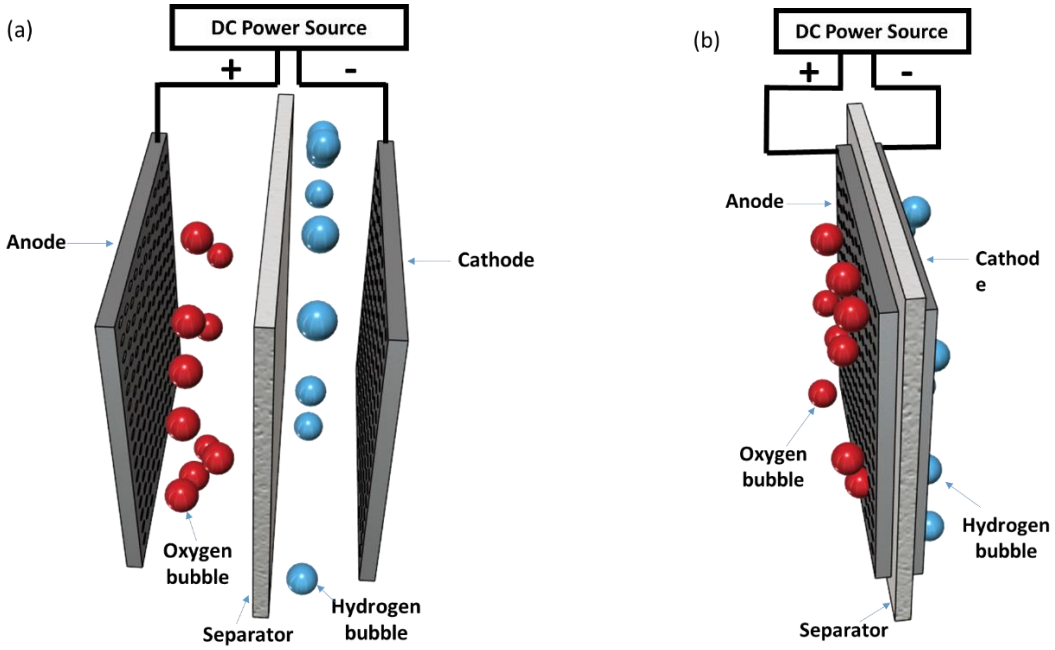


**Figure 1.14.** (a) Conventional configuration of alkaline electrolysis; (b) zero gap configuration of alkaline electrolysis.

The iV curves for conventional alkaline electrolysis and zero-gap configuration are shown in **Figure 1.15**. The cell electrochemical efficiency of the zero-gap cell is higher than a conventional one. The associated benefits include increased gas purity, particularly at high pressure and partial load, because the evolved gases are washed away and can no longer enter the counter-half cell.

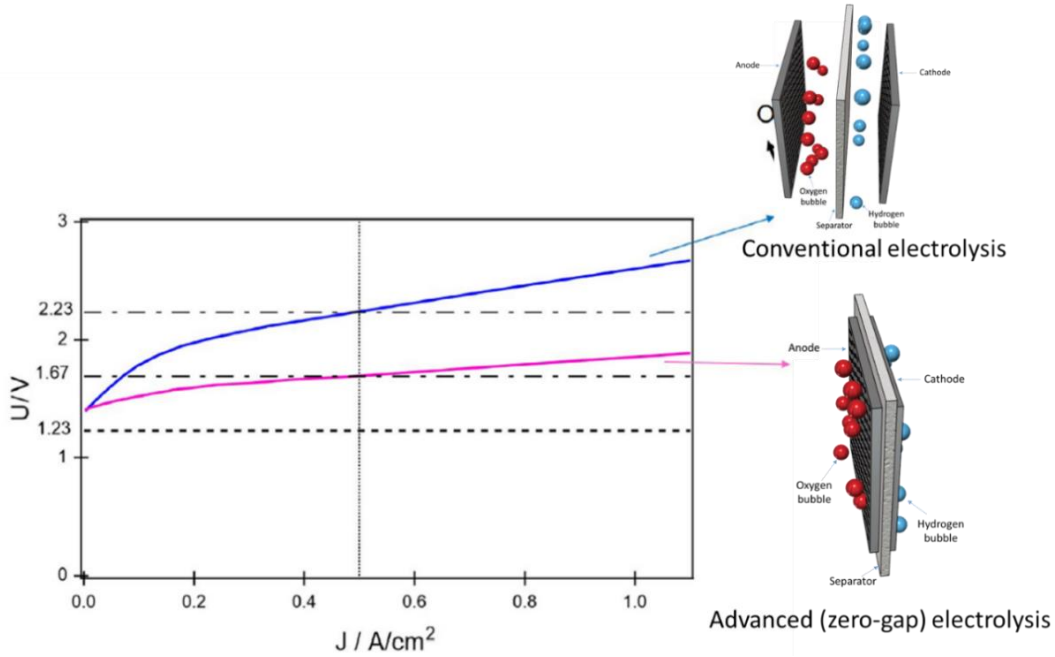


**Figure 1.15.** Zero-gap configuration has improved performance over conventional one (adapted from Ref.[36]).

[37] VERMEIREN P. *Evaluation of the ZirfonS separator for use in alkaline water electrolysis and Ni-H2 batteries*. Int J Hydrogen Energy 1998;23:321–4. https://doi.org/10.1016/S0360-3199(97)00069-4.

The balance of the plant of the alkaline electrolyzer is shown in **Figure 1.16**. In brief, an alkaline water electrolyser comprises an electrochemical reactor (typically a stack of cells) and a group of ancillary functions consisting of the balance of the plant. The primary components are the transformer and rectifier, water purification unit, liquid/gas separation unit, water cooling unit, and hydrogen purification and drying unit. It is worth mentioning that water is fed on the hydrogen side.

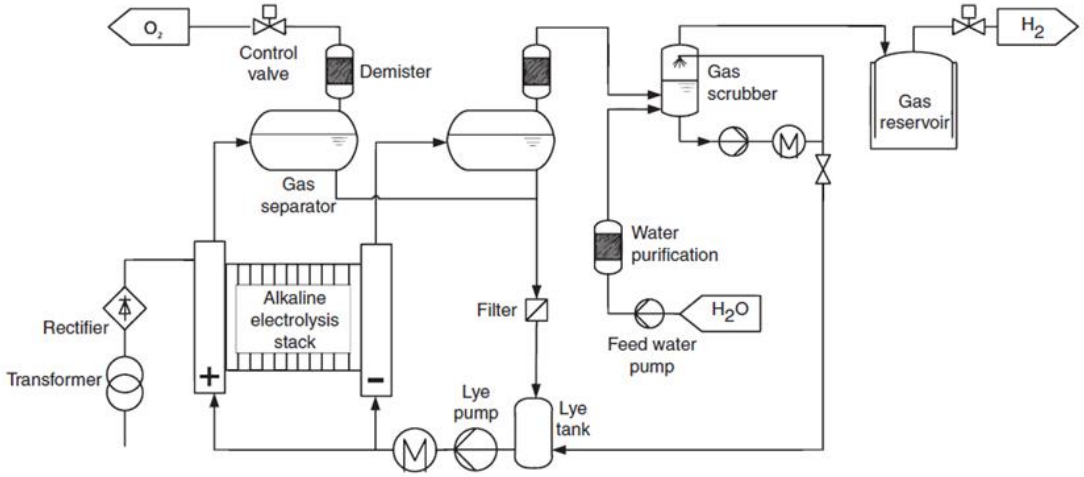


**Figure 1.16.** Balance of plant of the alkaline water electrolyzer[25].

The following is the SWOT analysis of the alkaline electrolysis technology:

- Highly mature technology, with extensive track-record
- High reliability and onsite demonstrated lifespan
- Reduced CAPEX compared to other technologies
- Large capacities commercially available, large footprint
- High energy efficiency since lower operating current density

The limitations of alkaline electrolysis technology:

- Operation at low current density
- Larger footprint than PEM
- The technology cannot operate efficiently under DP
- Limited flexibility for operation with transient power sources

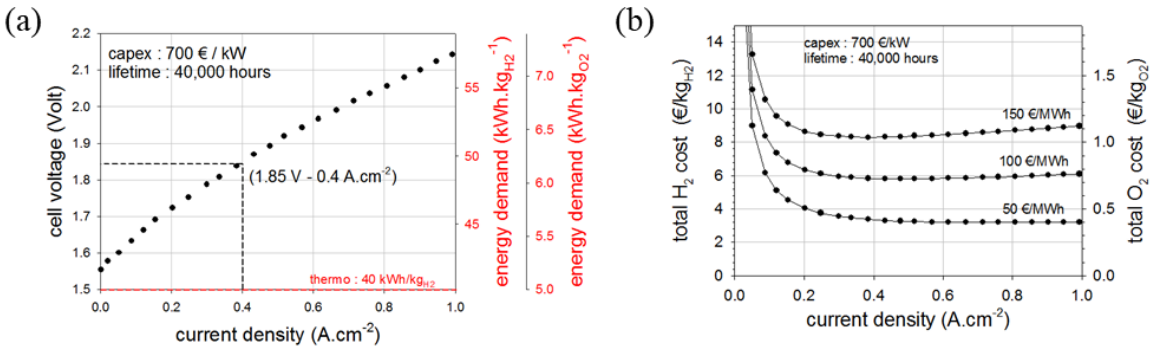


**Figure 1.17.** (a) typical iV curve of an alkaline water electrolysis cell; (b) total hydrogen cost as a function of operating current density for alkaline water electrolysis[21].

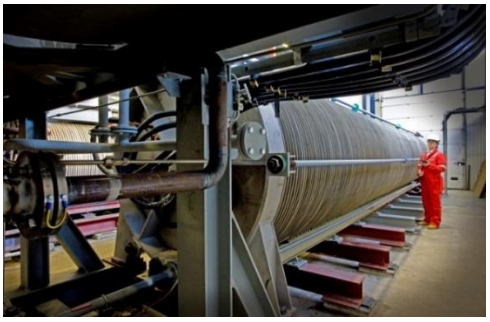

**Figure 1.18.** Picture of an industrial alkaline water electrolysis stack (courtesy of former Norsk Hydro Co.)

Compared to PEM electrolysis, alkaline electrolysis is less compact, operates at a lower current density and produces hydrogen with low energy consumption in a stationary manner. Progress has been made in recent years regarding flexibility and responsiveness, but operational constraints remain more significant than the PEM.

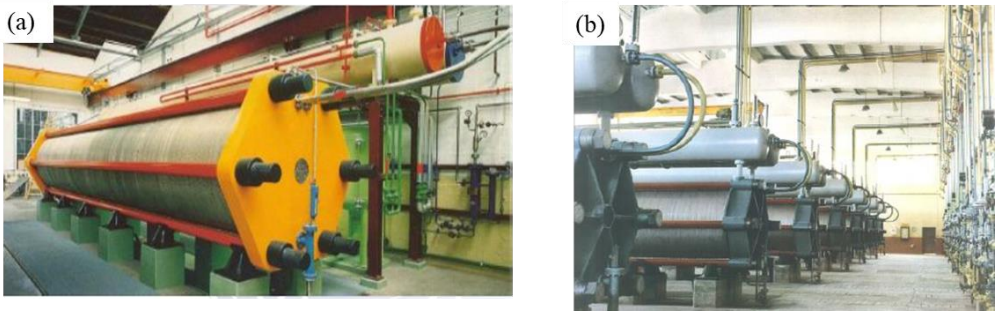


**Figure 1.19.** Industrial alakaline water electrolysers (ndustrie Haute Technologie, IHT, Switzerland).

Typical characteristics of the industrial alkaline system

- Possibility to operate under pressure (≈ 30 bar)
- Technology maturity: 760 $Nm^3/h$ $H_2$ per unit
- 4.0 MVA – 3.5MW (3300 A / 0.2 $A/cm^2$) i e., operation at a low current density
- Energy consumption 4.3 – 4.6 $kWh/Nm^3$, reduced energy consumption
- Proven technology with a significant track record
- High reliability and onsite demonstrated lifespan
- 25% → 100% max. output in 10 minutes, reduced operating range

### 1.2.3. Solid oxide electrolysis cell

High-temperature (HT) steam electrolysis is the most mature of these technologies, which will be discussed in this article. It is a promising technology, especially if a moderate-temperature heat source is available for evaporation, as in the chemical and steel industries. A significant portion of the energy input in this electrolysis is in the form of heat, and HT electrolysis achieves greater electrical system efficiency than low-temperature electrolysis. With HT technology, operation at the thermal neutral voltage, or 1.29 V at 800 °C (**Figure 1.7**), is possible at current densities near 1 $A/cm^2$. In contrast, low-temperature proton exchange membrane technology exhibits a voltage of 1.8 V at 0.6 $A.cm^{-2}$ and 2.2 V at 2.0 $A/cm^2$ [38]. In addition, the thermally activated reaction kinetics permits the use of 3D transition metals, such as nickel, as catalysts for the steam electrolysis reaction, as opposed to noble metal catalysts.

[38] Miller HA, Bouzek K, Hnat J, Loos S, Bernäcker CI, Weißgärber T, et al. *Green hydrogen from anion exchange membrane water electrolysis: a review of recent developments in critical materials and operating conditions.* Sustain Energy Fuels 2020;4:2114–33. https://doi.org/10.1039/C9SE01240K.

A schematic diagram of a solid oxide electrolysis cell (SOEC) and the corresponding electrochemical reactions for the electrolysis of water is shown in **Figure 1.20**. The fast electrode kinetics enables the use of the same cell for both electrolysis and fuel cell operation and co-electrolysis production of syngas ($H_2$ + CO)[39]. Solid oxide electrolysis cells have operated for more than 34,000 hours[40] at a current density of 0.6 A.cm$^{-2}$, 23,000 hours [41] of which 20,000 hours at a current density of 0.9 A/cm$^2$, and 8,400 hours[42] steady-state coupled with switching with low degradation at a current density of 0.7 A/cm$^2$.

Successful market introduction of solid oxide fuel/electrolysis cell technology for power-to-gas applications requires the reduction of degradation rates and a better understanding of the mechanisms of stack degradation. Consequently, a paper written by M. Lang *et al.*[43] compared the long-term behaviour of a solid oxide cell stack in electrolysis and reversible fuel cell/electrolysis operation. Sunfire GmbH (Dresden, Germany) provided the 30-cell accumulation of electrolyte-supported cells for the German-funded RSOC Project. The stack was operated in electrolysis mode for 3,370 hours and then in reversible fuel cell/electrolysis mode for 2,500 hours, each at a gas conversion efficiency of 70%. At the start of the test, the stack demonstrated excellent gas tightness, good performance, and high efficiencies in both SOEC and SOFC operations. During 3,370 hours of SOEC operation, a degradation rate of 0.5 % per 1,000 hours was observed. During 2,500 h of reversible fuel cell/electrolysis cycling, the stack's gas tightness decreased slightly, increasing temperature and accelerating degradation rates. Primarily, the increase in ohmic resistance contributed to the deterioration. Optimized operating conditions for reversible cycling and growth in the water's purity are planned to minimize stack degradation during reversible operation[43].

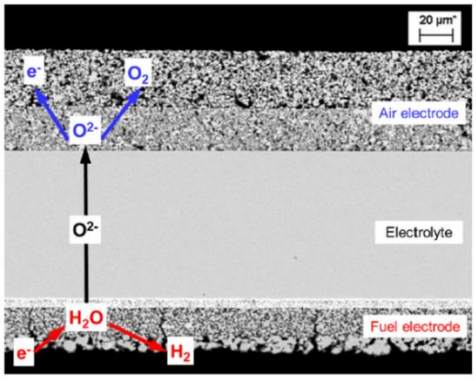


**Figure 1.20.** Schematic diagram of a SOEC and the corresponding electrochemical reactions for the electrolysis of water[43].

Aline Leon *et al.*[44] investigate the scaling up of a high-temperature electrolyzer system from a single cell to a stack. An integrated stack module causes an increase in degradation that must be evaluated to enhance the system's performance and longevity.

[39] Zheng Y, Wang J, Yu B, Zhang W, Chen J, Qiao J, et al. *A review of high temperature co-electrolysis of $H_2O$ and $CO_2$ to produce sustainable fuels using solid oxide electrolysis cells (SOECs): advanced materials and technology*. Chem Soc Rev 2017;46:1427–63. https://doi.org/10.1039/C6CS00403B.

[40] Schefold J, Poepke H, Brisse A. *Solid Oxide Electrolyser Cell Testing Up to the Above 30,000 h*. Time Range. ECS Trans 2020;97:553–63. https://doi.org/10.1149/09707.0553ecst.

[41] Schefold J, Brisse A, Poepke H. *23,000 h steam electrolysis with an electrolyte supported solid oxide cell*. Int J Hydrogen Energy 2017;42:13415–26. https://doi.org/10.1016/j.ijhydene.2017.01.072.

[42] Schefold J, Brisse A, Surrey A, Walter C. *80,000 current on/off cycles in a one year long steam electrolysis test with a solid oxide cell*. Int J Hydrogen Energy 2020;45:5143–54. https://doi.org/10.1016/j.ijhydene.2019.05.124.

[43] Lang M, Raab S, Lemcke MS, Bohn C, Pysik M. *Long-Term Behavior of a Solid Oxide Electrolyzer (SOEC) Stack*. Fuel Cells 2020;20:690–700. https://doi.org/10.1002/fuce.201900245.

[44] Léon A, Micero A, Ludwig B, Brisse A. *Effect of scaling-up on the performance and degradation of long-term operated electrolyte supported solid oxide cell, stack and module in electrolysis mode*. J Power Sources 2021;510:230346. https://doi.org/10.1016/j.jpowsour.2021.230346.

With an operation time of 4,224 h ( 0.5 A/cm$^2$) and 2,200 h (from 0.5 to – 0.3 A/cm$^2$), respectively, the degradation rate of a 30-cell stack (**Figure 1.21-a**) and a 90-cell module (both based on a similar 3YSZ (3% yttria-stabilized zirconia) electrolyte supported solid oxide cell) is evaluated. The voltage degradation rate of the 30-cell stack is 10.5 mV/kh (0.8% /kh based on the thermoneutral voltage of 1.3 V), including the temperature correction factor for a 2 °C/kh increase. It is the lowest degradation value reported to date for a stack of thirty electrolyte-supported cells after thermal factor correction. This indicates an increase of 5.5 mV/kh between the single cell and the stack. Every 2 minutes, two dynamic phases of 8,500 and 7,500 ON/OFF cycles were performed during the steady-state phase. It has been demonstrated that these significant load cycles do not result in further deterioration. Moving to the 90-cell module, irreversible damage has occurred due to the balance of plant incidents; based on their analysis, countermeasures are proposed[44].

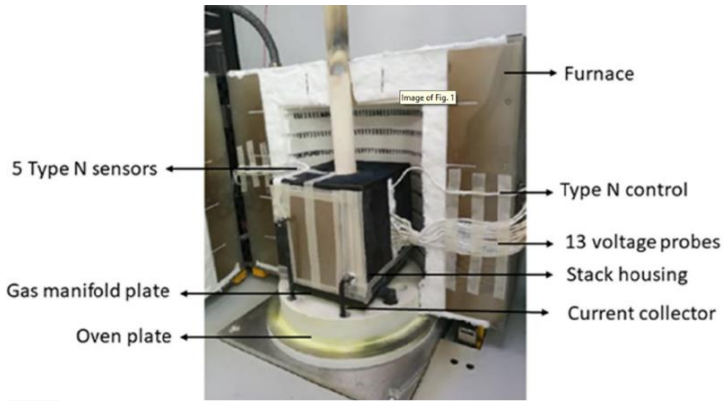


**Figure 1.21** Photograph of a 30-cell SOEC stack inserted into the hotbox and incorporated into the test station's furnace[44].

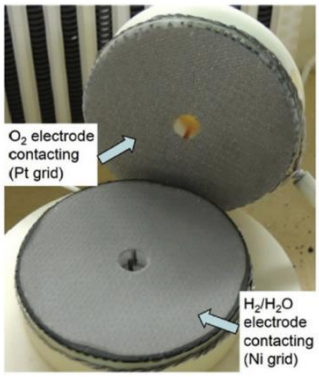


**Figure 1.22.** View of the ceramic housing blocks and contacting grids after 23,000 h of SOEC operation (disassembled cell)[41].

Josef Schefold *et al.*[41] used an electrolyte-supported solid oxide cell with a 45 cm$^2$ surface area (**Figure 1.22**) that was operated in the steam electrolysis mode for more than 23,000 hours before the scheduled shutdown, with a current density of 0.9 A cm$^2$ for 20,000 of those hours. The cell consisted of a scandia/ceria doped zirconia electrolyte, CGO diffusion-barrier/adhesion layers between the electrolyte and electrodes, and a lanthanum strontium cobaltite ferrite (LSCF) oxygen electrode, and a nickel/gadolinia-doped ceria (Ni/GDC) steam/hydrogen electrode. During the operation period with j = 0.9 A/cm$^2$, the voltage degraded by 7.4 mV/1000 h (0.57 %/1,000 h) and the area-specific resistance increased by 8 mΩcm$^2$/1,000 h. The final cell voltage (at 851°C) was 1.33 volts. After disassembly, the cell was neither broken nor fissured, and the $H_2$ electrode exhibited no visible damage; however, a portion (10%) of the $O_2$ electrode was delaminated. In addition, the $O_2$ electrode was affected by partially reversible pollution from the compressor air purging. At the steady-state DC density, impedance spectroscopy revealed a degradation dominated by an increasing ohmic term, primarily due to ionic conductivity decay in the electrolyte. In addition, a small non-ohmic and at least partially reversible $O_2$ electrode contribution to degradation, affected by (compressor) purge air contamination, was identified[41].

Using a current density of 0.9 A cm$^2$ for 20,100 hours results in a roughly linear cell voltage rise of 149 mV (**Figure 1.23**) or an average degradation rate of 7.4 mV/1000h (0.57 % /1000h). The increase in cell temperature is below 4 degrees Celsius, so it is disregarded in the calculation. The final voltage after 22,500 h. was 1.33 V at 851°C, which is significantly lower than the voltages achieved by electrolyzer cells operating at low temperature (100 °C) that have not degraded[41].

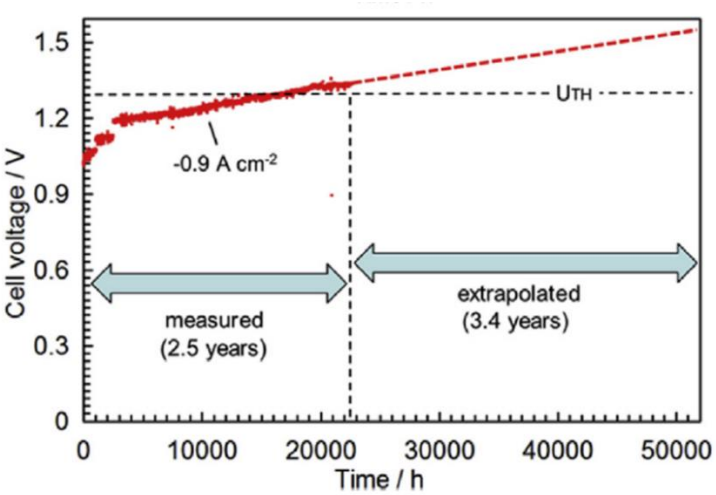


**Figure 1.23.** Time evolution of the cell voltage during the extended SOEC test extrapolated to 50,000 h. operation[41].

Transportable hydrogen can be produced by SOEC technology in which high-temperature electrolysis of steam was used. Due to low overpotentials and the ability to use waste heat for water evaporation, SOECs have a significant potential for high efficiencies. Before use or storage, hydrogen must be compressed for many industrial purposes. Due to improved electrode kinetics and downstream process requirements, pressurized operation of SOECs might be advantageous at both the cell and system levels. In a study conducted by M. Riedel *et al.*[45], experimental results of water electrolysis in a stack of 10 electrolyte-supported SOEC cells under pressure were described. A pressurized solid oxide electrolysis cell (SOEC) stack test facility is shown in **Figure 1.24**.


**Figure 1.24.** Pressurized solid oxide electrolysis cell (SOEC) stack test facility at German Aerospace Center (DLR)[45].

In addition, a 1000-hour test at 1.4 bar was conducted to analyze the deterioration in the exothermic steam electrolysis mode. Observations indicate that the open-circuit voltage increases with increasing pressure due to well-established thermodynamic relationships. When the pressure was increased, no increase in the limiting current density was seen for the ESC-stacks (electrolyte supported cells) studied in this work. Overall and activation impedance was observed to decrease somewhat as pressure increased. Within the impedance experiments, it was determined that the ohmic resistance of the examined electrolyte-supported cells of the stack contributed the most to the total cell resistance[45].

[45] Riedel M, Heddrich MP, Friedrich KA. *Analysis of pressurized operation of 10 layer solid oxide electrolysis stacks*. Int J Hydrogen Energy 2019;44:4570–81. https://doi.org/10.1016/j.ijhydene.2018.12.168.

A 1000-hour test of continuous current degradation at 1.4 bar with a second stack revealed a voltage degradation rate of 0.56% per 1000 h (**Figure 1.25**). The actual degradation rate was calculated to be slightly greater as a result of the voltage-driven parallel rise in stack temperature. With a thorough examination of the temperature dependence of the ohmic resistance of the stack, the voltage degradation rate was adjusted to account for the rise in temperature. The real rate of voltage depreciation was measured to be 0.64% per 1000 h.[45]

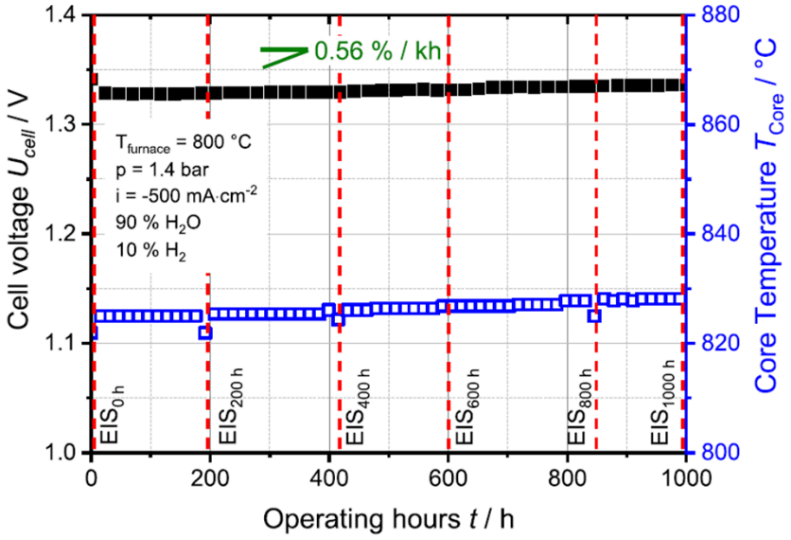


**Figure 1.25.** 1,000 h durability test at 1.4 bar, 800 °C, 90% $H_2O$ 10% $H_2$ with a 70% steam conversion rate at 0.5 A/cm$^2$[45].

## 1.3. PEM membranes

Perfluorosulfonated acids (PFSAs) are the most often utilized polymer membranes for PEM water electrolysis. Apart from their strong proton conductivity and mechanical and chemical robustness, this membrane type is widely established and readily available in PEM fuel cell technology[46]. However, the continued quest for alternate membrane materials is fueled by the expensive cost and environmental concerns connected with PFSAs' fluorine chemistry[47], as well as their significant gas (particularly $H_2$) permeability and poor mechanical stability at high temperatures (T > 80 °C)[48].

### 1.3.1. Nafion membrane

Nafion, developed in the late 1960s by DuPont (Chemours) Company, is the membrane most commonly used in electrolyzer applications. **Figure 1.26** depicts the structure of the polymer's skeleton, which is of the PFSA variety.

[46] Coms FD. *The Chemistry of Fuel Cell Membrane Chemical Degradation*. ECS Trans 2008;16:235–55. https://doi.org/10.1149/1.2981859.
[47] Feng M, Qu R, Wei Z, Wang L, Sun P, Wang Z. *Characterization of the thermolysis products of Nafion membrane: A potential source of perfluorinated compounds in the environment*. Sci Rep 2015;5:9859. https://doi.org/10.1038/srep09859.
[48] Fuel Cell Technical Team Roadmap, United States Driving Research and Innovation for Vehicle efficiency and Energy sustainability n.d.

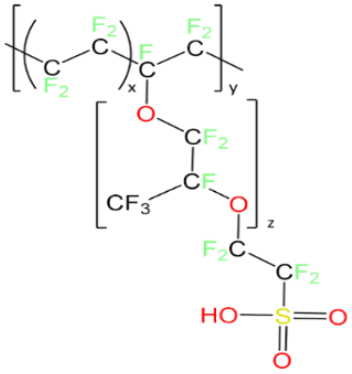

**Figure 1.26.** Chemical structure of the Nafion membrane.

The most popular grades for electrolyzers are Nafion 115 (N115), Nafion 117 (N117), and Nafion 1110 (N1110). Their characteristics are listed in **Tables 1.1 and 1.2**. The ion exchange capacity (IEC) of Nafion is 0.95 to 1.05 milliequivalents per gram (meq/g). Ito *et al.*[49] investigated the effect of Nafion thickness (N117 and N1110) on water swelling properties. In addition, they examined the gas permeation of $O_2$ and $H_2$ through hydrated and dry the Nafion membranes, demonstrating that the pressure increases the permeability parameters for hydrated membranes. In fact, a portion of the gases in a hydrated medium dissolve in water in order to be transported from one side of the surface to the other. Nafion 113 is a prototype membrane with a thickness of 76 µm provided by Chemours.

**Table 1.1.** Nafion membrane thickness at 25°C and 50% RH(50).

| Grade | Thickness (µm) |
|---|---|
| Nafion 1110 | 254 |
| Nafion 117 | 183 |
| Nafion 115 | 127 |
| Nafion 113 | 76 |

**Table 1.2.** Physico-mechanical properties of Nafion membrane[50].

| **Test condition** | **Breaking stress (MPa)** | **Elongation at break (%)** |
|---|---|---|
| 50% RH at 23°C | 43 | 225 |
| Hydrated at 23°C | 34 | 200 |
| Hydrated at 100°C | 25 | 180 |

Two typical iV curves, measured using PFSA membranes N117 and N115 of various thicknesses (185 and 135 m) and hence ionic conductivity, are shown in **Figure 1.27**.

[49] Ito H, Maeda T, Nakano A, Takenaka H. *Properties of Nafion membranes under PEM water electrolysis conditions*. Int J Hydrogen Energy 2011;36:10527–40. https://doi.org/10.1016/j.ijhydene.2011.05.127.
[50] Nafion™ Sulfonic Membranes, Chemours, https://www.nafion.com/en/products/sulfonic-membranes n.d.

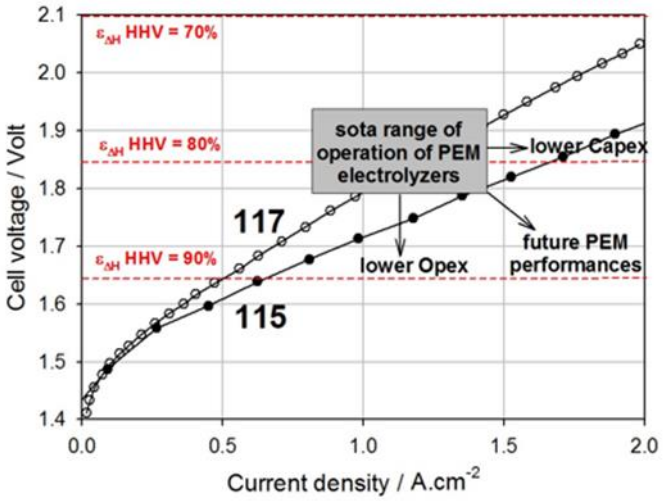


**Figure 1.27.** Typical iV curves of a PEM water electrolysis cell measured with two (Nafion 117 and Nafion 115) PFSA membranes[51].

### 1.3.2. Aquivion® membrane[52]

Solvay manufactures the Aquivion membrane that is suitable for water electrolyzers. Its chemical structure is similar to that of Nafion. However, it has a shorter side chain (Short Side Chain: SSC) (**Figure 1.28**), allowing for a reduction in the distance between proton sites and an increase in IEC.

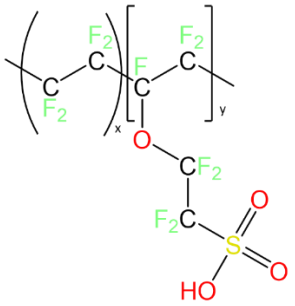

**Figure 1.28.** Chemical structure of the Aquivion membrane.

Siracusano *et al.*[53] conducted a comparative study on Aquivion E87-12S membranes versus Nafion (both membranes have a thickness of 120 µm) for water electrolyzers. Analysis of the polarization curves at 80°C (**Figure 1.29-a**) revealed that at a voltage of 1.8 V (targeted operating voltage window), the Nafion membrane has a current density of 1.5 A/cm$^2$ compared to 2.4 A/cm$^2$ for the Aquivion membrane. The authors have described that the improvement in the IR-free polarization curve of the Aquivion (**Figure 1.29-b**) is due not only to the increase in conductivity, which is a result of the decrease in equivalent weight (EW), but also to kinetic and diffusional properties of the membrane. Furthermore, these enhanced properties were a result of the distinct chemical and structural properties of Aquivions, which led to greater crystallinity, a higher glass transition temperature, and a lower equivalent weight.

[51] Millet P, Grigoriev S. *Water Electrolysis Technologies*. Renew. Hydrog. Technol., Elsevier; 2013, p. 19–41. https://doi.org/10.1016/B978-0-444-56352-1.00002-7.
[52] Aquivion is a registered trade name of Solvay Co. Aquivion® is replaced by Aquivion thoughout this thesis, https://www.solvay.com/en/brands/aquivion-ion-conducting-polymers n.d.
[53] Siracusano S, Baglio V, Stassi A, Merlo L, Moukheiber E, Arico′ AS. *Performance analysis of short-side-chain Aquivion perfluorosulfonic acid polymer for proton exchange membrane water electrolysis*. J Memb Sci 2014;466:1–7. https://doi.org/10.1016/j.memsci.2014.04.030.

The first two properties guarantee improved mechanical properties, while the third property increases conductivity and improves the catalyst–electrolyte characteristics. During an endurance test, the performance of the Aquivions membrane-based MEA did, however, degrade over time. This effect appears to be primarily related to a change in interface properties.

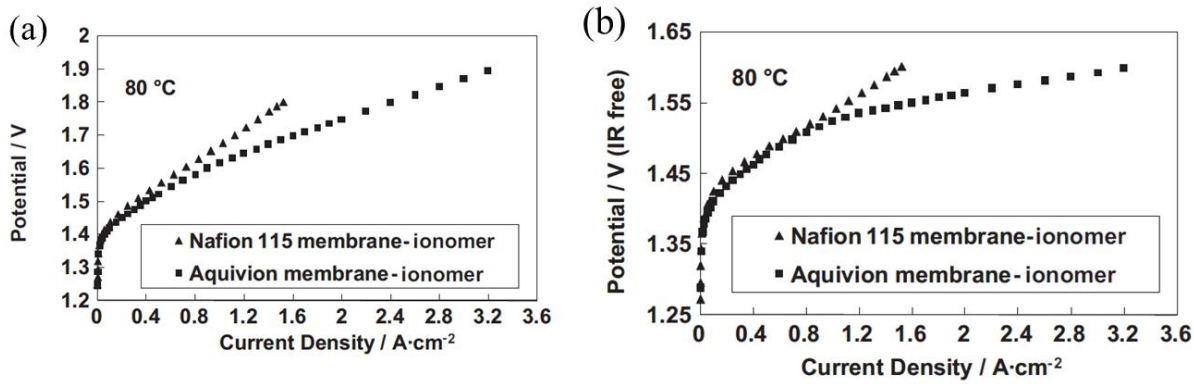


**Figure 1.29.** A comparison of the water electrolysis polarization behaviour of MEAs based on Aquivion and Nafion at 80°C. (a) measured iV curves (b) IR-corrected iV curves[53].

### 1.3.3. Phosphonic acid containing fluoropolymers

It is necessary to develop membranes with new proteolytic groups capable of proton conduction at 120 °C. Under these conditions, membranes containing phosphonic acid groups appear as promising candidates. The standard operating conditions for fuel cells are 120°C, 30% RH, and low pressure. Due to the loss of water, the performance of the perfluorosulfonic membrane is significantly diminished under these fuel cell conditions. Labalme *et al.*[54] have developed new polymer electrolyte films containing phosphonic acid groups fluoropolymers. They used a semi-interpenetrated networks (IPN) strategy involving a crosslinked fluorinated copolymer and a commercially available copolymer. Semi- IPN produced by blending poly(vinylidene fluoride-co-chlorotrifluoroethylene) (poly(VDF-co-CTFE). The highly florinated polymer used as inert matrix, mechanical support phase. The poly(VDF-co-CTFE) was blended with covalently crosslinked phosphonated polyelectrolytes (proton conducting phase) are potential PEM material candidates. The phosphonated polyelectrolytes terpolymer was prepared by radical terpolymerization of chlorotrifluoroethylene (CTFE), diethyl vinyl ether phosphonated (DEVEP), and 4-(vinyloxy) butyl methanesulfonate (VBMS) (**Figure 1.30**). Utilizing a cross-linked fluorinated copolymer for the cast proton exchange membrane fuel cell (PEMFC) enables us to increase the chemical resistance of the membranes to acidic and oxidizing environments. Even at a high crosslinking rate, the presence of fluorinated copolymer allows us to obtain a material with excellent mechanical properties. However, the prepared fluoro-phosphonic copolymer had an ionic conductivity of 10 mS/cm at 90 C, using a 5 wt% of crosslinker. To increase the proton conductivity of the membranes, it is necessary to synthesize a suitable terpolymer with only 2 or 3 % crosslinked monomer in a polycarbonate composition, therefore, enhancing the accessibility of phosphonic acid groups.

[54] Labalme E, David G, Souquet J, Buvat P, Bigarre J. *Use of a new crosslinking method to obtain semi-IPN membranes with phosphonic acid groups for a PEMFC application.* J Mater Chem A 2014;2:9792–802. https://doi.org/10.1039/C4TA01472C.

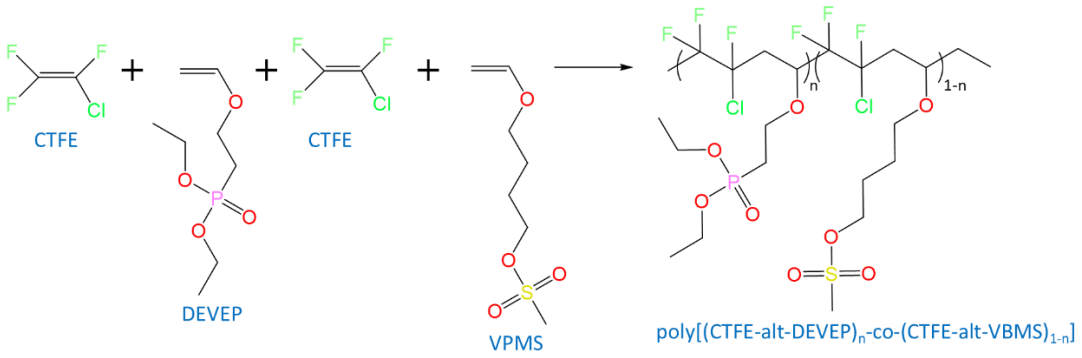


**Figure 1.30.** Radical terpolymerization synthesis of poly[(CTFE-alt-DEVEP)$_n$-co-(CTFE-alt-VBMS)$_{1-n}$

Labalme *et al.* have further developed the phosphonic acid-containing fluorinated polymer[55]. The authors prepared blend membranes synthesized from poly(VDFco-CTFE) and a fluorinated copolymer containing phosphonic acid (poly(chlorotrifluoro ethylene-alt diethyl vinyl ether phosphonated) referred to as poly(CTFEalt-DEVEP). They prepare this new phosphonic acid-containing fluorinated polymer (poly(CTFEalt-DEVEP)) by copolymerizing CTFE and 2-chloroethyl vinyl ether (CEVE) followed by phosphonation (**Figure 1.31**). Dynamic mechanical analysis was used to evaluate the mechanical properties of these blend membranes. The partial miscibility of the two polymers persists. To increase the miscibility of the two polymers, adding a hydrophobic and hydrophilic compatibilizing polymer during membrane preparation is possible. Consequently, a greater miscibility can enhance the microstructure of the blend polymer and result in a greater proton conductivity. Regarding the industrial development of fuel cell technologies, the cost of the proton exchange membrane is also crucial. Therefore, the blend technique permits the casting of inexpensive membranes. Their synthesis shows that fluorinated and phosphonated copolymers are less expensive than Nafions. The presence of fluorine atoms in poly(VDF-co-CTFE) permits the fabrication of membranes with improved structural integrity and enhanced resistance to oxidation in the presence of radicals. Under fully hydrated conditions, the best result reveals a 40 mS/cm proton conductivity at a temperature of 80°C.

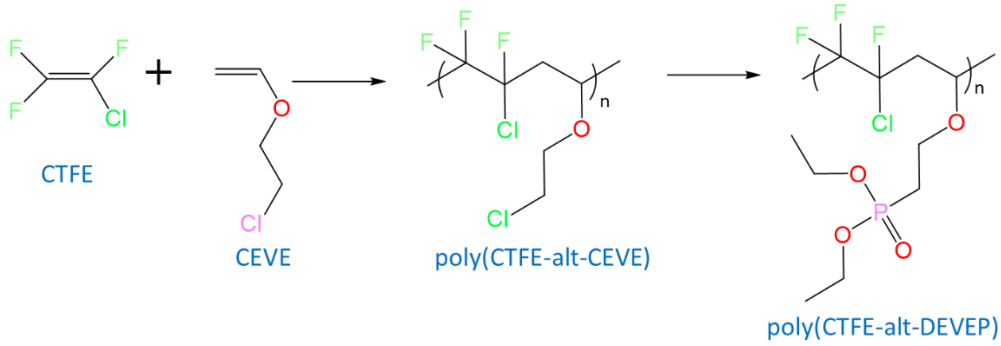


**Figure 1.31.** Synthesis of poly(CTFEalt-DEVEP)

[55] Labalme E, David G, Buvat P, Bigarre J. *A simple strategy based on a highly fluorinated polymer blended with a fluorinated polymer containing phosphonic acid to improve the properties of PEMFCs*. New J Chem 2019;43:11141–7. https://doi.org/10.1039/C9NJ03037A.

### 1.3.4. Nanocomposite membrane

Hybrid nanocomposite (HNC) membranes offer a desirable alternative to PFSAs. Their distinct properties prevent them from being used in PEM fuel cells. However, their morphology results in a significantly lower gas crossover, similar conductivity (especially when fully hydrated), better thermal stability, and lower production cost. Furthermore, HNC membranes are the primary step toward fluorine-free membranes, making them ideally suited for PEM water electrolysis.

Several attempts to prepare high proton conductivity nanocomposite membranes have been made by Seck *et al.*[56]. The authors directly synthesized Poly(vinylidene fluoride-co-hexafluoropropylene) (PVDF-HFP)/silica-SH nanocomposites in a single extrusion step. The authors demonstrated that it is possible to generate a high concentration of inorganic silica in a PVDF-HFP polymer via sole gel chemistry during extrusion without any degradation issues. The functional silica was produced using two distinct inorganic precursors, namely polydimethoxysiloxane (PDMOS) (**Figure 1.32-a**) as the structural precursor and mercaptopropyltriethoxysilane (MPTES) (**Figure 1.32-b**) as the grafting precursor. The authors used a 50 % hydrogen peroxide solution as an oxidation reagent to convert thiol groups into sulfonic groups (**Figure 1.32-c**). A theoretical IEC of 2 meq/g was calculated after the oxidation step based on the amount of SH content in the matrix. However, the experimental IEC value of 0.7 meq/g and ionic conductivity of only 9.6 mS/cm indicates that a partial amount of the SH groups has been oxidized to $SO_3H$.

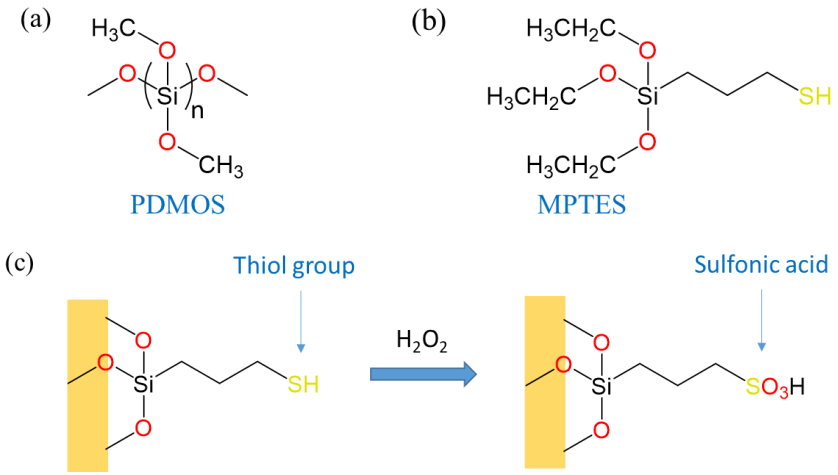


**Figure 1.32.** (a) shows the chemical structure of PDMOS, (b) MPTES and (c) oxidation of the thiol group to sulfonic acid.

The second attempt made by Seck *et al.* was the use of interfacial agents[57]. The authors tailored the interface between the matrix and the inorganic-rich phase to increase ionic conductivity. The effect of the addition of interfacial agents with varying concentrations of functional groups on the final morphology and electrochemical properties of membranes was studied. Specifically, the oxidative hydrolysis of mercapto groups into sulfonic acid functions allowed us to produce proton-conductive membranes. They replaced a part of the PVDF-HFP matrix with the synthesized poly[vinylidene fluoride-co-2-(trifluoromethyl) acrylic acid copolymers (poly(VDF-co-MAF)) as an interfacial agent (**Figure 1.33-a**).

[56] Seck S, Magana S, Prébé A, Niepceron F, Bounor-Legaré V, Bigarré J, et al. *PVDF-HFP/silica-SH nanocomposite synthesis for PEMFC membranes through simultaneous one-step sol–gel reaction and reactive extrusion*. Mater Chem Phys 2015;163:54–62. https://doi.org/10.1016/j.matchemphys.2015.07.014.

[57] Seck S, Magana S, Prébé A, Buvat P, Bigarré J, Chauveau J, et al. *New fluorinated polymer- based nanocomposites via combination of sol -gel chemistry and reactive extrusion for polymer electrolyte membranes fuel cells (PEMFCs)*. Mater Chem Phys 2020;252:123004. https://doi.org/10.1016/j.matchemphys.2020.123004.

They prepared the poly(VDF-co-MAF) by conventional radical copolymerization of VDF with different contents of MAF (α-trifluoromethacrylic acid). Maintaining a 15% equivalent silica concentration (a theoretical IEC of 2 meq/g), they got an experimental IEC ranging from 1.0 to 1.3 meq/g and conductivities up to 78 mS/cm (at 100% RH and temperature of 25°C) after incorporating a 5 wt% of poly(VDF-co-MAF) was incorporated into the reactive processing. The authors tried another way to tailor the interface between the PVDF-HFP and the $SiO_2$-rich phase. They use a PVDF-HFP polymer grafted with 0.75 wt% maleic acids (poly(VDF-co-HFP)-g-MA) as a matrix (**Figure 1.33-b**). The nanocomposite membrane reached a 54 mS/cm conductivity comparable to that of Nafion NR112 (52 mS/cm) at 100% RH and a temperature of 25°C. These findings highlighted the importance of the interface and its effect on the accessibility of sulfonic acid functions.

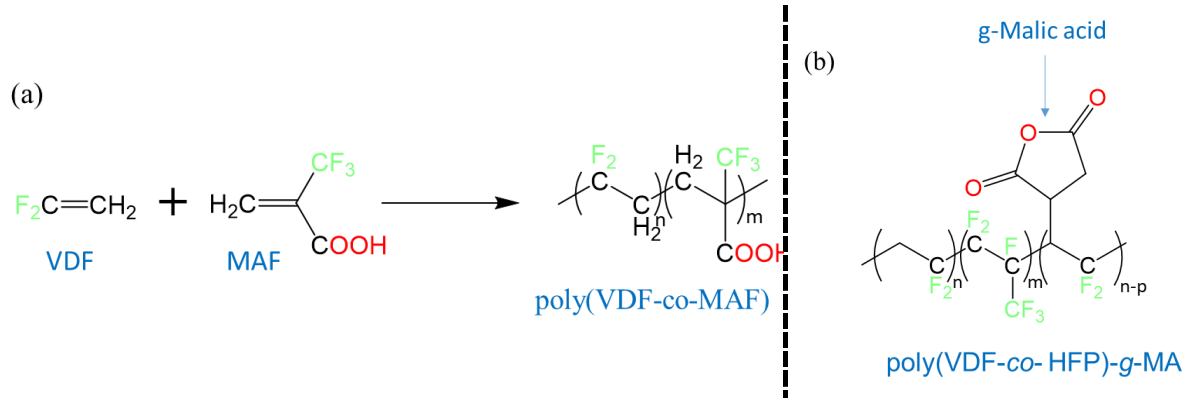


**Figure 1.33.** (a) radical copolymerization of VDF with MAF; (b) the structure of Maleic anhydride was grafted onto poly(VDF-co-HFP) to produce the poly(VDF-co-HFP)-g-MA.

## 1.4. Threats to fluoroinomers

PFSAs (perfluoro-sulfonic acids) are fluorinated compounds that are used in PEM fuel cells and water electrolysis. They are part of a larger group of fluorinated compounds called PFAS (per and polyfluorinated alkyl substances). PFAS represents a broad family of chemistries containing fluorine and carbon, encompassing various chemicals. Following the OECD definition, there are more than 4,700 known PFAS. These chemicals (gases, liquids or solids) have varying physical and chemical properties, health, environmental profiles, uses, and benefits.

In Europe, an ongoing procedure is taking place under the REACH agreement, which evaluates the possibility of banning such substances because some have been identified as endocrine disruptors. PFAS are chemicals used in the hydrogen value chain, not least of electrolysers and fuel cells. As no substitute is available today, an incautious ban would impact the hydrogen industry directly and heavily, jeopardising the achievement of the EU's Hydrogen Strategy targets and decarbonisation objectives. Such a situation will not necessarily lead to the prohibition of PFSAs. More likely, it will lead to stricter regulations and the need to control emissions into the environment better. Indeed, these materials are chemically very stable, they are not biodegradable and risk contaminating the environment and food chains in the long term. Nevertheless, finding alternatives to these polymer materials and reducing their cost stimulates research and the quest for less or non-fluorinated ionomers. The interest in chemically stable hydrocarbon membranes under the conditions of the use of PEM technology remains a difficult objective to achieve, to date unfinished.

## 1.5. Thesis objectives

Hybrid nanocomposite (HNC) membranes offer potentially an interesting alternative to PFSA membranes. R&D activities on that type of ionomer reinforces the quest for non-fluorinated ionomers. Those already known show several advantages: a significantly lower gas crossover, similar conductivity (especially when fully hydrated), better thermal stability, and lower production cost. The fact that they are the primary step toward fluorine-free membrane, should make them ideally suited for PEM water electrolysis. They also have some limitations, especially in terms of durability. The objective of this thesis is to study the properties of a proton-conducting HNC developed by the French CEA2 (Commissariat à l'Energie Atomique et aux Energies Alternatives) and the possibility of using it, instead of PFSAs, in PEM water electrolysis cells. Membrane samples used in this thesis were provided by CEA2. A polystyrene sulfonic acid (PSSA) chain is grafted onto silica nanoparticles which are then dispersed into a PVDF matrix. A cross-linking agent is used to anchor the functional acid groups to the hydrophobic organic phase. A cost analysis reveals that this type of material is potentially ten times cheaper than equivalent PFSAs, meanwhile having the same level of electrochemical performance. Our objective was to make CCM with such membrane, optimize the catalyst coating process, implement such hybrid nanocomposite proton-conducting membrane in PEM water electrolysis cells and determine their performance level, both in terms of electrochemical efficiency and durability.

The following approach and methodology, which is reflected in the organization of the chapters of the thesis, was used:

1. Learn the use of PEM water electrolysis cells and techniques for making PEM water electrolysis CCMs and measuring their electrochemical characteristics (**chapter 2**).
2. Measure and analyze the performance of a reference CCM (a commercial one) made of Pt/C for HER, Nafion PFSA for proton conduction and $IrO_2$ for OER (**chapter 3**).
3. Learn how to make lab-size CCM from commercially available Pt/C, Nafion PFSA and $IrO_2$, optimize the CCM manufacturing process and benchmark the electrochemical performances against those of the reference commercial CCM (**chapter 4**).
4. Learn how to make CCMs using the hybrid nanocomposite proton-conducting membrane, and optimize the manufacturing process. Evaluate the performance level, benchmark against commercial and lab-made references, analyze potential causes of performance losses (**chapter 5**).
5. Develop and test a 5-cell short stack of industrial size (**chapter 6**).

# Chapter 2. Experimental section

## 2.1. Ink manufacturing

In PEM water electrolysis, the electrodes are in fact, catalytic layers of micrometric thickness deposited on either side of the proton conduction polymer membrane. These layers contain nanoparticles of electrocatalysts coated with polymer chains of the same chemical nature as the membrane, which serve as a binder. The ink is the suspension that serves as a precursor to the manufacture of the layers. It essentially contains three components: nanoparticles of solid electrocatalysts, a dispersion of polymer chains in a solvent (usually a mixture of alcohols) and isopropanol which serves as a dispersant and allows the viscosity of the mixture to be adjusted. The nanoparticles are dispersed by sonication. A distinction is made between anodic ink containing iridium oxide nanoparticles in suspension and cathodic ink containing carbon black suspension on the surface of which platinum nanoparticles are deposited.

## 2.2. Catalyst-Coated Membrane (CCM) manufacturing tools & techniques

### 2.2.1. Hydraulic press with heated plates

The catalytic layers can be transferred by hot compression on the membrane. The operation requires a heated press. We used a Carvel hydraulic press (**Figure 2.1**) that provides a compressive force of up to 30 tons and a hot plate that can go to a temperature up to 343 °C. Such pressure and temperature were suitable for preparing large-area CCMs up to 300 $cm^2$ of the active area. This equipment was purchased for the specific needs of the thesis.

**Figure 2.1.** Hydraulic press (30 tons) with 30 x 30 cm hot plates (Carver, USA; 4128 Model 30-12H).

**Figure 2.2.** Hand spray airbrush.

### 2.2.2. Hand spray gun

The catalytic layers can be deposited manually or automatically, either directly on the surface of the membrane (direct method), or deposited on an *ad hoc* support before being transferred (DECAL method). We used an airbrush (**Figure 2.2**) as a spray tool for manual deposits on small surfaces. The advantage of airbrushes is the ease of use and the consumption of low amounts of catalysts, even if the thickness of the layer is less homogeneous than that obtained with a printer.

### 2.2.3. CNC ink printer device with ultrasonic nozzle

An ink printer (**Figure 2.3**) with computer numerical control (CNC) already available at our lab at the beginning of the project was used to standardize the deposit of the catalytic inks, either directly on the membrane (direct method) or a substrate before transfer (DECAL method). The machine is equipped with an ultrasonic nozzle to generate fine drops of ink a few microns in diameter, which ensures good dispersion of the electrocatalytic particles in the deposited layers.

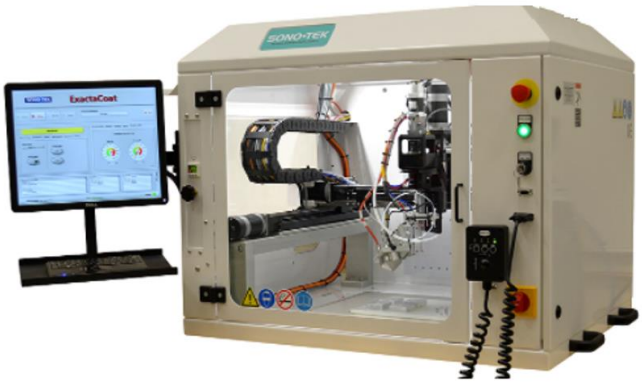


**Figure 2.3.** The ultrasonic inkjet printer SonoTeck (ExactaCoat) used for ink deposition.

## 2.3. Electrochemical characterization tools

### 2.3.1. Laboratory cell n°1 with controlled clamping pressure

During the research, the equipment was optimized. A compact water electrolysis cell (4 $cm^2$ active area) equipped with a system to adjust the clamping pressure (Fraunhofer ISE, Freiburg) was purchased and used (**Figure 2.4, left**). The cell has an aluminum frame and a screw with a compressive sensor to control the clamping pressure of the cell. The applied force is read by the Lorenz digital device (**Figure 2.4, right**).

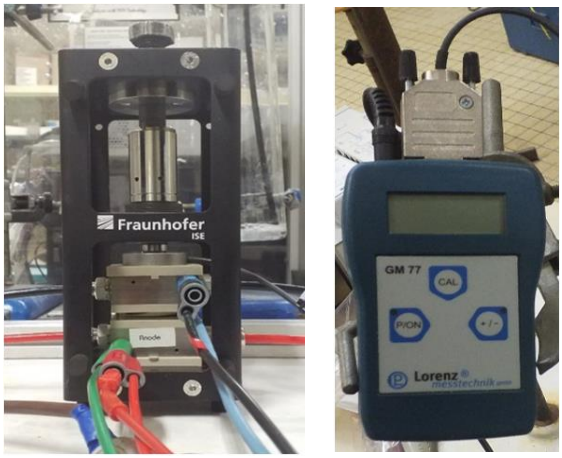


**Figure 2.4.** (left) 4 $cm^2$ water electrolysis lab-cell and (right) Lorenz digital device reader.

### 2.3.2. Cell components used in cell n°1

To achieve high electrolysis cell performance, liquid water must be supplied to the active catalyst sites at the anode. In **Figure 2.5**, we call the 'flowfield' the combination of a grid and a PTL (3 and 4): this term refers to the porous media used to allow water circulation in each cell compartment.

On the anode side, the grid with a reduced hydraulic resistance is used to circulate large amounts of water required to cool down the cell during operation. The PTL, which is less porous, is used to distribute the water flow over the entire CCM surface. On the cathode side, the electro-osmotic flow of liquid water produced by proton-reduction at the cathode is collected through the cathodic PTL (either made of titanium or carbon) down to the grid from which it is evacuated by pumping. The mass transport properties of the flowfields used and other effects (such as the unintended gas bubble accumulation on the catalyst layers) can starve some active catalyst sites from the necessary water, thus hurdle the cell from achieving high efficiency, and inducing mass transfer losses. On the anode side, the PTL is a critical component of the PEM electrolysis cell, allowing the movement of mass (diffusion of water and gases) simultaneously with being an electrical conductor. Many experimental studies describe the relationship between the PTL design and morphology and the electrolyser voltage losses, especially at high current density[58]. Several parameters of the PTL contribute to the mass transport limitations, including pores and particles size of the PTL, the thickness of flowfield and PTL, and water permeability in them. It is necessary to optimize the mass transport of water and gas across the PTL/Grid combination in order to obtain the highest cell performance using the reference CCM. The conventional cell components of a PEM water electrolysis cell are shown in **Figure 1.9**. Those used in our test cell are shown in **Figure 2.5**:


**Figure 2.5.** Internal cell components of the 4 $cm^2$ lab-cell with a graphic diagram of water inlet and outlet and optimized grid/PTL combination.

- Two flat titanium plates, one on each side, acting as bipolar plate (BPP) or current collectors; they can be equipped with different types of flowfields; the bottom of each plate is pierced with 5 small holes or liquid water inlet; the top also has 5 holes for collecting the biphasic liquid-gas mixture produced by electrolysis.
- The two flat titanium plates are separated by a thermoplastic frame made of PEEK (polyether ether ketone), which is used to create a void space (called a pocket or compartment) in which the internal cell components making the flowfield are placed; two rubber gaskets are used to seal around the periphery; by selecting gaskets of appropriate thicknesses, it is possible to adjust the depth of the cell compartments in order to put inside different combinations of cell components.
- Each half-cell compartment contains a flowfield; a flowfield has two functions: the first one which requires a high porosity component through which most of the water is pumped across the cell for cooling purpose (the hydraulic resistance needs to be minimized); the second one which requires a lower porosity component through which

[58] Lee CH, Banerjee R, Arbabi F, Hinebaugh J, Bazylak A. Porous Transport Layer Related Mass Transport Losses in Polymer Electrolyte Membrane Electrolysis: A Review. ASME 2016 14th Int. Conf. Nanochannels, Microchannels, Minichannels, American Society of Mechanical Engineers; 2016. https://doi.org/10.1115/ICNMM2016-7974.

circulate liquid water for the reaction and gases is placed against the CLs (the hydraulic resistance can be larger since the water flow is small); in each experiment reported in this report, the same flowfield was used symmetrically, in both compartments.

We tested four types of flowfields (by combining 2 types of grids and 2 types of PTL) to optimize water flow distribution in each cell compartment and to reduce mass transport limitations:

1. The first one, which is intended to mimic industrial electrolysis cells, contains a 1.0 mm thick Ti grid with Elogen's pattern and 0.5 mm thick Ti PTL (porous transport layer) on top of each other; the grid is placed against the flat Ti plate and the PTL against the CL of the CCM; the total depth of the pocket (which was adjusted by using thin gaskets) is 1.5 mm. We tested two types of PTL: one obtained by sintering small Ti particles hence having tiny pores (PTL-S), and one brought by sintering large Ti particles and hence having large pores (PTL-L, *Cf* **Figure 2.6**).
2. The second one (**Figure 2.7**), which is more sophisticated and intended to create better mass transport conditions, contains a 2.5 mm thick two-layer system (made of 1 Ti grid + a top Ti felt made of Ti fibers, all sintered together to minimize the ohmic resistance) shown in **Figure 2.7-a,b +** 0.5 mm thick Ti PTL on top placed against the CL of the CCM. The total depth of the pocket (which was adjusted by using thick gaskets) is 3.0 mm.

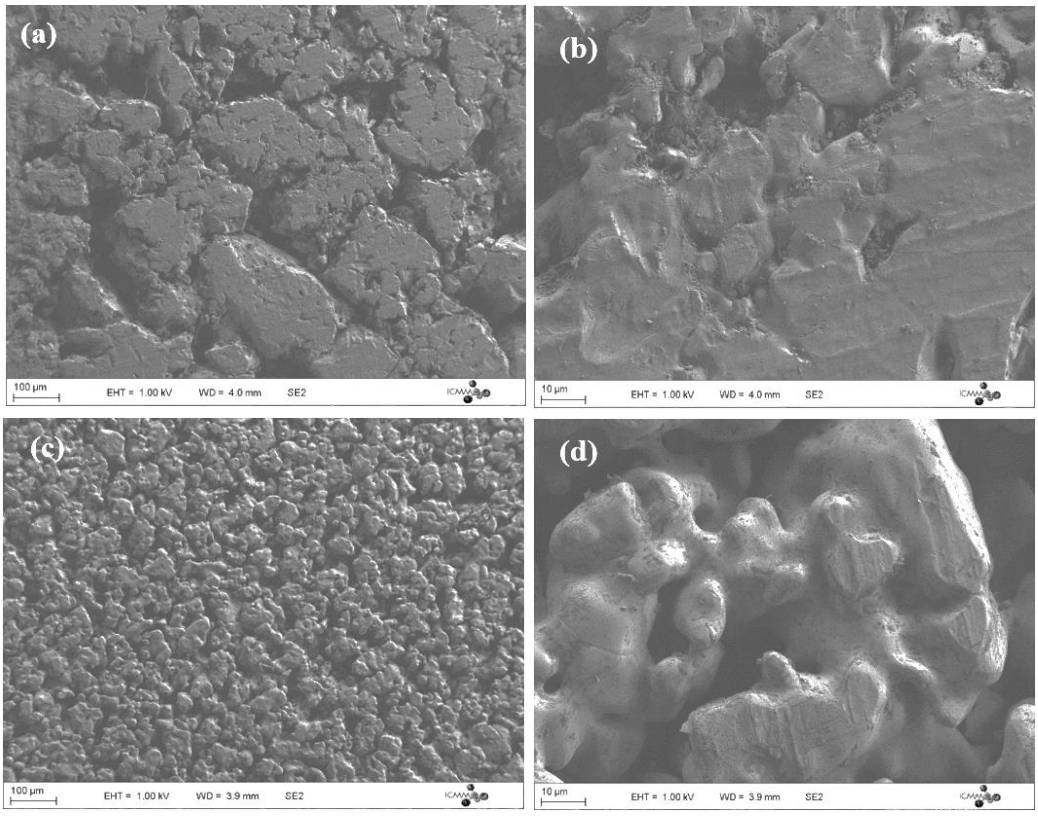


**Figure 2.6.** SEM images of the surface of PTL made of sintered titanium: (a, b) PTL-L with large Ti particles and (c, d) PTL-S with small Ti particles.

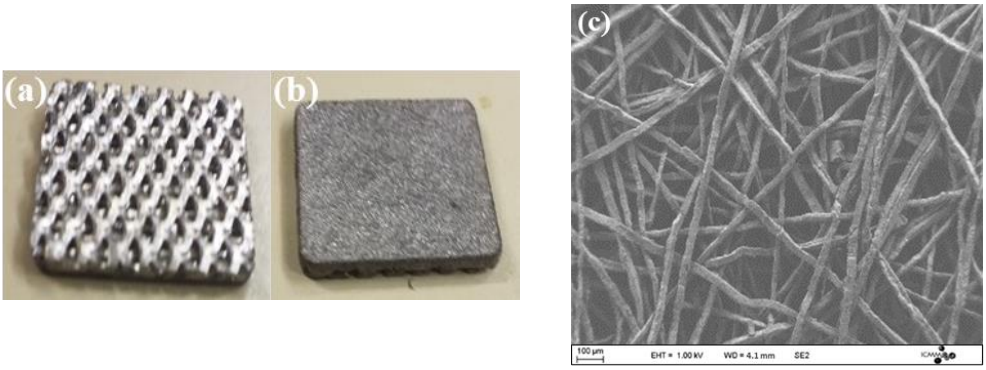


**Figure 2.7.** Recto-verso images of the two layer Ti flowfield: (a) bottom layer = grid; (b) top layer = felt. (c) SEM image of top Ti felt showing Ti fibers.

Nomenclature used

The four different flowfields tested are named 1S, 1L, 2S, 2L.

- 1S refers to 1.0 mm Ti grid with our laboratory-optimized pattern + 0.5 mm Ti PTL-S (**S**mall Ti particles and reduced porosity, USA supplier).
- 1L refers to 1.0 mm Ti grid with our laboratory-optimized pattern + 0.5 mm Ti PTL-L (**L**arge Ti particles and larger porosity (Chinese supplier).
- 2S refers to the combination of a 2.5 mm thick Ti bi-layer component + 0.5 mm Ti PTL-S.
- 2L refers to the combination of a 2.5 mm thick Ti bi-layer component + 0.5 mm Ti PTL-L.

The KPI used to measure quantitatively the cell efficiency is the polarization curve (iV curve) measured at 60°C (common process temperature) and atmospheric pressure (compatible with the test bench available at UPSay). After several trials, we found that the optimum cell configuration for reducing mass transport and cell voltage losses requires the use of a multilayer felt and a PTL made of sintered coarse particles of titanium (**Figure 2.6**).

### 2.3.3. Laboratory cell n°2

A second cell (from a former Paxitech company) of a larger surface area (6.25 $cm^2$) was also used to duplicate and confirm the results (**Figure 2.8-a**).

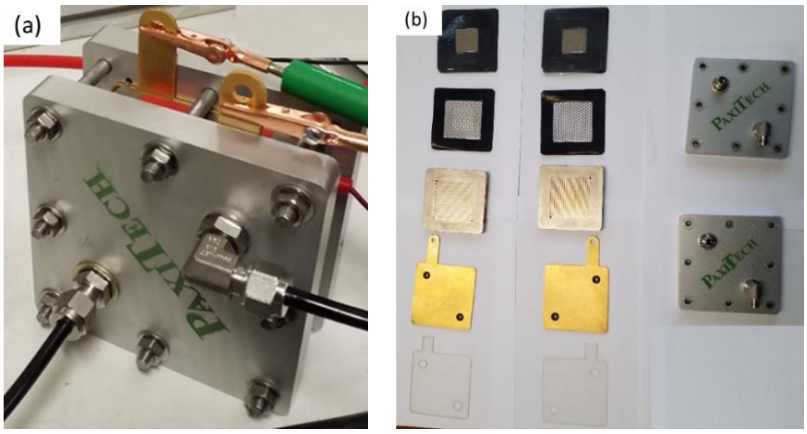


**Figure 2.8.** (a) 6.25 $cm^2$ water electrolysis lab-cell and (b) cell components.

The flowfield used in this cell was made of 5 layers Ti felt with 0.35 mm thickness and size of 2.5 X 2.5 $cm^2$ (6.25 $cm^2$). The Ti plates contain tiny flowfields (5 X 5 $cm^2$) machine-made in the thickness of the plates. To improve the water flow, we added a 1 mm thick grid with size of 5 X 5 $cm^2$. The details of the cell components used are shown in **Figure 2.8-b**.

### 2.3.4. Setup with a thermostated water

Electrochemical measurements must be made at controlled temperatures and pressure to be usable. All our measurements were carried out at atmospheric pressure. The temperature was fixed at the values of interest (between 40 and 80°C) thanks to the use of two thermostats with a centrifugal pump (Hurber minstat, Germany) placed on each of the two hydraulic circuits (anodic and cathodic). A glass cylinder was used on each circuit for liquid-gas separation, and polyamide tubes that can withstand hot water were used for the connection (**Figure 2.9**).

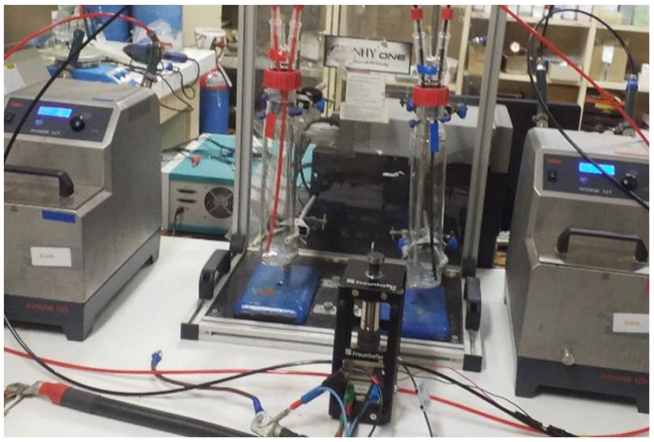

**Figure 2.9.** The two water thermostat pumps and the two glass cylinder gas for liquid gas separation.

A Voltalab potentiostat PGZ 301 was used to measure the electrochemical impedance spectroscopy (EIS) of the cell, to perform an accelerated stress test (AST), and record cyclic voltammograms (CV) of the CCM. The maximum current of the Voltalab Potentiostat is 1 A (corresponds to 250 mA/$cm^2$); therefore, an external power supply connected with a digital multimeter was also used to measure the iV curve of the cell at high current density (**Figure 2.10**).

**Figure 2.10.** Voltalab potentiostat (left) and external power supply with digital multimeter (right).

## 2.4. Electrochemical techniques

Three types of electrochemical measurements have been performed to characterize and evaluate the performance levels of CCM: (i) the measurement of stationary polarization curves (so-called iV curves); (ii) the use of Ageing Stress Tests or ASTs (mainly chronopotentiometry by applying to cells current cycles); (iii) cell cyclic voltammetry to measure the concentration of active electrocatalytic sites.

### 2.4.1. Polarization (iV) curves

The plot of the cell voltage versus the current density (polarization curve or iV curve) at fixed conditions of Temperature (T) and Pressure (P) is the main electrochemical characteristic of any PEM water electrolysis cell. The model iV curve (**Figure 2.11**) aggregates several voltage terms[59]:

- $E^{th}$ (V) : the thermodynamic or reversible cell voltage at T,P, j = 0 operating conditions; $E^{th}$ can be replaced by V(T,P), the thermoneutral cell voltage since the heat required for the entropy change of the reaction is provided inside the cell by dissipations[60],
- $\eta_{mem}$ (V): the ohmic drop across the proton-conducting PFSA membrane,
- $\eta_{act,an}$ (V): the OER overvoltage at the anode,
- $\eta_{act,cat}$ (V): the HER overvoltage at the cathode,
- $\eta_{mass\ trans}$ (V) : a possible mass transport limitation (water transport to reaction sites at the anode).

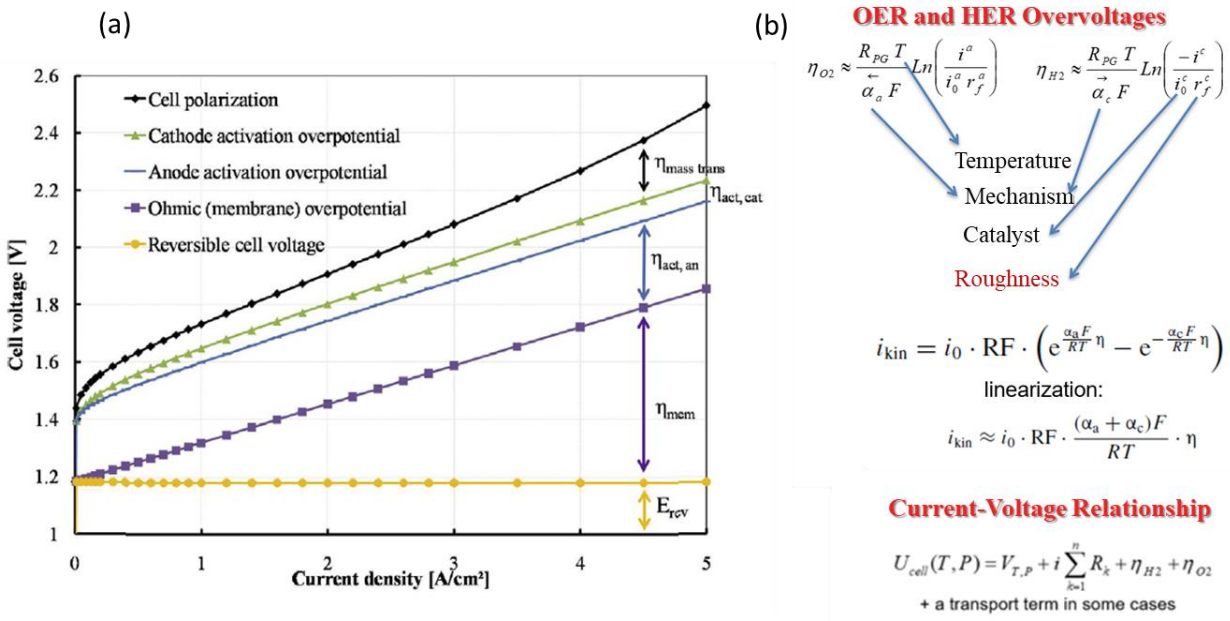


**Figure 2.11.** (a) model iV curve with the anticipated contribution of all irreversible losses to the iV curve of the cell at 80°C[61], (b) model iV curve with experimental parameters.

[59] P. Millet, *Conventional and Innovative Electrocatalysts for PEM Water Electrolysis*, ECS Transaction, 75(14) (2016) 28-35. https://doi.org/10.1149/07514.1073ecst

[60] C. Lamy, P. Millet, *Efficiency of near-ambient temperature water electrolysis*, J. Power Sources, 447 (**2020**) 227350-227364. https://doi.org/10.1016/j.jpowsour.2019.227350

[61] Ojong ET, Kwan JTH, Nouri-Khorasani A, Bonakdarpour A, Wilkinson DP, Smolinka T. *Development of an experimentally validated semi-empirical fully-coupled performance model of a PEM electrolysis cell with a 3-D structured porous transport layer*. Int J Hydrogen Energy 2017;42:25831–47. https://doi.org/10.1016/j.ijhydene.2017.08.183.

For illustration, **Figure 2.12** shows two experimental iV curves and their best fits obtained using the model equations of **Figure 2.11**. Best fits were obtained using the Levenberg-Marquardt algorithm, ie, the damped least-squares method. Fit parameters are compiled in **Table 2.1**.

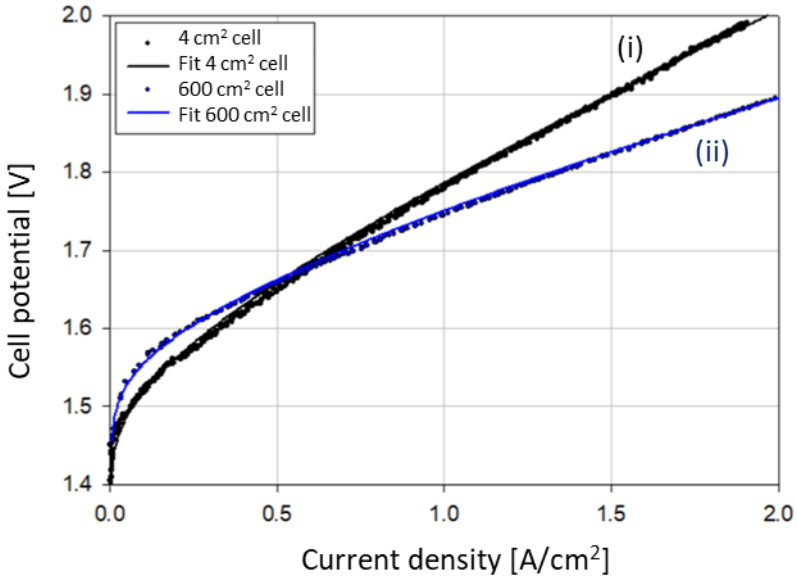


**Figure 2.12.** Experimental (symbols) and best fits (full line) iV curves measured at 60°C on (i) a 4 $cm^2$ laboratory cell; (ii) a 600 $cm^2$ industrial cell at Elogen.

**Table 2.1.** Best fit parameters of the two iV curves shown in **Figure 2.12**.

| | **4 $cm^2$ cell** | **600 $cm^2$ cell** |
|---|---|---|
| Cell resistance (mΩ.$cm^2$) | 183 | 106 |
| OER apparent exchange current density (mA/$cm^2$) | $8\times10^{-6}$ | $1.6\times10^{-6}$ |
| HER apparent exchange current density (mA/$cm^2$) | 0.20 | 0.23 |
| Symmetry factors | 0.5 | 0.5 |
| Mass transport | 0 | 0 |

In the low current density range (< 0.5 A/$cm^2$), the kinetics is controlled by the activity of OER and HER electrocatalysts. The ohmic cell contribution prevails in the high current density range (> 1.0 A/cm2). In this example, the two iV curves differ in both domains. The 4 $cm^2$ cell (Cell n°1) is more efficient in the activation domain but the cell impedance is higher and the iV curve steeper (since the same type of membrane was used in both experiments, such difference comes from the fact that titanium components are more oxidized in the small cell). The 600 $cm^2$ cell is less efficient in the activation domain (this can be due to the different types of catalyst used or less PTL-CL contact) but less steep at elevated current density (less oxidized titanium components are used).

### 2.4.2. Ageing Stress Tests (ASTs)

ASTs are commonly used to accelerate the ageing of PEM water electrolysis cells and gain information on their long-term performances. **Figure 2.13** shows a typical example of such test. The transient cell responses observed at the onset/offset of current steps result from non-isothermal effects. We used this type of test to assess the stability and durability of the CCM tested.

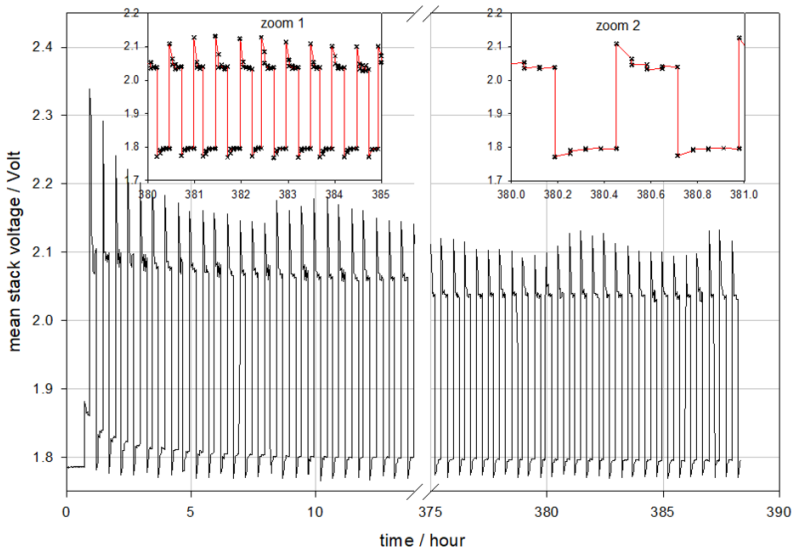


**Figure 2.13.** Chronopotentiometric AST measured between 1.2 and 2.0 A.cm$^{-2}$ at 60°C (source: Elogen).

### 2.4.3. Cyclic voltammetry (CV)

CV is a technique used to scan an electrochemical interface potentially. It is possible to install a reference electrode in a PEM cell, but there is a more straightforward way. Indeed, the cathode is made up of the Pt/$H^+$/$H_2$ electrochemical system, the most reversible redox couple. Therefore, it is possible to use the cathode as an internal reference electrode and scan the anode**.** **Figure 2.14** shows typical CVs measured on the anode of a PEM water electrolysis cell at different scan rates. By integrating the CVs between fixed cell voltage limits, it is possible to calculate a coulombic charge which is proportional to the concentration of $IrO_2$ catalytic sites. The technique, therefore, provides an easy and in-situ means to follow the ageing of anodes.

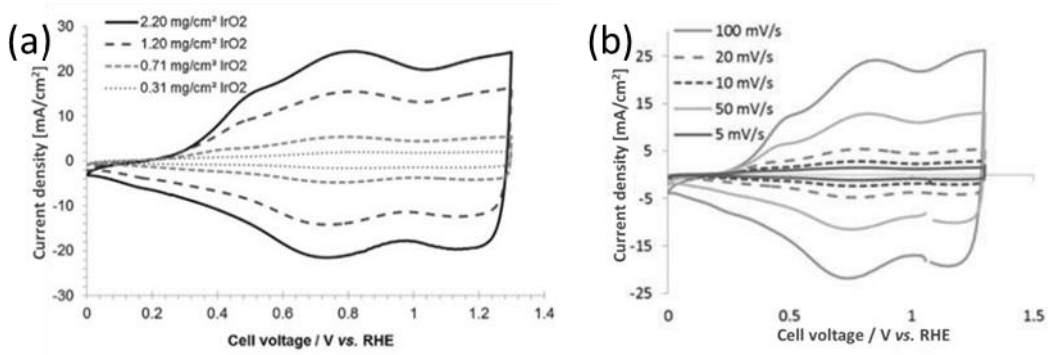


**Figure 2.14.** Cyclic voltammograms measured on the anode of a PEM water electrolysis cell (a) different loading at a scan rate of 20 mV/sec[62] (b) different scan rates at a loading of 1.3 mg cm$^{-2}$ $IrO_2$.[63]

### 2.4.4. Electrochemical Impedance Spectroscopy (EIS)

EIS provides an easy way to analyze the performance level of PEM water electrolysis cells[20]. Typical EIS spectra measured on a PEM water electrolysis cell at 25 mA/cm$^2$ (galvanostatic mode, using a perturbation amplitude of 2.5 mA/cm$^2$) are shown in **Figure 2.15** for illustration. A detailed discussion of the significance of these spectra is provided in the various chapters where the experimental results are presented and analyzed.

[62] Rozain C, Mayousse E, Guillet N, Millet P. Influence of iridium oxide loadings on the performance of PEM water electrolysis cells: Part I–Pure IrO 2 -based anodes. Appl Catal B Environ 2016;182:153–60. https://doi.org/10.1016/j.apcatb.2015.09.013.
[63] C. ROZAIN, PhD thesis, *Développement de nouveaux matériaux d'électrode pour la production d'hydrogène par électrolyse*, defended 27 septembre 2013. Paris-Saclay University. http://theses.fr/2013PA112177

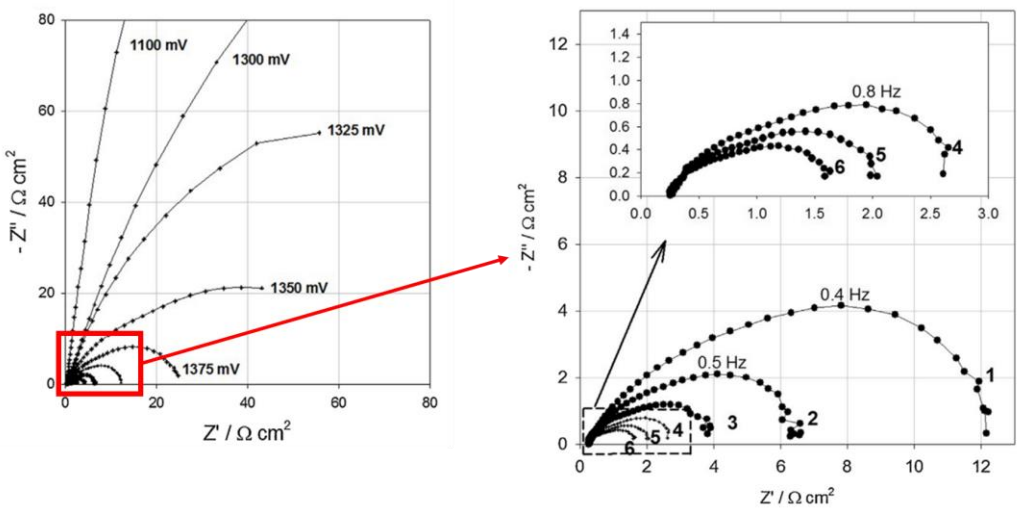


**Figure 2.15.** (left) EIS impedance Nyquist spectra measured at different cell voltages and 80 °C on a 23 $cm^2$ PEM water electrolysis cell. (right) and zoom of EIS impedance spectra of left figure for Ecell (mV) = 1- 1400; 2- 1425; 3- 1450; 4- 1475; 5- 1500; 6- 1525 mV.

## 2.5. Selection of best flowfield

As discussed above, we measured the behavior of four types of flowfields, referred to as 1S, 1L, 2S or 2L. In most experiments (otherwise specified), a clamping pressure of 3.5-Mega Pascal (MPa) was used. The iV curves were recorded at different water flow rates. The thermostat pump had a minimum speed of 1500 rounds per minute (rpm) and a maximum of 4500 rpm. All measurements were made at 60 °C. Results obtained with flowfields 1S and 2S are shown in **Figure 2.16**, and those obtained with flowfields 1L and 2L are shown in **Figure 2.17**.

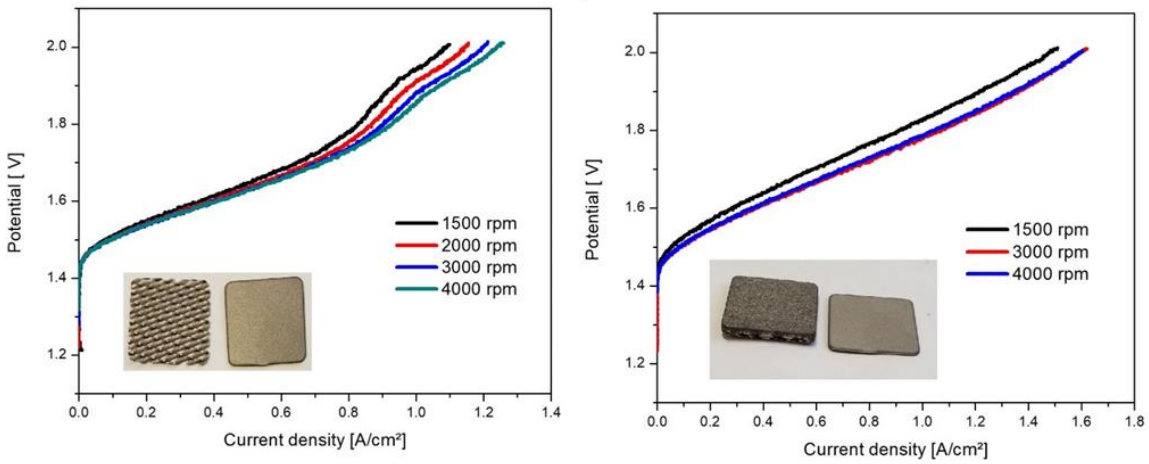


**Figure 2.16.** iV curves measured at 60°C (using cell n°1), $P_{H2} = P_{O2} = 1$ atm with the reference CCM: (a) 1S and (b) 2S flowfields (in insert, photographs of the grid and PTL).

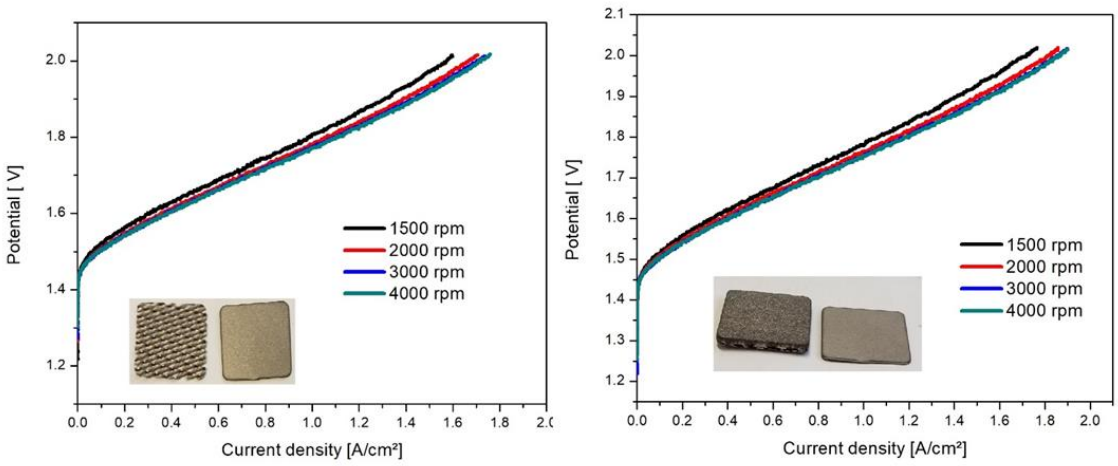


**Figure 2.17.** iV curves measured at 60°C (using cell n°1), $P_{H2} = P_{O2} = 1$ atm with the reference CCM: (a) 1L and (b) 2L flowfields (in insert, photographs of the grid and PTL).

According to the electrochemical performance of the two PTLs (S and L), PTL-L shows the lowest mass transport limitation and optimum electrochemical performance (**Figure 2.18**). Prior studies show that an appropriate range of pore sizes should be used to reduce mass transport losses, small enough to avoid massive gas slugs in the PTL. This was produced by an increase in pore diameters, which resulted in the buildup of more giant gas bubbles, reducing the amount of water available to the catalyst layer. At the same time, the pores should be large enough to avoid capillary effects[23]. The four Grid/PTL combination increases pump rotation speed from 1500 to 3000 rpm, improve electrolysis current, and reduces mass transport limitation. Further, increasing the pump speed to 4000 rpm did not significantly affect the electrolysis performance; therefore, the optimum pump speed was determined to be 3000 rpm. In the following, all experimental results were obtained using flowfield 2L in each cell compartment (anode and cathode).

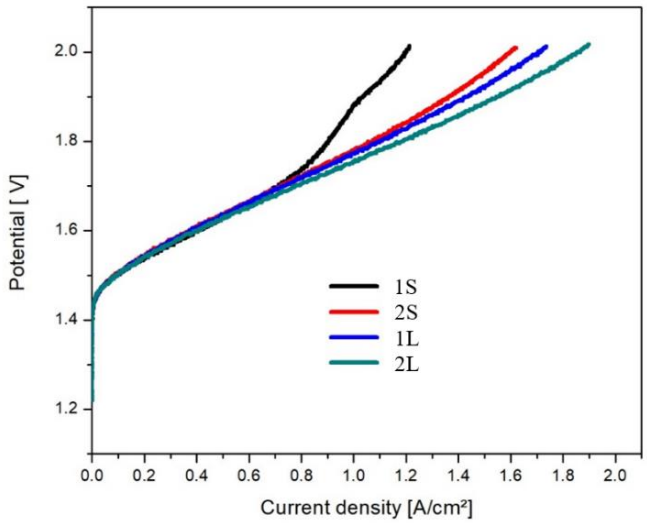


**Figure 2.18.** iV curves measured with the different types of flowfields at 60°C (using cell n°1) and $P_{H2} = P_{O2} = 1$ atm using a water pump rotation speed of 3000 rpm: 1S, 1L, 2S and 2L.

## 2.6. Ink recipes and coating methodologies for Nafion membranes

During our work, a significant effort was made to optimize the recipes used for making catalyst inks and coating catalyst layers onto membranes. Although some practical details remain confidential, the following information can be shared:

### 2.6.1. Membrane pre-treatment

Deionized water

- We used MilliQ quality deionized water throughout.

Membrane cleaning

- All experiments were made using either Nafion 115, Nafion 212 (Chemours) or the HNC membranes.
- Membranes were used either 'as-received' without pretreatment or after cleaning by standard procedure.
- The following standard Nafion membrane cleaning procedure was used: (i) the membrane was first soaked in fresh $H_2O_2$ 3 vol.% at 80°C for 1 hr; (ii) then the membrane was washed with deionized water and treated in a 0.5 mol/L sulfuric acid bath at 80°C for another 1 hr; (iii) finally, the membrane was bathed in deionized water at 80°C for 1 hr.

### 2.6.2. HER ink recipe

Recipe n°1 (conventional)

The HER (cathode) inks were prepared by dispersing Pt/C (40 wt%, Sigma Aldrich) in isopropanol (Merck, 99.5%) in an ultrasonic bath. A dispersion of Nafion PFSA ionomer (Nafion™ 1100W, Sigma Aldrich) was added (role: dispersing agent and source of proton-conducting polymer in the catalyst layer or CL). The Pt/C to ionomer weight ratio in ink was adjusted to reach 2:1.

Recipe n°2 (after optimization to maximize Pt/C transfer)

The HER (cathode) inks were prepared by dispersing Pt/C (48 wt%, Tanaka Precious Metals Inc.) in isopropanol in an ultrasonic bath. A dispersion of Nafion PFSA ionomer (D2020, Chemours) was then added (role: dispersing agent and source of proton-conducting polymer in the CL). The Pt/C to ionomer weight ratio in the ink was adjusted to reach 2:1.

### 2.6.3. OER ink recipe

Recipe n°1

The anode ink was prepared by dispersing $IrO_2$ (SurePure Chemetals Inc.) in isopropanol using the same procedure as for the HER. The weight ratio of $IrO_2$ to Nafion ionomer in the CL was adjusted to 4:1.

### 2.6.4. HER and OER catalyst layer deposition by direct spray

Recipe used (using either the hand spray or the ink printer)

The CCM was prepared by direct spray coating of catalyst inks over the membrane. The same coating conditions were used for both HER and OER catalyst layers. In a typical HER experiment, 1.4 mL (14 mg Pt/C) of cathode ink was directly sprayed over Nafion membrane over a membrane area of 6.25 $cm^2$. The hot plate temperature was set to 60°C to prevent isopropanol absorbtion by the membrane. In a typical OER experiment, 1.4 ml (28 mg $IrO_2$) of anode ink was directly sprayed over Nafion membrane over the area of 6.25 $cm^2$. The hot plate temperature was also set to 60°C.

The CCM was then clamped between two polytetrafluoroethylene (PTFE) sheets and hot-pressed. A 100% transfer yield was obtained at the anode side and a 95% transfer yield was obtained at the cathode side. The transfer yield of Pt/C by direct deposition is higher than the one obtained by DECAL (see 2.6.5).

### 2.6.5. HER and OER catalyst layer deposition by DECAL

Recipe used (using either the hand spray or the ink printer)

The CCM was prepared by indirect spray coating of HER & OER inks over two different PTFE substrates followed by their transfer to the virgin membrane by the so-call DECAL process. In a typical experiment, 1.4 mL (14 mg Pt/C) of cathode ink was sprayed over the HER-PTFE substrate (surface area of 6.25 $cm^2$). 1.4 ml (28 mg $IrO_2$) of anode ink was sprayed over the OER-PTFE substrate (surface area of 6.25 $cm^2$). In both cases, the PTFE sheets were placed on a hot plate at 60°C, allowing solvent evaporation. The HER and OER catalyst layers formed on the PTFE substrates were then transferred to the Nafion membrane by DECAL. A virgin membrane (Nafion or HNC) was clamped between the two PTFE sheets and hot-pressed. After process optimization, the mean catalyst transfer yield from the PTFE sheet to the membrane was 80% for Pt/C and 100% for $IrO_2$. The transfer yield was calculated by the weight difference of the PTFE sheet before and after the transfer divide by CCM area.

## 2.7. Ink recipes and coating methodology for HNC membrane

*(see chapter 5 for chemistry details)*

### 2.7.1. Membrane pre-treatment

The HNC membrane was always used ‘as-received’, without any pre-treatment or cleaning, because of its suspected high sensitivity to hydrolysis. This did not prevent obtaining strong adhesion of the catalytic layers to the dry membrane.

### 2.7.2. HER ink recipe

Typical recipe

- Isopropanol was replaced by cyclohexanol (99%, Alfa Aesar) because the HNC membrane swells a lot in isopropanol but not too much in cyclohexanol.
- 100 mg of Pt/C (20% Sigma-Aldrich) and 850 mg Nafion ionomer solution (5% sigma) were dispersed in 9 g of cyclohexanol and sonicated for several hours.
- Final composition of the ink: 10 wt.% of Pt/C, 5 wt.% of ionomer, and 85.0 wt.% of cyclohexanol.

### 2.7.3. OER ink recipe

Typical recipe

- cyclohexanol was also used as solvent.
- 115 mg of $IrO_2$ and 575 mg of Nafion ionomer solution (5% from Sigma-Aldrich) was dispersed in 11 g of cyclohexanol and sonicated for several hours.
- Final composition of the ink: 10 wt.% of $IrO_2$, 2.5 wt.% of ionomer, and 87.5 wt.% of cyclohexanol.

### 2.7.4. HER and OER catalyst layer deposition by direct spray

The HNC membrane has a very low glass transition temperature which is -35°C for polyvinylidene fluoride (PVDF). The material is much softer than Nafion. For this reason, we never used the DECAL method but only the direct spray method.

Catalyst deposition

The two catalyst layers were deposited onto the HNC membrane by direct spray of the respective inks. This was done by first putting the HNC membrane on a hot plate kept at a constant temperature of 60°C. Then the inks were directly sprayed over the membrane (one face after another) using the hand spray gun described in the experimental section.

Compression details

After ink deposition, in order to increase the compactness and adherence of the catalyst layers, the CCM were clamped between two PTFE sheets and pressed at room temperature (25°C) by applying a force of 5 ton. Ambient temperature was chosen because of the low glass transition temperature of the PVDF polymer used in the HNC membrane. The PTFE foils were used to prevent direct contact between the metallic plates of the press and the catalyst layers in order to avoid surface contamination.

## 2.8. Manufacture of large area (250 $cm^2$) CCM

### 2.8.1. Ink printer parameters

The 250 $cm^2$ CCM used for testing the hybrid nanocomposite membranes in industrial conditions (see detailed results in Chapter 6) contained three membranes: a central HNC membrane clamped between two Nafion 212 membrane equipped with a CL on one side only. The CL were deposited onto the Nafion 212 membranes by DECAL. For each CCM, a PTFE foil (20 x 20 cm) was used as substrate. A mask with a circular hole of 17.8 cm in diameter and adhered to the PTFE substrate was used to delimit the ink coating area. The anode ink contains 94.5 wt% isopropanol, 4.5 wt% $IrO_2$ and 1 wt% PFSA ionomer. The cathode ink contains 94 wt% isopropanol, 4 wt% of Pt/C and 2 wt% of PFSA ionomer. The catalyst ink was ultrasonically sprayed over the substrate using the ink printer (**Figure 2.3**). Spray parameters are compiled in **Table 2.2**.

**Table 2.2.** Ink printer parameters.

| Parameter | anode | Cathode |
|---|---|---|
| Substrate temperature (°C) | 100 | 100 |
| Syringe feeding rate (mL/min) | 0.5 | 0.5 |
| Number of coated cycles | 130 ± 20 | 90 ± 15 |
| Covered area ($cm^2$) | 240 | 240 |

### 2.8.2. Catalyst layer coating

Four square $IrO_2$/Nafion 212 (20 x 20 cm) half CCM were prepared using the Decal transfer method. Once sprayed onto the PTFE substrate, the $IrO_2$-CLs were dried in an oven at 80 °C for 15 h, and then hot pressed against the Nafion 212 membrane at 135°C under 25 tons for 60 min. Then, four Pt-C/Nafion 212 half CCM of the same size were prepared. The cathode CLs sprayed over the PTFE substrates were dried in an oven at 80 °C for 1 h, and then hot pressed against the Nafion 212 membranes, at 135°C under 25 tons for 60 min. The $IrO_2$ and Pt/C loading of each CCM was determined by weighing the PTFE substrate before and after catalyst transfer. The catalyst loadings obtained are compiled in **Table 2.3**. The hybrid nanocomposite membrane (HNC-180-2) was then sandwiched between an anodic and a cathodic half CCM and pressed at 25 tons at room temperature. Finally, the sandwich CCM thus obtained was cut into a circle of a 19 cm in diameter. The steps followed for manufacturing the sandwich CCM are summarized in **Figure 2.19**.

**Table 2.3.** Detail of catalyst loadings used in the 5 CCMs tested in the industrial 5-cell short stack.

| Loading | Cell number | anode (mg/cm$^2$) | | cathode (mg/cm$^2$) | |
|---|---|---|---|---|---|
| | | $IrO_2$ + ionomer | $IrO_2$ | Pt/C + ionomer | Pt/C |
| Moderate-HNC | Cell#1 | 1.62 | 1.296 | 1.01 | 0.677 |
| Laboratory reference (Moderate loading) | Cell#2 | 1.66 | 1.328 | 1.05 | 0.704 |
| Commercial reference | Cell#3 | 3 | 2.43 | 2.05 | 1.43 |
| Low-HNC | Cell#4 | 1.55 | 1.24 | 0.86 | 0.602 |
| High-HNC | Cell#5 | 1.88 | 1.504 | 1.17 | 0.784 |

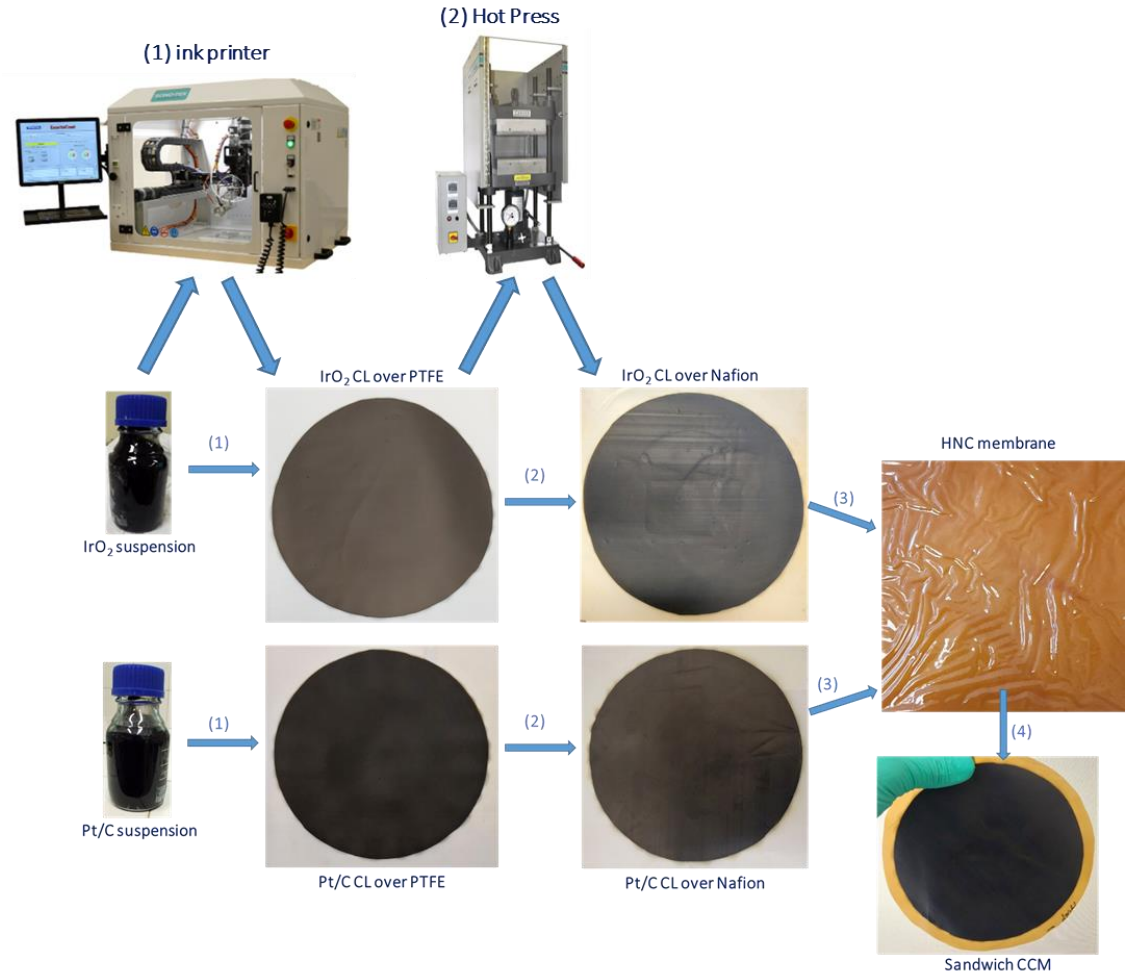


**Figure 2.19.** Overview of the CCM manufacturing process. (1) deposition of CL over PTFE substrate with the ink printer; (2) Decal transfer of the CL from PTFE to Nafion 212 membrane using the hot press; (3) Cold press of sandwich CCM (Nafion 212/HNC/Nafion 212); (4) Cutting of the sandwich CCM to the desired circular shape.

### 2.8.3. Electrochemical characterization

The five CCMs were assembled into a short stack and tested at Elogen Co. using the industrial test bench shown in **Figure 2.20-c**.

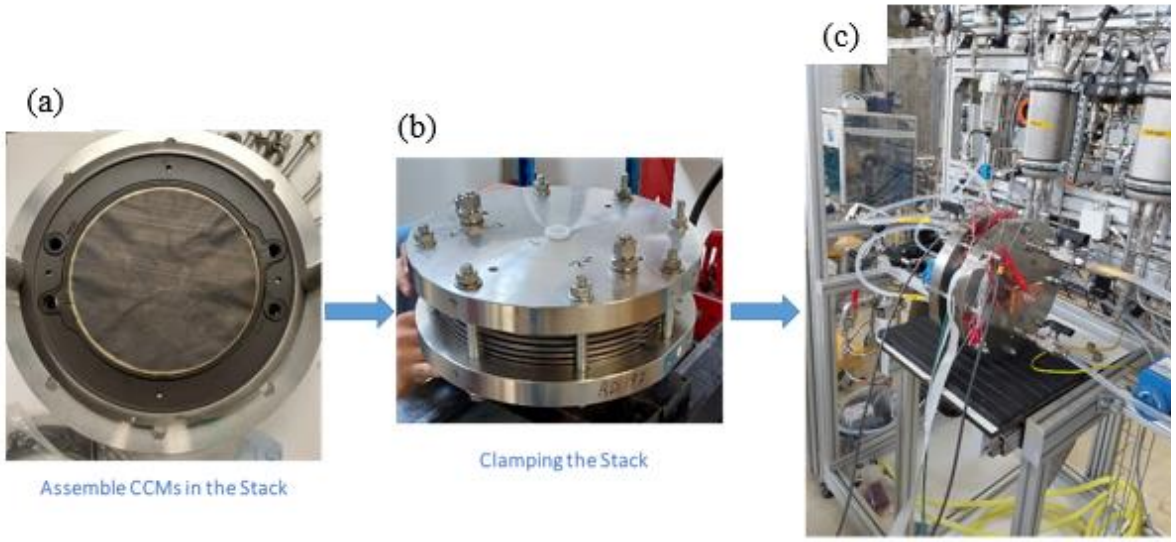


**Figure 2.20.** Photographs showing (a) the placement of a CCM on the stack; (b) the 5-cell short stack after clamping; (c) the stack on the test bench.

The electrochemical characteristics of the short stack were determined using the Autolab potentiostat shown in **Figure 2.21**. It is equipped with a 20 A current booster. Audit measurements (CVs, iV curves, EIS) were made on each cell separately at different time (0, 2, 11, 70 and 240 h) along a chronopotentiometric stability test. Experimental details are :

- The cyclic voltammograms were recorded at a scan rate of 10 mV/sec, in the cell voltage range between 0 and 1.4 V. The HER electrode was used as reference electrode.
- The iV curve were recorded by scanning the cell voltage at 0.4mA/cm$^2$.sec. The potentiostat was used for measurements at low current densities up to 50 mA/cm$^2$; the rectifier of the test bench was used for measurements up to 750 mA/cm$^2$.
- EIS spectra were recorded in galvanic mode at frequencies between 10,000 and 0.1 Hz, at two low current densities of 25 and 50 mA/cm$^2$. Ten impedance points were recorded per decade of frequency, using a galvanic amplitude of 2.5 mA/cm$^2$. The EIS fitting was performed using ZView software.
- The stability test has been designed to obtain the maximum current without the voltage of any of the 5 cells exceeding a maximum voltage of 2.3 V (a high value dictated by the use of uncoated titanium cell components). The current density was cycled between $j_{min}$ and $j_{max}$. At the beginning of the stability test, $j_{min}$ was set to 25 mA/cm$^2$ and $j_{max}$ to 250 mA/cm$^2$. Then, $j_{max}$ was progressively reduced because of the loss of performances and finally, the current cycles were replaced by a simpler chronopotentiometry test at a current density of 25 mA/cm$^2$ for 240 h.

As soon as a cell reaches the maximum permitted cell voltage (2.3 V), the test was stopped, and the hybrid nanocomposite membrane is removed. Then, fresh DI water was used to rinse the stack and to collect the silica nanoparticles grafted with sulfonic compounds trapped at the nanocomposite/Nafion membrane interfaces. The collected water was then dried using a rotary evaporator, and the collected residue was further characterized using energy dispersive X-ray analysis (EDS) and Fourier-transform infrared spectroscopy (FTIR).

Finally, the stability test was resumed by pressing the two Nafion half CCM together (without the HNC membrane) and placing the CCM in the stack for further electrochemical studies. The HNC membrane surface have also been characterized using FTIR, IEC by titration, and EDS.


**Figure 2.21.** Photograph of the Autolab potentiostat equipped with amperometric booster.

# Chapter 3. Characterization of the reference commercial CCM

## 3.1. Description

There are several CCM manufacturers. The manufacturing processes used are well-controlled; therefore, the performances are well-established and reproducible. From a methodological point of view, it is, therefore, helpful to use this type of CCM as a reference to evaluate the performance of our CCMs by comparison. For reasons of confidentiality vis-à-vis the supplier, it is not possible to describe the reference CCM in detail. However, it is possible to say that the membrane is Nafion 115 (127 µm thick), that the cathode catalyst is made of carbon black platinized carbon and that the anode catalyst consists of unsupported iridium oxide nanoparticles.

## 3.2. SEM characterization

**Figure 3.1** shows some surface views of the catalyst's layers, and **Figure 3.2** the EDS spectra measured on these layers. From the SEM images, it is clear that there is more polymeric binder (shown as a compact area inside the blue circles) on the cathode side of the cell (**Figure 3.1-e**) than on the anode side (**Figure 3.1-f**).

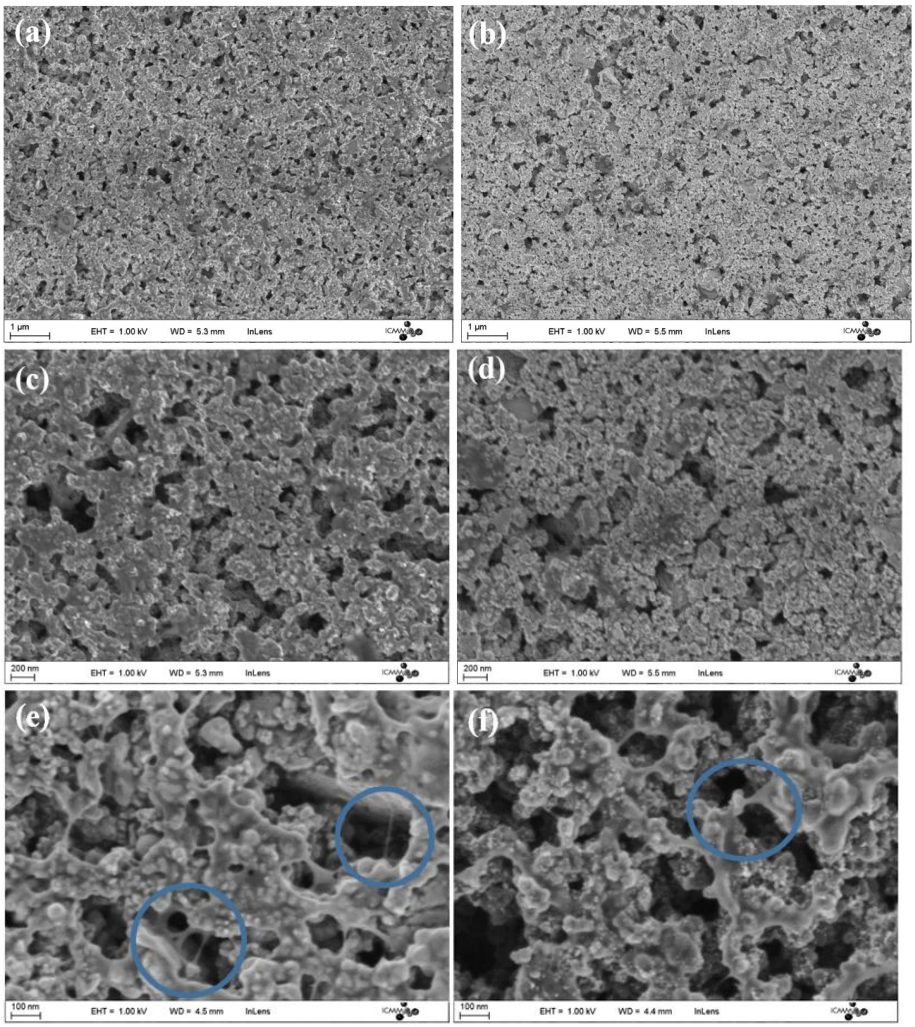


**Figure 3.1.** SEM images of commercial CCM: (a,c,e) cathode and (b,d,f) anode at three different magnifications.

We also perform EDS to see the elemental compositions of both the anode and cathode sides. The fluorine content is higher in the cathode than in the anode. Also, a relatively more carbon was detected in the cathode than anode due to using Pt supported over carbon as a cathode catalyst. Sulfur could not be detected in the cathode due to the insufficient resolution of the EDS detector as a result of overlapping between Pt and S peaks.

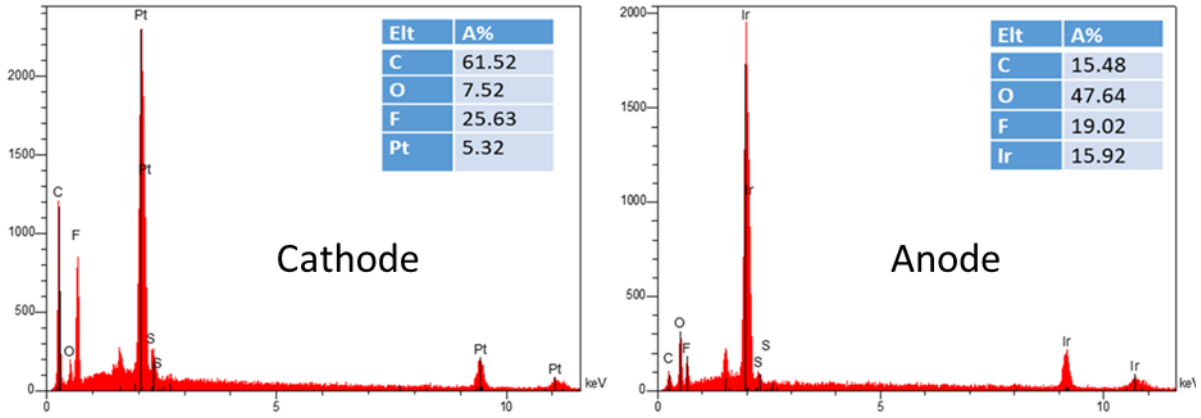


**Figure 3.2.** EDS spectra of (left) cathode and (right) anode of commercial CCM used as reference.

## 3.3. Electrochemical characterization

Besides performances, the durability of electrochemical performances is another KPI of great practical interest. In the industry, water electrolysers need to be operated up to 100000 hours to be cost-competitive. During operation, a gradual increase of each cell's cell voltage in a stack tends to increase. Starting at approximately 1.8 Volt (the exact value depends on the nominal operating current density), the so-called EoL (End of Life) is reached when the mean cell voltage reaches a value of 2.3 Volt. Ageing Stress tests (ASTs) are used to assess the long-term performances by applying fast current cycles.

AST

An AST is *current density cycling* which was performed to evaluate the behavior of the reference CCM and set a performance durability baseline. The cell had a 2L-type flowfield in each cell compartment and a water pump rotation speed of 3000 rpm at 60 °C. The chrono-potentiometric experiment was performed by cycling the current density between 25 and 250 mA/cm$^2$, using the Voltalab potentiostat. The experiment was stopped at each end of day and weekends and restarted the next open day. After 70 hours of AST (**Figure 3.3-a**), an additional chrono-potentiometric experiment was performed for 20 hours, at a constant current density of 1A/cm$^2$, using the external DC power source (**Figure 3.3-b**), to determine the stability of the response in stationary operating conditions. **Figure 3.3-a** shows an initial rise of the cell voltage, which then tends to stabilize: this corresponds to a type of activation process. After that, performances remain stable (**Figure 3.3-b**).

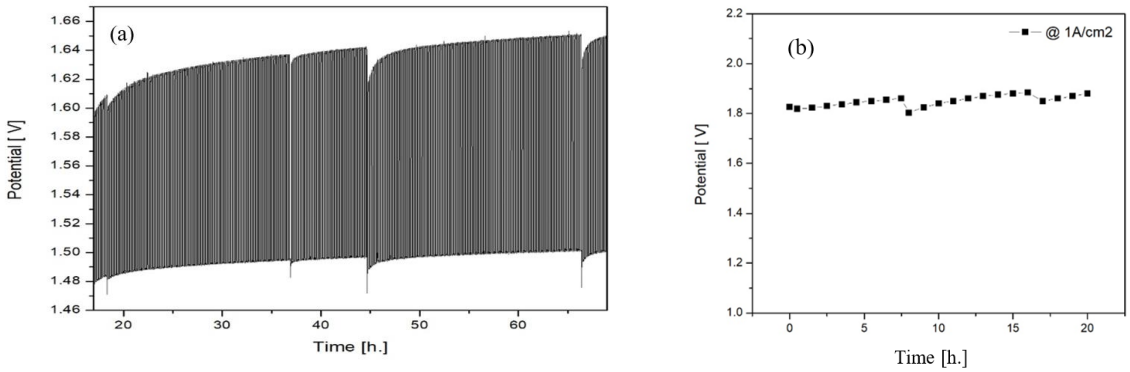


**Figure 3.3.** AST test performed on the reference CCM at 60 °C using cell n°1 with 2L flowfield: (a) chronopotentiometry at 25 and 250 mA/cm$^2$ for 70 h and (b) chronopotentiometry at 1A/cm$^2$ for 20 h.

However, significant changes took place during the test despite its brevity. The iV curves measured at 60°C at BoT (Beginning of Test) and EoT (End of Test) after 90 cumulated hours of operation are shown in **Figure 3.4-a**. The corresponding EIS spectra are shown in **Figure 3.4-b**. A significant degradation of performance occurred during the test. The iV curve becomes sloppy (increased internal cell resistance), and the mass transport limitation effect takes place at lower current density. The EIS spectra measured at 25 mA/cm$^2$ (a current density value less than the one at which mass transport is observed) show two semicircles. The high-frequency (HF) one was attributed to the HER, and the low-frequency (LF) one to the OER. In case of a mass transport problem, an additional semicircle may appear, indicating that the cell does not operate correctly (not the case here).

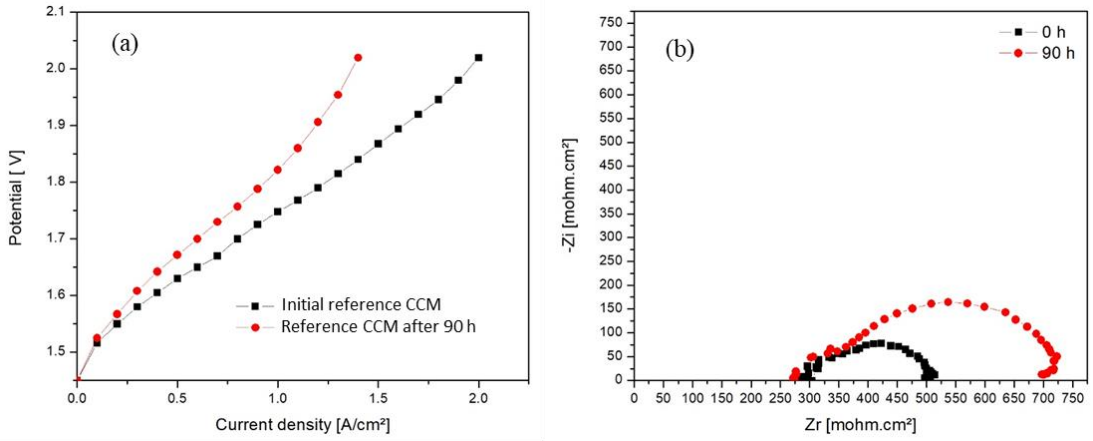


**Figure 3.4.** (a) iV curve and (b) EIS measurements at 25 mA/cm$^2$ on commercial CCM before and after AST. The measurement was performed at 60 °C using cell n°1 with 2L flowfield.

## 3.4. Memory effects

Another experiment was performed over a longer period of time (up to 200 hours) to check reproducibility and gain more insights on the fast degradation reported in **Figure 3.4**. **Figure 3.5-a** shows the response of the cell voltage during cycling between 15 and 150 mA/cm$^2$ only (such low current density was chosen on purpose). **Figure 3.5-b** shows the fast degradation of the iV curves during the test**. Figures 3.5-c and 3.5-d** show the EIS spectra recorded at 25 and 100 mA/cm$^{2,}$ respectively. A kind of *memory effect* was observed on this reference CCM. Afterwards, it has been concluded that such behavior can be considered as an artefact, possibly resulting from the drying of the CCM during weekends or even weeks when the setup was used for testing other CCM in parallel.

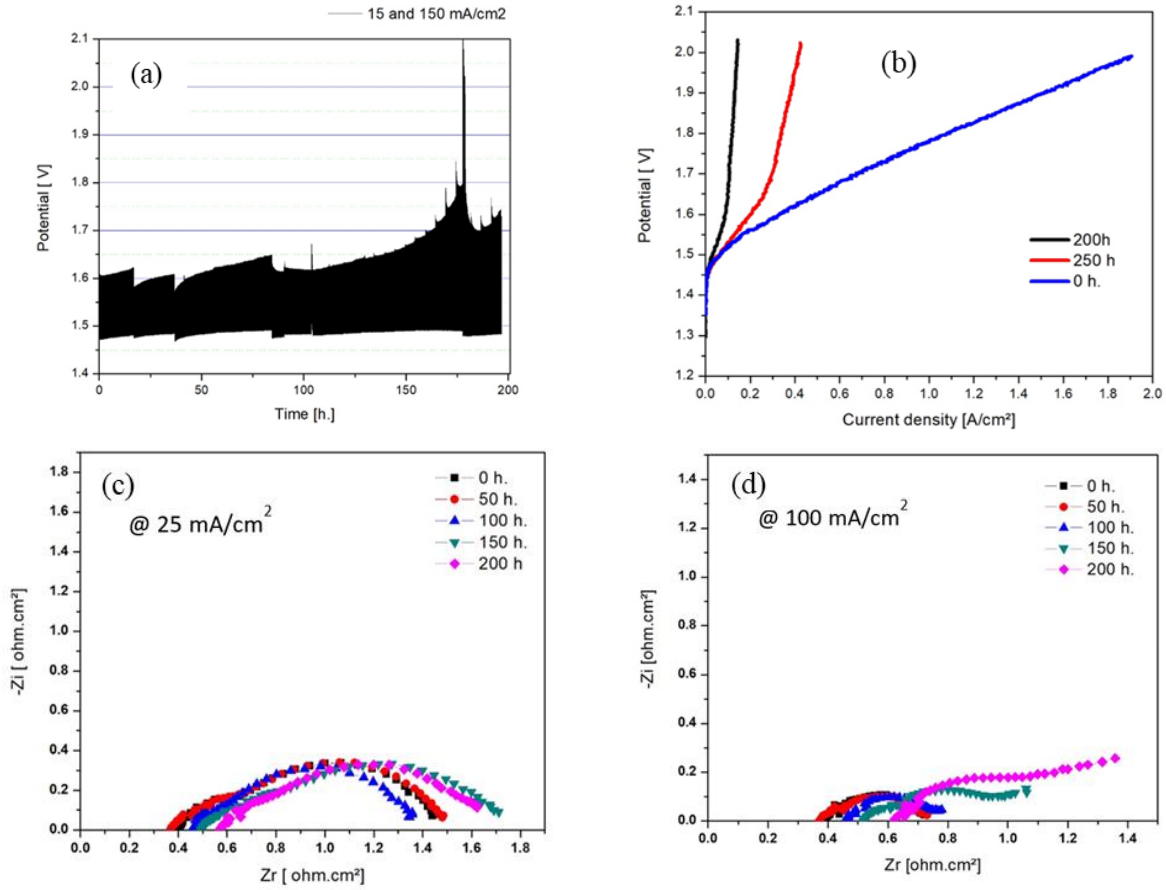


**Figure 3.5.** AST test performed on the reference CCM at 60 °C and atmospheric pressure using cell n°1 with 2L-type flowfield: (a) chronopotentiometry at 15 and 150 mA/cm$^2$ for 200 h; (b) iV curves recorded at different times; (c) EIS spectra measured at 25 mA/cm$^2$ during the test; (d) EIS spectra measured at 100 mA/cm$^2$ during the test.

We performed an accelerated stability test between 15 and 150 mA/cm$^2$ for 200 h, we observed large degradation in CCM performance, especially at higher current density. The CCM memorizes the current that is used during the AST and cannot go higher. As shown in **Figure 3.5-b,** water electrolysis starts at the same potential for all curves, but after 200 h of AST at 15 and 150 mA, the iV curve goes up vertically and cannot reach a higher current.
In an attempt to erase the memory effect, voltages of 2V were applied to the cell for 50h. A slight improvement was observed on iV curve after 250 hours, but it was not sufficient to further improve the CCM. From the EIS measurements, at 100mA (**Figure 3.5-d**), a diffusion effect starts to appear after 150h of AST, probably related to water transport to the anode and inappropriate cell clamping (cell hardware problem). Such an effect did not exist at a lower current density (25 mA/cm$^2$). A slight increase in the HFR of the CCM was observed as a result of titanium PTL oxidation at the anode.

*Cyclic voltammetry*

**Figure 3.6** shows examples of cyclic voltammograms measured on the cell at three different scan rates.

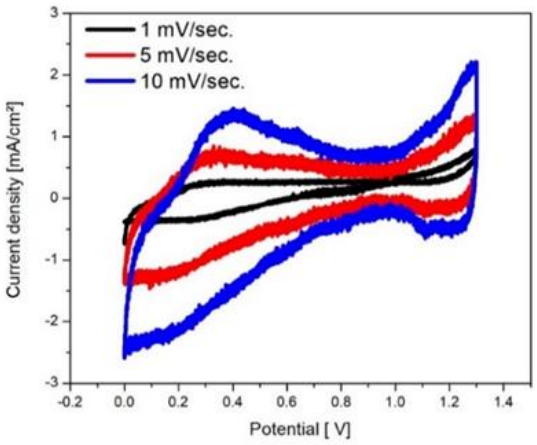


**Figure 3.6.** Cyclic voltammograms were measured on the reference CCM (at 60°C using cell n°2) at three different scan rates.

The effect of hydrogen flushing and chronopotentiometry has been observed at 150 mA/cm$^2$ for a few minutes. As shown in **Figure 3.7-b**, saturating the cathode compartment with hydrogen before CV did not affect the shape of the CV. While applying chronopotentiometry for a few minutes alters the shape of the first cycle, the change in shape is temporary and disappears in the third cycle of the CV (**Figure 3.7**).

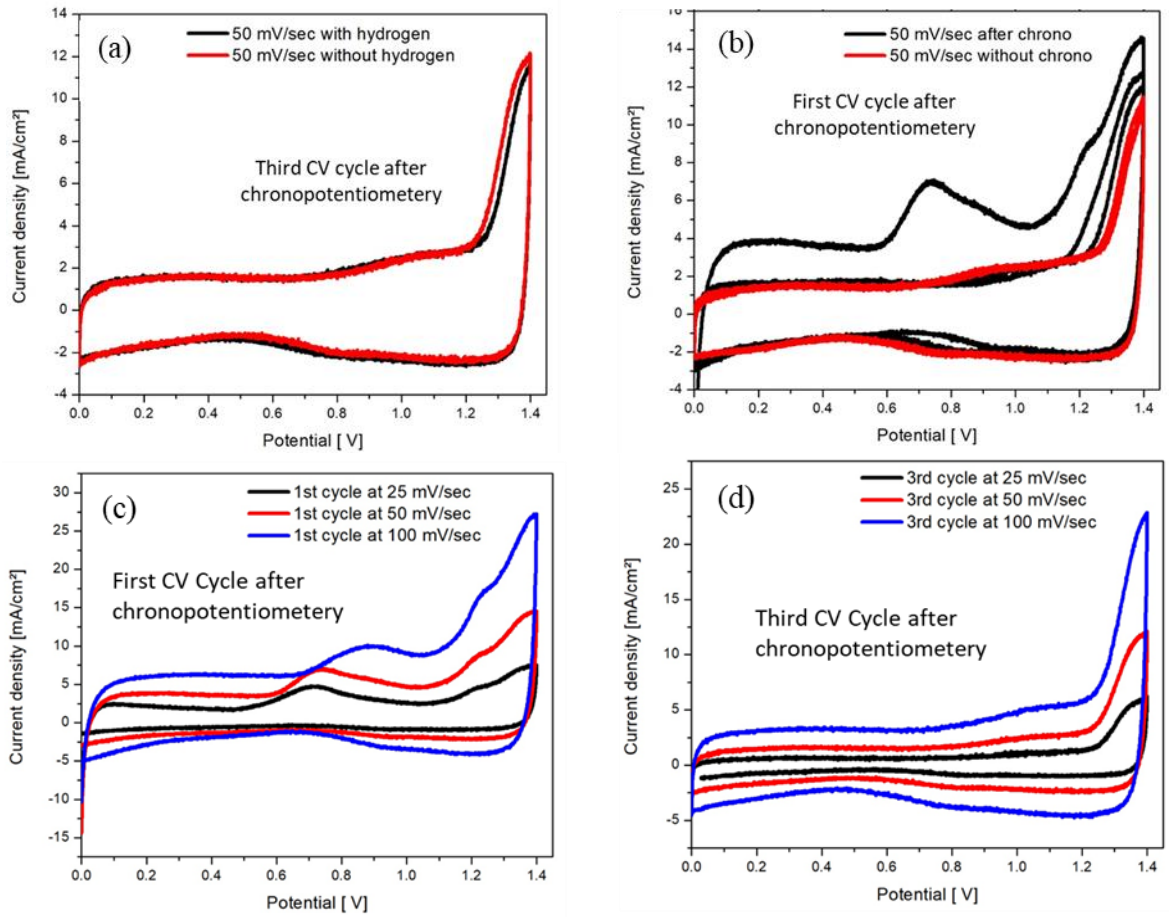


**Figure 3.7.**Cyclic voltammograms measured, Effect of hydrogen saturation of the cathode before CV(a) and effect of chronopotentiometry on CV curve shape (b), and the impact of chronopotentiometry on CV curve shape at three different scan rates (c,d). The measurement was performed at 60 °C using cell n°2.

The specific capacitance (the sum of the electric double-layer capacitor (EDLC) and the pseudocapacitance) of the catalyst layer in the commercial CCM was estimated from the CV using the following equation[64]:

$$Cs = (\int Idv)/2\,(v.\Delta V)$$

Where $C_s$ is the specific areal capacitance (mF/cm$^2$), I is the current density (mA/cm$^2$), v is the scan rate (mV/sec.), and $\Delta V$ is the voltage window (1.4 V).

**Figure 3.8** shows examples of cyclic voltammograms measured on the cell at three different scan rates and at two different times of the AST (after 35 h and 250 h of AST). A measure of the coulombic charge between appropriate potential limits provides information about the number of catalytic sites available (those in ionic contact with the membrane).

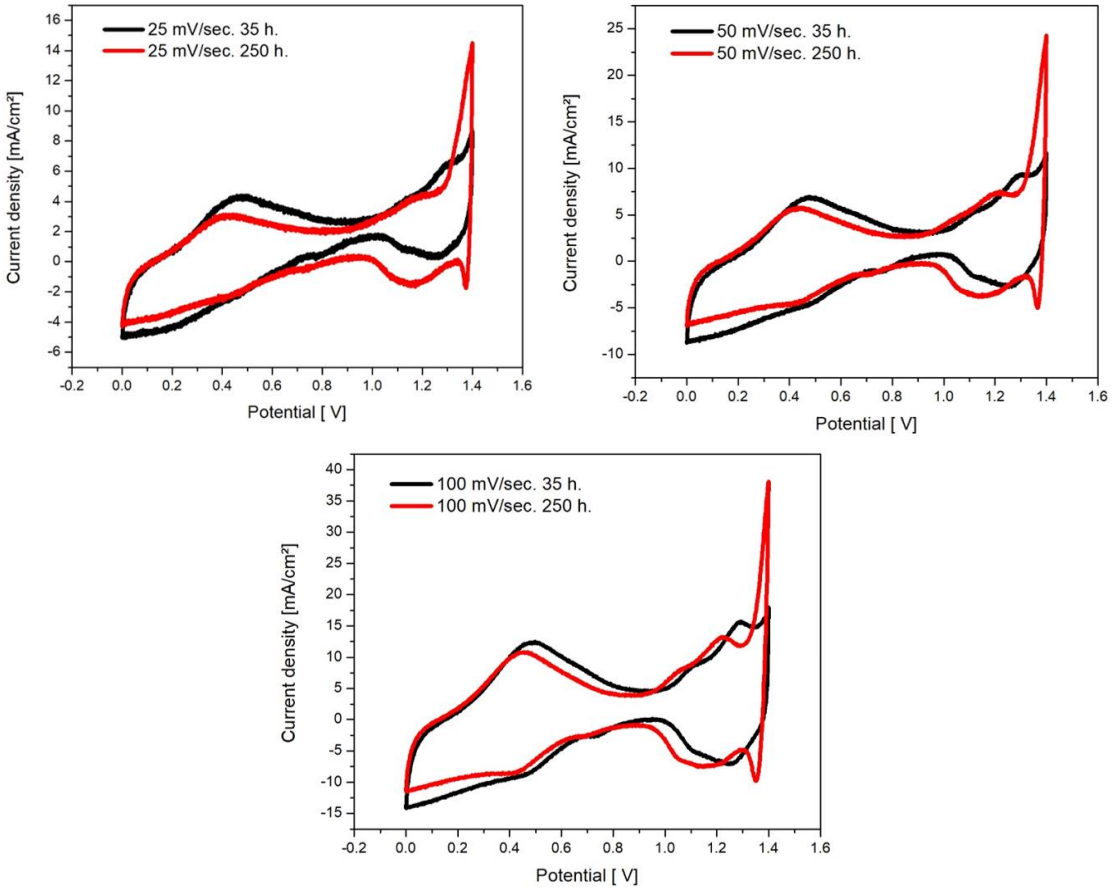


**Figure 3.8.** Cyclic voltammograms measured at three different scan rates after 35 hours and 250 hours of AST. The measurement performed at 60 °C using cell#1.

The specific surface capacitance of the commercial CCM before and after AST did not change significantly, as calculated from integration of CV at different scan rate (**Table 3.1**).

**Table 3.1.** Compilation of specific areal capacitance values measured at three different scan rates.

| Scan rate (mV/sec.) | 25 | 50 | 100 |
|---|---|---|---|
| $C_s$ 35 h (mF/cm$^2$) | 79.5 | 72.5 | 65 |
| $C_s$ 250 h (mF/cm$^2$) | 83.5 | 73 | 63 |

[64] Zhao S, Yu H, Maric R, Danilovic N, Capuano CB, Ayers KE, et al. *Calculating the Electrochemically Active Surface Area of Iridium Oxide in Operating Proton Exchange Membrane Electrolyzers*. J Electrochem Soc 2015;162:F1292–8. https://doi.org/10.1149/2.0211512jes.

The Specific areal capacitance is assumed to be proportional to the number of active sites on a catalyst. CVs are integrated to obtain the coulombic charges over the voltage window of interest (limits are dictated by the half-cell reaction of interest, here, HER and OER). Due to diffusion into the porosity of the catalyst and the catalyst layers, all active sites in contact with the electrolyte can be detected at a low scan rate, whereas at a high scan rate, only the most accessible active sites are detected[65]. This is to say that the integral of the CVs is a function of the scan rate used to collect the CVs.

Conclusion

The measurements show that this *memory effect* is not related to a loss of catalytic sites. We can therefore speculate that the 'pseudo degradation' measured on the iV curves is an artefact related to mass transport issues inside the cell.

Note

The memory effect also appeared in another experimental situation. We first prepared a new CCM (using $IrO_2$/Pt catalysts) and recorded its iV curve (**Figure 3.9-b**, black curve). Then, we applied a succession of chronoamperometric steps by changing the cell voltage from 0 up to 1300 mV with 100 mV voltage increments (**Figure 3.9-a**). The experiment was stopped at 1.3 V, just before the water electrolysis onset voltage of 1.45 V at 60°C. Then a second iV curve was recorded (**Figure 3.9-b**, red curve). Again, the reported memory effect is clearly seen.

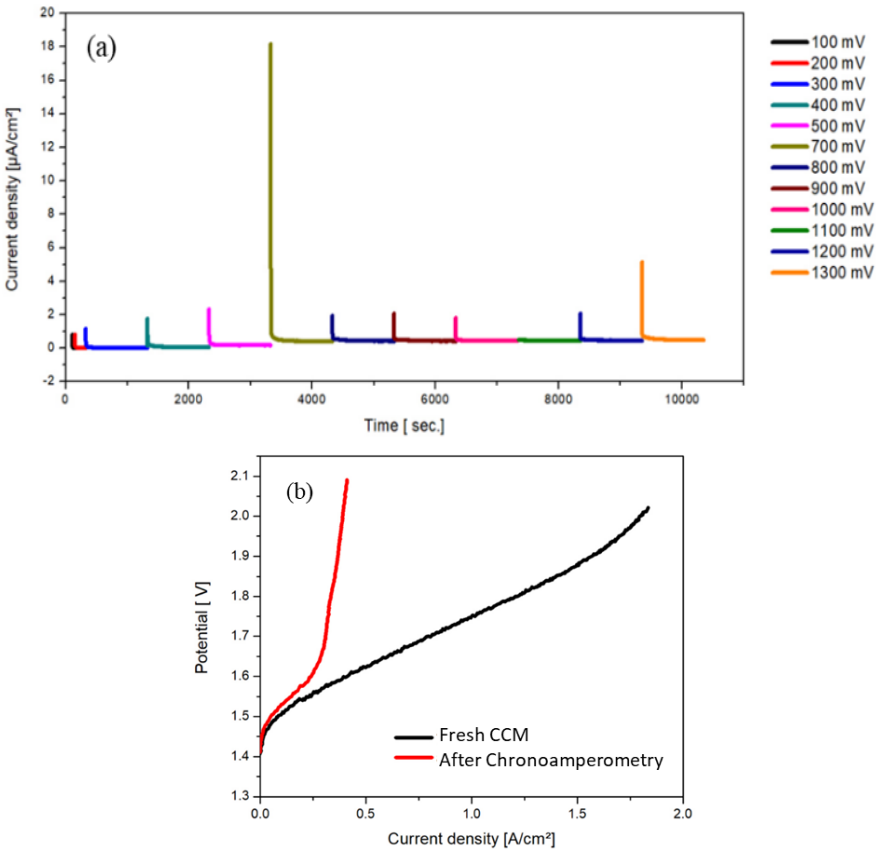


**Figure 3.9.** (a) Chronoampermetry test; (b) iV curve measured after chronopotentiometry at low voltage. The measurement was performed at 60 °C using cell n°2.

[65] Audichon T, Mayousse E, Morisset S, Morais C, Comminges C, Napporn TW, et al. *Electroactivity of $RuO_2$–$IrO_2$ mixed nanocatalysts toward the oxygen evolution reaction in a water electrolyzer supplied by a solar profile*. Int J Hydrogen Energy 2014;39:16785–96. https://doi.org/10.1016/j.ijhydene.2014.07.170.

Based on these different experimental results, we finally reached the conclusion that this memory effect is an experimental artefact, not the signature of a fast loss of electrochemical performances of the CCM. The shape of the iV curves (**Figure 3.5-b** and **Figure 3.9-b**) indicates that there is a mass transport problem in the cell. Such a phenomenon has already been observed and reported in the literature[66]. It was attributed to a so-called gas-screening effect, which is the accumulation of a gaseous film at the interface between the PTL(s) and the CCM. It occurs when the cell is not sufficiently tightened or when the seals used are too thick to allow a good electrical contact. It can be erased by increasing the current density to force gas evacuation through the PTLs.

*Attempts made to reverse the memory effect*

We tried to erase this memory effect by changing the max current density of the AST. Results are shown in **Figure 3.10-a**. The initial iV curve (0 h) shows no mass transport limitation up to 2 A/cm$^2$. Then an AST was applied by cycling between 25 and 150 mA/cm$^2$ for 50 hours. Then, the AST was stopped, and a second iV curve was recorded. A strong mass transport limitation appears at 0.75 mA/cm$^2$ (not at 150 mA/cm$^2$. This effect may be attributed to the fact that the AST was not applied for a sufficiently long period of time (**Figure 3.10**).

Then, a constant cell voltage of 2 V was applied to the cell for 5 minutes, followed by 1.5 V for an additional 5 min. As shown in **Figure 3.9-a**, the current density at which the mass transport limitation is observed is now shifted to the higher current density range between the 50 and 58 hours of the AST. Performing an iV curve measurement after 8 hours **(Figure 3.10-a)** of high current AST can reverse a major part of the iV curve shape and the memory effect to some extent. However, applying an additional AST at the same high current density value has a minimum effect on the electrochemical performance of the cell. The iV curve measured after 100 hours shows a lower memory effect compared with the one measured after 50 hours. Therefore, it can be speculated that the origin of the memory effect is the AST performed at low current density. Additional information was gained from EIS measurements made at low current density (before mass transport takes place). In this case, the shape of the EIS spectra at low frequency (**Figure 3.10-b**) confirms that there is no mass transport problem. The diameter of the EIS semicircle measured after at 40 mA/cm$^2$ after 0 and 100 hours remains almost unchanged. As shown on the iV curve, this part of the curve is not affected by mass transport issues.

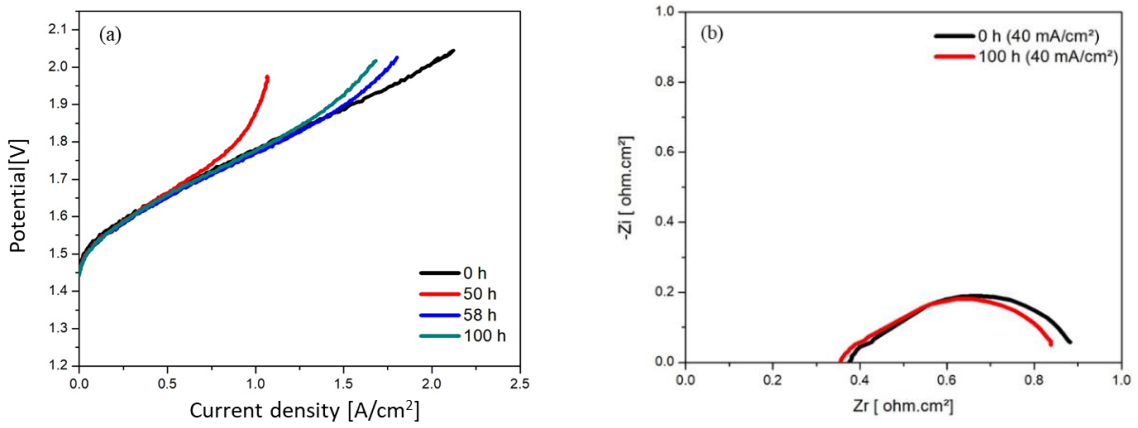


**Figure 3.10.** (a) iV curve and (b) EIS measurements at 40 mA/cm$^2$ on commercial CCM (cell n°2) before and after AST at 60°C.

[66] Millet P, Ranjbari A, de Guglielmo F, Grigoriev SA, Auprêtre F. *Cell failure mechanisms in PEM water electrolyzers*. Int J Hydrogen Energy 2012;37:17478–87. https://doi.org/10.1016/j.ijhydene.2012.06.017.

Note: for safety reasons, the stability test at high current density was performed during the lab working hours. Therefore, a fluctuation in applied voltage is observed as a result of several switches on/off of the cell (**Figure 3.11**).

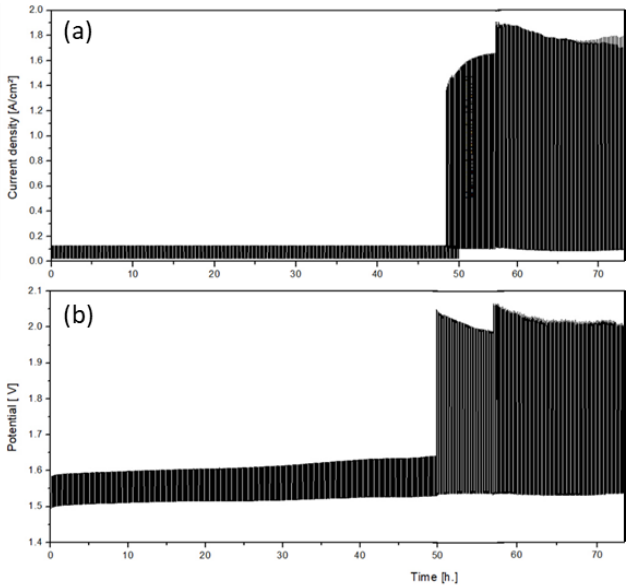


**Figure 3.11.** commercial CCM stability test at 60°C using cell n°2 : (a) chronopotentiometry (b) chronoamperometry. The applied current was between 25 and 150 mA/cm$^2$ for 50 h; then applied cell voltage was between 1.5 and 2 V for an additional 50 h.

The cyclic voltammograms measured before and after the AST are plotted in **Figure 3.12**. The coulombic charge measured by the integration of the cyclic voltammograms depends on the scan rate. After 100 hours of AST, a higher specific capacitance of the CCM electrodes was measured, indicating electrochemical activation of the electrocatalyst during the AST. Furthermore, the areal-specific capacitance increases with a reducing scan rate (**Table 3.2**). We interpret this effect as follows. At a low scan rate, ions have enough time to diffuse and adsorb over the catalyst surface: this explains the high areal capacitance measured at 1 mV/sec. We speculate that a reduction of the scan rate helps electrolyte to penetrate pores more thoroughly and to make greater contact with the internal surface of the electrode material, resulting in a larger measured capacitance, which is closer to the intrinsic capacitance. At a higher scan rate, however, electrolyte and electrode are in contact for a very brief period of time, resulting in less charge being stored on the electrode surface and, consequently a low capacitance.

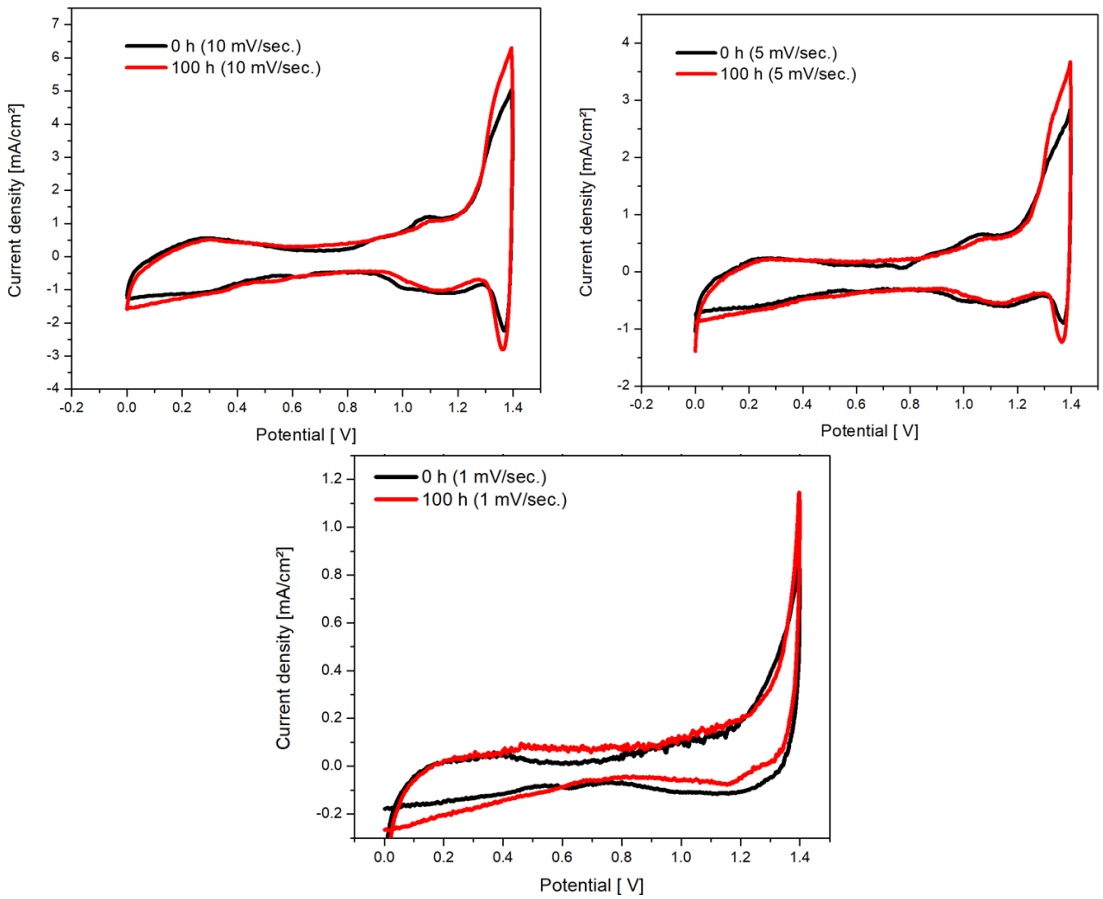


**Figure 3.12.** Cyclic voltammograms measured at three different scan rates after 0 hours and 100 hours of AST. The measurement performed at 60 °C using cell n°2.

**Table 3.2.** Comparison of surface areal capacitance values measured at three different scan rates.

| | Scan rate (mV/sec.) | | |
|---|---|---|---|
| | 1 | 5 | 10 |
| $C_s$ 0 h (mF/cm$^2$) | 91.75 | 90.95 | 83.5 |
| $C_s$ 100 h (mF/cm$^2$) | 97.5 | 96.35 | 87.5 |

## 3.5. Conclusions

The best flowfield has been used to measure the performances of a reference commercial CCM. The main problem that we had to solve was to get rid of mass transport limitations which tend to appear during the tests. Such artefact should not be considered as a CCM degradation but rather as the result of not sufficiently controlled experimental conditions. The performance level and durability behavior of the reference commercial CCM have been measured. The commercial CCM is stable at experimental conditions and will be used as a reference in the following to benchmark the results obtained with the HNC membrane.

# Chapter 4. Synthesis & characterization of lab-made PFSA-based CCMs

Objective: we report here a set of results relating to the manufacture and measurement of the performance of CCMs manufactured by ourselves using standard materials, in particular Nafion 115 (PFSA) membranes, Pt/C HER catalyst and $IrO_2$ OER catalyst. The objective is on the one hand, to succeed in manufacturing CCMs with the same level of performance as the commercial reference, and on the other hand, to master the manufacturing process of the process before using it to manufacture CCMs integrating the hybrid nanocomposite (HNC) membrane developed by the CEA.

## 4.1. Cleaning and conditioning procedures

### 4.1.1. Effect of membrane-pretreatment and hot pressing on Nafion morphology

The pretreatment procedure used for cleaning the membrane was as follows: Nafion membrane was placed in an aqueous bath containing 3 % $H_2O_2$ at 80 °C for one hour. Then the membrane was washed with deionized water and treated in a 0.5 mol/L sulfuric acid bath at 80°C for another one hour. Finally, the membrane was bathed in deionized water at 80°C for one hour. The effect on the morphology of hot press on untreated and pretreated membranes is shown in the **Figure 4.1**. Nafion 115 membrane was cut into small pieces of 2 $cm^2$ and hot-pressed at 2 tons (98 MPa) for 5, 10, and 30 minutes at 135°C. Unlike directly sprayed samples, all pressed membranes showed a slight reduction in transparency without turning into yellow color.

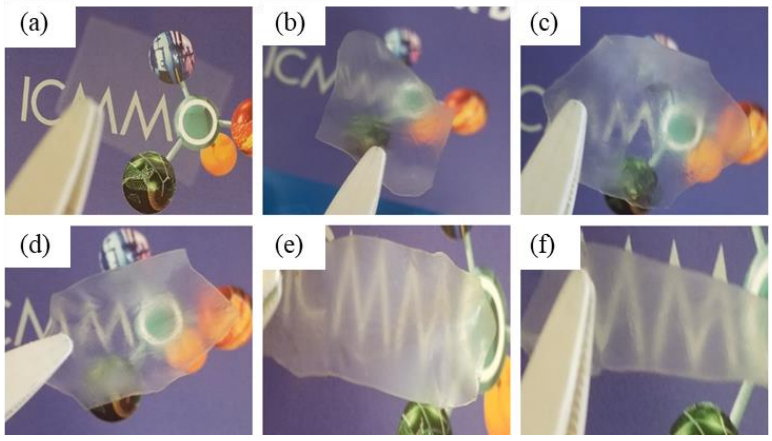


**Figure 4.1.** Photographs of Nafion 115 hot-pressed at 98 MPa for, (a) 0 min, (b) 5 min, (c) 10 min, (d) 30 min, and $H_2O_2/H_2SO_4$ pretreated Nafion membrane hot-pressed at 98 MPa for (e) 10 min and (f) 30 min. The untreated membrane shows a slight reduction in transparency without turning into yellow color, while $H_2O_2/H_2SO_4$ pretreated membrane shows slight yellowish color at the corners.

### 4.1.2. Effect of alcohol and hot pressing on Nafion morphology

By visual appearance, we can conclude that a direct spray of isopropanol-based ink over Nafion membrane induces yellowish color, increasing over time at normal atmospheric conditions. Nafion membrane in contact with the catalyst also slightly induces yellowish color (**Figure 4.2).** It is generally admitted in the literature that the color is due to degraded chemicals (taken from air or solvents) but not to membrane degradation. The impact on mechanical properties and proton-conductivity is unknown. This is why direct ink spray onto the membrane is not considered as the best option for CCM manufacturing.

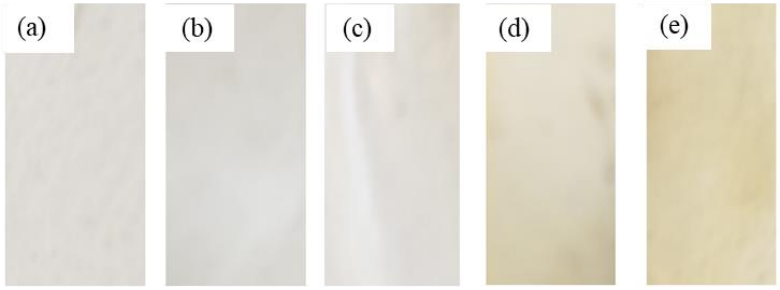


**Figure 4.2.** (a) As-received Nafion membrane, (b) hot pressed Nafion membrane, (c) pretreated hot pressed Nafion membrane, (d) periphery of pretreated hot pressed Nafion membrane after the DECAL transferred CCM, and (e) and periphery of pretreated hot pressed Nafion membrane after direct spray-coated CCM.

## 4.2. CCM manufactured using the hand spray gun

This laboratory method has been used first because it provides a fast and simple way to make CCM and validate ink recipes.

### 4.2.1. Catalyst ink preparation

*See §2.6 in the experimental section.*

### 4.2.2. Manufacturing of CCMs by direct spray coating

*See §2.6 in the experimental section.*

The recipe was optimized to avoid isopropanol absorption, and the Nafion remained transparent after **deposition** (**Figure 4.3-a)**. However, after hot pressing the CCM, a slight color change in the corner of the Nafion membrane was observed, which may be attributed to a small amount of isopropanol absorbed with the membrane starting to interact with the membrane at high temperature **(Figure 4.3-b)**. **Figure 4.3-c** shows that approximately 20 wt% of the Pt/C catalyst remained adsorbed onto the PTFE sheet. On the other hand, the CCM after 30 hours of electrolysis is shown in **Figure 4.3-d**.

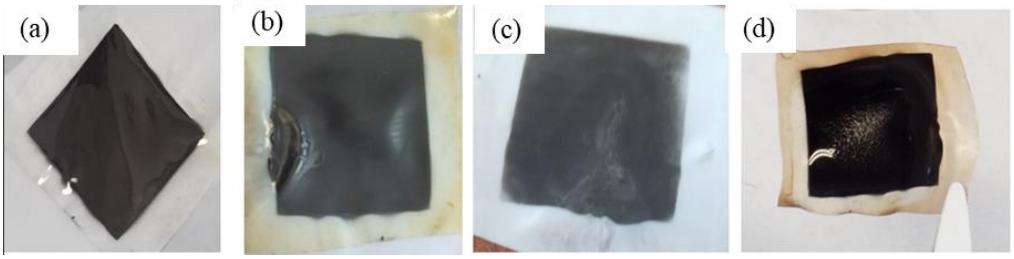


**Figure 4.3.** (a) Flat morphology of the Nafion membrane after cathode spray (the membrane did not swell nor wrinkle), (b) CCM after hot press at 135°C for 7 min. (c) PTFE sheet coated with 20% Pt/C catalyst that transferred from Nafion to PTFE upon hot pressing and (d) CCM after 30 h of electrolysis.

Poor kinetics of the directed deposited catalyst over the Nafion membrane was attributed to membrane swelling during CL deposition and causing inhomogeneities. In our investigation, such inhomogeneities were not detected due to the catalyst ink flow rate was low, which that used for spray coating, which reduced swelling and allowed consistent electrode deposition.

### 4.2.3. Manufacturing of CCMs by DECAL

*DECAL-CCM manufacturing: see recipe in §2.4*

**Figure 4.4-a** shows a picture of a typical CCM prepared by DECAL. A slight change in the color of the Nafion film at the sheet corners was observed as a result of hot pressing at a high temperature, as described in section 4.2.2.

**Figure 4.4-b** shows PTFE sheet coated with 40 wt% of Pt/C catalyst that transferred from Nafion to PTFE upon hot pressing, indicating that 60 wt% of the Pt/C catalyst was transferred from the inert substrate to the membrane. On the anode side, a 100% transfer yield was obtained. The CCM prepared by DECAL is less yellowish than direct spraying, and we speculate that isopropanol contributes to the formation of this yellowish color.

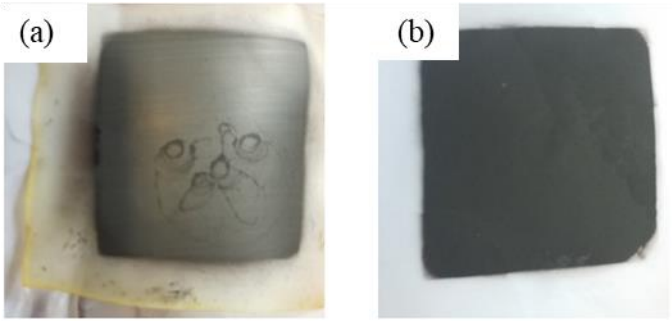


**Figure 4.4.** (a) CCM after hot press at 135 C for 7 min and (b) PTFE sheet coated with 40% of Pt/C catalyst that transferred from Nafion to PTFE upon hot pressing.

*Electrochemical performance of DECAL-CCM*

The CCM was placed in the test cell to measure the level of performance (iV curves) and the durability behavior under AST. **Figure 4.5-a** shows the chronopotentiometric cell response measured for approximately 100 hours by cycling the current density between 25 and 250 mA.cm$^{-2}$ for 5 minutes/cycle. **Figure 4.5-b** shows the chronoamperometric cell response measured for approximately 9 hours by cycling the cell voltage between 1.55 and 1.9 V. In both cases, despite a good performance level at the BoT, a rapid performance loss is observed after *ca* 80 hours of chronopotentiometric AST (**Figure 4.5-a**) and 9 hours of chronoamperometric AST (**Figure 4.5-b**).

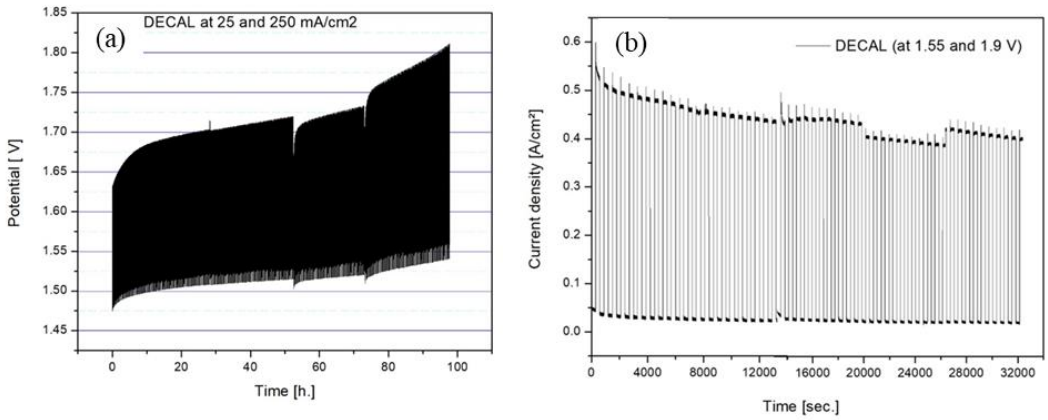


**Figure 4.5.** Stability of DECAL CCM at 60 °C using cell n°1 with 2L flowfield (a) chronopotentiometry at 25 and 250 mA/cm$^2$ and (b) chronoamperometry at 1.55 and 1.9V.

The iV curves measured at BoT and EoT are plotted in **Figure 4.6**. Likewise, a fast degradation is observed. This can be attributed to four different potential root causes :

1. Cell contamination during the test.
2. Delamination of at least one or may be two catalyst layers.
3. Oxidation of internal titanium components.
4. Gas screening effects resulting from an inappropriate level of compression of cell components on top of each other.

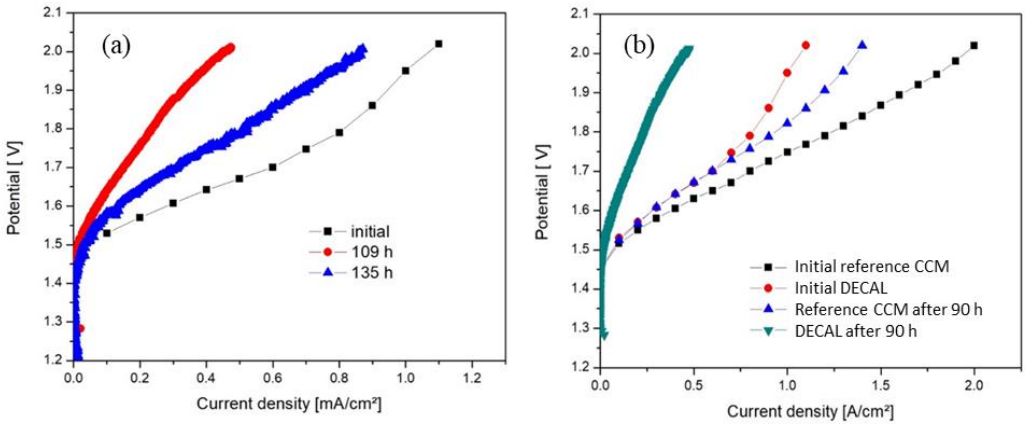


**Figure 4.6.** iV curves measured on a CCM prepared by DECAL before and after AST: comparison of the performance of (a) DECAL CCM with (b) the reference CCM. The measurement was performed at 60 °C using cell n°1 with 2L flowfield.

*Regeneration of activity of DECAL-CCM by acid cleaning*

The CCM prepared by DECAL was dismantled from the cell and soaked in 1 mol/L acidic solution overnight at room temperature to remove any impurities in order to improve electrochemical performances. Then the CCM was placed in the same cell and performance were measured again. **Figure 4.7** shows the situation during the AST after regeneration. A significant reduction in the AST voltage indicates improving in performance. The somewhat greater degradation rate could be due to the lack of a deionizer on the test bench, and potential iron-ion contamination was only mitigated by replacing the reservoir water every 50 hours[67]. The contamination of the cathode with iron impurities is known to be the main reason for the activity reduction of the CCM. The acidic solution can dissolve the Fe impurities and expose the Pt active sites to restore activity. **Figure 4.7** displays the voltage history of the regenerated CCM during a 120-hour AST at 25 and 250 mA/cm$^2$. The Nafion-CCM voltage was reduced by 100 mV at 250mA/cm$^2$ after the acid treatment process.

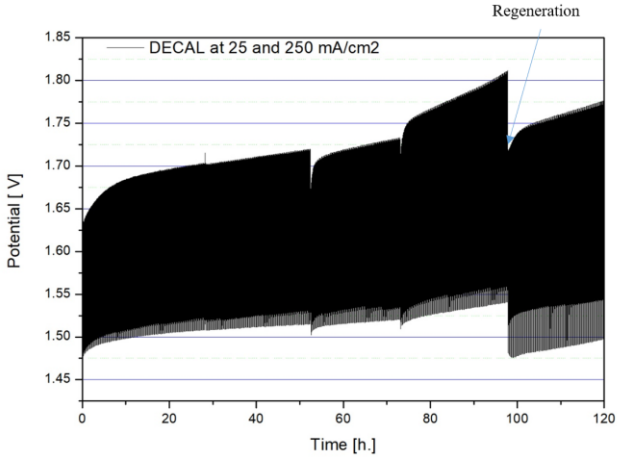


**Figure 4.7.** Chronopotentiometry of DECAL sample for 120 h at 25 and 250 mA.cm$^{-2}$. Measurements were performed at 60 °C using cell n°1 with 2L flowfield

[67] Klose C, Saatkamp T, Münchinger A, Bohn L, Titvinidze G, Breitwieser M, et al. *All-Hydrocarbon MEA for PEM Water Electrolysis Combining Low Hydrogen Crossover and High Efficiency*. Adv Energy Mater 2020;10:1903995. https://doi.org/10.1002/aenm.201903995.

The iV curves measured on the CCM at different times along the AST are shown in **Figure 4.8**. The blue curve represents the polarization curve after regeneration in an acidic medium.

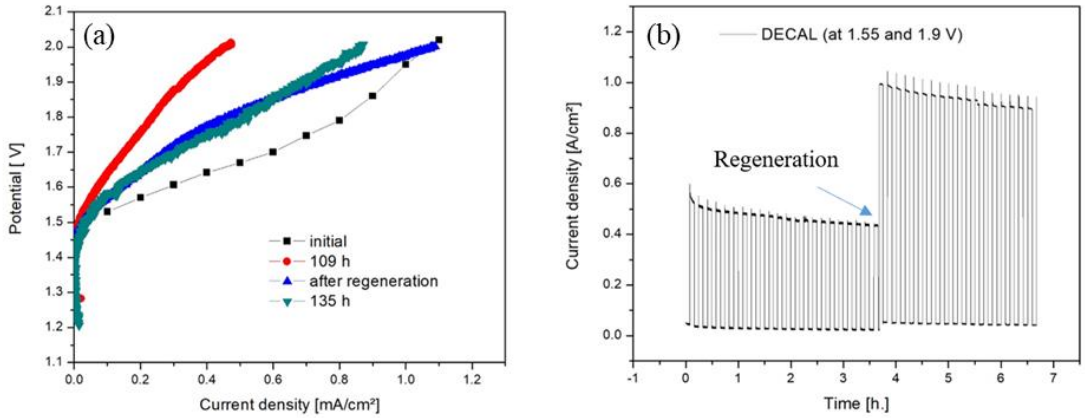


**Figure 4.8.** (a) iV curves and (b) chronoamperometry of DECAL CCM before and after regeneration with 1 mol/L acidic solution. Measurements were performed at 60 °C using cell n°1 with 2L flowfield.

### 4.2.4. Effect of catalyst layers drying on the performance of CCM

Alcohol used to prepare ink has a high affinity with the Nafion membrane and can have deleterious effects (*e.g.*, alteration of the water nanochannel inside the Nafion membrane). Thus, it is necessary to remove all alcohol traces from sprayed ink prior to DECAL transfer. After spraying the catalyst ink over the PTFE, the catalyst layer was dried in the oven at 80 °C for 24 hours before DECAL transfer. The CCM was then electrochemically characterized using AST at 25 and 250 mA/cm$^2$ for 83 h and 25 and 1000 mA/cm$^2$ for 7 hours. The CV of the dried sample **(Figure 4.9)** shows a better shape than the undried one. Even though, the electrochemical performance of the dried sample in the AST was similar to the undried one **(Figure 4.10)**.

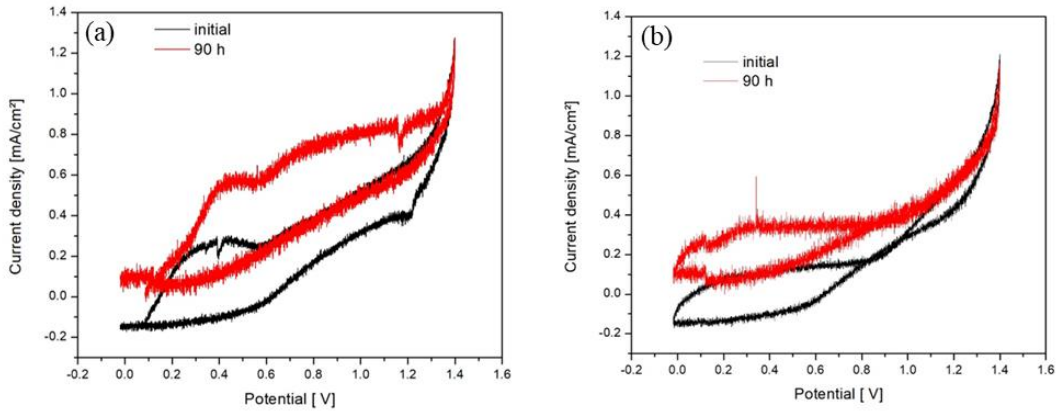


**Figure 4.9.** CV of dried DECAL sample before and after AST. (a) 1$^{st}$ CV cycle just after hydrogen saturation at the cathode, (b) 2$^{nd}$ CV cycle. The measurement was performed at 60 °C using cell n°1 with 2L flowfield.

**Figure 4.10-a** shows the cell voltage response during the AST: the cell voltage continuously increases (1295 µVolt/hour). The iV curves (**Figure 4.10-b**) show that mass (water) transport problems exist at BoT while during the test, the situation degrades: catalytic sites are lost.

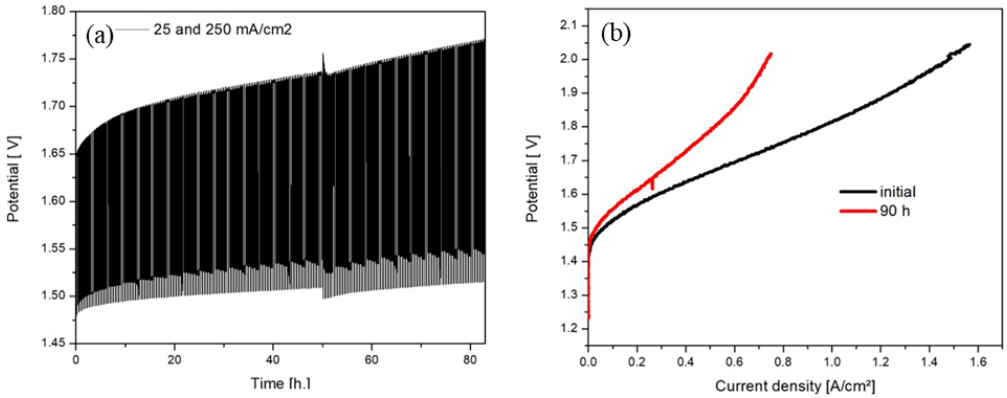


**Figure 4.10.** (a) AST of PTFE DECAL dried sample between 25 and 250 mA/cm$^2$; (b) iV curves measured before and after AST. The measurement was performed at 60 °C using cell n°1 with 2L flowfield.

The same behavior is observed during the chronoamperometric test at 1.5 and 2 V (**Figure 4.11**).

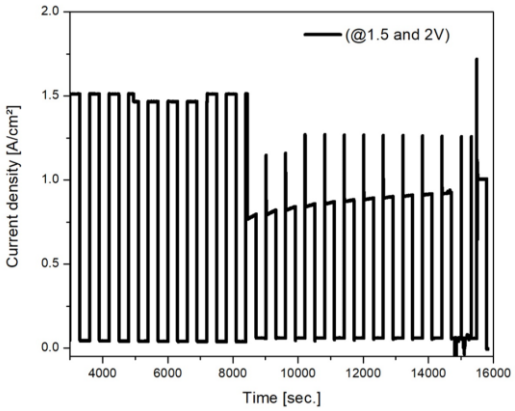


**Figure 4.11.** Chronoamperometry of dried DECAL CCM cycled between 1.5 and 2.0 V.

## 4.3. CCM manufactured using the ink printer

The Sono-Teck ExaCoat inkjet printer was used to make CCM in an automated and controlled method (see details in the experimental section).

### 4.3.1. SEM characterization

The automated ink printer has the advantage of preparing better (more homogeneous and uniform) catalyst layers due to the homogeneity of the coating process. The ultrasonic nozzle in the ink printer atomizes the ink into microdroplets that deposit over the substrate to form a highly porous layer. Hand sprayed $IrO_2$ catalyst layer for comparison has agglomerated film with low porosity, while $IrO_2$ prepared by ink printer has higher porosity. The Pt/C sprayed by the ink printer shows the highest porosity (**Figure 4.12**).

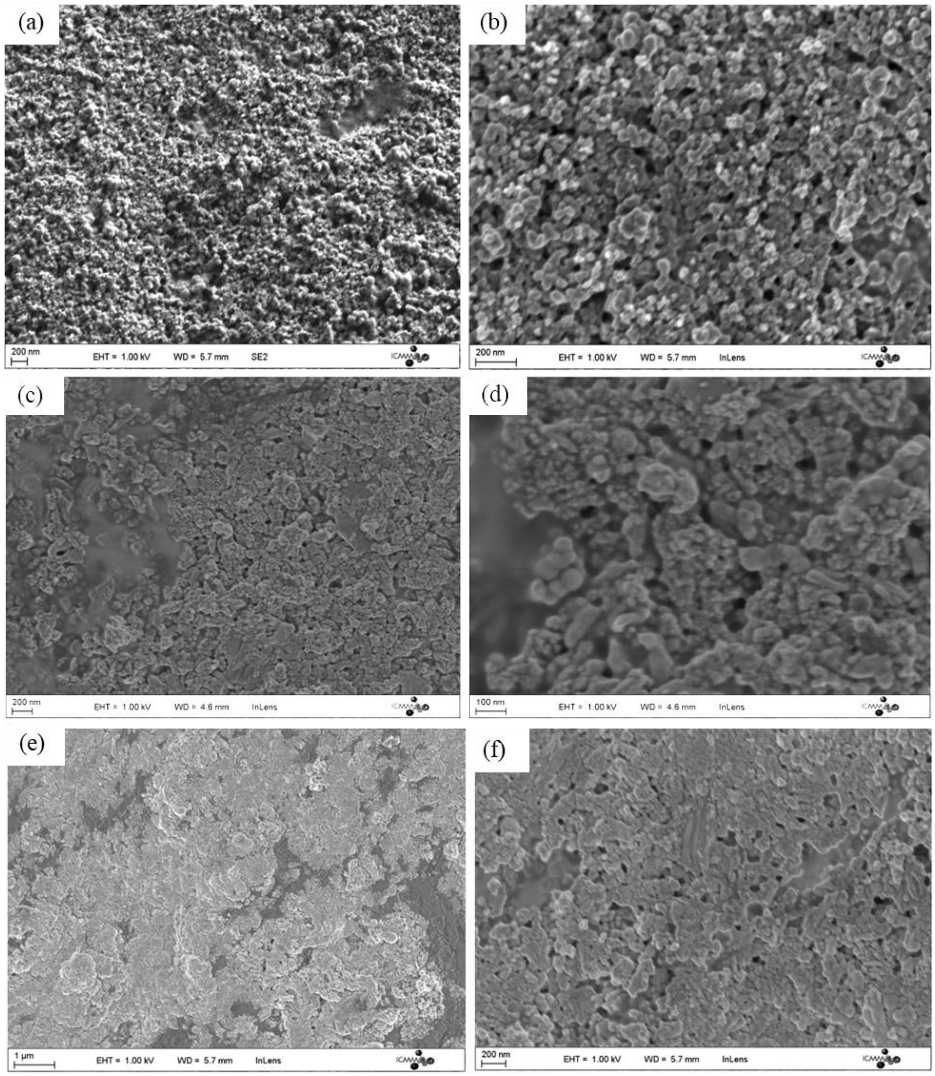


**Figure 4.12.** (a,b) Pt/C sprayed by ink printer and transferred by DECAL; (c,d) $IrO_2$ sprayed by ink printer and transferred by DECAL; (e,f) $IrO_2$ sprayed by airbrush hand spray and transferred by DECAL. (a,c,e) are the low magnification; (b,d,f) are the high magnification.

### 4.3.2. CCM prepared by DECAL using the ink printer

*DECAL-CCM manufacturing: see ink recipe and coating methodology in §2.6*

- the membrane is Nafion 115 without pretreatment.
- Pt/C CL loading of 1.3 mg/cm$^2$ equivalent to 0.36 mg Pt/cm$^2$
- $IrO_2$ Cl loading of 1.5 mg/cm$^2$ equivalent to 1.2 mg $IrO_2$/cm$^2$
- this DECAL-CCM was obtained using a PTFE substrate (pure isopropanol ink, 20% ionomer, 80°C). The HER and OER catalyst layers were separately transferred to the membrane by DECAL. The HER was transferred first, and the OER was transferred afterwards.
- Hot press transfer at 135°C and 2 tons for 5 min.

Thus, the CCMs obtained were electrochemically characterized using the same cell and procedures. Results are plotted in **Figure 4.13**. Data of **Figure 4.13-a** show that the cell voltage (at 250 mA/cm$^2$) increases with time but at a lower rate (411 µVolt/hour against 1295 µVolt/hour for the CCM made with the hand spray gun (**Figure 4.10-a**)).

EIS spectra (**Figures 4.13-b and 4.13-c**) show that the cell impedance remains constant during the test and that there is still a slight loss of catalyst. This indicates that the catalyst layer's adherence is not yet fully optimized.

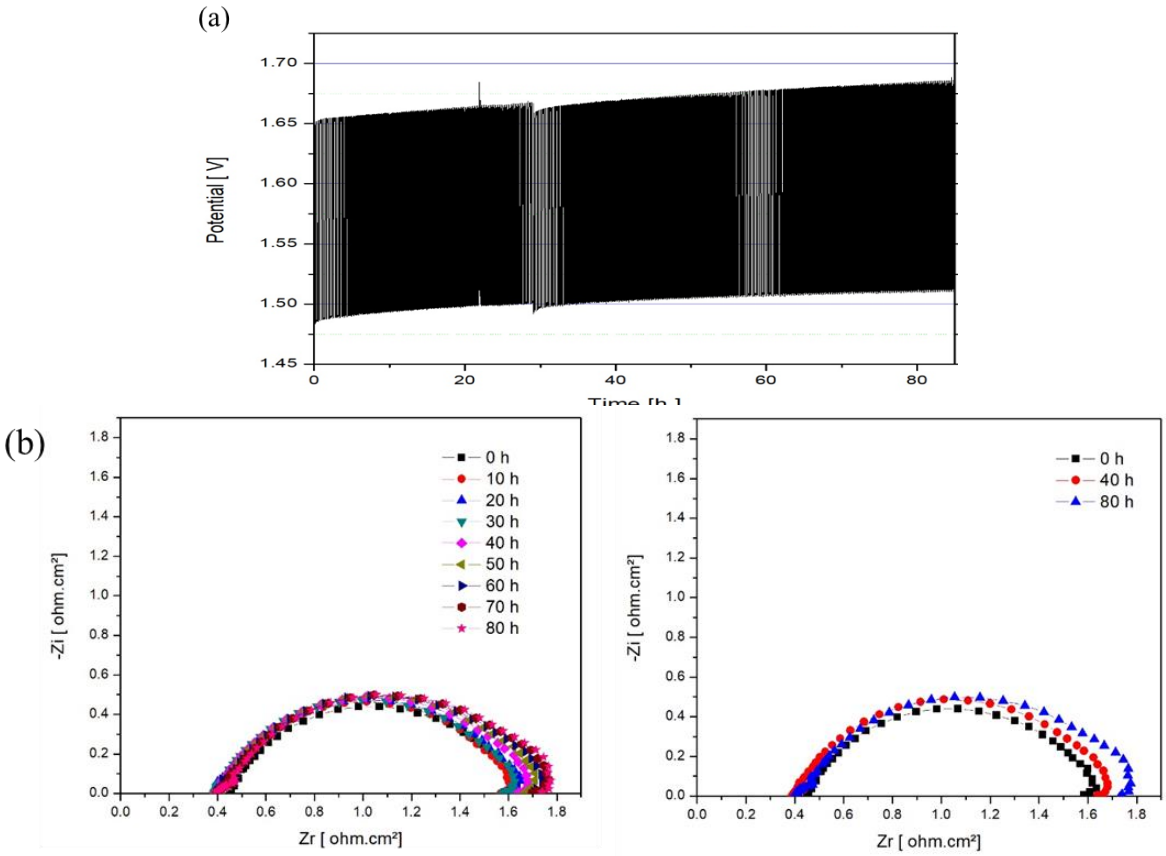


**Figure 4.13.** Electrochemical characterization of lab-made using the ink printer and DECAL method. The measurement was performed at 60 °C using cell n°1 with 2L flowfield (a) AST cell response during current cycling between 25 and 250 mA.cm$^{-2}$ and (b) EIS spectra at 25 mA/cm$^2$.

In conclusion, CCMs made by the ink printer have higher stability than hand spray ones, but there is still room for improvement. However, it should be outlined here that the AST was performed with a maximum current density up to 250 mA/cm$^2$ only because of a current limitation with the potentiostat used. This is potentially a source of the problem because the first hundreds of hours of operation correspond to a kind of activation of the CCM, and it seems that it is preferable to go up from the start of the tests to a high current density rather than to gradually increase. It is possible that the choice of the current density conditions the way in which the catalytic layers are structured under gas evolution.

### 4.3.3. CCM prepared by direct deposition of alcohol-free ink over Nafion membrane using the ink printer

Direct ink deposition onto the membrane is simpler than DECAL. This approach was firstly tested. However, it is known that the direct spray of alcohol onto the membrane has a negative impact because alcohols are PFSA solvents. Therefore, we tried to prepare alcohol-free inks. The following recipes and methodologies were used to prepare the CCM. The catalyst particles were first dispersed in a solution of isopropanol/ionomer. Then the solution was dried (solvent evaporation). The collected powder of catalyst/ionomer was re-dispersed in de-ionized water.

HER catalyst deposition

The mixture of dry Pt/C powder and ionomer (33 wt.% Nafion ionomer) was successfully dispersed in deionized water at 1 wt.% after 10 hours of bath sonication. The ink was then sprayed directly over the Nafion 115 membrane using the ink printer. The ink printer parameters were set as follows: 400 deposition cycles at a speed of 40 mm/s and a distance of 6 mm between lines. The hot plate temperature was set at 100°C to increase water evaporation. The half CCM thus obtained was then placed between two PTFE sheets and hot-pressed for 5 min (2 tons at 135°C) to consolidate the CL and increase its adherence. The result was successful, and 100% of the Pt/C layer became well-adhered to the Nafion membrane.

OER catalyst deposition

$IrO_2$ powder was dispersed in isopropanol solvent (using 20 wt% Nafion ionomer), bath sonicated for 10h, followed by drying in an oven at 80°C for 24 hours. However, the solid powder did not disperse in pure water, even after a long bath sonication time. Therefore, the anode of the CCM was transferred to the membrane using the DECAL transfer method. In brief, a new isopropanol ink of $IrO_2$ was prepared and sprayed over the PTFE substrate using the ink printer (similar ink deposition parameters to the cathode). After coating the ink onto the PTFE sheet, the PTFE/catalyst film was dried in the oven at 100°C for 2 hours (to remove the adsorbed alcohol). Finally, the anode catalyst layer was transferred to the Nafion 115 membrane by hot pressing (2 tons at 135°C for 5 min).

The main drawback of the direct deposition method is drying the Nafion 115 membrane during the process, which adversely affects its proton conductivity. Direct deposition of ink requires placing the Nafion membrane on the hot plate of the ink printer at 100°C for a long period of time. The membrane loses its water and becomes poorly conductive. Rehydration with boiling water is required to restore ionic conductivity. Therefore, the CCM was soaked in boiling water for 15 min to rehydrate the Nafion 115 membrane.

The electrochemical results of the prepared CCM are shown in **Figure 4.14**. After 82 h of AST, the power was turned off (for a technical intervention), and then AST continued after 15 min; an excellent electrochemical performance restoration was obtained, suggesting that mass transport effects are contributing to the level of cell performance.

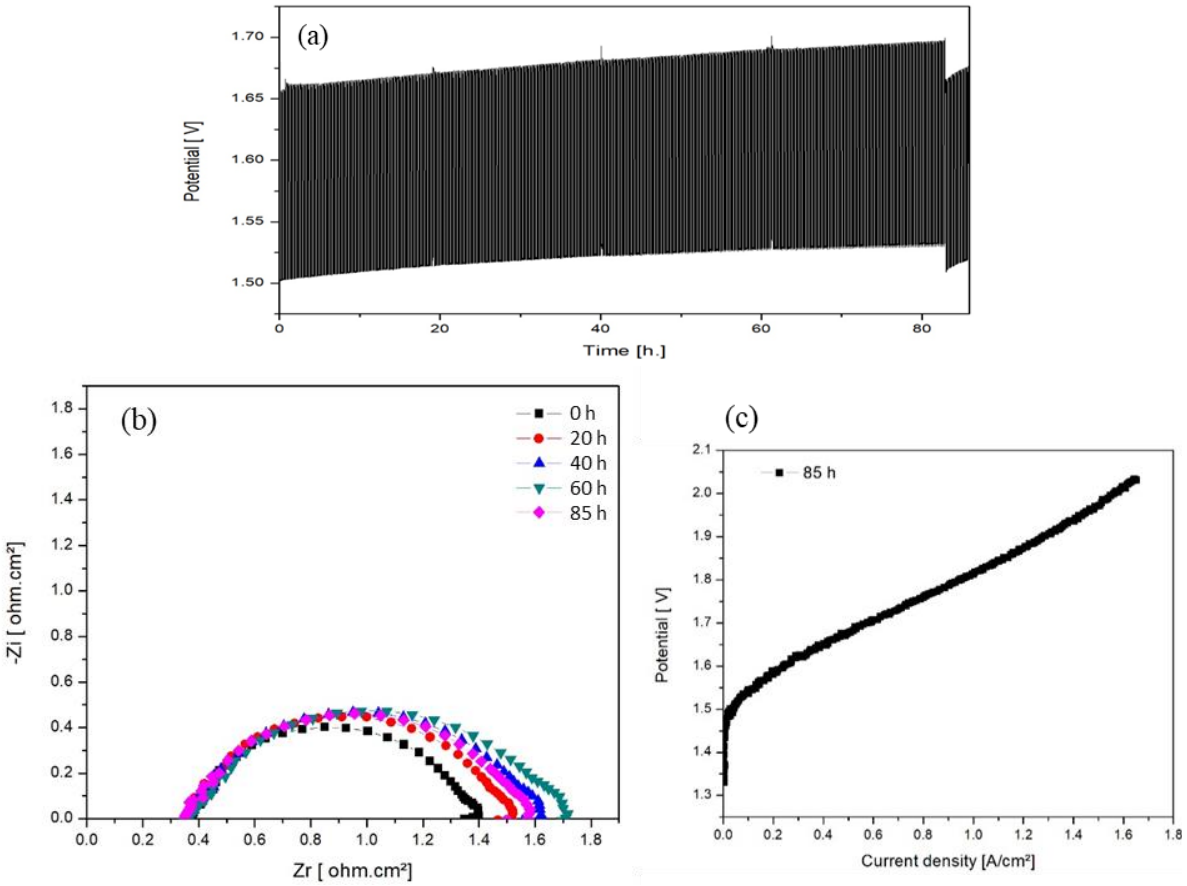


**Figure 4.14.** (a) cell voltage during the AST at 25 and 250 mA.cm$^{-2}$, (b) EIS measured along the AST at 25 mA/cm$^2$ and (c) iV curve after 85 hours of AST. The measurement was performed at 60 °C using cell n°1 with 2L flowfield.

## 4.4. Conclusions

We have gathered in this paragraph the results obtained during the manufacturing and characterization of 'in-house' CCMs using conventional core materials (Nafion, Pt/C and $IrO_2$). The following conclusions have been reached :

1. We have succeeded in making ‘conventional’ CCMs with PFSA membrane and PGM catalysts.
2. The performance levels obtained are consistent with those measured on the reference CCM.

# Chapter 5. Characterization of lab-made CCMs with the hybrid nanocomposite (HNC) membrane

## 5.1. Description of the HNC membrane

The Méthycentre project is a Power-to-Gas demonstration project led by Storengy to support the energy transition (**Figure 5.1**). Its objective is to test an innovative process for converting electricity into green gas. This solution is based on Power-to-Gas technology. The gas thus produced will make it possible to meet clean mobility needs and partially replace fossil methane in Engie's gas networks.

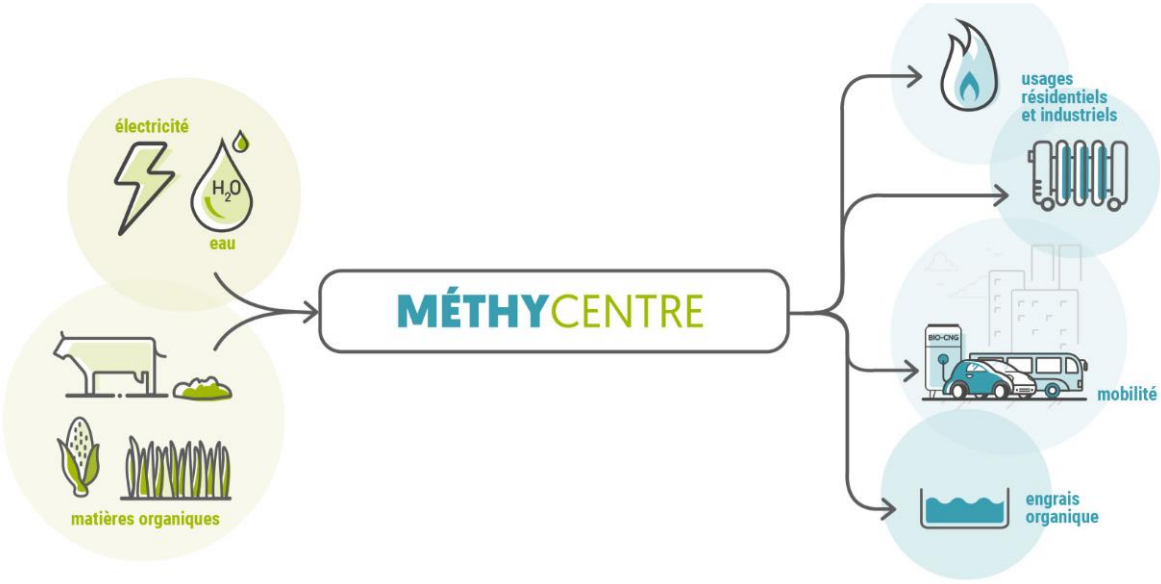


**Figure 5.1.** Overview of the Méthycentre project.

A PEM water electrolyser is used to produce green hydrogen from renewable electricity. On the R&D side, a generation 2 'PEM2G' concept is developed and tested by a subset of consortium members. The objective is to replace the conventional PFSA membrane by a less expensive material developed and patented by CEA in 2012 for PEM fuel cell applications. This is a hybrid nanocomposite (HNC) membrane (**Figure 5.2**). A polystyrene sulfonic acid (PSSA) chain is grafted onto silica nanoparticles which are then dispersed into a PVDF matrix. A cross-linking agent is used to anchor the functional acid groups to the hydrophobic organic phase.

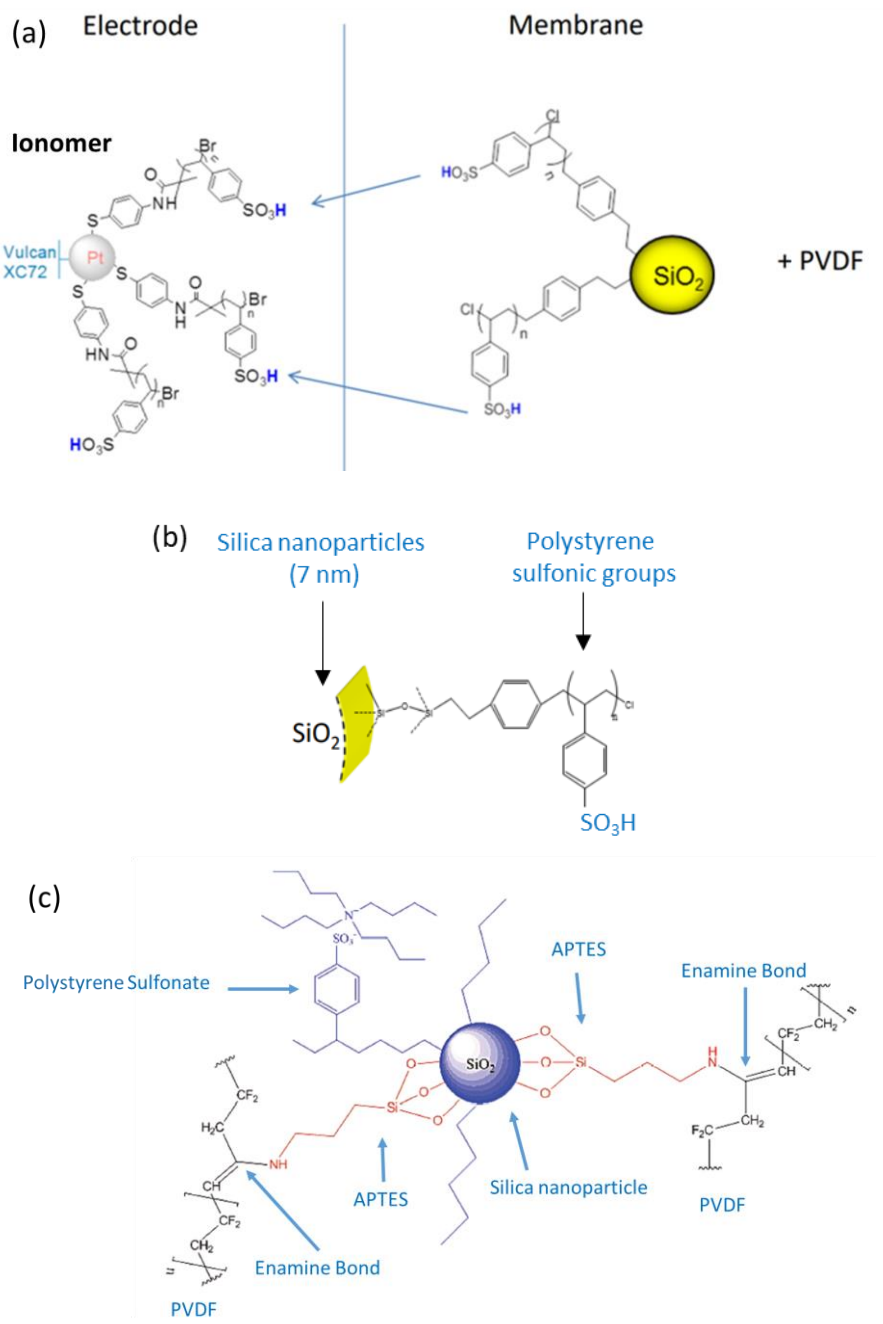


**Figure 5.2.** (a) chemical structure of HNC membrane and electrode, (b) grafting of the polystyrene sulfonic acid chain onto supporting silica nanoparticles and (c) crosslinking the nanocomposite to the PVDF matrix[68-69]

.

The same idea was used to synthesize Pt nanoparticles covered by a similar organic chain containing sulfonic acid functions. The membrane is called a hybrid nanocomposite membrane since silica nanoparticles (inorganic) are functionalized with polystyrene sulfonic groups (organic) required for proton-conductivity. The solid hybrid organic/ inorganic nanoparticles are dispersed in an organic polymer medium[68].

[68] Ph.D Thesis, *Elaboration and characterization of crosslinked hybrid nanocomposite membranes for PEMFC and PEMEC application* by Thibaut Bredel. French national number: 2019NORMR146. https://tel.archives-ouvertes.fr/tel-02968922/document.
[69] Niepceron F, Lafitte B, Galiano H, Bigarré J, Nicol E, Tassin J-F. *Composite fuel cell membranes based on an inert polymer matrix and proton-conducting hybrid silica particles*. J Memb Sci 2009;338:100–10. https://doi.org/10.1016/j.memsci.2009.04.022.

This type of material has already been tested in PEM water electrolysis, notably within the framework of the MHyel project (2019) financed by the French ADEME (Agence de la Transition Energétique). A lab-size CCM made with the first generation of the nanocomposite membrane is shown in **Figure.5.3 (left). Figure 5.3 (right)** shows the iV curves measured using the nanocomposite membrane at different temperatures and the reference iV curve measured with a PFSA membrane. The project concluded that the membrane was satisfactory in terms of performance at the beginning of life but lacked durability. It was decided to continue the developments in the frame of a new R&D project (Méthycentre) and improve the durability by optimizing the technique used to coat the catalyst layers.

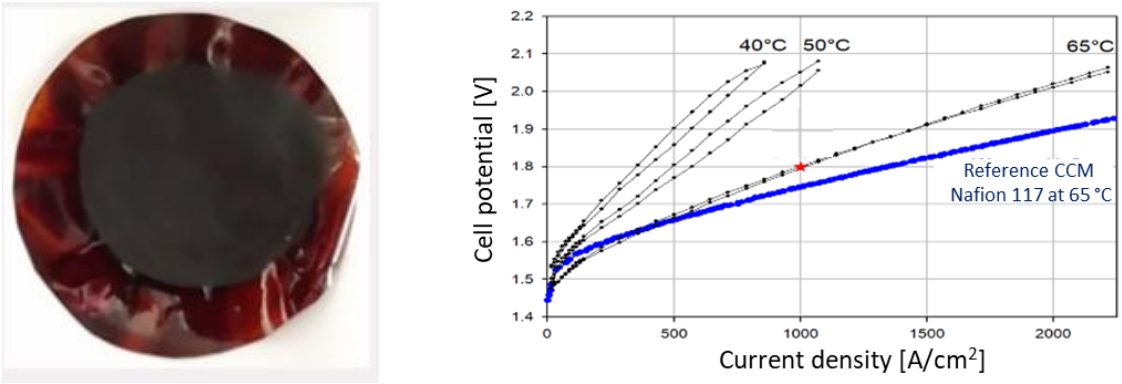


**Figure 5.3.** (left) lab-size CCM with HNC membrane (MHyel project); (right) iV curves measured at different temperatures with project target and reference curve.

Ionomer dispersion

For manufacturing the catalytic layers, it is necessary to have a dispersion of ionomer chains. The dry PFSA structure acts as a binder to maintain the shape and integrity of catalyst layers and to bring the necessary proton-conductivity during electrolysis. In the case of the HNC membrane, the dispersion is made of silica nanoparticles functionalized with sulfonic groups and a diamine molecule as cross-linker (thermal crosslinking can be made at 180°C). However, this type of HNC-dispersion was not available for our studies; therefore, all results reported in this report were obtained using a Nafion dispersion instead of a HNC ionomer dispersion. The impact this can have on results will be evaluated and discussed.

## 5.2. Physical properties of the HNC membrane

### 5.2.1. Different HNC membrane generations

CEA has provided four different types (4 generations) of hybrid nanocomposite membranes for the Méthycentre project. The appearance of the 4 HNC membranes is shown in **Figure 5.4**. Whereas the first generations were heterogeneous (**Figures 5.4-1 and 5.4-2**), better samples have been obtained after process optimization (**Figures 5.4-3 and 5.4-4**). A heat treatment was applied to increase homogeneity (dispersion of phases) and cross-linking.

1- Inhomogeneous membrane (referred as to HNC-inhomogeneous).

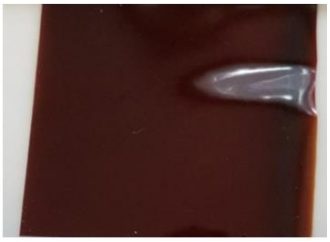

2- Membrane treated at low temperature (referred as to HNC-low).

3- Membrane treated at 180 °C for 2 h. (referred as to HNC-180-2).

4- Membrane treated at 180 °C for 6 h. (referred as to HNC-180-6).

**Figure 5.4.** Different types of HNC membranes are available for the thesis.

### 5.2.2. Swelling ratio and water uptake of HNC membranes

The swelling ratio (SR) and water uptakes were calculated according to the following equations[70]:

$$\text{Swelling ratio} = \frac{(X_w - X_d)}{X_d} \times 100\ \%$$

$$\text{Water uptake} = \frac{(m_w - m_d)}{m_d} \times 100\ \%$$

The water uptake (WU) of the HNC membranes was measured and compiled in **Table 5.1**. In summary, HNC-inhomogenous membranes, HNC-low (nanocomposite membrane treated at low temperature), HNC-180-2, HNC-180-6, and Nafion 115 revealed respective water uptake values of 70 and 72%, respectively 65%, 73%, and 22.1%. Both inhomogenous and membrane treated at low temperatures have low polymer crosslinking contents resulting in higher water uptake and volume expansion. Further increasing the crosslinking temperature of the HNC membrane (treatment at 180°C for 2 h, HNC-180-2) enhances polymer crosslinking, prevents membrane expansion, and reduces water uptakes. However, increasing the thermal treatment duration to 6 hours negatively impacted crosslinking and increased volume expansion and water uptakes (HNC-180-6). The swelling ratio and water uptake of Nafion 115 membranes are 10 and 22.1 %, respectively, in agreement with the values reported in literature[70]. The swelling properties of the HNC membranes were determined in accordance. The accompanying swelling data followed the same pattern as the water uptake capacity data. The swelling ratios for membrane HNC-inhomogenous, HNC-low, HNC-180-2, HNC-180-6, and Nafion 115, were 26 %, 30 %, 23.3%, 30 %, and 10 %, respectively (cf. **Table 5.1**).

[70] Kumar V, Kumar P, Nandy A, Kundu PP. *A nanocomposite membrane composed of incorporated nano-alumina within sulfonated PVDF-co-HFP/Nafion blend as separating barrier in a single chambered microbial fuel cell*. RSC Adv 2016;6:23571–80. https://doi.org/10.1039/C6RA03598A.

**Table 5.1.** Compilation of characteristics of the HNC membranes received and Nafion 115.

| Membranes | HNC-Inhomogeneous | HNC-low | HNC-180-2 | HNC-180-6 | Nafion 115 |
|---|---|---|---|---|---|
| Dry Length (mm) | 30 | 30 | 30 | 30 | 30 |
| Wet length (mm) | 38 | 39 | 37 | 39 | 33 |
| Water uptake (wt. %) | 70 | 72 | 65 | 73 | 22.1 |
| Swelling ratio (length %) | 26 | 30 | 23.3 | 30 | 10 |

## 5.3. Optimization of CCM preparation conditions

We report here on the successive attempts made to make and optimize CCM with the hybrid nanocomposite membrane. The merit functions used for assessing the quality of the CCM are qualitative: (i) homogeneity and (ii) adherence of the catalyst layers. It should be noted that the recipe used for making CCM with Nafion 115 cannot be used directly because the mechanical properties of both materials are quite different. In particular, the glass transition temperature $T_g$ of Nafion (135°C) is much higher than the glass transition temperature of the nanocomposite membrane material (-35°C, *i.e.* the $T_g$ of PVDF, the polymer used for making the HNC membrane). Consequently, the DECAL method was not used (see § 2.7). In addition, nanocomposite ionomer dispersion was not available to prepare catalytic inks. For the latter reason, PFSA (Nafion) dispersion was used.

### 5.3.1. Effect of hot pressing

In a first attempt, the second type of nanocomposite membrane (the one heated at 180°C for 6 h called sample HNC-180-6) was coated with 1.4 ml cyclohexanol-based ink using a hand spray gun and then hot-pressed at 80°C under 4 tons for 15 min. Poor catalyst transfer was observed (**Figure 5.5**). After several trials, we concluded that heating during the compression step is not recommended and results in poor catalyst transfer. We also observed that the measurements made on the nanocomposite-CCM prepared without the compression step led to a loss of the catalyst after a few minutes of water circulation only without any electrochemical analysis (no surface adherence of the catalyst layers).

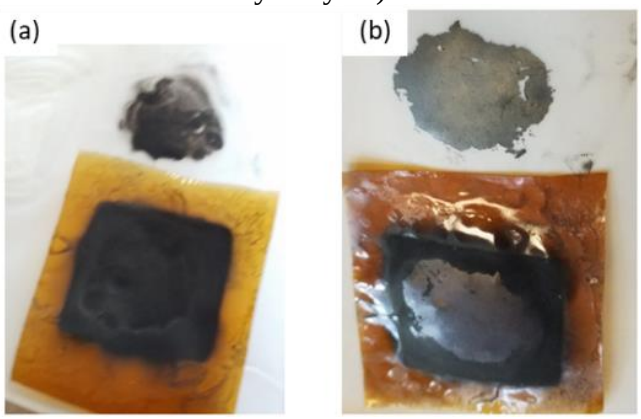


**Figure 5.5.** (a) cathode ink and (b) anode ink transferred from membrane to PTFE during a hot press at 80 C under 4 tons for 15 min.

### 5.3.2. Effect of water wetting before clamping inside the cell

The HNC membrane (the one heated at 180°C for 2 hours, called sample HNC-180-2) was coated with 1.4 ml cyclohexanol-based ink using a hand spray gun and pressed at 4 tons for 5 min. Excellent catalyst transfer was obtained but soaking the CCM in water at ambient temperature resulted in the delamination of the catalyst from the membrane as shown in **Figure 5.6**. The large swelling ratio of the nanocomposite membrane (23 %) generates a mechanical strain on the catalyst layer (which does not expand at the same extent) and induces delamination. This experiment shows the importance of mounting the CCM inside the electrochemical cell in a dry state before setting the water circulation to avoid catalyst losses.

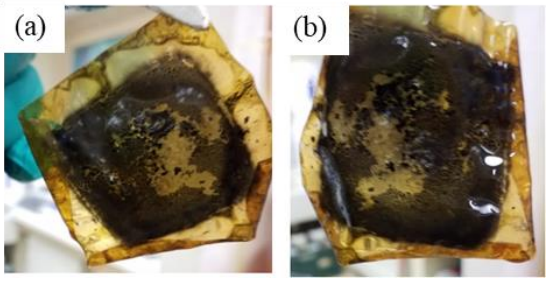


**Figure 5.6.** CCM CL delamination after treatment with de-ionised water for 5 min, due to membrane swelling occurring on both (a) anode and (b) cathode.

### 5.3.3. Catalyst deposition on wet HNC membrane

The hybrid nanocomposite membrane (HNC-180-2) was wetted with water at ambient temperature and then coated with the anode ink (12 mg $IrO_2$, 65 mg $H_2O$, 70 mg Nafion binder 5%) and left overnight till dryness. However, a non-uniform coating was obtained **(Figure 5.7),** and the method was then disregarded.

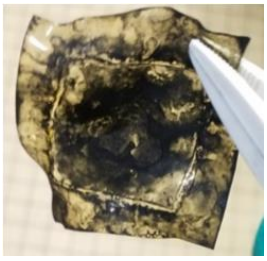

**Figure 5.7.** HNC membrane coated in wet condition with $IrO_2$ ink.

### 5.3.4. Direct spray coating with room temperature pressing

The following methodology and recipe were used in the last attempt to prepare HNC membrane-based CCM. The catalyst-coated nanocomposite membrane (HNC-CCM) was compressed between two PTFE sheets using the press at room temperature. A stable CCM with limited or no catalyst loss was successfully obtained (**Figure 5.8**). As shown in **Figure 5.8-d**, the PTFE of the anode side has no black color after compression, indicating that most of the catalyst remained adhered to the nanocomposite membrane. On the cathode side **(Figure 5.8-c**), only an insignificant amount of Pt/C was transferred from the nanocomposite CCM to the PTFE sheet during the compression process **Figure 5.8-d**. However, this did not affect the electrochemical properties of the CCM. In conclusion, the direct spray coating of anode and

cathode inks over the membrane shows a high transfer percentage to the membrane of 100% and 90% for $IrO_2$ and Pt/C, respectively.

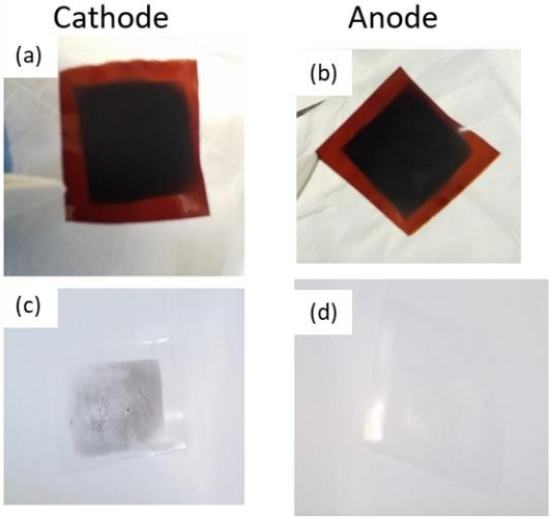


**Figure 5.8.**Pictures of the HNC-CCM. (a) cathode side; (b) anode side. (c) cathode PTFE substrate after the compression step; (d) anode PTFE substrate after the compression step.

From all these experiments, we concluded that to optimize catalyst coating over the HNC membrane, pressing the PTFE-CLs on the membrane should be performed at room temperature pressing (without heating) under 4 tons. It is also recommended to avoid wetting the HNC membrane before or after catalyst transfer to maintain a good CCM structure.

## 5.4. Electrochemical characterization of CCMs based on HNC membrane

### 5.4.1. Electrochemical characterization of inhomogeneous membrane

A CCM made with an inhomogeneous HNC membrane (**Figure 5.9-b**) was tested. In the electrochemical cell, we used a simplified flowfield (*i.e.* the 2.5 mm thick bi-layer system shown in **Figure 5.9-a**) on both sides of the CCM. The iV curve measured on the HNC-CCM **(Figure 5.9-d)** revealed that it was less efficient than the reference CCM due to (i) fewer catalytic sites, (ii) higher ohmic resistance and (iii) mass transport limitation appearing at j > 200 $mA.cm^{-2}$. After 68 minutes of electrochemical measurements at 60°C, a short circuit occurred **(Figure 5.9-e).**

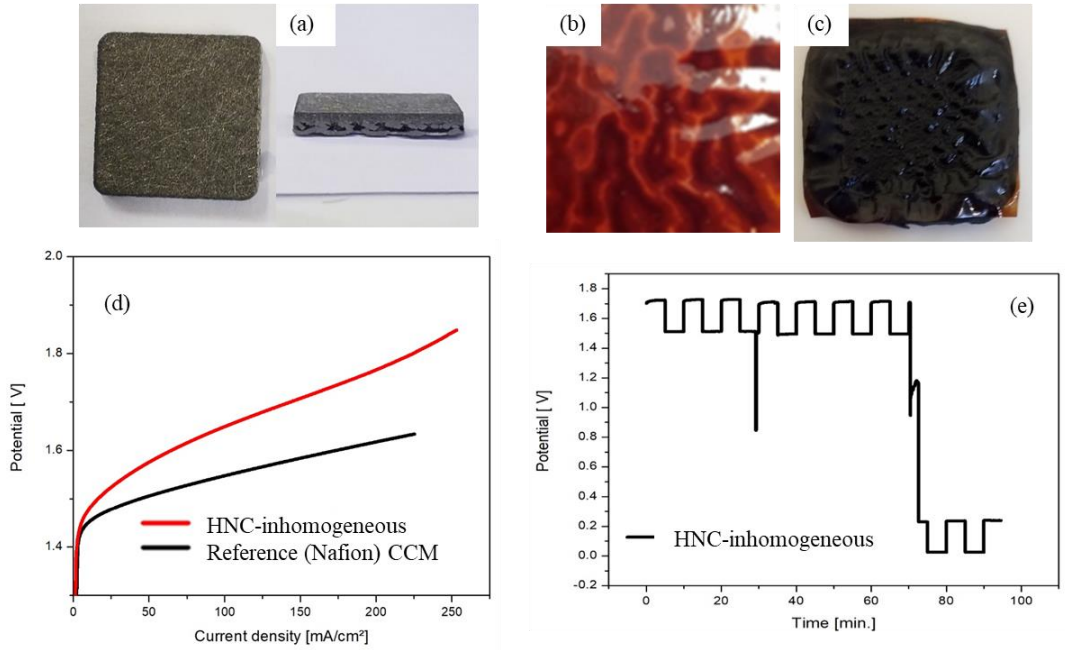


**Figure 5.9.** (a) 2.5 mm thick two-layer flowfield made of 1 Ti grid + Ti felt made of sintered Ti fibers, (b) inhomogeneous HNC membrane tested, (c) CCM after electrolysis showing wrinkles, (d) iV curve of HNC-inhomogeneous CCM compared with reference CCM and (e) chronopotentiometry at 25 and 250 mA/cm$^2$ performed in cell n°1 at 60°C.

The short-circuit of **Figure 5.9-e** was attributed to two factors: (i) the reduction of the mechanical properties of the membrane after water swelling and (ii) the high clamping pressure used in the cell to press the PTL firmly against the catalyst layers. Since the PTL is made of titanium fibers sintered together, there is a risk of short-circuiting when soft, and un-reinforced membranes are used.

### 5.4.2. Electrochemical characterization homogenous membrane treated at low temperature (HNC-low)

Two CCM (sample 1 and sample 2) were prepared from a HNC-low membrane treated at low temperatures. The electrochemical measurements (**Figure 5.10-a**) performed at 60°C using the thick Ti felt as a flowfield (those of **Figure 5.10-a)** show the same level of performance as those measured during the MHyel project. EIS spectra recorded in galvanostatic mode at 100 mA/cm$^2$ (add the amplitude) (**Figure 5.10-b**) show a larger cell resistance for the HNC-CCM compared to the reference Nafion-CCM. Charge transfer resistances are also larger (two semi-circles), suggesting a lower number of catalytic sites in contact with the membrane and the need for further optimization of the CCM manufacturing process. However, after a few hours of water circulation and electrochemical measurements, a short circuit (attributed to membrane swelling and loss of mechanical strength) took place. When the CCMs were dismantled from the cell after the electrochemical tests, we observed that they were wrinkled (**Figure 5.11**). Several holes were observed at the surface of sample 1 (**Figure 5.11-a**) as if the membrane had burned locally.

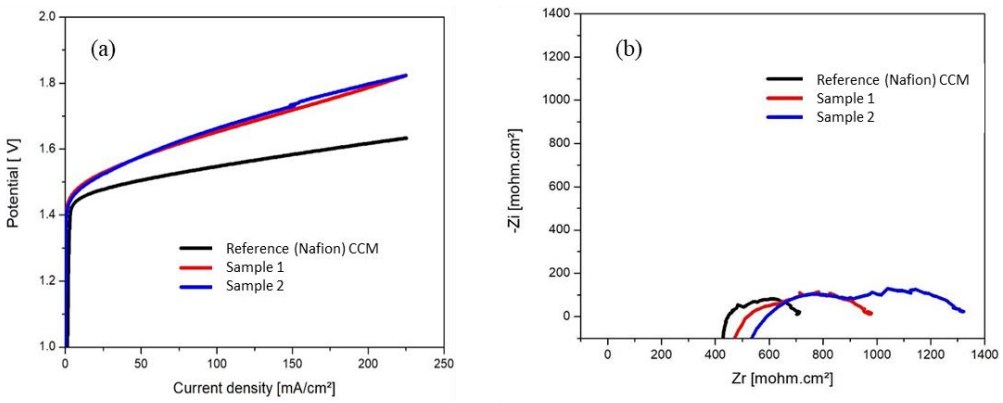


**Figure 5.10.** Electrochemical measurements of CCM provided by the supplier (reference CCM) and HNC-low based CCMs at 60 °C using the thick Ti felt as flowfield and cell n°1, (a) iV curve at a scan rate of 1 mV/sec, (b) EIS measurements at 100mA/cm$^2$.


**Figure 5.11.** Photographs of holes in sample 1 and wrinkles in sample 2.

## 5.5. Effect of the thermal treatment temperature on membrane durability

### 5.5.1. HNC membrane treated at low temperature (HNC-low)

*PTL-L with grid (1L flowfield of **Figure 2.17-a**)*

On both sides of the cell, we used a titanium PTL made of sintered powder (**Figure 5.12-a**) and a CCM made of a homogenous HNC membrane (treated at low temperature). An AST was run in the cell **(Figure 5.13)**. After 72 h of electrochemical tests, the CCM remains intact, and little wrinkles are formed **(Figure 5.12-d)**. However, we observed that the high-frequency resistance increased from 0.7 to 1.3 Ω.cm$^2$ after 72 h (sample referred to as HNC-low CCM).

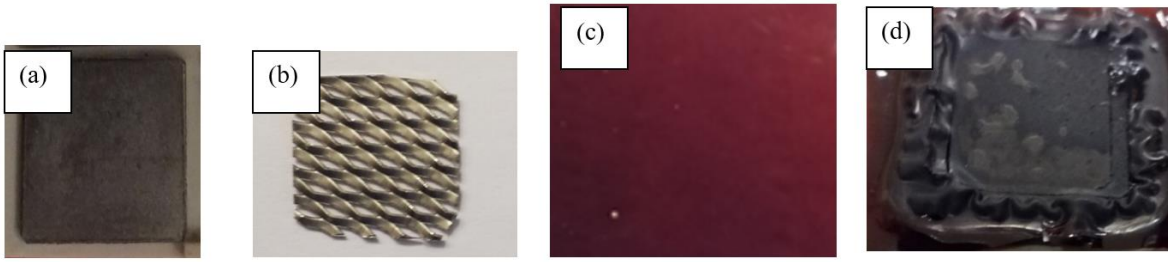


**Figure 5.12.** (a) Sintered Ti particles as PTL (1L flowfield), (b) course grid as flowfield,(c) homogeneous HNC membrane and (d) CCM after 73 h electrolysis using cell n°1.

The 1L flowfield (**Figure 5.12-a, b**) was used to perform the electrochemical measurements. The AST test was performed by applying 25 mA/cm$^2$ for 5 min and then 250 mA/cm$^2$ for 5 min. Water circulates on both the anode and cathode side at a constant temperature of 60°C, and the potentiostat recorded the cell voltage. The maximum potential was set at 2 V. Therefore, when cell potential went higher, the potentiostat stopped the measurements at 250mA/cm$^2$ and went down to 25mA/cm$^2$. The lower line represents potential at 25mA/cm$^2$.

**Figure 5.13-a** shows the AST test of the nanocomposite membrane treated at low temperatures, and the cell voltage reaches 2.3 V after only 2.5 h. Then we switched to a chronoamperometry at 2 V (**Figure 5.13-b**), and the cell's current is gradually reducing, indicating a loss in the electrolysis performance of the CCM. The iV curves in **Figure 5.13-c** also confirm the instability of the HNC-based CCM. The EIS data of **Figure 5.13-d** show that the cell high-frequency resistance (HFR) increases significantly during the test, which casts suspicion on the polymer membrane and possible degradation (loss of conductivity).

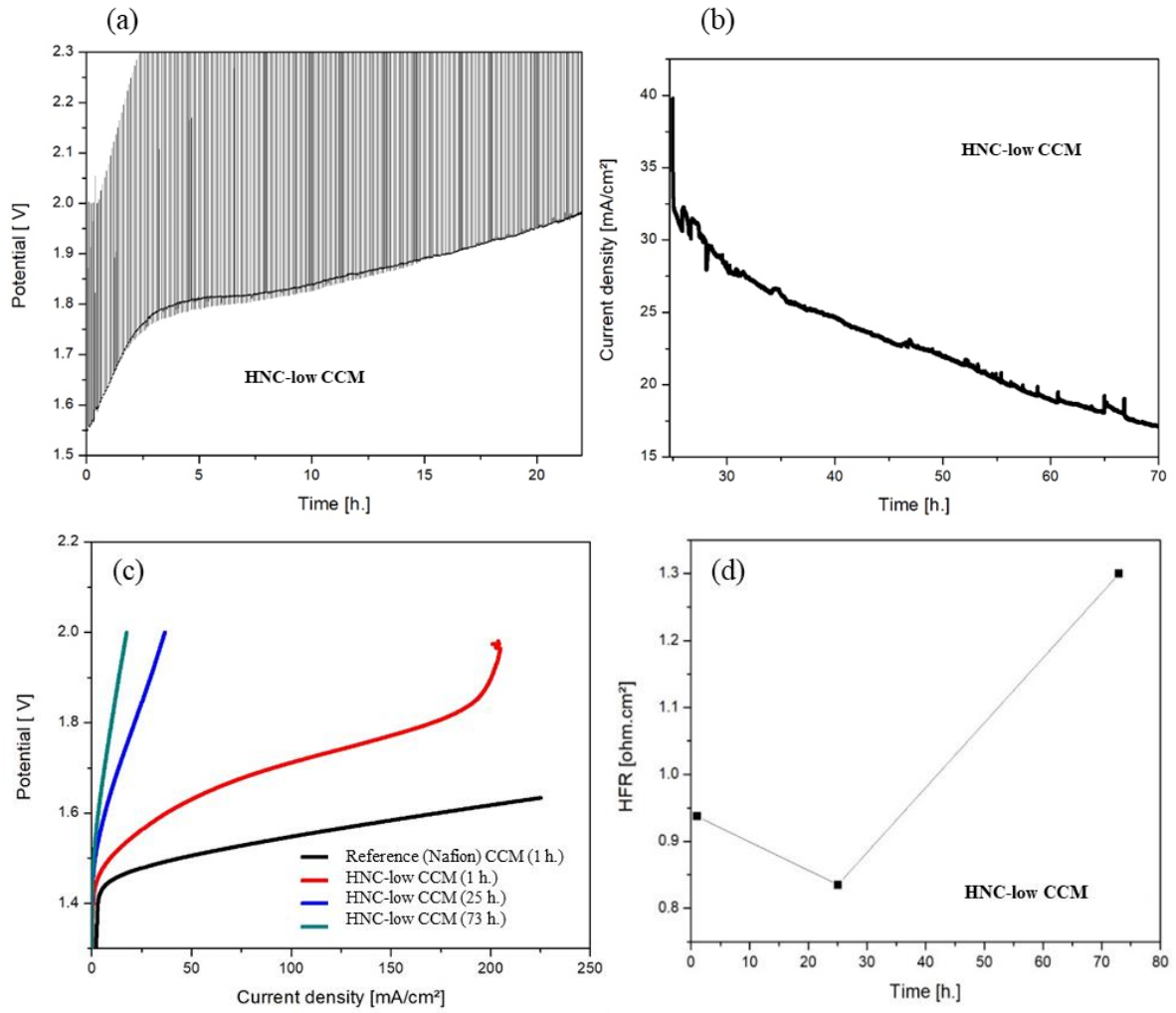


**Figure 5.13.** (a) chronopotentiometry for 25 h at 25 and 250 mA/cm$^2$ (AST), (b) chronoamperometry at 2 V for an additional 48h, (c) iV curve of HNC-low HNC CCM at different times and (d) High-Frequency Resistance (HFR) at different time. All measurements were performed at 60°C using cell n°1 with 1L as a flowfield.

### 5.5.2. CCM with membrane HNC-180-2 (treated 2 hours at 180°C)

*The use of PTL-L in combination with the two layers of Ti flowfield (2L flowfield of **Figure 2.17-b** )*

Short circuits can easily form when the stiff titanium felt is pressed against the soft polymer membrane with low mechanical strength. Some of Ti microfibers **(Figure 5.14-a)** perpendicular to the surface of the CL can penetrate the membrane and induce short circuits. In order to prevent short circuits, we decided to use a PTL made of sintered Ti powder **(Figure 5.14-b)**, instead of fibers (the 2L flowfield).

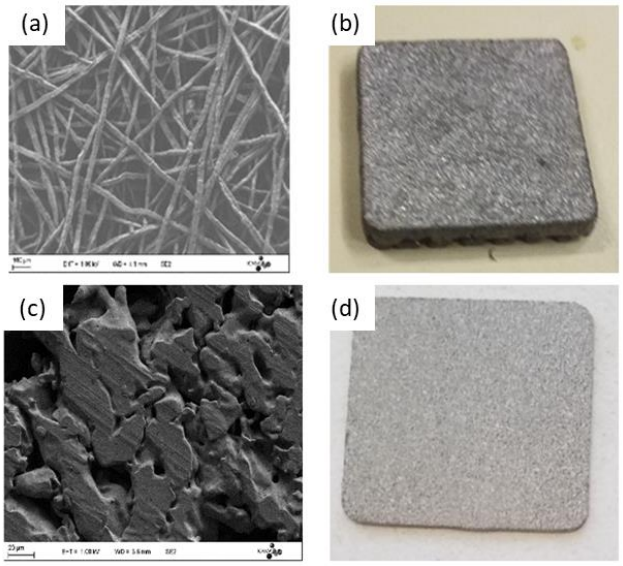


**Figure 5.14.** (a) SEM image of the fibrous Ti felt of the two layers Ti flowfield; (b) optical photograph of the the two layers Ti flowfield; (c) SEM image of the PTL-L and (d) optical photograph of the PTL-L.

The CCM **(Figure 5.15-a)** was made from nanocomposite membrane HNC-180-2 as follows: 1.4 ml of anode and cathode ink (Cyclohexanol-based ink) were directly spray-coated over HNC membrane thermally treated at 180°C for 2 hours. The hot plate temperature was 60°C. The cold press was done under 6 tons at room temperature.


**Figure 5.15.** Images of HNC-CCM with HNC-180-2 membrane (a) before and (b) after electrochemical measurements.

An AST (between 25 and 250 mA/cm$^2$) was applied to the cell until the cell voltage reached a value of 2.3 Volt (**Figure 5.16-a**). The slope of the iV curves measured before and after the AST (**Figure 5.16-b**) show that the cell resistance increased during the test. This is consistent with the EIS spectra (**Figure 5.16-c**) and HFR measurements.

Compared to the results obtained with the membrane HNC-low, the thermal treatment applied to the nanocomposite membrane at a higher temperature (180°C for 2 h) extended the life service of the CCM up to 21 hours. The rapid increase in cell voltage indicates a reduction performance of the CCM. In fact, the high-frequency impedance of the sample increases with time indicating a reduction in membrane ionic conductivity during the AST. To explain such reproducible behavior (not a measurement artefact), we speculate that the ionic conductivity of the membrane decreases under operation. Electrophoresis is a process in which nanoparticles move under the effect of applied potential. The PVDF matrix of the nanocomposite membrane swells with water and acts as a gel. We speculate that the silica nanoparticles can migrate through the PVDF network. As the silica nanoparticles coated with polystyrene sulphonic are charged with negative sulphonic groups, they move toward the anode. This can potentially create a depletion area on the cathode side and increase the high-frequency resistance of the cell.

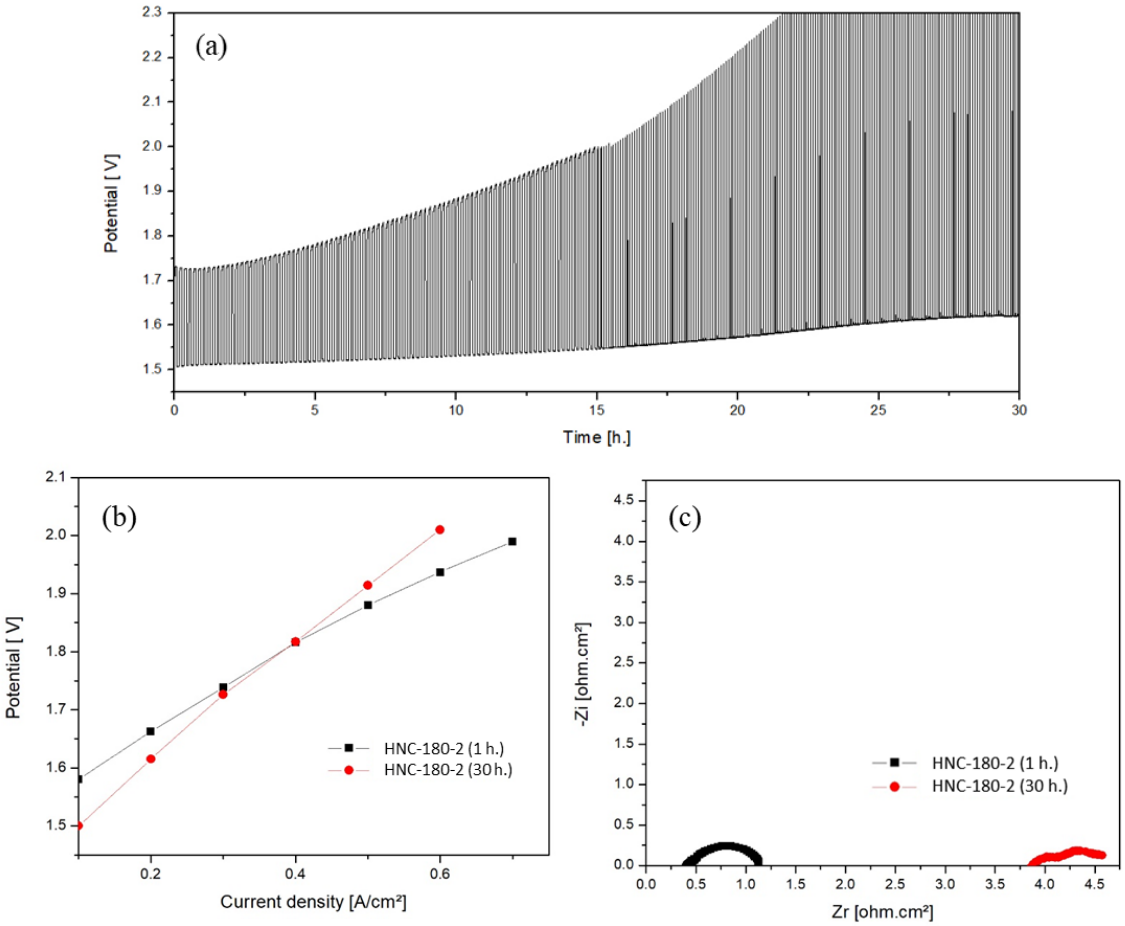


**Figure 5.16.** (a) chronopotentiometery between 25 and 250 mA/cm$^2$; (b) iV curve of the HNC-CCM with HNC-180-2 membrane treated at 60 °C (using cell n°1 and 2L flowfield) before and after 30 h of electrolysis; (c) corresponding EIS spectra.

### 5.5.3. CCM with membrane HNC-180-6 (treated 6 hours at 180°C)

The CCM was made as follows: 1.4 ml of anode and cathode ink (Cyclohexanol-based ink) were direct spray-coated over the HNC membrane and treated at 180°C for 6 hours. The hot plate temperature was 60°C. The cold press was done under 6 tons at room temperature. The electrocatalyst appears to be attached to the membrane after 30 h of electrolysis (**Figure 5.17**).


**Figure 5.17.** Sample HNC-180-6 (a) before and (b) after electrochemical measurements.

Electrochemical data are plotted in **Figure 5.18**. The CCM with HNC-180-6 membrane is unstable and shows a short circuit after a few hours of operation. Again, we speculate that the reason for the short circuit is the swelling of the membrane in water, which increases the area of the membrane by 161 % (from 9 $cm^2$ to 14.5 $cm^2$). Water swelling softens the membrane and facilitates the short-circuit of anode and cathode PTL under the cell clamping pressure (35 to 40 bar). It is important to note that all nanocomposite membranes (treated at low and high temperatures) swell to the same extent in water. It is also worth noting that reducing the clamping pressure applied to the electrolysis cell was useful for stopping the short-circuit and restoring electrolysis performance.

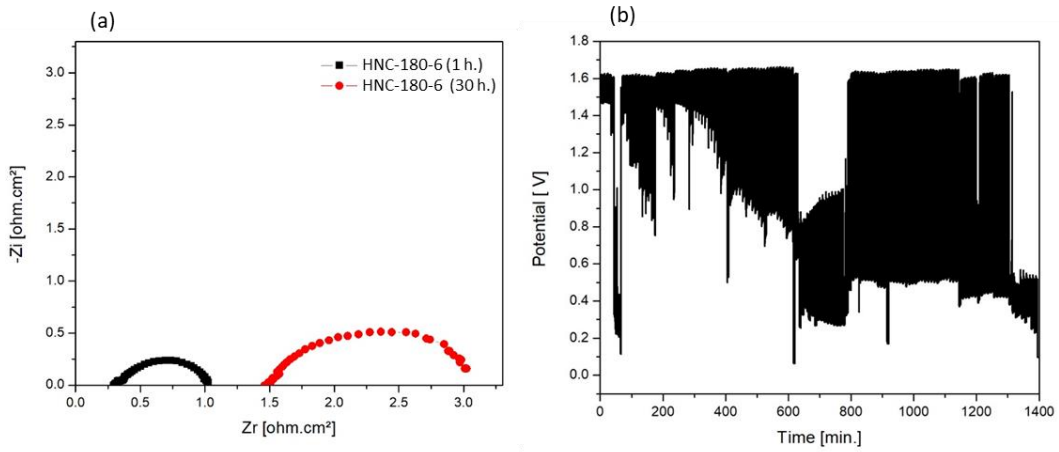


**Figure 5.18.** CCM with HNC-180-6 membrane. (a) EIS spectra at BoT and after 30 hours; (b) chronopotentiometry between 25 and 250 mA/$cm^2$ at 60°C using cell n°1 and 2L flowfield.

Empirically, we found the best-operating conditions to prevent the formation of short-circuits: a compromise has to be found between high clamping pressure and risk of short-circuits and low clamping pressure and risk of poor electrical contact between the PTL and the CCM.

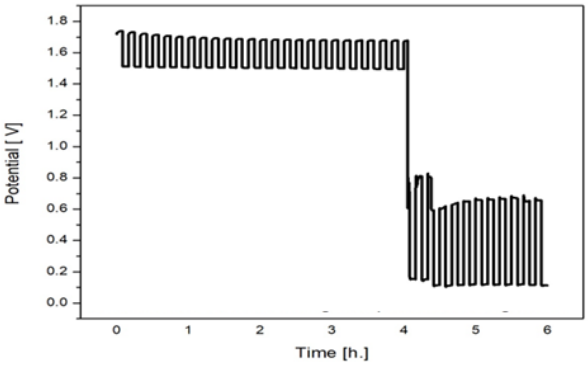


**Figure 5.19.** Typical AST showing the instability of CCM made with HNC-180-6 membranes (treated at 180°C for 6 hours). The AST ends with a short circuit after only 4 hours of operation. The measurements were performed at 60 °C using cell n°1 and flowfield 2L.

In conclusion, the HNC membrane treated at high temperatures for a longer time (6 h) was found mechanically less stable and stiff than the membrane treated for a shorter time. A short circuit happened inside the cell after only a few hours of AST **(Figure 5.19).** This is not an experimental artefact: these results were reproducible - several CCMs were prepared with this membrane, and a short circuit occurred every time. A more details analysis of the effect of the clamping pressure of the cell is reported in § 5.6.

### 5.5.4. Comparison of commercial CCM and HNC CCM

We then compared the electrochemical performances measured on our reference CCM and on the CCM with HNC membranes. EIS spectra are shown in **Figure 5.20** for comparison. These data were obtained despite the fast degradation of the membrane (swelling and short-circuit) which prevent full electrochemical characterization. At the beginning of the test (**Figure 5.20-a**), the HFR resistances are very similar and close to 300-400 mΩ.cm$^2$. The charge transfer resistance is higher on the HNC-CCM, indicating that there is still a place for performance improvement. At the end of the test, the differences are clear. In comparison, the performances of the reference remain almost unchanged (after 90 hours of AST, the HFR was reduced from 300 to 250 mΩ.cm$^2$, and the LFR increased from 700 to 750 mΩ.cm$^2$ (probably part of the CCM activation), the HFRs of HNC-CCM was significantly increased, indicating a loss of proton-conductivity.

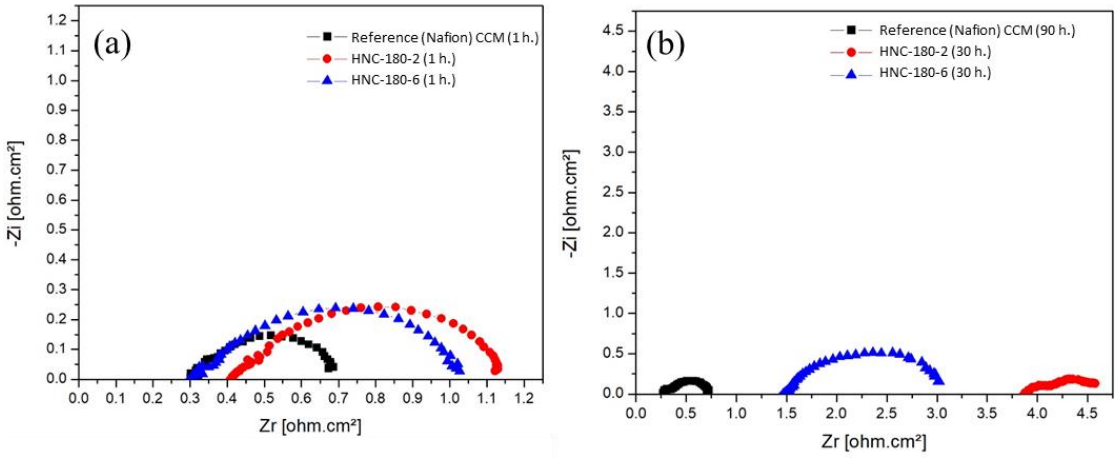


**Figure 5.20.** EIS spectra in Nyquist coordinates (a) before electrolysis and (b) after the stability test. The measurement was performed at 60 °C using cell n°1 and 2L flowfield at 25 mA/cm$^2$.

## 5.6. Effect of clamping pressure on the durability of HNC membrane

The high electronic conductivity of the PTL and CCM, as well as strong interfacial contact between them, are critical for optimum performance. The high-frequency resistance of the titanium PTL in contact with the CCM was measured in order to see the optimum durability of an electrolysis cell. In the followings, we show the results obtained for three different cell clamping pressure: 45, 35 and 25.

### 5.6.1. CCM with membrane HNC-180-2 clamped at 4.5 MPa

The HNC-CCM was made as follows: the HNC membrane was heated at 180°C for 2 hours (hence its name HNC-180-2) to increase homogeneity and cross-linking. Then it was coated with the catalyst as shown in the experimental section of this report by direct spray coating using the hand spray gun. Next, the HNC-CCM was mounted in the test cell, and a clamping pressure of 4.5 MPa was applied. However, the applied force exceeded the membrane strength, and a short circuit rapidly occurred in less than 2 hours (**Figure 5.21**).

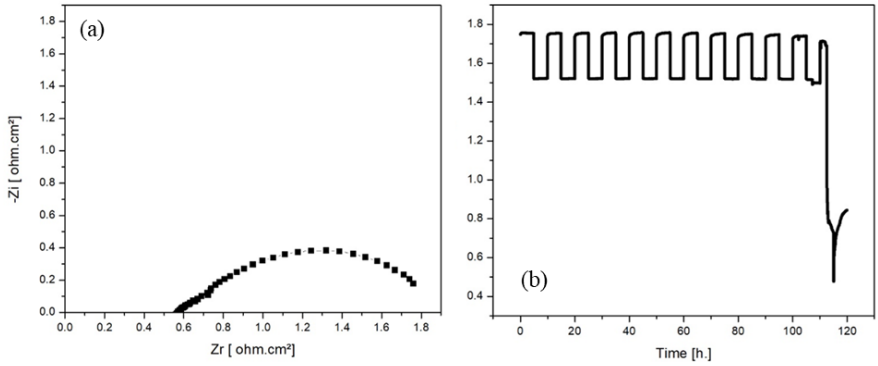


**Figure 5.21.** CCM with thermal treated HNC membrane under cell clamping pressure of 45 bar (a) EIS at 25 mA/cm$^2$ and (b) chronopotentiometry (AST) for 2 hours between 25 and 250 mA/cm$^2$. The measurements performed at 60°C using cell n°1 with 2L flowfield.

It is worth mentioning here that short circuits occur even if no current is applied to the cell simply by water circulation. When wetted with water, the nanocomposite membrane loses its mechanical strength and becomes very soft to some extent. **Table 5.2** compares the tensile strength of HNC-180-2 membrane in dry and wet states at room temperature**.** The tensile strength of the wet HNC-180-2 membrane is 3.1 times lower than a dry one. Moreover, the tensile strength of the wet Nafion 115 membrane is almost twice of the wet HNC membrane.

**Table 5.2.** Comparison of tensile strength between HNC-180-2 in dry and wet state.

| | **Dry HNC-180-2** | **Wet HNC-180-2** | **Wet Nafion 115** |
|---|---|---|---|
| Water uptake (%) | - | 70 | 22 |
| Swelling ratio (%) | - | 30 | 10 |
| Tensile strength (MPa) | 43 ± 3 | 14 ± 2 | 26 ± 1 |

### 5.6.2. CCM with membrane HNC-180-2 clamped at 3.5 MPa

A reduced clamping pressure of 3.5 MPa was used in the next experiment. The CCM was made using the HNC membrane heated at 180°C for 2 hours. The HNC-CCM showed relatively higher stability and lasted for 9.5 h then a short circuit occurred after 9.5 hours (**Figure 5.22-a**).

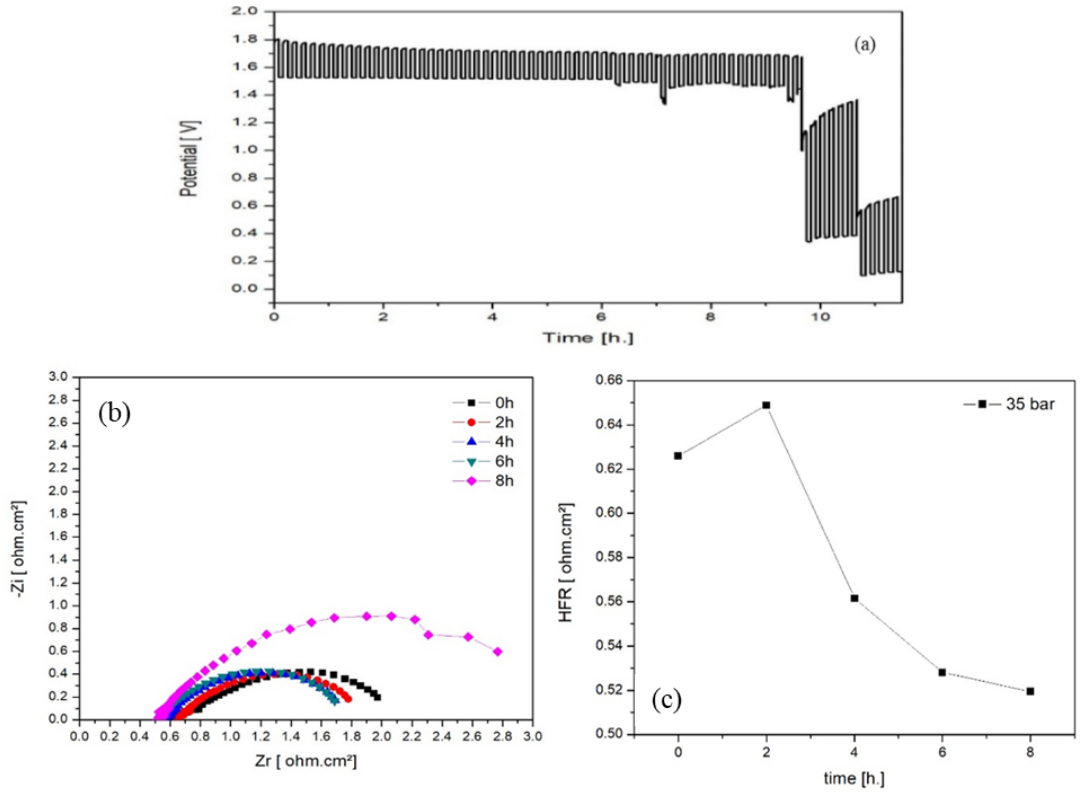


**Figure 5.22.** AST test of a CCM with HNC-180-2 HNC membrane under a cell clamping pressure of 35 bar. (a) chronopotentiometry (AST) for 12 h at 25 and 250 mA/cm$^2$; (b) EIS measurements at 25 mA/cm$^2$; (c) HFR at a different time. The measurements were performed at 60°C using cell n°1 with 2L flowfield.

The HFR which is a measure of the total cell impedance (ie, the sum of all bulk and interface resistances: membrane, cables, Ti current collector, the multilayer felt and the interfacial resistance between the CCM and the PTL) was plotted as a function of AST time (**Figure 5.22-c**). The HFR slightly decreased from 0.62 to 0.52 ohm.cm$^2$ during the first few hours. This can be explained by the softening effect of water, which reduces the mechanical resistance of the HNC membrane and decreases its thickness and ionic resistance.

### 5.6.3. CCM with membrane HNC-180-2 clamped at 2.5 MPa

A further reduction in the clamping pressure of 2.5 MPa was used. The CCM was made using the nanocomposite membrane heated at 180°C for 2 hours. The HNC-CCM was stable for 6.5 h then a short circuit occurred (**Figure 5.23-a**), and a slight reduction in the HFR (**Figure 5.23-b,c**). Therefore, there is no significant difference from the previous test at 35 bars, and there is no need to reduce the clamping pressure further.

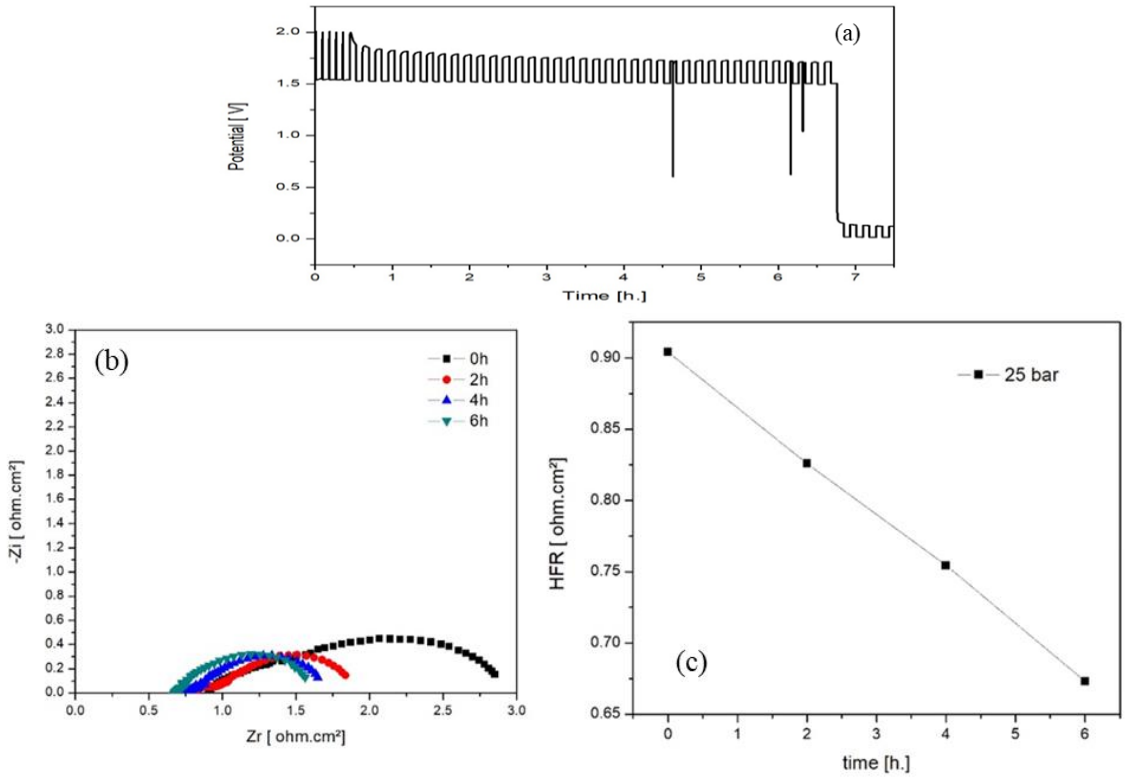


**Figure 5.23.** CCM with HNC-180-2 HNC membrane under a cell clamping pressure of 25 bar. (a) chronopotentiometry (AST) for 8 h between 25 and 250 mA/cm$^2$ ; (b) EIS measurements, (c) HFR at different time. All measurements performed at 60°C using cell n°1 with 2L flowfield.

### 5.6.4. Conclusion

These different results show that the swelling of the HNC membrane (and associated dimensional changes) is a critical issue. This is a weakness of the material when the objective is to form durable CCMs. Catalyst particles delaminate from the nanocomposite membrane if the HNC-CCM is put in contact with liquid water before clamping the cell (as reported in **Figure 5.6**). It can therefore be said that water swelling alone can delaminate, at least partly, the catalyst layers upon contact with water inside the cell. Clamping the HNC-CCM between two porous Ti-PTL inside the electrolysis cell at 35 bar may physically trap the CL over the membrane and improve CCM stability. The membrane swelling (water uptake and dimensional changes) reduces the mechanical strength of the membrane, and short circuits can occur after only a few hours of electrolysis.

Conclusions for the effect of clamping pressure on CCM performance:

- In all cases, a short circuit happened due to softening of the membrane in water and a reduction in membrane strength and thickness.
- During the first 10-15 hours of electrolysis, when the membrane swells water, the high-frequency resistance (HFR) is slightly reduced; this is attributed to membrane softening and thickness reduction due to the large clamping pressure applied to the cell.
- After 15-20 hours of electrolysis, the HFR increases dramatically due to electrophoresis and the movement of Si particles in response to the applied electrical field.
- The thermally treated membrane (at 180°C for 2 or 6 hours) which has high proton conductivity, is, for now, the best candidate we tested for PEM electrolysis; however, there is still a need to optimize (or boost) its durability.
- We should find a solution for the reduction of the mechanical strength of the membrane (maybe by introducing a mesh or a grid inside to improve tensile strength).

## 5.7. Multi-layer CCM for improved durability

Results presented in the previous paragraphs led us to the conclusion that the nanocomposite membrane is neither chemically nor mechanically stable for operation in PEM water electrolysis. At this stage, chemical degradation mechanisms are still unclear, but the loss of proton-conductivity lead us to some speculative degradation processes (*e.g.*, chemical oxidation on the anode side, loss of silica nanoparticles or transfer of silica nanoparticles to the cathode side of the cell during electrolysis). To better understand the situation and increase the life service of the nanocomposite membrane, we decided to make and test multi-layer CCM with the following approaches:

1. Pressing two nanocomposite membranes together to double the membrane thickness and prevent short-circuits.
2. Inserting of polyphenylene sulfide (PPS) mesh between two layers of nanocomposite membrane.
3. Using one layer of Nafion 113 on the anode side and one HNC membrane on the cathode side.
4. Clamping the nanocomposite membrane between two thin Nafion membranes.

Each of the mentioned-above approaches is described in the following sections.

### 5.7.1. Two-layer HNC-180-2

A first HNC-180-2 membrane was used on the cathode side: an HER catalyst layer was deposited on one of its sides. A second HNC-180-2 membrane was used on the anode side: an OER catalyst layer was deposited on one of its sides. The catalyst layers were coated by direct spray coating using a hand spray gun, as described in section 2.2.2. Each catalyst-coated membrane was pressed separately. The attempts made to “weld” the two catalyst-coated membranes and reduce their interfacial resistance by pressing them at room temperature under 4 tons failed. The two catalyst-coated membranes were clamped in the cell at a clamping pressure of 3.5 MPa. Electrochemical results are shown in **Figure 5.24**. The life service (the duration of the AST before a short-circuit occurred) was doubled: the AST test ended up after 25 hours (**Figure 5.24-a**). As expected, the HF resistance of the CCM has increased compared to the previous case where only one membrane was used (**Figure 5.24-b**: the HF resistance has not exactly doubled since the internal cell resistance due to titanium components remains almost the same during the two experiments). During the AST, an increase in the HF resistance is still observed (**Figure 5.24-b**), which can be explained as follows. Two opposite phenomena occur inside the HNC membrane and affect the HFR in opposite ways. First phenomena: the HNC membrane swells and loses mechanical resistance; the membrane thickness reduces at the applied clamping pressure, leading to a gradual decrease of the HFR. This also explains why the HFR does not double when two nanocomposite membranes are pressed together. The second phenomena: is the detachment and transport of silica nanoparticles (functionalized with polystyrene sulfonic groups) from the PVDF backbone and electrophoresis toward the anode. At the beginning of the AST, the reduction of the membrane thickness is expected to occur simultaneously with nanoparticles detachment and electrophoresis in equal proportions; therefore no change is expected in the HFR. After 10 to 15 hours of AST, the detachment of nanoparticles and electrophoresis most probably predominate, and the HFR increases.

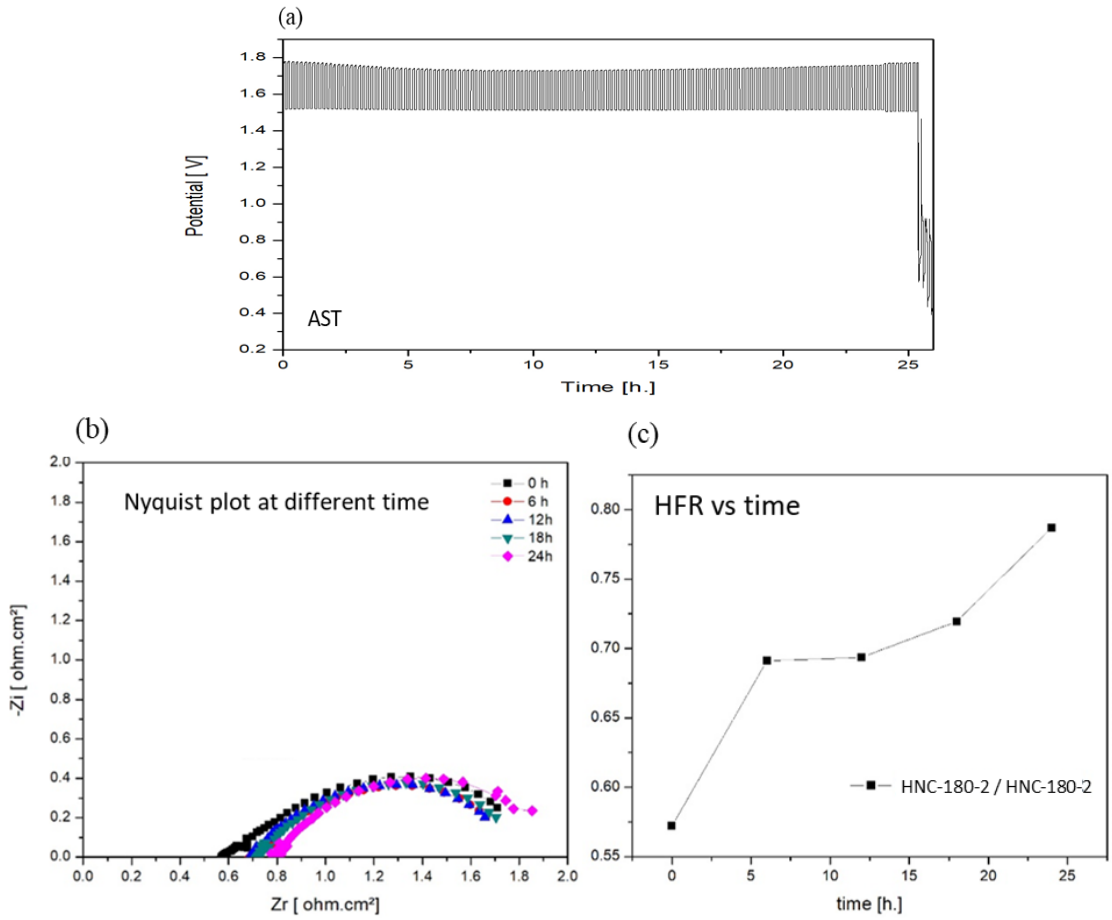


**Figure 5.24.** Electrochemical measurements on CCM with 2 HNC-180-2 membranes pressed against each other. (a) AST between 25 and 250 mA/cm$^2$ for 26 h, (b) EIS measurements at a different time of AST and (c) HFR evolution with AST time. The measurements performed at 60°C using cell n°1 with 2L flowfield.

Conclusion: despite an increase of the life service (from 10 to 26 hours of operation), a short circuit occurred after 26 hours of operation. Therefore, there is a relation between the membrane thickness and the life service where doubling the membrane thickness doubles the life service but does not solve short-circuit problems.

### 5.7.2. Two-layer HNC-180-2 with PPS reinforcement in between

It was then decided to clamp two HNC membranes over a PPS mesh used as reinforcement to prevent short-circuit. The HNC-CCM was made the same way as the two-layer HNC-180-2 reported in the previous paragraph, but a PPS mesh was placed between the two membranes. A commercial PPS mesh (thickness ~ 60 µm and porosity ~ 48%) was used for that purpose (**Figure 5.25-a**). The mesh was inserted between two HNC membranes inside the cell and clamped directly inside the cell, using a clamping pressure of 5.5 MPa to ensure that the two membranes get in ionic contact.

Electrochemical results are shown in **Figure 5.25**. The life service during the AST was significantly extended (above 50 hours) without short-circuit (**Figure 5.25-b**), giving enough time to perform a more detailed EIS analysis of the situation. The EIS spectra (**Figure 5.25-c**) show two semicircles. The new high–frequency small semicircle was ascribed to the HNC membrane-membrane interface. The high-frequency cell resistance and the diameter of the high-frequency semicircle increased during the 50 h of the long AST test (Figure 5.25-d), indicating that fast degradation occurs.

The second and larger semicircle observed at lower frequencies was attributed to the OER half-cell reaction. This semicircle was almost constant during the test, thus showing the stability of the anode CL.

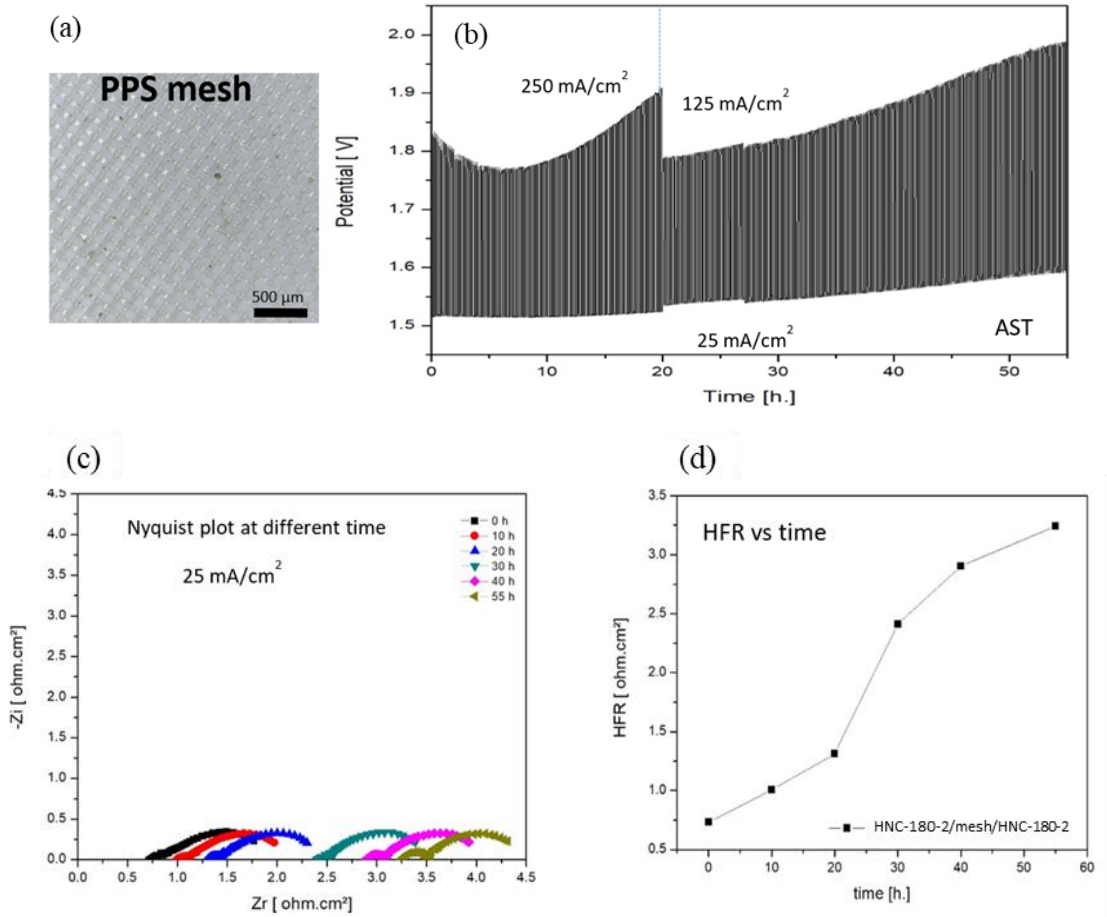


**Figure 5.25.** (a) Image of the PPS mesh and electrochemical measurements of the reinforced membrane (2 layers membrane + mesh) : (b) AST between 25 and 250 mA/cm$^2$ for 20 h followed by another AST between 25and 125 mA/cm$^2$ for 35h, (c) EIS measurements at a different time of AST and (d) plot of the HFR versus AST time. The measurements were performed at 60°C using cell n°1 with 2L flowfield.

### 5.7.3. One layer HNC-180-2 at the cathode and Nafion 113 at the anode

This CCM was prepared as follows. A thin Nafion 113 membrane was coated with $IrO_2$ using the DECAL method, dried in an oven at 80°C for 1 h, and hot pressed at 135°C under 2 tons for 5 min. The nanocomposite membrane (HNC-180-2) was coated on one side with Pt/C using a direct spray of 1.4 ml Cyclohexanol-based ink. The two membranes were placed bare side against bare side inside the test cell. The cell was tightened using a clamping pressure of 3.5 MPa. The 2-membrane CCM was not stable during the applied AST test, as shown in **Figure 5.26-a**. The HFR increased with time (**Figure 5.26-b**) and reached a maximum after 40 h of electrolysis (4.6 ohm.cm$^2$).

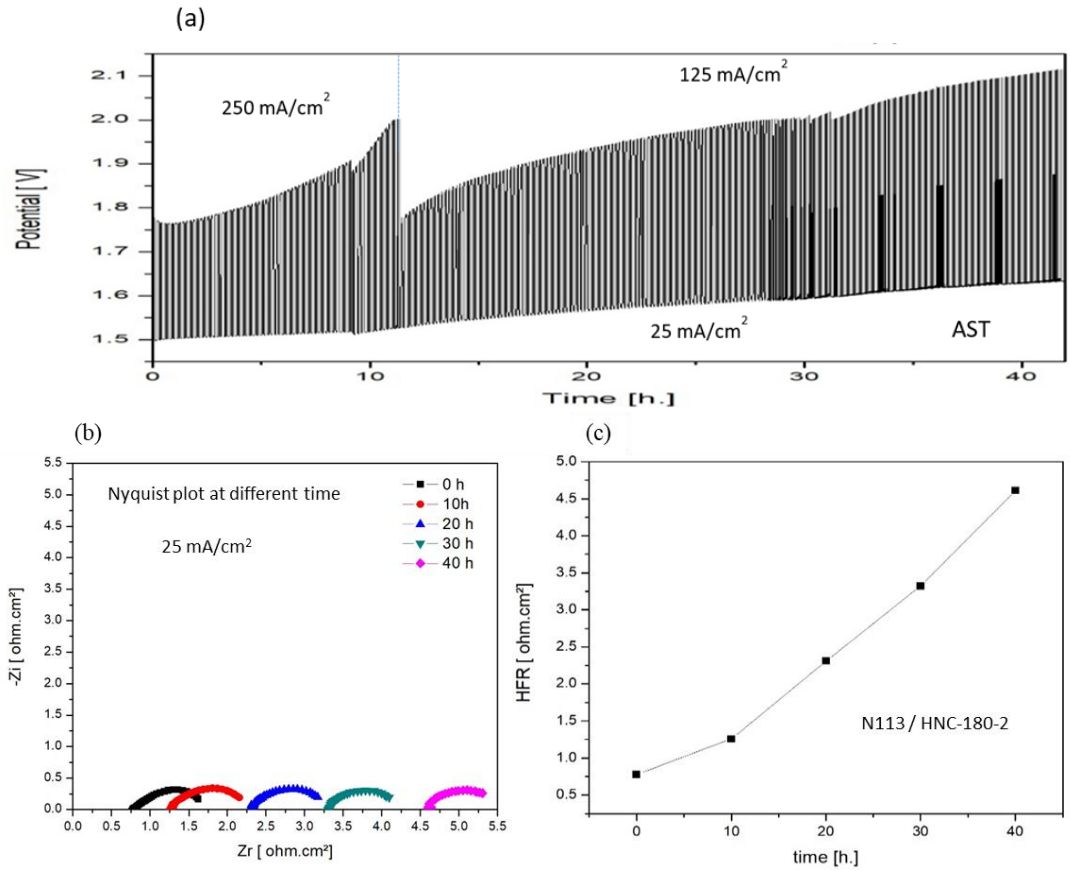


**Figure 5.26.** Electrochemical measurements of two-layer, HNC-180-2 at the cathode side and Nafion 113 at the anode. (a) the AST between 25 and 250 mA/cm$^2$ for 12 h followed by an AST between 25 and 250 mA/cm$^2$ for 30h. (b) EIS measurements at a different time of AST, (c) HFR vs time. Measurements were performed at 60°C using cell n°1 with 2L flowfield.

### 5.7.4. One layer HNC-180-2 clamped between two Nafion 113 layers

Finally, in the last attempt to significantly increase the life service of HNC-CCM, we decided to clamp the nanocomposite membrane between two Nafion 113 membranes in order to determine if degradation leads to the release of silica nanoparticles from the membrane, as now suspected. The first Nafion 113 membrane was coated with $IrO_2$ ink (20 wt% Nafion ionomer) using the DECAL transfer method, dried in an oven at 80 °C for 1 h, hot pressed at 135°C, and 2 tons for 5 min. The $IrO_2$ loading was 1 mg/cm$^2$. The second Nafion 113 membrane was coated with Pt/C (33 wt% Nafion ionomer) by direct deposition (DECAL was not used because direct ink deposition was found easier and more efficient on thin Nafion membranes; an optimization is required to use the DECAL method) and hot-pressed separately at 135°C under 2 tons for 5 min. The Pt loading was 0.5 mg/cm$^2$. The HNC-180-2 membrane was then sandwiched between the two layers of Nafion 113 and placed inside the cell at clamping pressure of 35 bar. Results are shown in **Figures 5.27-5.28**. Even though the nanocomposite membrane was confined between the two Nafion membranes, a significant reduction of the cell efficiency was observed during the test (**Figure 5.27-a**). EIS spectra (**Figure 5.27-b**) show two main semi-circles. The diameter of the high-frequency semicircle (which most probably represents the interface resistance) increased with time, but the HFR did not change significantly. The diameter of the low-frequency semicircle (the second semicircle, which most probably represents the charge transfer resistance of the OER catalytic reaction) remained constant during the AST. This suggests that its origin comes from membrane-membrane interfaces. During the AST itself (**Figure 5.27**), the cell voltage continuously increased, as was already the case with 1 or 2 membrane CCM.

To avoid cell voltage going higher than 2 V, which may oxidize the titanium PTL at the anode and increase the cell's internal resistance, the current density was periodically reduced as indicated in **Figure 5.27**. The iV curves measured during the AST (**Figure 5.28-a**) show an increasing internal cell resistance and a loss of catalyst during the AST. This is confirmed by the EIS spectra measured during the AST at 25 mA.cm$^{-2}$ (**Figure 5.28-b**): the low-frequency cell resistance continuously increases during the AST.

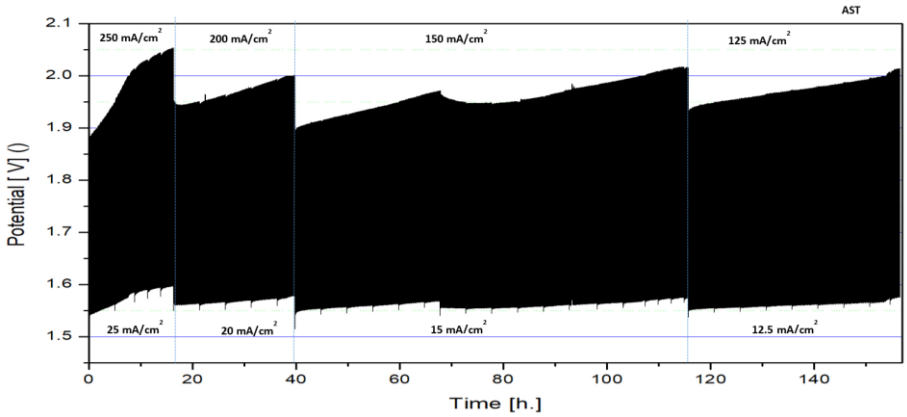


**Figure 5.27.** AST performed on the 3-membrane CCM at 60°C and atmospheric pressure using cell n°1 with 2L flowfield.

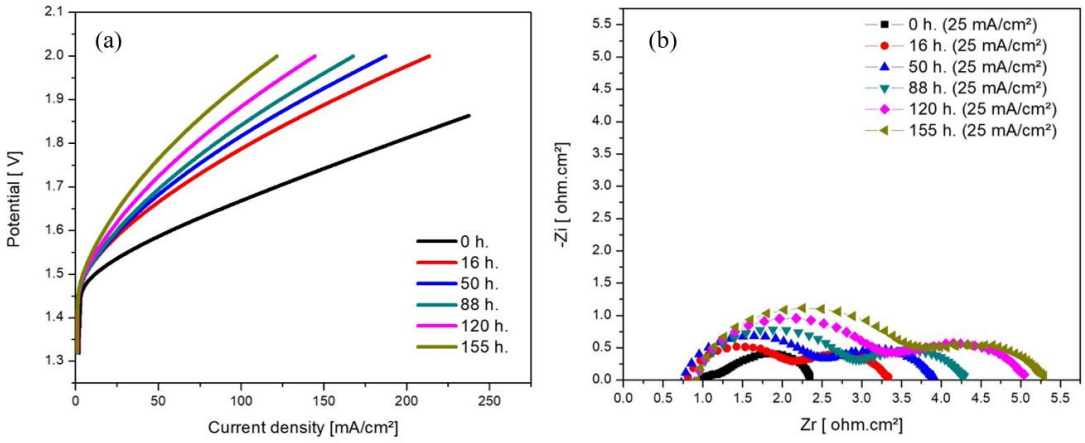


**Figure 5.28.** (a) iV curves measured along the AST and (b) corresponding EIS spectra. Measurements performed at 60°C using and atmospheric pressure, using cell n°1 with 2L flowfield.

EIS measurements made at different current densities show that the diameter of the high-frequency semicircle remains almost constant, indicating this semicircle is not related to charge transfer reaction (not related to the catalytic reaction): this first semicircle is therefore attributed to the membrane-membrane interfaces and associated interface resistances and capacitances. Furthermore, the diameter of the high-frequency semicircle is increasing with time, as shown in **Figure 5.29**, in agreement with the reduction in CCM performance. While the semicircle at lower frequencies changes with current density and is most probably related to the charge transfer resistance of the OER at the anode (the kinetics of the HER on Pt is fast and does not show a specific EIS semicircle). We conclude from these EIS measurements that the high-frequency semicircles are most probably related to the diffusion of protons at the interfaces between the membranes.

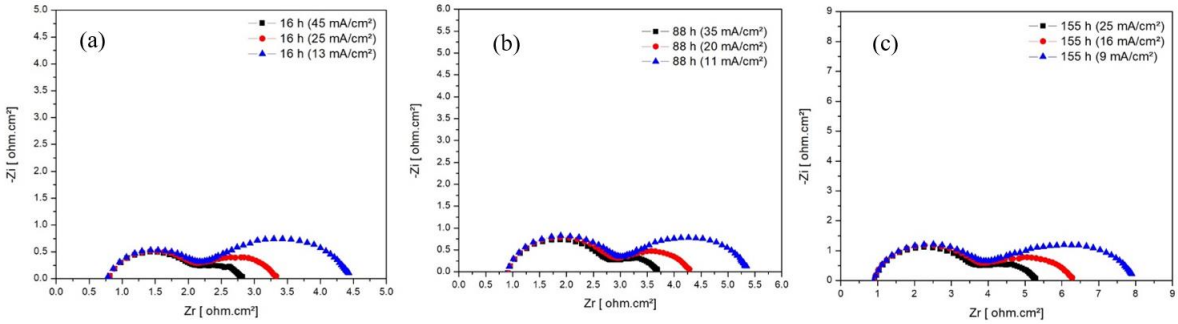


**Figure 5.29.** EIS measurements of the 3-membrane CCM at three different current densities and different times of AST of (a) 16 hrs, (b) 88 hrs and (c) 155 hrs.

To better characterize the 3-membrane CCM, the cell was dismantled after completion of the AST and the nanocomposite membrane was removed from the sandwich structure. Then the two Nafion membranes were combined again to form a new CCM with 2 membranes only. The AST continued with the new CCM from 155 to 235 hours (**Figure 5.30-a**). The iV curves (**Figure 5.30-b**) and EIS spectra **(Figure 5.30-c)** were periodically recorded. An insignificant change in the high-frequency semicircle over 83 h of additional AST indicates that the interface between two Nafion membranes is more stable than the HNC-180-2/Nafion interface. Also, the polarization curves of the two Nafion membrane CCM did not change significantly during the AST.

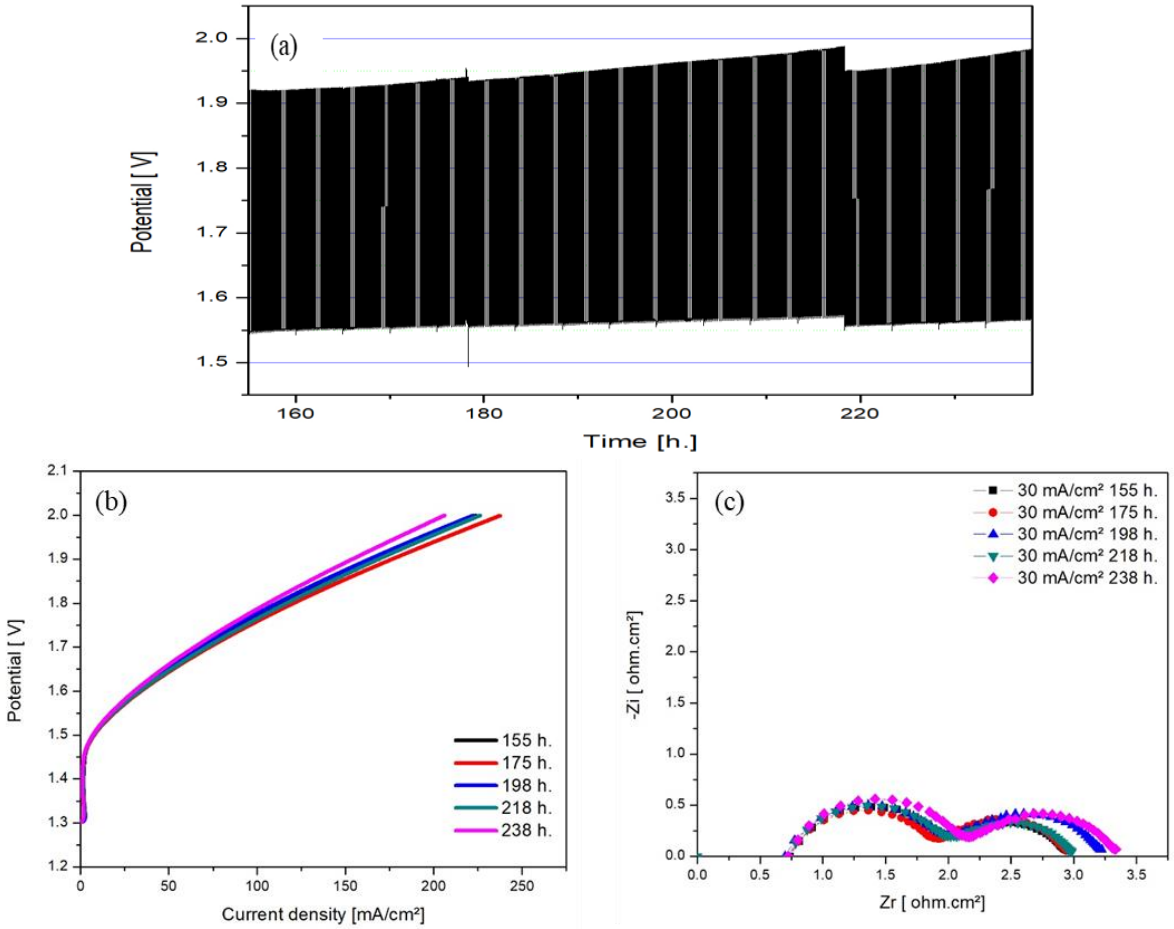


**Figure 5.30.** 2-membrane CCM after removal of the central HNC membrane : (a) AST; (b) iV curves; (c) EIS spectra. Measurements were performed at 60°C under atmospheric pressure, using cell n°1 with 2L flowfield.

As can be seen from **Figure 5.31**, the HFR remained constant once the nanocomposite membrane was removed. The diameter of the HF semicircle becomes smaller after the removal of the nanocomposite membrane: this is consistent with the fact that one membrane-membrane interface is removed. It also remains independent of the current density applied to the cell. The diameter of the low-frequency semicircle (attributed to the OER charge transfer resistance) remains potential-dependent and slightly increases with time but not as fast as when the nanocomposite membrane was on-board. Therefore, it can be concluded that once the nanocomposite membrane is extracted from the cell, the electrochemical performances are stable.

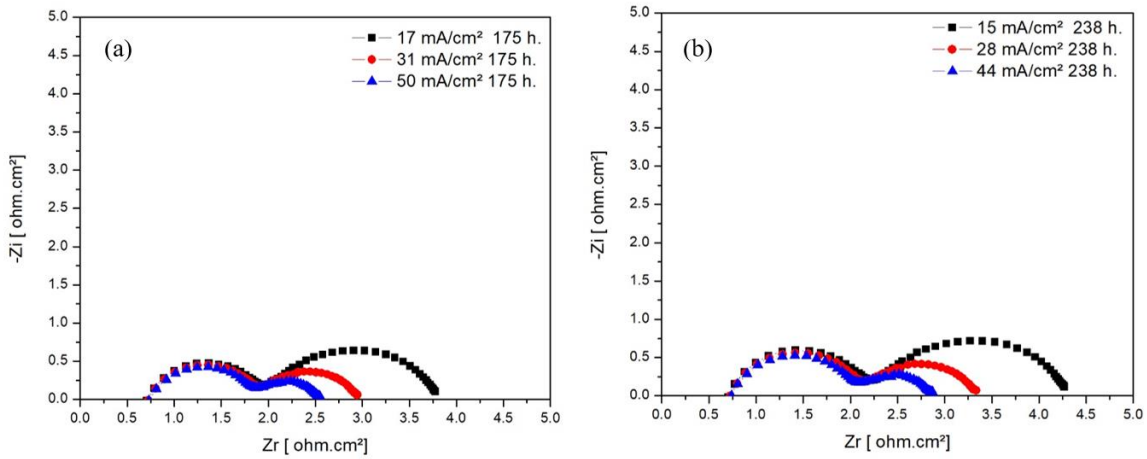


**Figure 5.31.** EIS spectra of 2-membrane CCM measured at different current densities after (a) 175 hours and (b) 238 hours of AST.

## 5.8. Analysis of the degradation of HNC membranes

### 5.8.1. Post-mortem analysis of the 3-membrane CCM

**Figure 5.32** shows pictures of the 3-membrane CCM after having dismantled the cell. The patterns at the periphery are those of the seals used in the cell. The Nafion113-cathode **(a)** was easy to remove from the central HNC-180-2 membrane. The Nafion113-anode adhered more strongly to the HNC-180-2 **(b).** Thus, it was necessary to take time to separate both. The HNC-180-2 membrane, after delamination after the test, is shown in **Figure 5.32-c**. After cutting the 4 $cm^2$ area in the core of the HNC membrane (shown in the black square of **Figure 5.32-c**), the membrane was weighted. A mass of only 26 mg was obtained: this is 50% less than the initial weight (52 ± 2 mg). This is an indication that the membrane lost chemical elements during the test. Furthermore, the ion exchange capacity of the cut 4 $cm^2$ HNC CCM was below the detection limit (less than 0.1 meq/g), much lower than the initial value of 1.8 meq/g. We then tried to prove the chemical degradation of the HNC membrane into evidence.

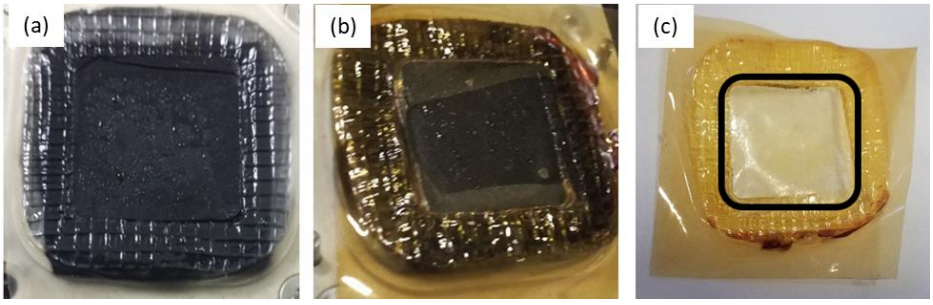


**Figure 5.32.** 3-membrane CCM after the AST: (a) the cathode side; (b) the anode side, and (c) the HNC-180-2 after delamination.

FT-IR measurements made by attenuated total reflectance (ATR) on the HNC membrane before and after the electrochemical test are shown in **Figure 5.33**. A significant reduction of two peaks (those at 1150 $cm^{-1}$ and at 1220 $cm^{-1}$ that correspond to the symmetric and asymmetric stretching vibration of $SO_3$ groups in the solid phase[71]) are observed. This indicates that the nanocomposite membrane lost sulfonic groups during the AST.

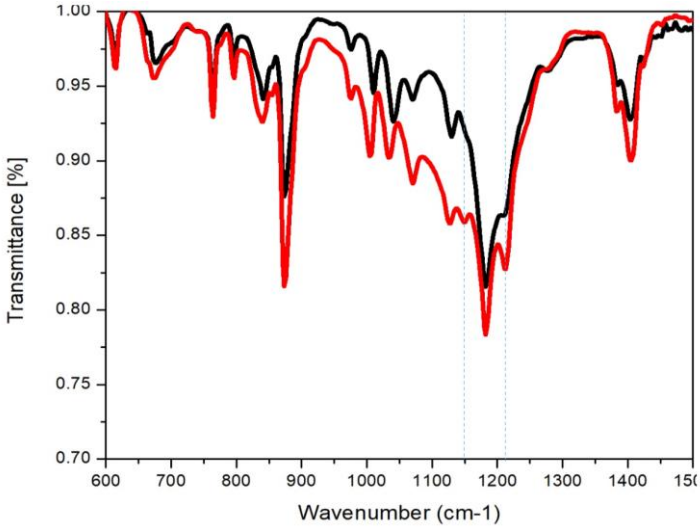


**Figure 5.33.** FT-IR spectra were measured on the HNC membrane before (red) and after (black) the AST.

EDS spectroscopy was also performed to determine elemental composition changes of the nanocomposite membrane after electrolysis. EDS is a technique that can determine the chemical composition down to a few micrometres below the sample surface depending on the intensity of the electrons and the design of the sample. EDS spectra of the HNC-180-2 membrane before and after electrolysis is shown in **Figure 5.34**. A significant reduction of the HNC membrane's oxygen, silicon and sulfur contents was put into evidence. These measurements confirm the decrease in the IEC of the HNC membrane during the test.

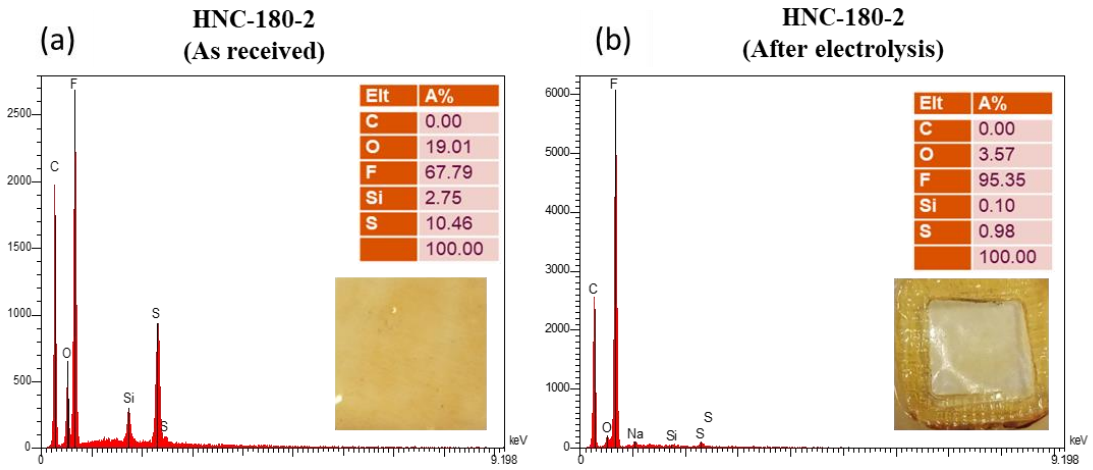


**Figure 5.34.** EDS analysis of the HNC membrane : (a) before; (b) after AST (the carbon content was excluded from the atomic ratio of the elements since we are using a conductive carbon tape as a substrate that may interfere with the results). Insert tables represent elemental composition measured by EDS.

[71] Tripathi BP, Chakrabarty T, Shahi VK. *Highly charged and stable cross-linked 4,4'-bis(4-aminophenoxy)biphenyl-3,3'-disulfonic acid (BAPBDS)-sulfonated poly(ether sulfone) polymer electrolyte membranes impervious to methanol*. J Mater Chem 2010;20:8036. https://doi.org/10.1039/c0jm01183e.

These results led us to the conclusion that the nanocomposite membrane is not chemically stable during electrolysis. It loses matter and, most importantly, its acid (*i.e.* proton conducting) functions. This is consistent with the increase of the membrane resistivity observed during the ASTs. The HNC membrane was initially developed for fuel cell applications[Error! Bookmark not defined.], where the quantities of water present are less than in water electrolysis. The large electro-osmotic water flow which takes place during electrolysis accelerates the degradation of the membrane. Silica nanoparticles functionalized with poly (styrene sulfonic acid) are dispersed in a PVDF-HFP matrix to form the HNC. These nanoparticles may be extracted from the polymer matrix by electrophoresis or by simple elution. The cross-linking was increased so that the nanoparticles are chemically constrained to remain in the matrix. HNC membrane crosslinked with 2,2,4-trimethyl-1,6-hexanediamine (THDA) and post-annealed at 180 °C for 2 or 6 hours are relatively stable and show satisfactory fuel cell performances. The $NH_2$ groups of the THDA were grafted to the activated PVDF polymer through Michael addition to form imine bond (**Figure 5.35**).

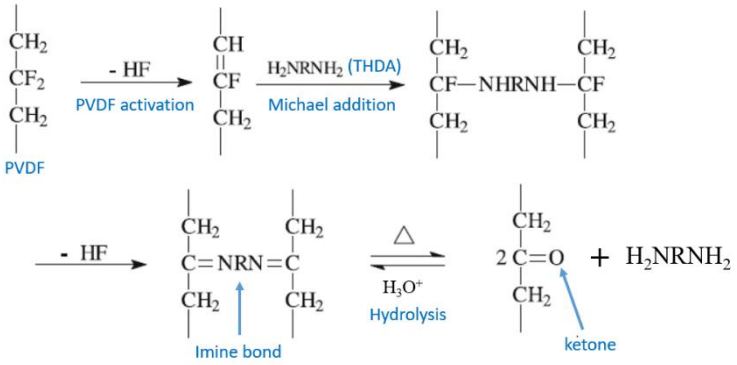


**Figure 5.35.** Mechanism of THDA crosslink to PVDF in the HNC membrane[68].

The authors used 3-Aminopropyl-triethoxysilane (APTES) to crosslink the silica nanoparticle (functionalized with polystyrene sulfonate) to the PVDF matrix using enamine bond, as shown in **Figure 5.2.c.**

A literature review confirmed the considerable sensitivity of imine and enamine functional groups to hydrolysis[72]. The **imine and enamine** bonds are acidly hydrolysable, i.e. they can be thermally decomposed to amine and carbonyl groups in water and an acidic medium (**Figure 5.36**). This is the typical condition of PEM water electrolysis. The water electrolysis technology requires excess hot water (to feed the reaction and remove extra heat produced in the cells). At the same time, the sulfonic groups of the membrane are responsible for the acidity and proton-conductivity inside. Therefore, the imine bond inside the proton exchange membrane is not stable. Furthermore, the protons' migration inside the membrane (when a DC electric voltage is applied) will increase the chance of attacking the imine bond by protons and accelerate the degradation of the imine bonds. In the other hand, the enamine bonds are nucleophilic because they have a significant resonance form with a negative charge on the alpha carbon. They are hydrolyzed using concentrated acid. Moreover, imine and enamine undergo tautomerization: enamine can transform into imine and vice versa.

[72] Abdel-Magid AF. 8.02 *Reduction of CN to CH–NH by Metal Hydrides.* Compr. Org. Synth. II, Elsevier; 2014, p. 85–150. https://doi.org/10.1016/B978-0-08-097742-3.00802-8.

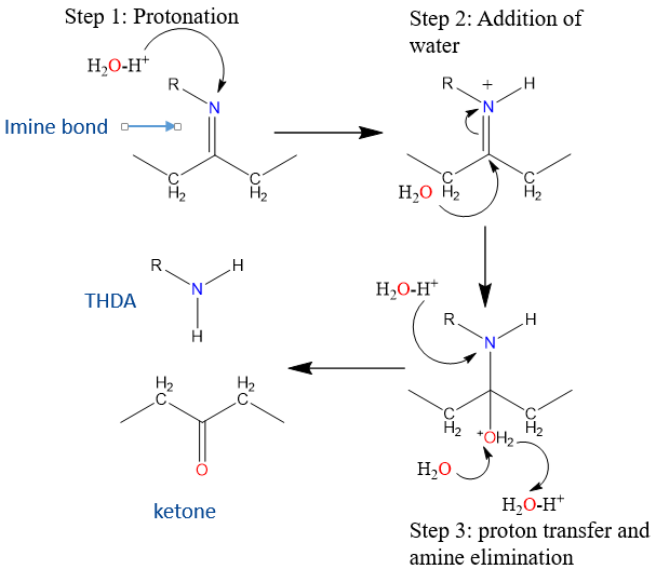


**Figure 5.36.** Mechanism of imine bond hydrolysis in an aqueous acidic medium[73].

Additionally, the polystyrene sulfonic polymer is also not stable and prone to oxidative degradation, as shown in **Figure 5.37**. Under the practical operating conditions of water electrolysis, local decomposition of the polystyrene backbone can occur due to a chemical attack by free radicals (mainly hydroxyl radicals (OH•) formed during electrochemical conversion in PEMWE. This can result in the disruption of the structure's regularity and can accelerate the membrane's degradation. The OH• can rapidly add to the ortho position of aromatic rings, forming isomeric hydroxy-cyclohexadienyl radicals (**Figure 5.37**, reaction A). The resultant OH-adduct may generate other highly reactive radicals. Furthermore, (OH•), can react with an aliphatic linear polymer chain via abstraction of the labile tertiary protons and forming benzyl radicals (**Figure 5.37**, reaction B), followed by chain scission and polymer degradation. A similar oxygen degradation mechanism was observed in the radiation-grafted polymer membrane used as an electrolyte for water electrolysis. The oxidative radical attached to the tertiary carbon of the benzyl groups can cause polymer chain scission (**Figure 5.37**, Reaction C)[74]. In addition to the sensitivity of crosslinked imine and enamine groups to acid hydrolysis, there is perhaps an insufficient quantity of cross-linking between PVDF chains and/or between PVDF and silica nanoparticles.

[73] Innocenti R, Lenci E, Trabocchi A. *Recent advances in copper-catalyzed imine-based multicomponent reactions*. Tetrahedron Lett 2020;61:152083. https://doi.org/10.1016/j.tetlet.2020.152083.
[74] Albert A, Lochner T, Schmidt TJ, Gubler L. *Stability and Degradation Mechanisms of Radiation-Grafted Polymer Electrolyte Membranes for Water Electrolysis*. ACS Appl Mater Interfaces 2016;8:15297–306. https://doi.org/10.1021/acsami.6b03050.

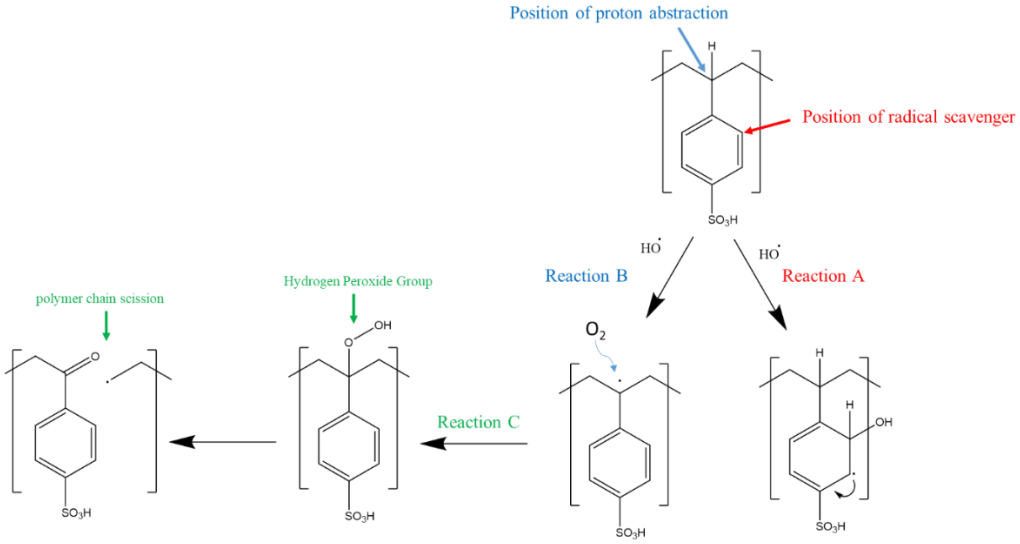


**Figure 5.37.** the principal oxidative degradation reactions occur in polystyrene sulfonate polymer [75].

### 5.8.2. Hydrothermal membrane degradation

The effect of water alone (without electrochemistry) was then investigated by treating a 100 $cm^2$ of the HNC membrane (1050 mg) with deionized liquid water under stirring at 60°C for 200 h. The water was collected periodically and titrated with 0.1 M NaOH to determine the leached acidity from the HNC membrane to the water (indirect titration) during the 200 hours long test. **Figure 5.38** shows the change in IEC of the HNC membrane versus the time.

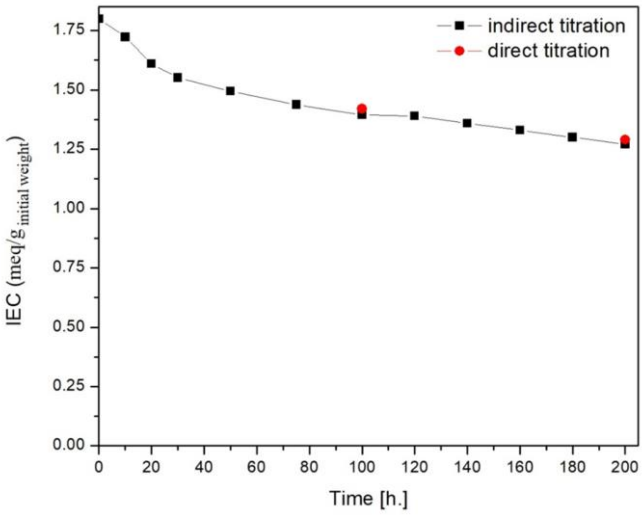


**Figure 5.38.** Time variation of the IEC of the HNC-180-2 membrane treated with water at 60°C for 220 hours.

During the first 40 hours of the test, the IEC of the membrane declined rapidly from 1.8 to 1.5 meq/g. Then the ICE declined at a reduced rate up to 100 hours. Finally, the degradation rate became constant, and the IEC decreased linearly with time after additional 120 hours. The direct titration was performed by exchanging protons of the membrane with sodium ions and titrating the collected acidic salty solution. These results show that the HNC membrane is unstable in hydrothermal conditions, even without current flow. The instability is probably due to the hydrolysis of imine bonds in contact with water.

[75] Walkowiak-Kulikowska J, Wolska J, Koroniak H. *Polymers application in proton exchange membranes for fuel cells (PEMFCs)*. Phys Sci Rev 2017;2. https://doi.org/10.1515/psr-2017-0018.

## 5.9. Attempts to improve crosslinking between sulfonic groups and PVDF matrix

### 5.9.1. Gamma radiation in dry condition

An attempt to improve the chemical stability of the nanocomposite membrane via a better cross-linking of silica nanoparticles onto the PVDF matrix was made by using gamma radiation. Gamma radiation is a high-energy photon that generates radical species in the PVDF polymer. In literature, many groups take advantage of the generated radicals to act as a nucleus for the grafting polymerization of styrene monomer on the PVDF[76]. The high-energy photon can also generate radicals in the PSSA polymer; therefore, gamma irradiation of the casted nanocomposite membranes can potentially generate radicals in both PSSA and PVDF and bring the possibility to crosslink both and form a stable C-C bond (**Figure 5.39**).

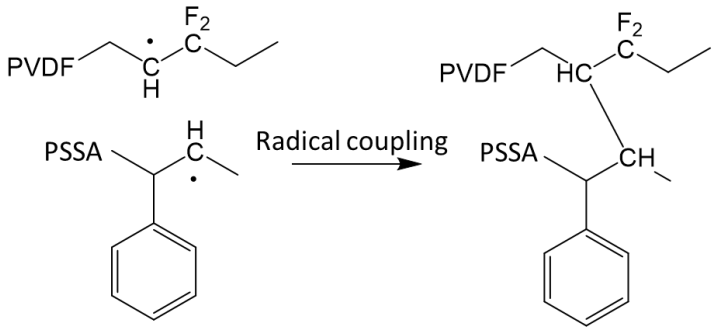


**Figure 5.39.** Mechanism leading to the cross-linking of PVDF and PSSA polymers.

A piece of dry nanocomposite membrane was irradiated by gamma-ray at the dose of 2.5 kGy (at room temperature), then coated with Pt/C ink and used as a cathode. While Nafion 113 (coated with $IrO_2$ ink) was used as the anode. The electrochemical performance of the prepared CCM is shown in **Figure 5.40**. No significant stability improvement was obtained. The HFR of the cell increased up to 4.8 ohm.cm$^2$ after 50h of AST.

[76] Marmey P, Porté M., Baquey C. *PVDF multifilament yarns grafted with polystyrene induced by γ-irradition: Influence of the grafting parameters on the mechanical properties*. Nucl Instruments Methods Phys Res Sect B Beam Interact with Mater Atoms 2003;208:429–33. https://doi.org/10.1016/S0168-583X(03)00887-5.

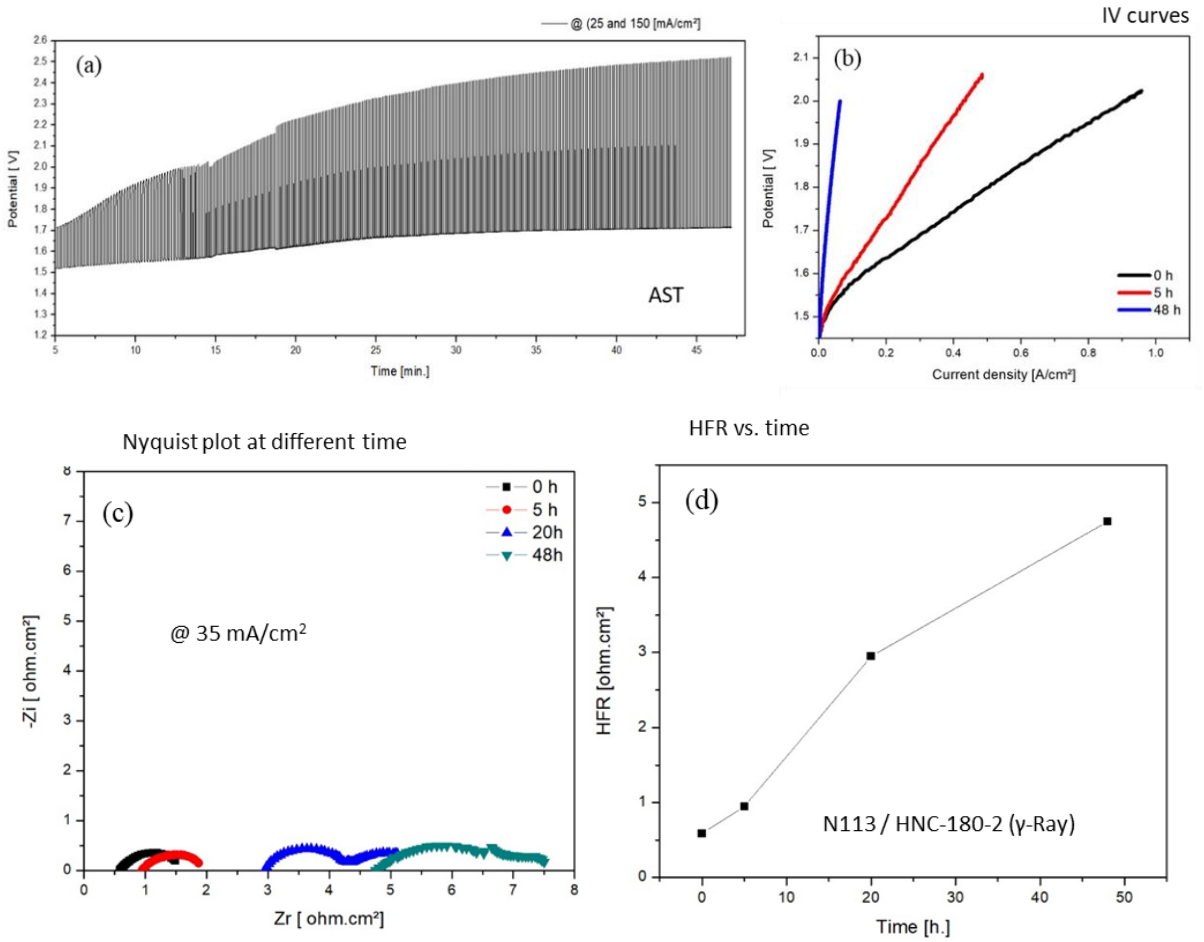


**Figure 5.40.** Electrochemical measurements of the two-layer membrane (HNC-180-2 exposed to gamma rays) at the cathode side and Nafion 113 at the anode. (a) The AST at 25/150 mA/cm$^2$ for 48 h; (b) iV curves; (c) EIS measurements along the test; and (d) HFR vs time. Measurements were performed at 60°C using atmospheric pressure, using cell n°1 with 2L flowfield.

### 5.9.2. Gamma radiation in wet condition

To further increase the amount of radical in the hybrid nanocomposite membrane, the membrane was treated with a higher gamma dose (20 kGy) and in the presence of liquid water. The membrane was soaked in water during gamma irradiation. The swollen membrane is softer and has a higher polymer chain mobility than the dry one. The water molecules can absorb gamma rays and generate a hydroxyl radical (OH·). The OH· radicals can then extract a hydrogen atom from the polymer chain and create more radicals on the chain. The radicals formed in different polymer chains can react together to form a stable C-C bond (**Figure 5.41**), turning into a crosslinked gel in water[77].

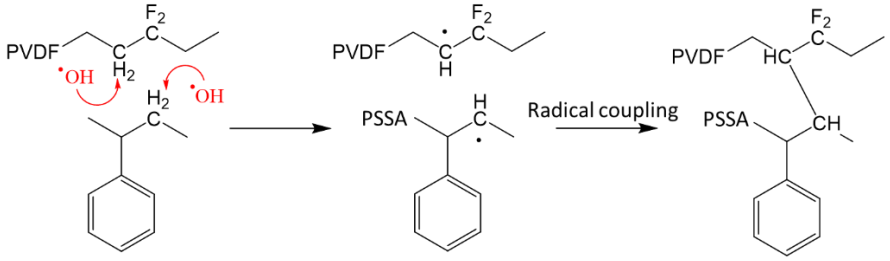


**Figure 5.41.** Mechanism of hydroxyl radical attack on polymer chain to induce crosslinking.

[77] Ding Y, Wang J, Song S. *Synthesis and Characterization of Linear Polyisoprene Supramolecular Elastomers Based on Quadruple Hydrogen Bonding.* Polymers (Basel) 2020;12:110. https://doi.org/10.3390/polym12010110.

The wet gamma-irradiated membrane was sandwiched between two Nafion 212 membranes to increase the CCM durability during the electrochemical measurements. As described in the experimental chapter 2, the first Nafion 212 half CCM was coated with $IrO_2$ ink, and the second was coated with Pt/C ink. The CCM was tested for 75 hours. The current was cycled between 25 and 125 mA/cm$^2$. Contrary to the previous sandwich CCM, only one flattened semicircle is observed on the EIS spectra. The absence of the second semicircle (interface semicircle) indicates a low interface resistance between the HNC and the Nafion membranes. The possible explanation is that in this experiment, the HNC membrane was sufficiently wetted with water when clamped in the electrochemical cell, improving the contact with the Nafion membrane. The water softens the HNC membrane and improves interfacial contact with the Nafion membrane. Furthermore, the HFR increased during the AST and reached 3.3 Ω.cm$^2$ after 75 h. The degradation of electrochemical performance is clearly seen in **Figure 5.42**.

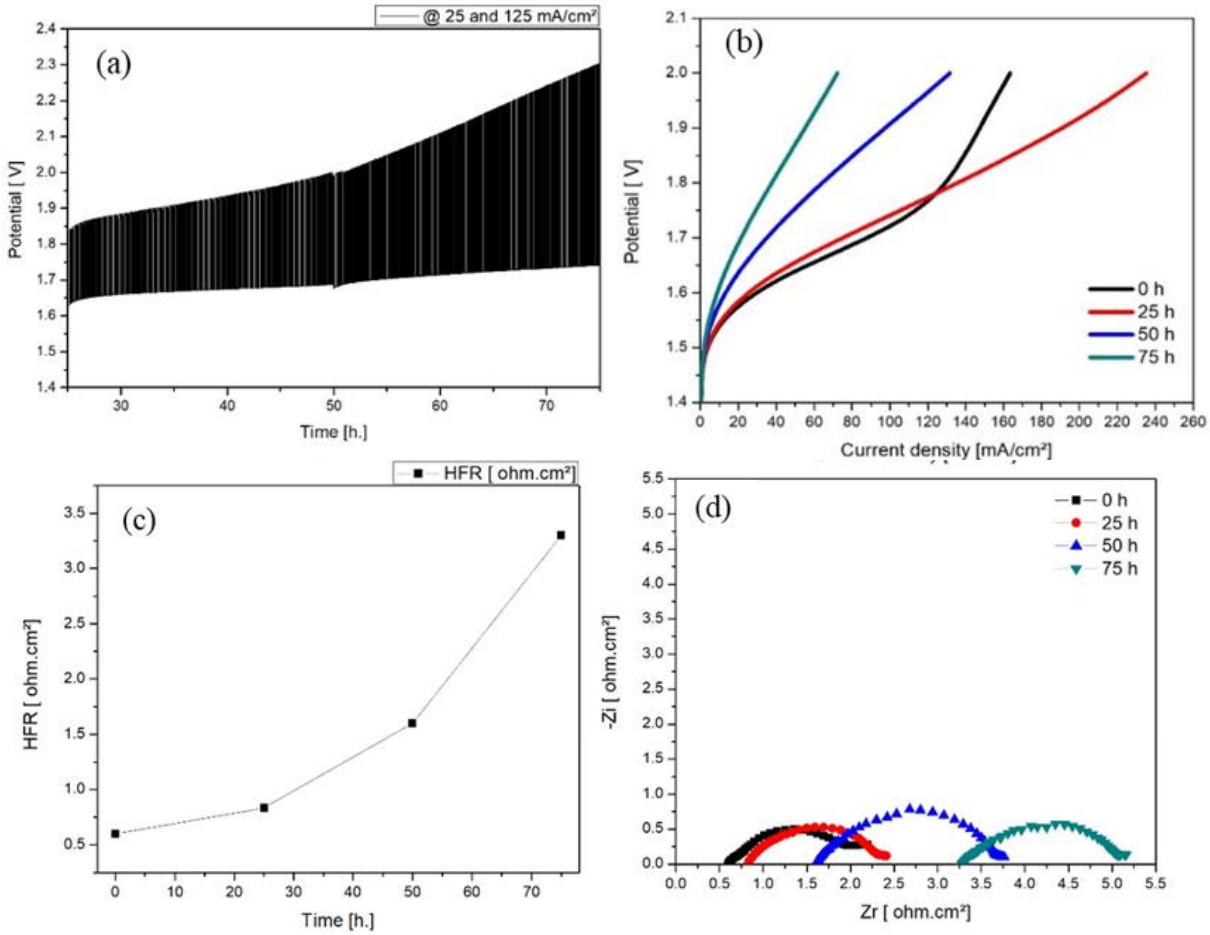


**Figure 5.42.** Electrochemical measurements on the three-layer membrane sandwich CCM. (a) The AST at 25/125 mA/cm$^2$ for 75 h; (b) iV curves; (c ) HFR vs time; and (d) EIS spectra during the AST. Measurements were performed at 60°C using atmospheric pressure, using cell n°1 with 2L flowfield.

After 75 h of AST, the CCM was removed from the cell, and the sandwich CCM was delaminated. Then the nanocomposite membrane was removed, and the two Nafion 212 membranes were clamped together in the cell without the nanocomposite membrane. Another AST cycle was applied. The iV curves and EIS spectra were recorded along the test. The two-layer CCM shows better electrochemical stability (in particular, there is no significant increase of the HFR during the additional 75 h of AST). The AST performance with and without the nanocomposite membrane are shown in **Figure 5.43-a** and **Figure 5.43-b**. The cell voltage was significantly increased with the nanocomposite membrane and became relatively stable after

removing the nanocomposite membrane. Furthermore, the HFR significantly reduced from 3.3 to 0.45 ohm.cm$^2$ after the removal of the nanocomposite membrane and was slightly increased to 0.5 Ω.cm$^2$ after the 145 h of AST. The iV curve improved once the nanocomposite membrane was removed.

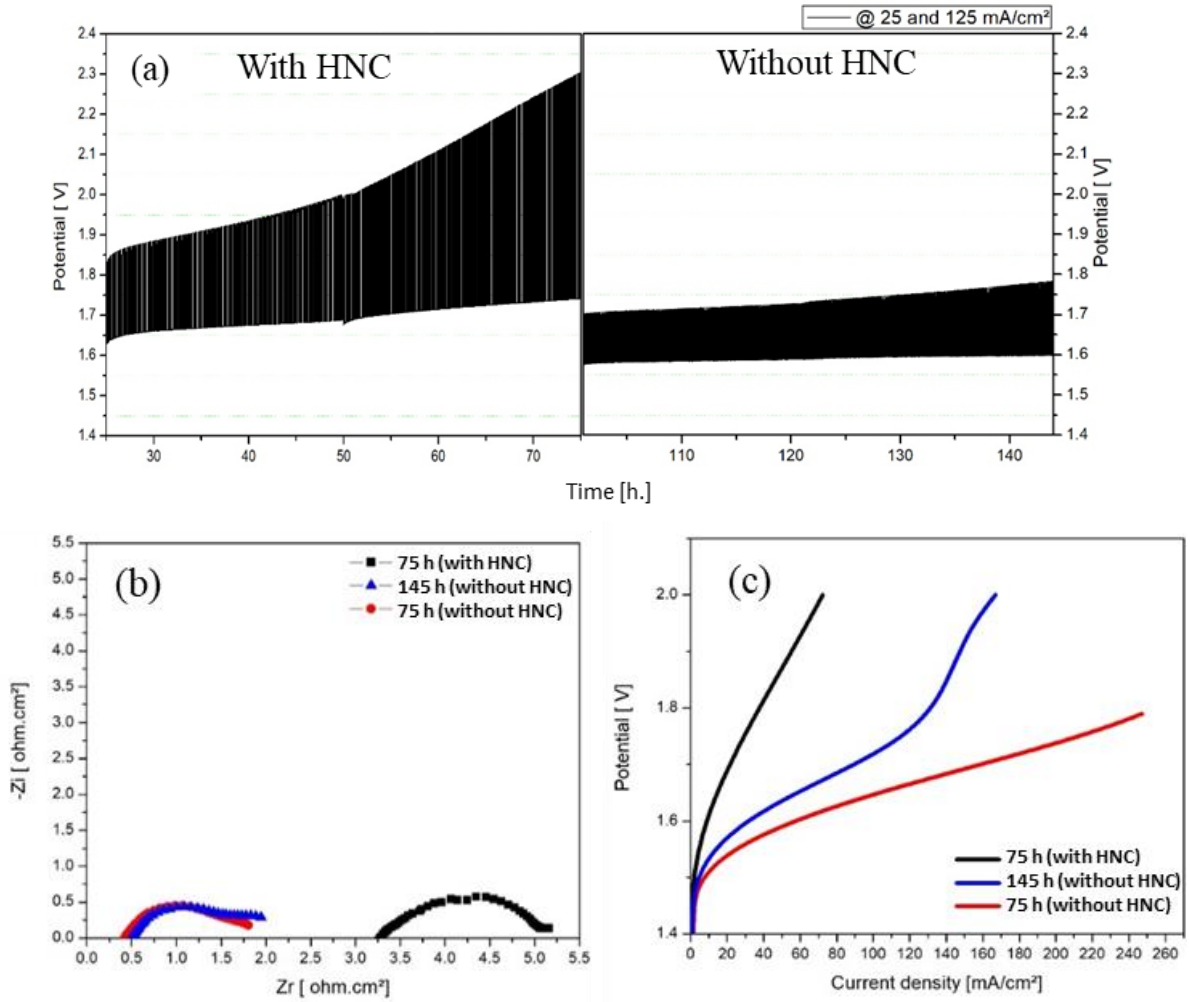


**Figure 5.43.** Comparison of the electrochemical measurements of the CCM with and without the HNC membrane (a-left) The AST of the CCM with HNC membrane at 125/25 mA/cm$^2$ for 75 h; (a-right) The AST of the CCM without HNC membrane at 125/25 mA/cm$^2$ for an additional 70 h; (b) EIS measurements and; (c) HFR vs time at specific times IV curves. Measurements were performed at 60°C using atmospheric pressure, using cell n°1 with 2L flowfield.

### 5.9.3. Conclusion

The attempt of crosslinking with gamma radiation of the nanocomposite membrane did not stop the degradation. A significant reduction of membrane conductivity is observed during electrolysis, indicating a loss of conducting sulfonic groups.

## 5.10. Conclusions

Using lab-scale experiments (CCM of a few cm$^2$), we have shown that the nanocomposite membrane is very sensitive to hydrolysis (both imine or enamine bonds are degraded). This leads to a loss of acid functions and to the rapid degradation of electrochemical performances. The only option left to extend the life service and make tests in cells of a larger surface area (as described in the following chapter) is to clamp the nanocomposite membrane between two PFSA membranes. This option was used in an attempt to scale-up and test the nanocomposite membrane in industrial conditions.

# Chapter 6. Scale-up and short stack testing in industrial environment

## 6.1. Objectives

Despite the stability problems encountered during the lab-scale experiments, the decision was taken to scale up and test the performance of the hybrid nanocomposite (HNC) membrane in the followings) using a 5-cell short stack (CCMs of circular shape, 250 $cm^2$ active area each). A special batch of membrane was produced: a thermal post-treatment (at 180 C for 2 hours) was used to further increase the cross-linking in order to increase stability. We then prepared four large areas CCMs (250 $cm^2$) in the laboratory at Paris-Saclay University and then tested them at Elogen company. The catalyst layers were deposited on Nafion 212 PFSA membranes by Decal transfer, and the HNC membrane was then clamped between the resulting two half-CCM. As discussed in the previous chapter, this was done mainly for two reasons: 1) to ensure that good quality and robust catalyst layers were obtained to maximize the duration of the tests; 2) to confirm that degradation leads to the release of silica nanoparticles and sulfonic compounds, as suspected. In this sandwich structure with three membranes pressed against each other, the silica nanoparticles and sulfonic compounds, which are larger in diameter than the water nanochannel of the Nafion membrane[78] are expected to be confined at the interfaces between the HNC and Nafion membranes. In order to also evaluate the role of catalyst loading on cell performance, the decision was also taken to build a so-called 'rainbow stack', i.e. a stack with different types of CCM inside for direct in-situ comparison. We, therefore, prepared three CCM with a sandwich structure (PtC/Nafion 212// HNC membrane //Nafion 212/$IrO_2$). In these three CCM, three types of catalyst loadings were used: low, medium and high (manufacturing details are provided in chapter 2). In this chapter, these CCM are referred to as **HNC-low, HNC-medium and HNC-high**, respectively. We also prepared one CCM made of two Nafion 212 as a reference (without HNC membrane, i.e. PtC/Nafion 212//Nafion 212/$IrO_2$) and referred to **Ref-lab**. Finally, a commercial Nafion-based CCM was also placed in the stack (PtC/Nafion115/$IrO_2$) and referred to as a **Ref-commercial**.

Details of the 5 different CCMs used in the 5-cell short stack **(Figure 6.1)**:

- Cell#1 : Pt-C / Nafion 212 // HNC membrane // Nafion 212 / $IrO_2$ (moderate catalyst loadings).
- Cell#2 (laboratory reference CCM) : Pt-C / Nafion 212 // Nafion 212 / $IrO_2$ (moderate catalyst loadings).
- Cell#3 (commercial reference CCM) : Pt-C / Nafion 115 / $IrO_2$ (high catalyst loadings).
- Cell#4 Pt-C / Nafion 212 // HNC membrane // Nafion 212 / $IrO_2$ (low catalyst loadings).
- Cell#5 : Pt-C / Nafion 212 // HNC membrane // Nafion 212 / $IrO_2$ (high catalyst loadings).

[78] Duan Q, Wang H, Benziger J. *Transport of liquid water through Nafion membranes*. J Memb Sci 2012;392–393:88–94. https://doi.org/10.1016/j.memsci.2011.12.004.

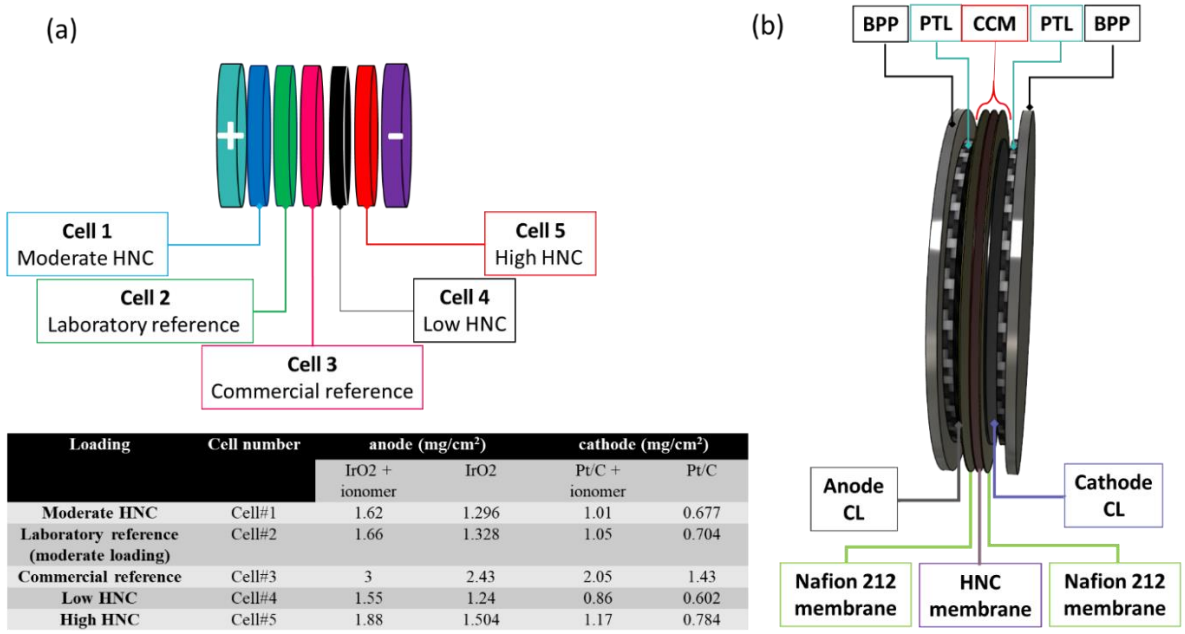


| Loading | Cell number | anode (mg/cm²) | | cathode (mg/cm²) | |
|---|---|---|---|---|---|
| | | IrO2 + ionomer | IrO2 | Pt/C + ionomer | Pt/C |
| Moderate HNC | Cell#1 | 1.62 | 1.296 | 1.01 | 0.677 |
| Laboratory reference (moderate loading) | Cell#2 | 1.66 | 1.328 | 1.05 | 0.704 |
| Commercial reference | Cell#3 | 3 | 2.43 | 2.05 | 1.43 |
| Low HNC | Cell#4 | 1.55 | 1.24 | 0.86 | 0.602 |
| High HNC | Cell#5 | 1.88 | 1.504 | 1.17 | 0.784 |

**Figure 6.1.** (a) schematic description of the 5-cell short stack used in the experiments; (b) 3D view of a unit cell.

## 6.2. Experimental details

Experimental details are discussed in section 2.8. First, the stack was installed on the test bench **(Figure 2.19),** and water was circulated for a few hours at a nominal flow rate and nominal temperature of 60°C to reach thermal equilibrium. The general methodology used is to combine a set of performance assessments (using appropriate key performance indicators or KPIs) and then an Aging Stress Test (AST). Performances are measured at the beginning of the test (BoT) and then periodically. The AST, which is defined according to the target application (e.g., stationary power, grid service power, PV-power, wind-power), is performed continuously and stopped periodically to re-assess the performance levels. By plotting the KPI as a function of time, it is possible to quantify the durability of cell components.

## 6.3. Performance analysis

### 6.3.1. Initial performance

Experimental results

The iV curves of each cell were measured at BoT: results are shown in **Figure 6.2-a**. Oscillations are due to the temperature regulation system of the test bench. Then EIS spectra and cyclic voltammograms (CVs) were measured on each cell: results are shown in **Figure 6.2-b**. Then a soft AST was applied to evaluate the performance stability of the different CCMs: current density was cycled between 25 and 250 mA/cm$^2$. A maximum cell voltage of 2.3 Volt was allowed. During the AST, if any of the cells reach that threshold value, the AST was stopped, and the max current density was reduced. This occurred twice: the max current density was reduced from 250 to 125 mA/cm$^2$ and then from 125 to 25 mA/cm$^2$.

Discussion

The iV curves of each cell measured at BoT (**Figure 6.2-a**) show quite significant differences.

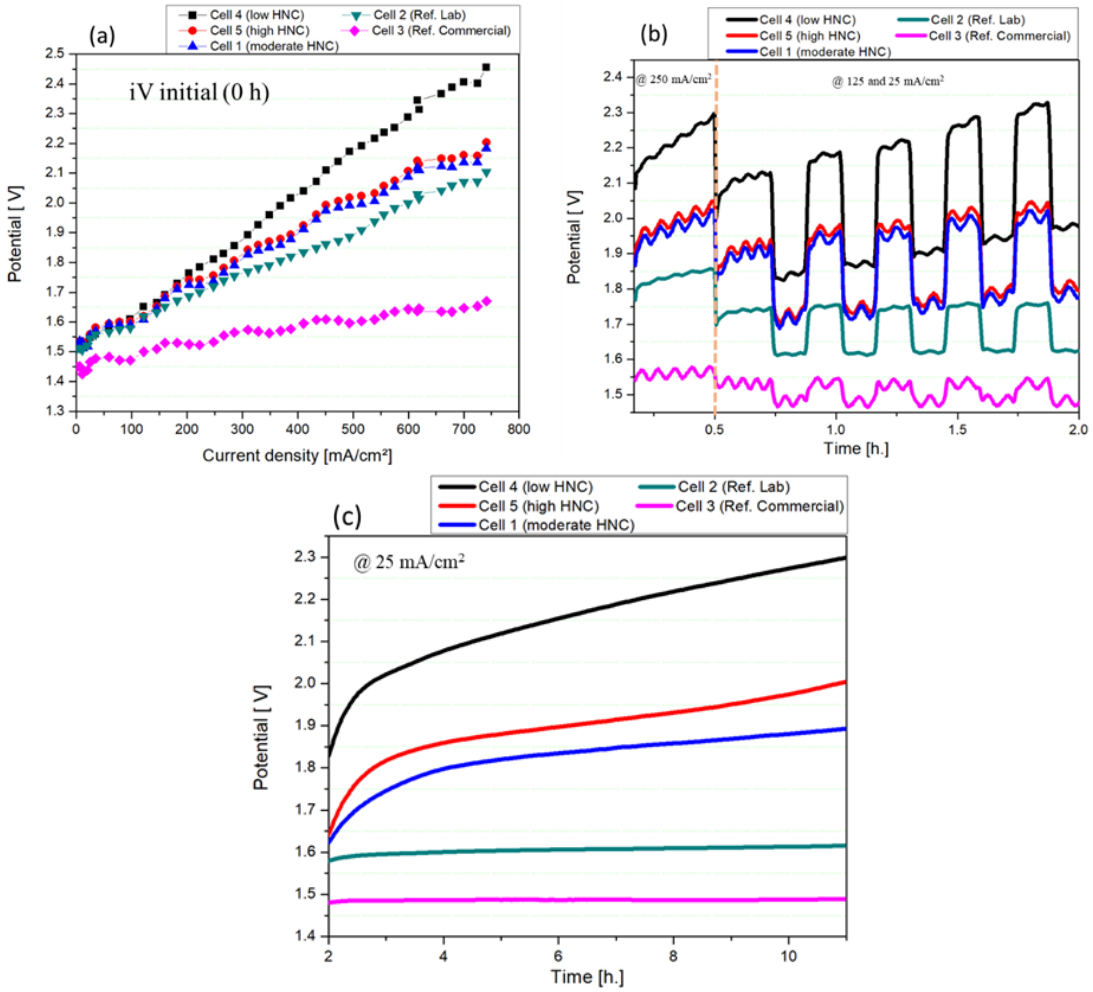


**Figure 6.2.** (a) iV curves at BoT = 0 h, (b) AST test at 250 and 125 mA/cm$^2$ and (c) chronopotentiometry test at 25 mA/cm$^2$ for 11 h.

The commercial reference CCM (cell#3) showed the best performance and stability (1.65 V @ 750 mA/cm$^2$). The laboratory reference CCM (2.1 V @ 750 mA/cm$^2$) despite the use of two thin Nafion 212, ie with a total membrane thickness lower than the thickness of the commercial reference with Nafion 115. Cell#1 and Cell#5 with the HNC membrane and medium/high catalyst loadings (2.2 V @ 750 mA/cm$^2$). Cell#4 (the one with HNC membrane and lowest catalyst loading), shows the highest cell potential (2.45 V @ 750 mA/cm$^2$). The variation of individual cell voltages during the first 2-hours of the AST are shown in **Figure 6.2-b**. During that period, the voltage of cell#4 continued to increase quickly compared to other cells. After only 30 minutes, Cell#4 hit the max voltage of 2.3 Volt, and the max current density was reduced from 250 to 125 mA/cm$^2$. The test continued for only 1.5 additional hours before reaching 2.3 V again. The top current density was then further reduced from 125 to 25 mA/cm$^2$ for an additional 9 h, after switching from current cycling to chronopotentiometric mode. The total duration of the stability test was 11h.

During this first AST, both laboratory-made and commercial reference CCM were electrochemically stable. However, the performance of the three HNC-based CCM rapidly declined and then reached a linear degradation rate. The situation prevailing after 9 hours of chronopotentiometry at 25mA/cm$^2$ was assessed by recording the iV curve (**Figure 6.2-c**) :

- Cell#1 (moderate HNC): considerable cell voltage increase of 263 mV (from 1.63V to 1.893 V).
- Cell#2 (laboratory reference): slight cell voltage increase of 31 mV (from 1.585V to 1.616 V).
- Cell#3 (commercial reference): non-significant cell voltage increase; only 5 mV (from 1.484V to 1.489 V).
- Cell#4 (low HNC): highest cell voltage increase of 460 mV (from 1.84V to 2.3 V).
- Cell#5 (high HNC): large cell voltage increase of 355 mV (from 1.65V to 2.005 V).

The CV and EIS spectra (**Figure 6.3**) of each cell was measured after 11 h of the stability tests to determine the reason for cell voltage increases. The EIS spectra have different features (in the followings, HF = high frequency and LF = low frequency). The commercial reference has only one time-constant (one semicircle) and a reduced HF resistance. No change was observed during the AST. The four other cells have two time-constants and high HF-resistances. After 11 hours of AST, the LF resistance of the laboratory resistance is almost unchanged. However, those of the three CCM equipped with the HNC membrane significantly increased (**Figure 6.3-b**). The largest increase was measured on cell#4 (low catalyst loading), a result consistent with the data of **Figure 6.2**. This LF resistance increase was moderate for cell#5 and cell#1, and an insignificant change was measured on cell#2.

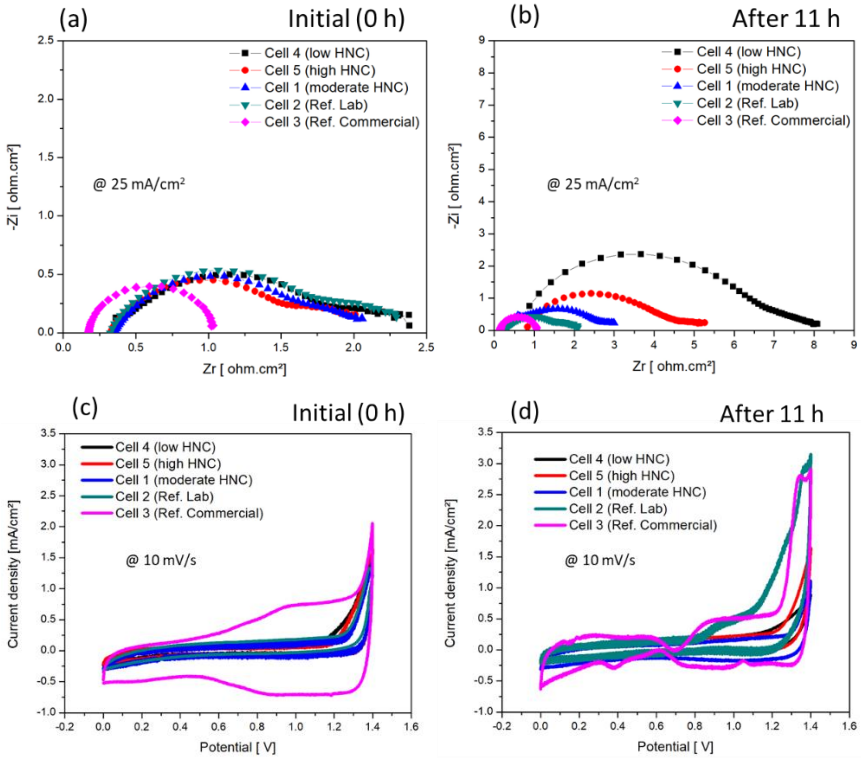


**Figure 6.3.** EIS measurements of the 5 CCMs at 10 mA/cm$^2$ after (a) 0 hours, (b) 11 hours of AST. Cyclic voltammograms measured at scan rates of 10 mV/s, after (c) 0 hours, and (d) 11 hours of AST.

Then the cyclic voltammograms of each cell were measured as discussed in the experimental section (Chapter 2), and the specific areal capacitances (Cs) of the CCMs, before and after the stability test, were determined. Results are compiled in **Table 6.1**. Except for the commercial reference (cell#3), the Cs of the four lab-made CCMs increased, during the AST. This is attributed to catalyst activation and demonstrates that no catalyst loss occurred during the test.

**Table 6.1.** Specific areal capacitance values measured at different times (scan rate is 10 mV/sec.)

| | $C_s$ (mF/cm$^2$) | | |
|---|---|---|---|
| **Time** | **0 h** | **2 h** | **11 h** |
| Cell#1 (HNC-moderate) | 9.5 | 11.3 | 13.5 |
| Cell#2 (Ref-Lab) | 11.0 | 21.1 | 23.8 |
| Cell#3 (Ref-commercial) | 49.6 | 28.6 | 34.0 |
| Cell#4 (HNC-low) | 9.5 | 10.7 | 10.8 |
| Cell#5 (HNC-high) | 9.7 | 11.3 | 14.5 |

Cs values tend to slightly increase except for cell#3. The shape of the CV after 11h shows $IrO_2$ contamination but the impact on the iV curve was limited.

Besides these electrochemical results, a rapid increase in the ionic conductivity of the water in circulation on the cathode circuit was observed. Even before applying any current to the stack, the water conductivity of the cathode side increased up to 12 µS/cm (**Figure 6.4**). This means that there are impurities released by the stack and their concentration exceed the absorption capacity of the ion exchange resin put on line.

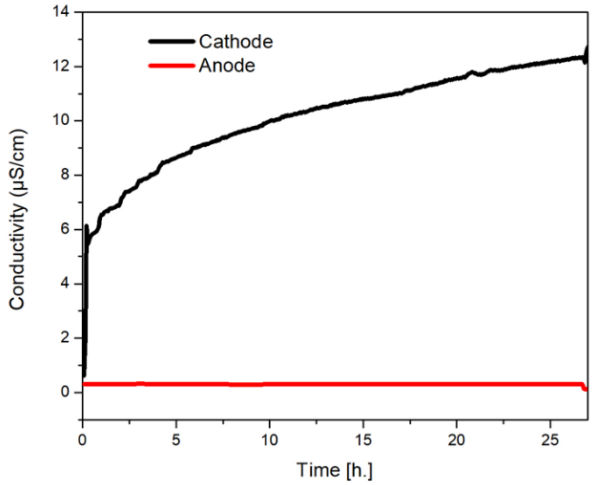


**Figure 6.4.** Plot of the ionic conductivity of circulated water in cathode and anode before any electrochemical measurements.

We suspect that this increase of ionic conductivity is due to the HNC membranes, which leak impurities into the circulated water. The total organic carbon (TOC) and water conductivity were measured on the circulated water collected after 11 hours of AST (**Figure 6.5**). Significant increases in the TOC in both anode and cathode circuits confirm the presence of organic material originating from the stack. The level of contamination is higher on the cathode side. This is probably due to the electro-osmotic flow of water across the membranes, which transport impurities to the cathode compartment; therefore, most impurities follow the ionic conduction and are collected at the cathode side.

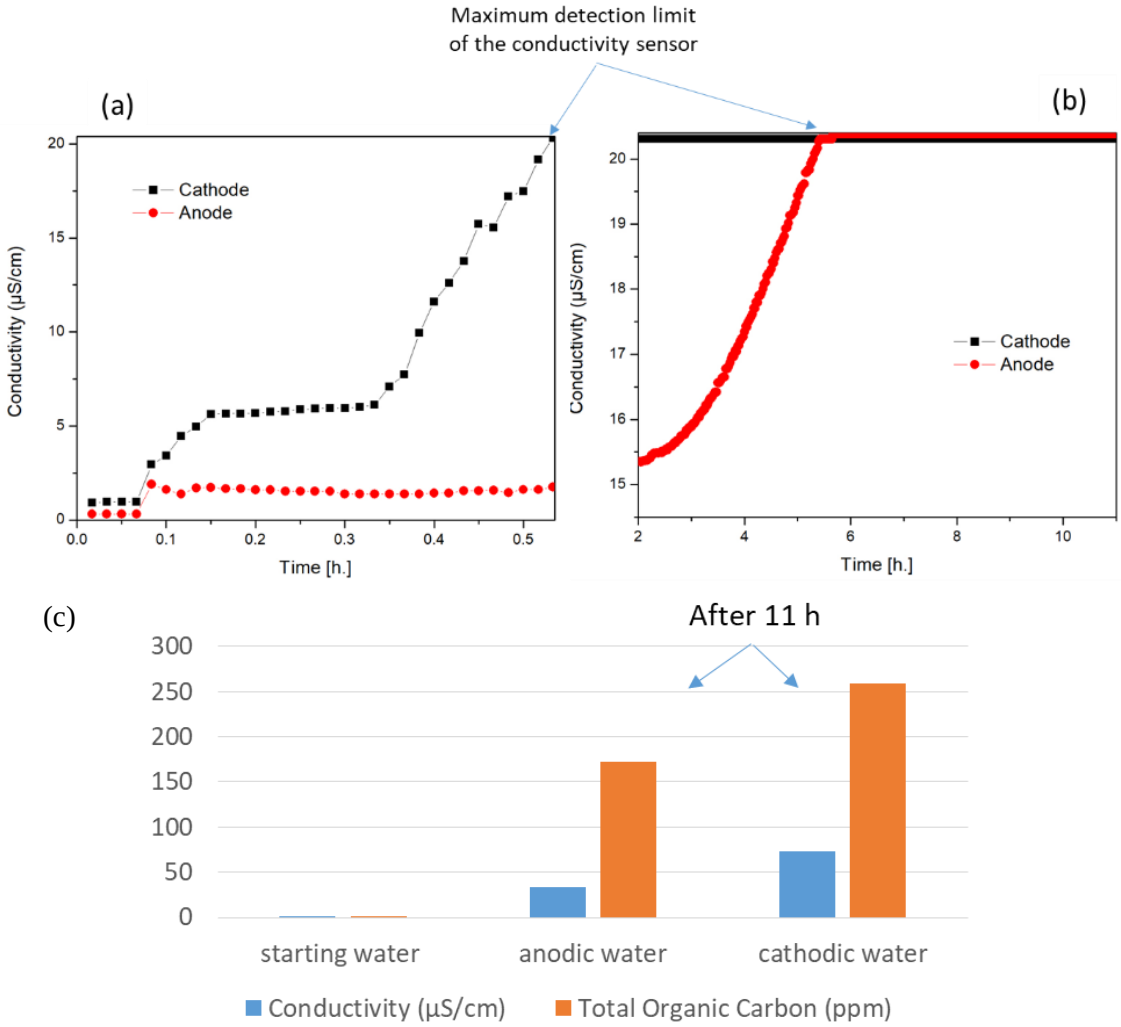


**Figure 6.5.** The conductivity of circulated water in cathode and anode during the 11- hours long stability test, (a) measured between 0 and 0.5 h, (b) between 2 and 11 hours, and (c) water conductivity and total organic carbons before and after 11 h of stability test.

We then decided to extract the HNC membranes from cell#4 and cell#5 while keeping it in cell#1 (the best performing one). The stack was dismantled, the HNC membranes were removed from the sandwich cells, the Nafion 212 half CCM were then re-pressed against each other and remounted in the stack to continue electrochemical analysis with 5 cells. When the stack was opened, the presence of droplets of a yellow liquid was observed on the bipolar plate (**Figure 6.6**). This liquid had a pH of ≈ 2 (acidic) and an ionic conductivity of 1204 µS/cm, which is 4000 times higher than initial water before electrolysis (0.3 µS/cm). The excess water was removed from the collected yellow liquid using the rotary evaporator, and a polymeric resin film was deposited on the wall of the glass flask. After scratching the polymeric films, an amount of 400 mg was obtained.

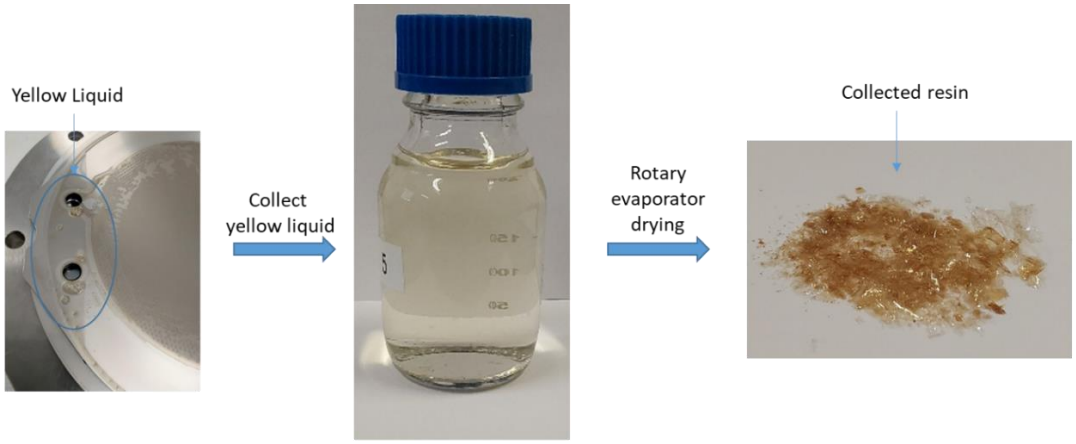


**Figure 6.6.** Collection and treatment of yellow liquid from the stack and rotary evaporation drying after 11 hours of AST.

Furthermore, the HNC membranes that were removed from the stack (cell#4 and cell#5) were characterized. The as-received HNC membrane has the following characteristics: areal density of 1105 mg/100 $cm^2$ and IEC of 1.8 meq/g. The HNC membrane extracted from cell#4 has an areal density of 820 mg/ 100 $cm^2$ (25.8% less than the initial weight). Its IEC (measured by titration) was 1 meq/g (45% less than the initial value). The HNC membrane extracted from cell#5 has a density of 840 mg/ 100 $cm^2$ (24% weight less than the initial value), and an IEC of 0.91 meq/g (50% less than the initial value). The HNC membrane in cell#5 was flatter and less wrinkled (**Figure 6.7-b**) and had an acceptable ionic contact with the Nafion 212 membrane, which may accelerate IEC losses. However, the HNC membrane in cell#4 was found wrinkled (**Figure 6.7-a**), had poor ionic contact and conductivity, retained more protonic organic groups inside and had a slighter higher IEC than HNC-5.

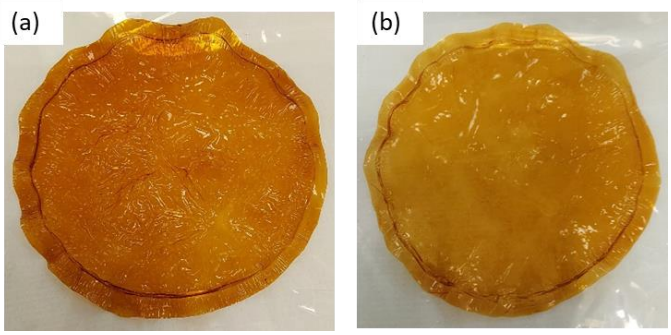


**Figure 6.7.** Photographs of HNC membranes extracted from the 5-cell short stack after 11 hours of AST: (a) cells#4 ; (b) cell#5.

A qualitative analysis tells that the color is different (cell#5 is paler) which is it consistent with the fact that this cell has lost more ionic functions.

The chemical modifications of the HNC membrane induced by electrolysis were determined by comparing the FT-IR spectra before and after electrolysis (**Figure 6.8**). The "as-received" HNC membrane contains two phases: (i) PVDF-HFP (host matrix) and (ii) the $SiO_2$-grafted PSSA (ionic conducting phase).

*Characteristic FT-IR peaks of PVDF-HFP*[79,80,81]

The crystalline α-phase was identified in the FT-IR spectrum of PVDF–HFP by the vibrational bands observed at 760, 790, 973, and 1210 $cm^{-1}$. Furthermore, the crystalline β-phase of PVDF-HFP was assigned at 870 $cm^{-1}$. The $CH_2$ bond wagging was detected at 1380 $cm^{-1}$, corresponding to the vinylidene group of the host polymer.

*Characteristic FT-IR peaks of PSSA*[82,83,84]

The FT-IR spectrum of PSSA is characterized by the presence of the benzene ring. The out-of-plane bending of C−H in a 1,4-substituted benzene ring was assigned at 664 $cm^{-1}$. Meanwhile, the C-H wagging and bending were observed at 775 and 830 $cm^{-1}$, respectively. The in-plane deformation of the benzene ring was detected at 1004 and 1031 $cm^{-1}$. The presence of O=S=O vibration stretching at 1125 and 1210 $cm^{-1}$ is specific to the sulfonic groups of the PSSA.

There is an overlapping between the O=S=O stretching of the PSSA and the vibrational band of crystalline α-phase PVDF-HFP at 1210 $cm^{-1}$. The summery of the FT-IR peaks of PVDF-HFP and PSSA are shown in **Table 6.2.**

**Table 6.2.** Characteristic IR features of PVDF-HFP and PSSA.

| Wavenumber ($cm^{-1}$) | PVDF-HFP | Wavenumber ($cm^{-1}$) | PSSA |
|---|---|---|---|
| 762, 794, 974, 1210 | crystalline α-phase of PVDF-HFP | 664 | bending of C−H in 1,4-substituted benzene ring (out-of-plane) |
| 871 | crystalline β-phase PVDF-HFP | 775 | C−H wagging |
| 1068 | -C-C- bending | 830 | C-H bending |
| 1180, 1278 | -$CF_2$- bending | 1004, 1031 | deformation in aromatic ring (in-plane) |
| 1383 | -$CH_2$- bond wagging | 1123, 1210 | O=S=O stretching |

[79] L. Y, M. N, P. AS, H. V, M. B, Dwivedi J, et al. *Optical properties and ionic conductivity studies of an 8 MeV electron beam irradiated poly(vinylidene fluoride- co -hexafluoropropylene)/$LiClO_4$ electrolyte film for opto-electronic applications.* RSC Adv 2018;8:15297–309. https://doi.org/10.1039/C8RA00970H.

[80] Feng Y, Li WL, Hou YF, Yu Y, Cao WP, Zhang TD, et al. *Enhanced dielectric properties of PVDF-HFP/$BaTiO_3$-nanowire composites induced by interfacial polarization and wire-shape*. J Mater Chem C 2015;3:1250–60. https://doi.org/10.1039/C4TC02183E.

[81] Parangusan H, Ponnamma D, Al-Maadeed MAA. *Stretchable Electrospun PVDF-HFP/Co-ZnO Nanofibers as Piezoelectric Nanogenerators*. Sci Rep 2018;8:754. https://doi.org/10.1038/s41598-017-19082-3.

[82] Braglia M, Ferrari IV, Djenizian T, Kaciulis S, Soltani P, Di Vona ML, et al. *Bottom-Up Electrochemical Deposition of Poly(styrene sulfonate) on Nanoarchitectured Electrodes*. ACS Appl Mater Interfaces 2017;9:22902–10. https://doi.org/10.1021/acsami.7b04335.

[83] Lei Y, Luo Y, Chen F, Mei L. *Sulfonation Process and Desalination Effect of Polystyrene/PVDF Semi-Interpenetrating Polymer Network Cation Exchange Membrane*. Polymers (Basel) 2014;6:1914–28. https://doi.org/10.3390/polym6071914.

[84] Fathy M, Abdel Moghny T, Awad Allah AE, Alblehy A. *Cation exchange resin nanocomposites based on multi-walled carbon nanotubes*. Appl Nanosci 2014;4:103–12. https://doi.org/10.1007/s13204-012-0178-5.

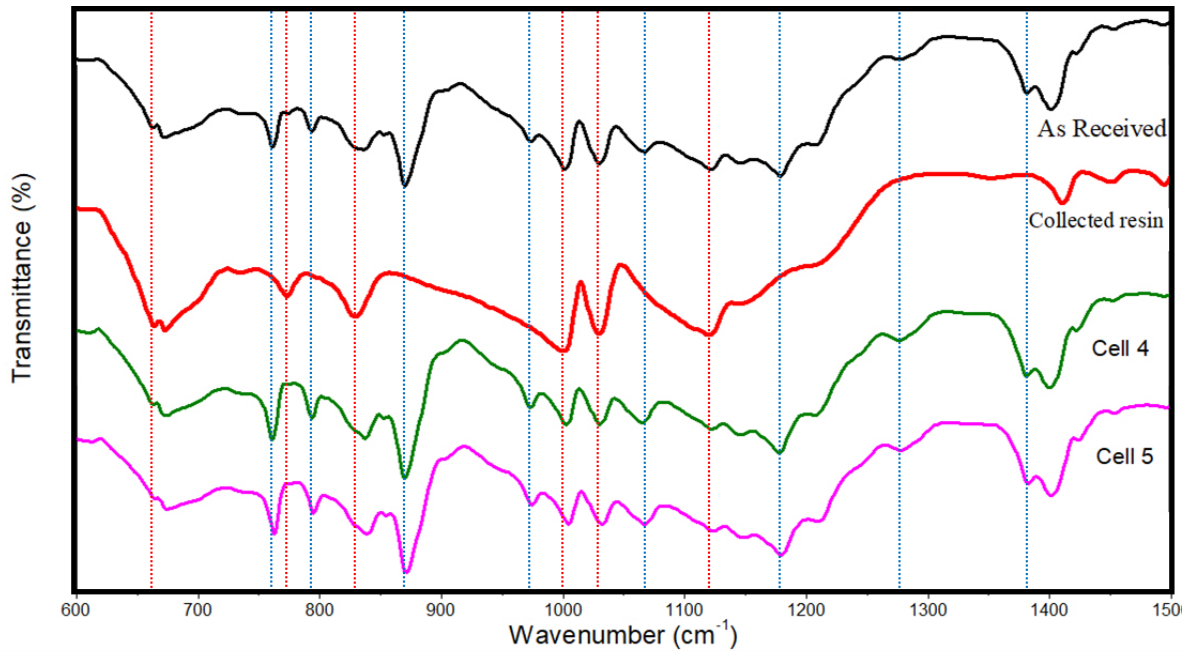


**Figure 6.8.** FT-IR spectra of : (black) "as-received" HNC membrane; (red) the collected resin; (green) HNC membrane from cell#4; (pink) HNC membrane from cell#5. The (blue) dots lines mark the characteristic peaks of PVDF-HFP. The (red) dots lines mark the distinct peaks of PSSA.

Because there are only < 50% losses in the IEC of the nanocomposite membrane obtained from cell#4 and cell#5, both PVDF-HFP and PSSA peaks were observed. However, a slight reduction in the PSSA peak intensity is observed on aged membranes.

The EDS analysis of the hybrid nanocomposite membranes (**Figure 6.9**) was performed to detect elements of the membranes and to compare with the collected resin (obtained from yellow liquid after rotary evaporator drying). The collected resin mainly shows carbon, oxygen and sulfur elements, while fluorine traces are barely within the detection limit of the EDS. The EDS spectra also shows some cation exchange of Na and K that may be originated from the circulated water used during electrolysis. Polystyrene sulfonate was known for its absorption capability for cation. The EDS results show that the "as-received" HNC membrane has an initial sulfur-to-fluorine ratio of 1:10.6, which increased to 18.3 and 20.7 for the membranes collected from cell#4 and cell#5, respectively. The sulfur content was reduced by 42 and 48.8 % in the HNC membranes of cell#4 and cell#5. This result is in agreement with FTIR and IEC measurements.

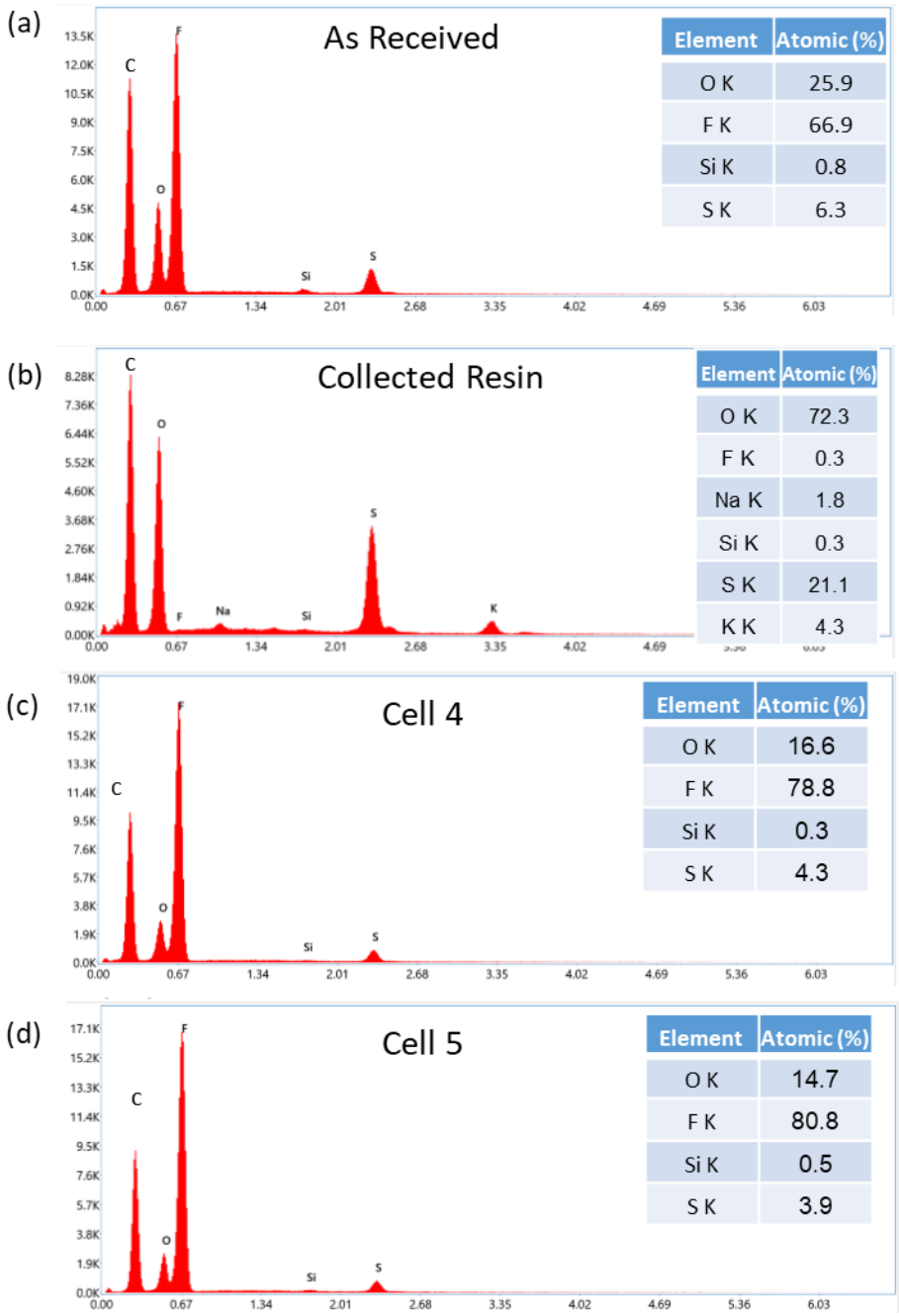


**Figure 6.9.** EDS data of (a) "as-received HNC membrane; (b) collected resin; (c) HNC membrane from cell#4 and (d) from cell#5. Insert tables represent elemental composition measured by EDS.

Conclusion

Despite excellent initial performance levels, these different results clearly show that the membranes are not chemically stable in PEM water electrolysis conditions. The test was continued with the remaining HNC membrane in cell#1.

### 6.3.2. Performance after extraction of HNC membranes from cell 4 and 5

Once the HNC membranes of cell#4 and cell#5 were removed, the stack was clamped again and run at 25 mA/cm$^2$ for an additional 59 h (hence a total stability test of 70 h). As shown in **Figure 6.10**, the voltage of cell#4 and cell#5 is still high but stable after the HNC membranes have been removed. Cell#1, the only remaining cell with a HNC membrane, shows an increase in potential, indicating a continuous degradation in the cell performance.

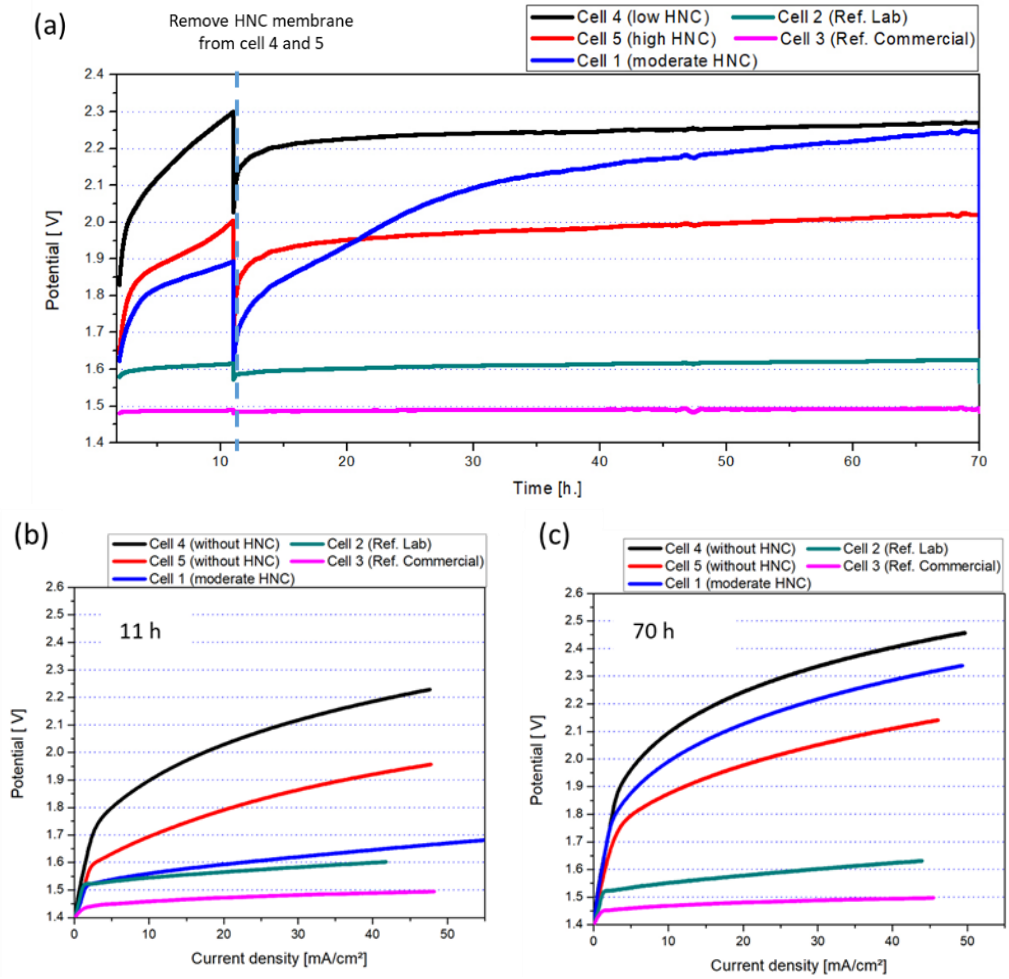


**Figure 6.10.** (a) chronopotentiometry of the 5 CCMs at 25 mA/cm$^2$; iV curves after (b) 11 h, and (c) 70 h of AST.

After having removed the HNC membrane from cell#4 and cell#5, the contaminated water of both the anode and cathode circuits was replaced with a fresh one. Also, the only ion-exchange resin was replaced by a fresh one. It was then observed that the water conductivity at the cathode side still increased (**Figure 6.11**), leading us to the conclusion that the HNC membrane still present in cell#1 was also leaking contaminants into the feed water.

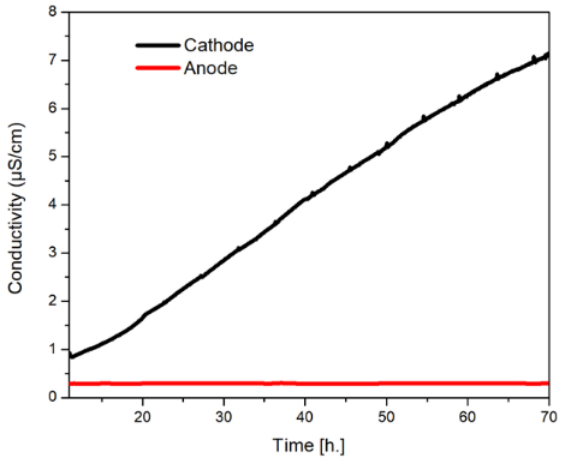


**Figure 6.11.** Plots of the ionic conductivity of water circulated in the cathode and anode circuits during the AST from 11 to 70 h.

### 6.3.3. Washing and tightening the stack

The stack was then removed from the test bench and rinsed with deionized water for 15 minutes to wash the CCMs and remove any accessible impurities. The stack was then clamped at a higher pressure to improve contact between components and reduce the internal cell resistance. The HFR and the diameter of the high-frequency semicircles of cell#1 and cell#5 both decreased, but only a slight reduction was obtained for cell#1 (**Figures 6.12-a, b**). The iV curves measured on the re-tightened stack (**Figures 6.12 c,d**) show a reduction of the onset potential in cells 1, 4 and 5, indicating an improvement of cell performance.

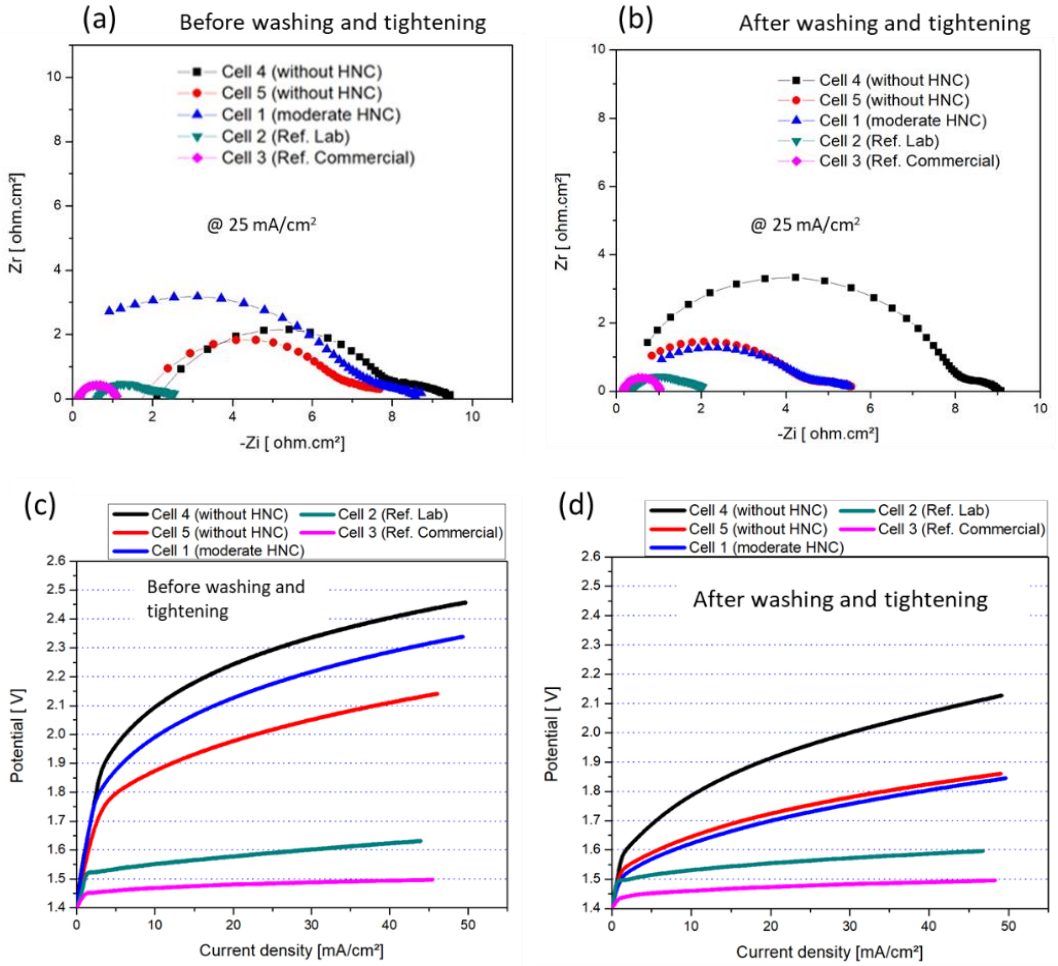


**Figure 6.12.** EIS measurements of the 5 CCMs at 10 mA/cm$^2$ (a) before, (b) after washing and tightening. iV curves of the CCMs (c) before and (d) after washing and tightening.

### 6.3.4. Chronopotentiometry extended to 225 h

The full chronopotentiometry test is shown in **Figure 6.13**. The voltage of cell#1 is not stabilized and continues to increase even if the rate of increase is much less than the one measured before on cell#4 and cell#5. The voltage of cell#4 (once the HNC membrane was removed) slightly increased at the beginning but remained constant at 2.25 V till the end of the test.

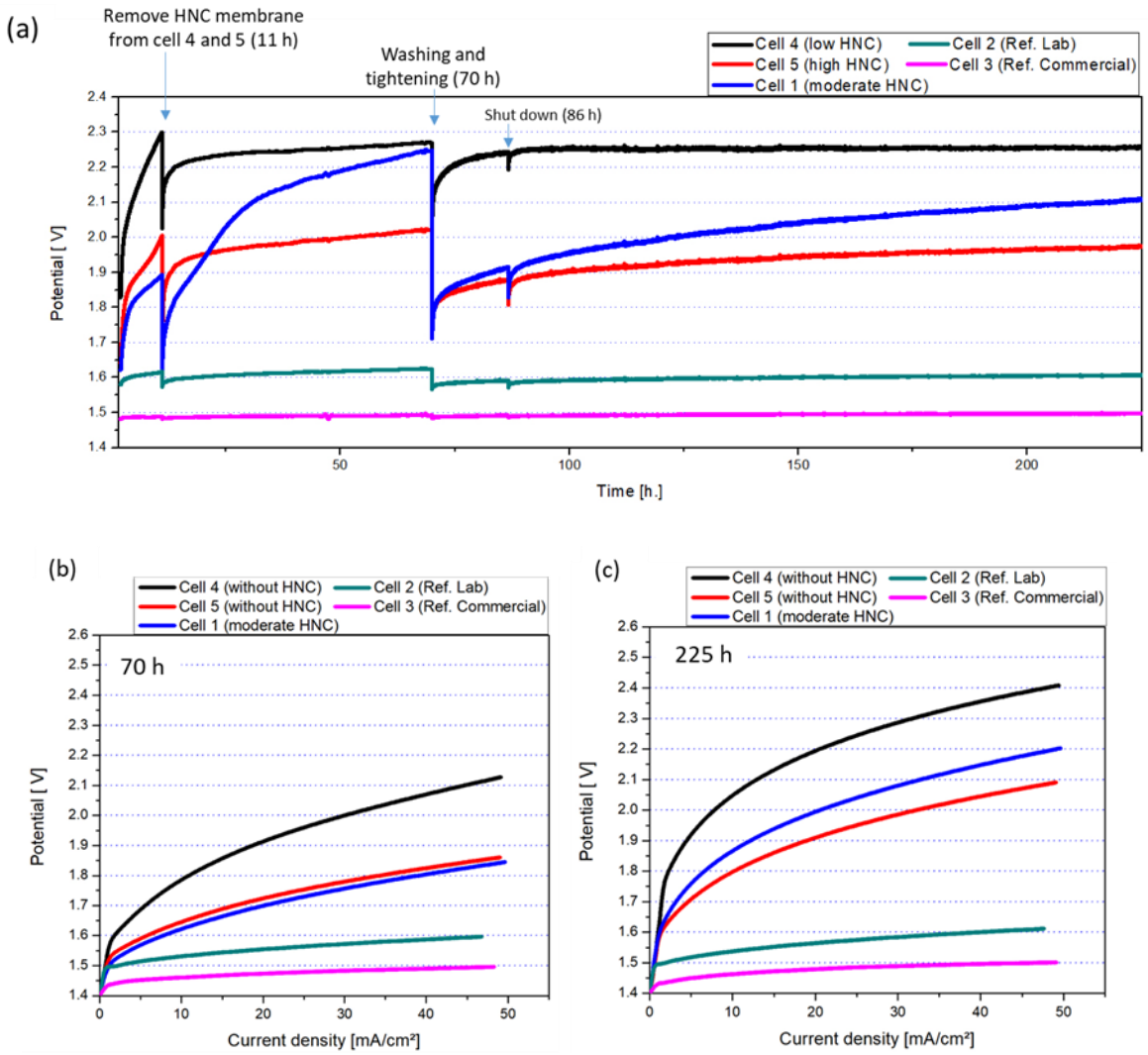


**Figure 6.13.** (a) chronopotentiometry of the 5 CCMs at 25 mA/cm$^2$; iV curves after (b) 70 h, and (c) 225 h of AST.

In agreement with the chronopotentiometry and iV measurements, the EIS spectra (**Figure 6.14 a,b)** confirm that the resistivity of cell#1 is higher after 225 h (larger diameter of the 1$^{st}$ semicircle). Both reference CCMs (lab and commercial) are relatively stable compared to CCMs with the HNC membrane. The CVs (**Figures 6.14-c,d**) show an increase of Cs for the 4 lab-made CCMs, especially the Ref-Lab (cell#2) CCM with the highest Cs of 36.9 mF/cm$^2$, very close to the Ref-Commercial CCM, which had Cs of 38 mF/cm$^2$ (**Table 6.3**).

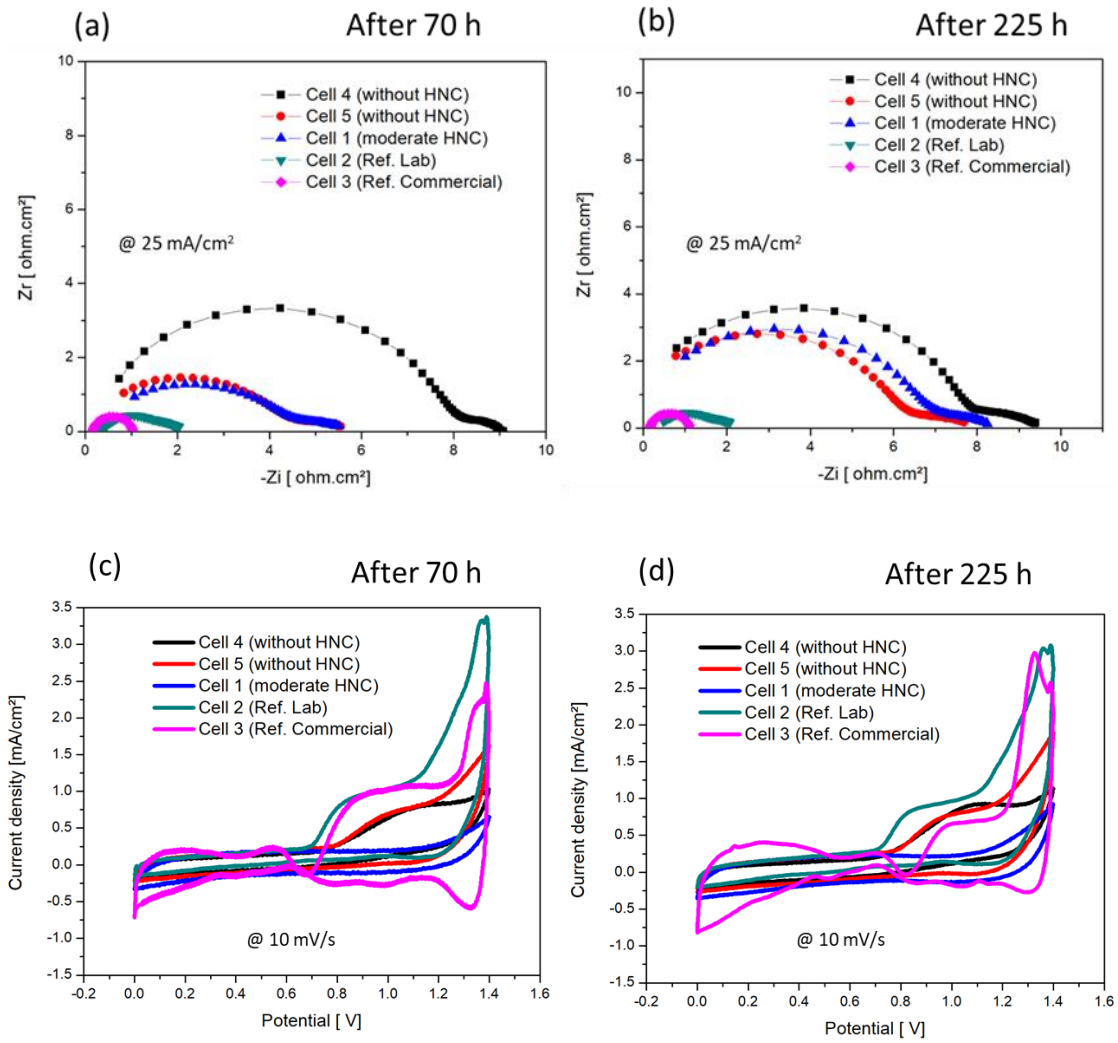


**Figure 6.14.** EIS measurements of the 5 CCMs at 10 mA/cm$^2$ after (a) 70 hours, (b) 225 hours, cyclic voltammograms of the CCMs were measured at scan rates of 10 mV/s, after (c) 70 hours, and (d) 225 hours.

**Table 6.3.** Specific areal capacitance values of the CCMs measured at a scan rate of 10 mV/sec at different times of the AST.

| | **Specific areal capacitance (mF/cm$^2$)** | | |
|---|---|---|---|
| **Time** | **11 h** | **70 h** | **225 h** |
| Cell#1 (moderate-HNC) | 13.5 | 14.4 | 18.6 |
| Cell#2 (Ref-Lab) | 23.8 | 32.3 | 36.9 |
| Cell#3 (Ref-commercial) | 34.03 | 40.6 | 38.2 |
| Cell#4 (Low-HNC) | 10.8 | 15.5 | 19.1 |
| Cell#5 (High-HNC) | 14.5 | 20.92 | 25.7 |

At the end of the electrochemical characterization, the stack was opened, and the last HNC membrane was removed from cell#1. Similar to cells 4 and 5, a yellow liquid was observed (**Figure 6.15-a**) trapped at the interface between the HNC and Nafion 212 membranes. However, the amount of powder collected after removing excess water was only 62 mg. We suspect that most of the organic impurities released by the HNC membrane leaked through the Nafion membrane's pores during the stability test.

The surface of the HNC membrane was almost flat (**Figure 6.15-b**) and had good ionic contact with the Nafion 212 membrane, which explains the better performance of cell#1 compared to cell#4 and cell#5. The HNC membrane of cell#1 had a very low IEC of less than < 0.1 meq/g, 95% less than the initial IEC. Furthermore, this membrane's areal density was 618 mg/ 100 $cm^2$ which is 44 % less than the initial density value. These results confirm the loss of conductive sulfonic groups in the HNC membrane during electrolysis.

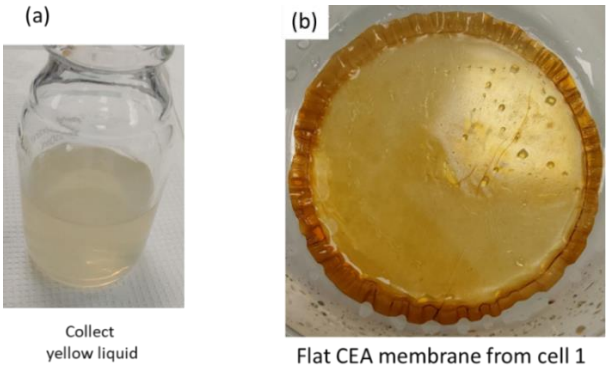


**Figure 6.15.** (a) the collected yellow liquid from cell#1 and (b) the flat HNC membrane extracted from cell#1 after 225 h of stability tests.

FT-IR spectra of the HNC membrane of cell #1 (**Figure 6.16**) reveal a complete absence of the characteristic PSSA peaks; only the pure PVDF-HFP peaks are observed. This result is in agreement with the IEC titration measurements, which also show that an insignificant amount of sulfonic groups remains present in the HNC membrane at the end of the test.

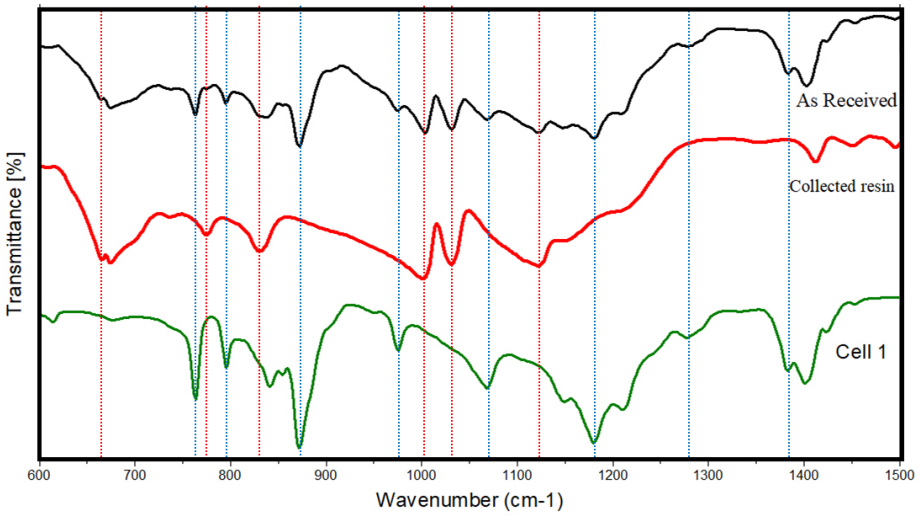


**Figure 6.16.** FT-IR spectra of: (black) "as-received" HNC membrane; (red) the collected resin; (green) the HNC membrane of cell#1. The (red) dots lines mark the distinct peaks of PSSA. The (blue) dots lines mark the characteristic peaks of PVDF-HFP.

The EDS measurements were done to further characterize the HNC membrane extracted from cell#1 (**Figure 6.17**). The As-received membrane has an initial sulfur-to-fluorine ratio of 1:10.6. while, the membrane collected from cell#1 shows an atomic ratio of sulfur to fluorine of 1:234.5, which is 22 times less than the original value (equivalent to a 95.5% reduction). The oxygen content decreased dramatically as a result of losing sulfonic groups.

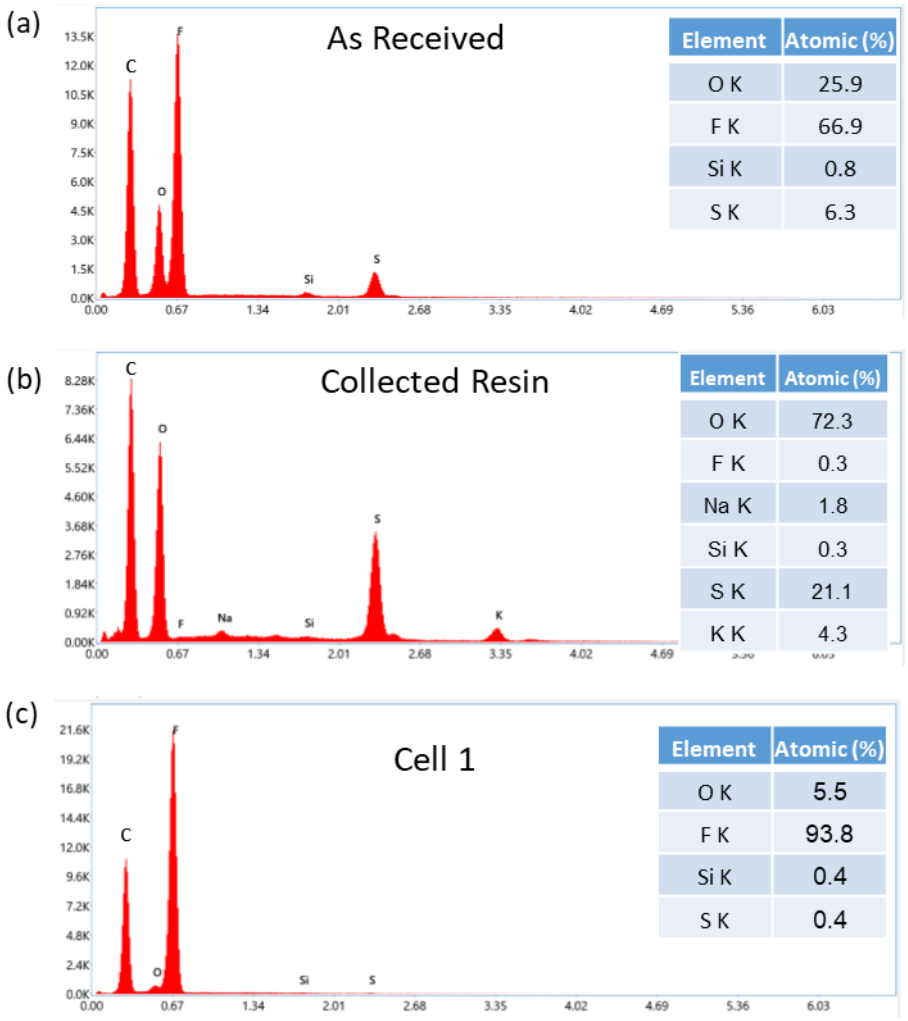


**Figure 6.17.** EDS analysis of (a) as-received HNC membrane; (b) collected resin, and (c) HNC membrane collected from cell#1. Insert tables represent elemental composition measured by EDS.

## 6.4. Detailed cell-by-cell electrochemical characterization

In this section, we present a more detailed analysis of the different CCMs used in the 5-cell stack to highlight the behavior of the HNC membranes compared to the selected references.

### 6.4.1. Commercial reference CCM (Cell#3)

We start with an analysis of our commercial reference :
cell#3 (commercial reference CCM): Pt-C / Nafion 115 / $IrO_2$ with high catalyst loadings.

Chronopotentiometry

The stability of the commercial reference (cell#3) was assessed by using a chronopotentiometry test at a constant current density of 25 mA/cm$^2$. This is of course a low current density but since this is the maximum one which could be used with the HNC membrane, this value was selected to have a baseline in similar operating conditions. The test lasted for 225 hrs. Results are shown in **Figure 6.18**.

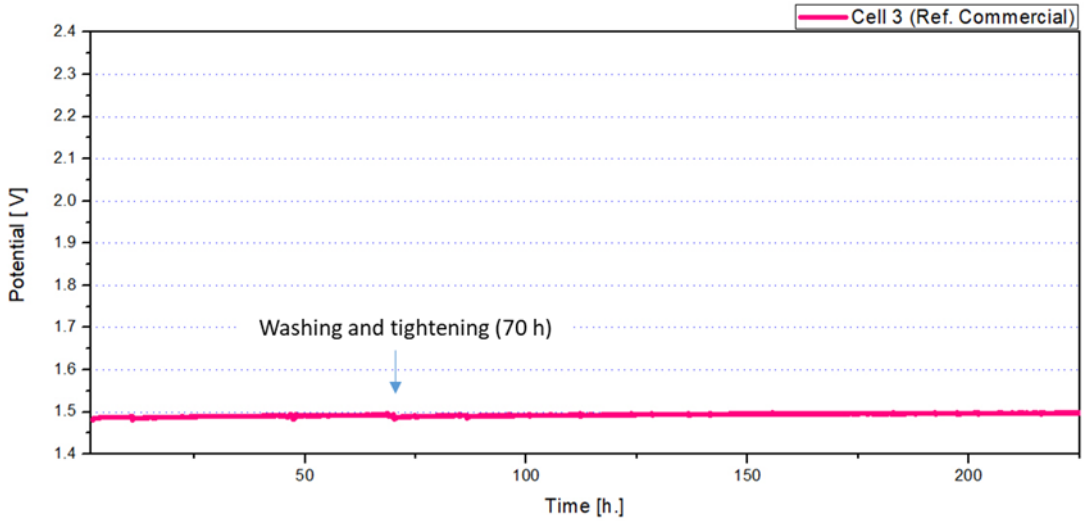


**Figure 6.18.** Chronopotentiometry of cell#3 at 25 mA/cm$^2$ for 225 h.

The loss of performance was very limited during the test. A 10 mV cell voltage increased (from 1.485 to 1.495 V) was measured up to 70 hours of AST. After washing with fresh DI water and tightening adjustments, the cell voltage was reduced down to 1.484 V and then increased by 14 mV (1.498 V) after 225 hours. Therefore, it was concluded that under such conditions, the commercial reference CCM was stable and could be used as an in-situ stability reference.

Cyclic Voltammograms (CV)

The CVs measured on the commercial reference, using the cathode as a reference, are shown in **Figure 6.19**. They were used as a simple test to determine the coulombic charge per cm$^2$ of the active area, an indirect measure of the concentration of electrochemical reaction sites in contact with the polymer electrolyte at the anode and participating to the electrochemistry of the cell (see details in the experimental chapter n°2). The shape of the curves clearly shows the presence of impurities adsorbed on the surface of the iridium oxide. Numerical values are compiled in **Table 6.4**. The surface capacitance (Cs) was high (49.6 mF/cm$^2$) before the stability test but reduced to 28.5 after 2 hours of stability test. After 225 h, the Cs increased again to 38.2-49.6 mF/cm$^2$. It is known that passing a current through the CCM induces activation of the catalyst layers and increases the catalyst's electrochemical surface area. It can also be speculated that local water swelling variations are involved.

These tests indicate that no catalyst losses (eg, due to water circulation or electrochemical etching) occurred during that period, and that the CL firmly adheres to the membrane surface.

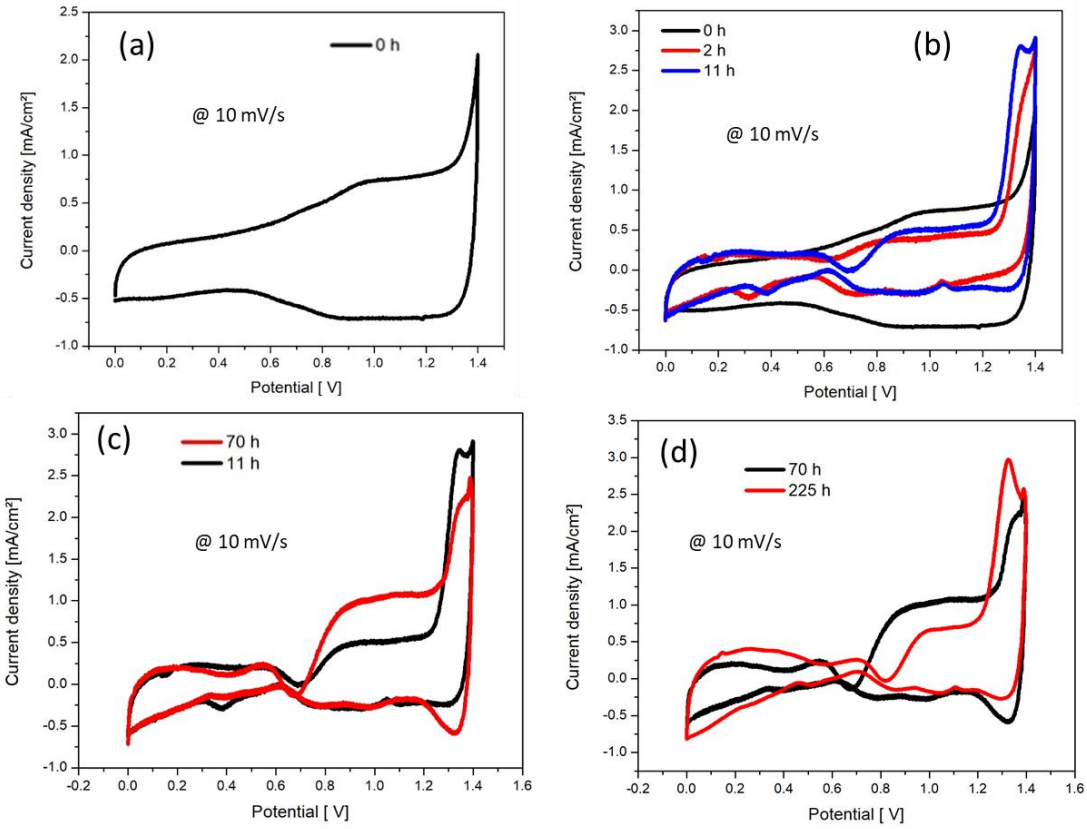


**Figure 6.19.** Cyclic voltammograms were measured on the commercial reference CCM at scan rates of 10 mV/s, after (a) 0 hours (b) 0, 2, 11 hours (c) 11, 70 hours and (d) 70, 225 hours.

**Table 6.4.** Specific areal capacitance values of the commercial reference CCM were measured at a scan rate of 10 mV/sec, at different times of the ASTs.

| **Cell 3** | **0 h** | **2 h** | **11 h** | **70 h** | **225 h** |
|---|---|---|---|---|---|
| Cs ($mF/cm^2$) | 49.6 | 28.57 | 34.03 | 40.64 | 38.21 |

iV curves

The iV curves measured on the commercial reference CCM (cell#3) at a different time of the AST are plotted in **Figure 6.20** (measurements were made at a scan rate of 0.4 $mA/cm^2$.s as discussed in chapter 2). Zoom is made on the low current density range were potential activation, or contamination problems can be more easily seen. Initial performances were quite good, and the degradation observed during the first 11 hours of the AST (**Figure 6.20-a**) is attributed to the contaminations resulting from the degradation of the HNC membrane, which contaminates the feed water. the  This degradation was reversible after washing with fresh DI water (**Figure 6.20-b**). A 10 mV cell voltage increase (from 1.485 to 1.495 V) was measured during 59h of the AST. The iV curves measured before and after the stability test show a 10 mV increase of the onset electrolysis voltage (from 1.44 to 1.45 V). The 10 mV is the exact value of cell potential increases observed by iV and chronopotentiometry test. After having the stack washed and tightened again, the onset potential returns to its original value. Finally, after 155 h of additional chronopotentiometry, the cell voltage was slightly increased (**Figure 6.20-c**).

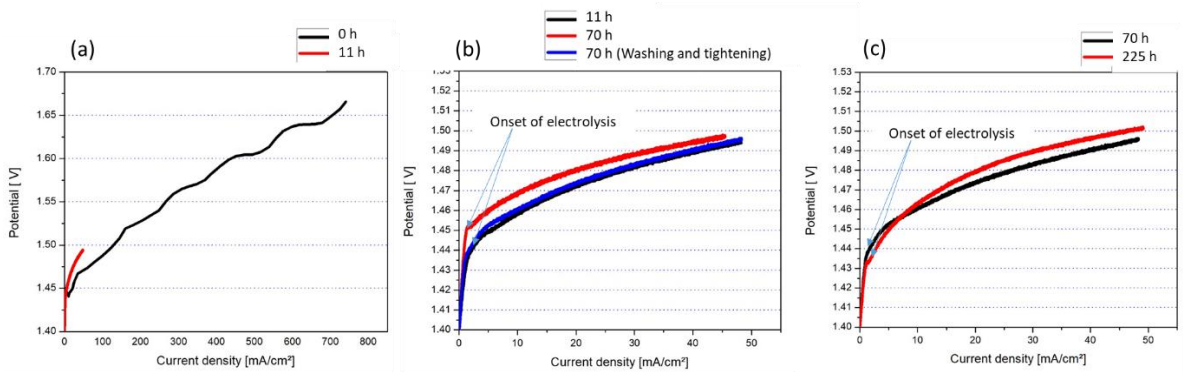


**Figure 6.20.** iV curves of Ref-commercial CCM were measured after (a) 0, 11 hours (b) 11, 70 hours, 70 hours after washing and tightening, and (c) 70, 225 hours.

EIS

The experimental EIS spectra of the PEM water electrolysis cell#3 (at 25 mA/cm$^2$) and their best-fits are displayed in (**Figure 6.21**). A more detailed analysis was performed. Experimental spectra exhibit a single but slightly flattened semicircle indicating the presence of at least two main time constants of close value. Therefore, the equivalent electrical circuit of **Figure 6.21-a,** which is the simplest analogy to use and the most likely to yield good quality fits, was used to model the data[20]. Such phenomenological modelling is probably not as convincing as an approach based on the resolution of the kinetic equations of electrochemistry. It is essentially based on the number of interfaces present in the cells and the various microscopic processes in series, which condition the total cell impedance. Nevertheless, such an approach facilitates the discussion. The model used contains an *inductor* ($L_1$) to account for the measurement cables, an ohmic resistance (HFR) to account for the internal resistance of the cell (a combination of the ionic resistance of the polymer electrolyte and the electrical resistance of internal titanium cell components). Both are placed in series with two *R//C circuits*, each one made of a charge transfer resistance ($R_1$, $R_2$) and a capacitance, which were replaced by the usual constant phase elements (*CPE*) to account for rough electrode/electrolyte interfaces[85]. The impedance of a CPE is given by:

$$Z_{CPE} = \frac{1}{T(i\omega)^P}$$

where $Z_{CPE}$ is the impedance of the CPE, $i$ is the imaginary unit, and $\omega$ is the radial frequency ($\omega = 2\pi f$). The *CPE* contains two terms: CPE-T (pseudo capacitance, corresponding to C) and CPE-P (referred to the exponent n). CPE-T is a frequency-independent constant in **F.cm$^{-2}$.s$^{n-1}$** (here, n = CPE-P), and CPE-P is a factor ranging between 0 and 1, usually between 0.6 and 1.0. CPE-T tends to a pure capacitance C as CPE-P tends to 1. CPE-P values provide information on the mean roughness of the two cell interfaces: values very close to unity are usually obtained with 'ideal interfaces' or for 'perfect capacitors'. For rough interfaces, values as low as 0.9 can be commonly obtained.

Regarding the physical significance of the different time constants observed experimentally (two in the case under discussion here), contradictory interpretations are reported in the literature[86]. The high-frequency semicircle is attributed to either the HER[87] or a

[85] E. Barsoukov, J. R. Macdonald, *Impedance Spectroscopy : Theory, Experiment and Applications*, Wiley, 2nd Edition, 2005. https://doi.org/10.1002/0471716243

[86] Suermann M, Pătru A, Schmidt TJ, Büchi FN. *High-pressure polymer electrolyte water electrolysis: Test bench development and electrochemical analysis*. Int J Hydrogen Energy 2017;42:12076–86. https://doi.org/10.1016/j.ijhydene.2017.01.224

[87] Siracusano S, Trocino S, Briguglio N, Baglio V, Aricò A. *Electrochemical Impedance Spectroscopy as a Diagnostic Tool in Polymer Electrolyte Membrane Electrolysis*. Materials (Basel) 2018;11:1368. https://doi.org/10.3390/ma11081368.

charge transfer process that combines electrical and/or ionic conductive double-layer effects between the ionomer (binder) and the active catalyst layer[88]. Also, it is tempting to ascribe one time constant to each of the two half-cell reactions (HER and OER), and this is what we did here to facilitate the discussion. However, it has already been reported elsewhere[89] that this is not necessarily the case: measurements made using an internal reference electrode show that the OER alone can generate two semicircles. The reason is that the HER, which, on platinum in acid electrolytes, a one-electron process with electro-desorption as a rate-determining step (rds), is a quite fast process which, in other words, can be modelled by a small RC time constant which is sometimes observed on the high frequency (HF) side of the EIS spectra. On the contrary, the OER is much slower. It involves two electron transfer steps as rds. This is why the two flattened semicircles are sometimes ascribed to the OER only. Regarding the validity of the simple electrical analogy presented in **Figure 6.21-a**, it should be noted that the situation is sometimes more complex, especially at elevated current density when charge transfer limitations are also observed. However, this can be neglected in the experiments reported here since the measurements were made in the low current density range where electrochemical activation prevails.

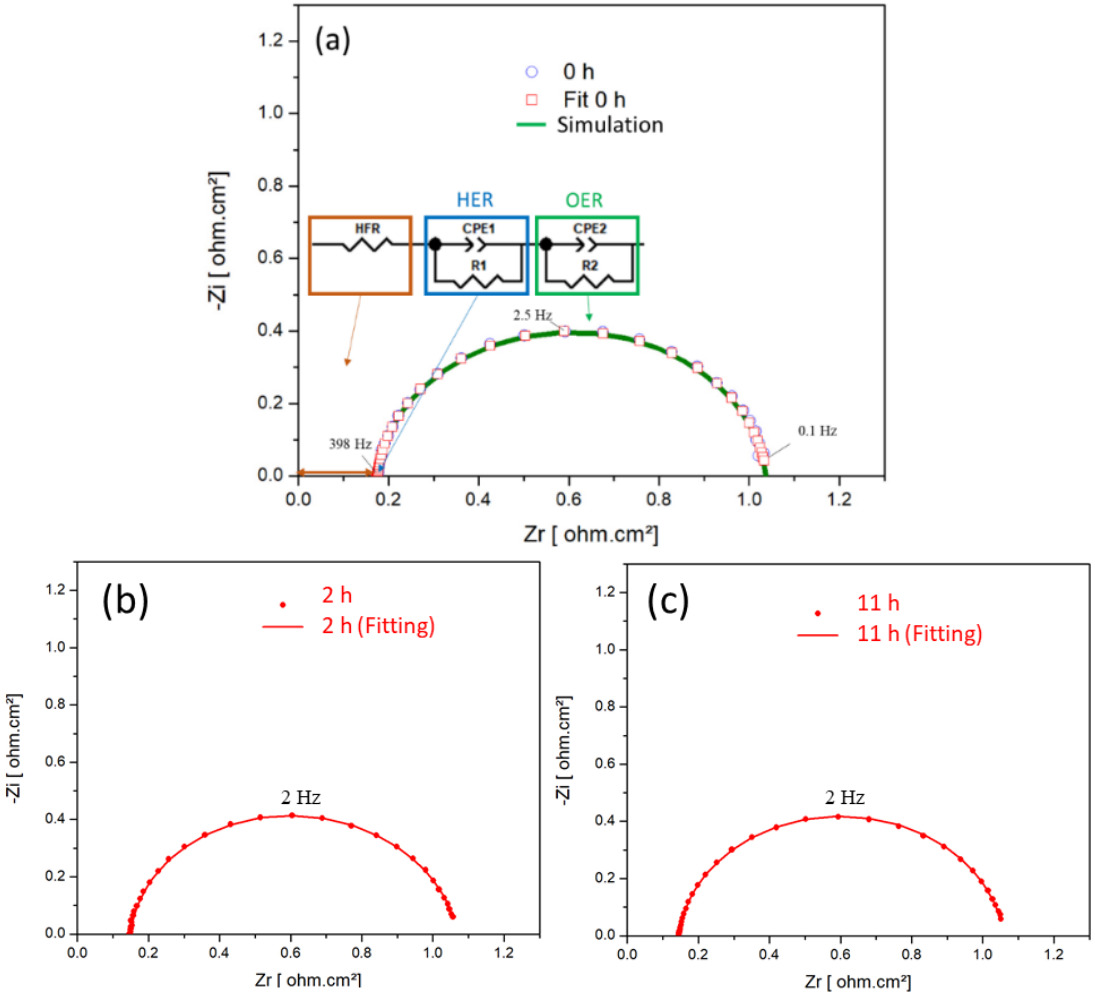


**Figure 6.21.** Experimental and best-fit EIS spectra measured on the commercial reference CCM at 25 mA/cm$^2$ during the stability test (a) electrical analogy used for the fit; EIS spectra after (a) 0 h, (b) 2 h and (c) 11 h of AST.

[88] Lettenmeier P, Wang R, Abouatallah R, Helmly S, Morawietz T, Hiesgen R, et al. *Durable Membrane Electrode Assemblies for Proton Exchange Membrane Electrolyzer Systems Operating at High Current Densities*. Electrochim Acta 2016;210:502–11. https://doi.org/10.1016/j.electacta.2016.04.164.

[89] Ph.D Thesis, Electrocatalysis in water electrolysis with solid polymer electrolyte by Egil Rasten, (2001) Faculty of Natural Sciences and Technology, NTNU. https://ntnuopen.ntnu.no/ntnu-xmlui/handle/11250/244448

Best-fits values obtained during the stability test are compiled in **Table 6.5**. In this reference CCM (Cell#3 = Pt-C / Nafion 115 / $IrO_2$ with high catalyst loadings), the CPE-P values deduced from the best-fits are close to unity (0.95). During the 225 hours-long stability test, all fit parameters remained almost constant, indicating that no change occurred in either the number of electrochemical active sites or reaction mechanisms.

**Table 6.5.** List of best-fit EIS parameters extracted from the data of **Figure 6.21** (note: the capacitance can be determined from CPE values[90]).

| | **Represent** | **0 h @25 mA/cm$^2$** | **2 h@ 25 mA/cm$^2$** | **11 h @25 mA/cm$^2$** |
|---|---|---|---|---|
| $R_0$ ($\Omega$.cm$^2$) | HFR | 0.17 | 0.15 | 0.137 |
| $R_1$ ($\Omega$.cm$^2$) | $R_{ct}$ of HER | 0.005 | 0.067 | 0.007 |
| $CPE_1$-T (mF/cm$^2$) | HER | 0.01 | 0.02 | 0.03 |
| $CPE_1$-P (adim) | HER | 1 | 1 | 1 |
| $R_2$ ($\Omega$.cm$^2$) | $R_{ct}$ of OER | 0.86 | 0.848 | 0.91 |
| $CPE_2$-T (F/cm$^2$) | OER | 0.087 | 0.1 | 0.1 |
| $CPE_2$-P (adim) | OER | 0.95 | 0.95 | 0.94 |

EIS spectra were also measured during the stability test at two different current densities (25 and 50 mA/cm$^2$). This was done to confirm that both semicircles are potential–dependent and, therefore, related to charging transfer processes. Results are plotted in **Figure 6.22,** and best-fit parameters are compiled in **Table 6.6**. Results show that the two charge transfer resistances decrease when the current density increase. Such potential dependency confirms that both are related to charge transfer processes and not to mass transport limitations, as already reported in various papers[91,86]. In each case, CPE-P values remain above 0.9 even at high current density.

[90] B. Hirschorn, M.E. Orazem, B. Tribollet, V. Vivier, I. Frateur, M. Musiani, Determination of effective capacitance and film thickness from constant-phase-element parameters, Electrochim. Acta, 55(21) (2010) 626218-6227).
[91] P. Millet**,** R. Ngameni, S.A. Grigoriev, N. Mbemba, F. Brisset, A. Ranjbari, C. Etiévant, *PEM water electrolyzers : from electrocatalysis to stack development,* Int. J. Hydrogen Energy, 35 (**2010**) 5043-5052. DOI: https://doi.org/10.1016/j.ijhydene.2009.09.015

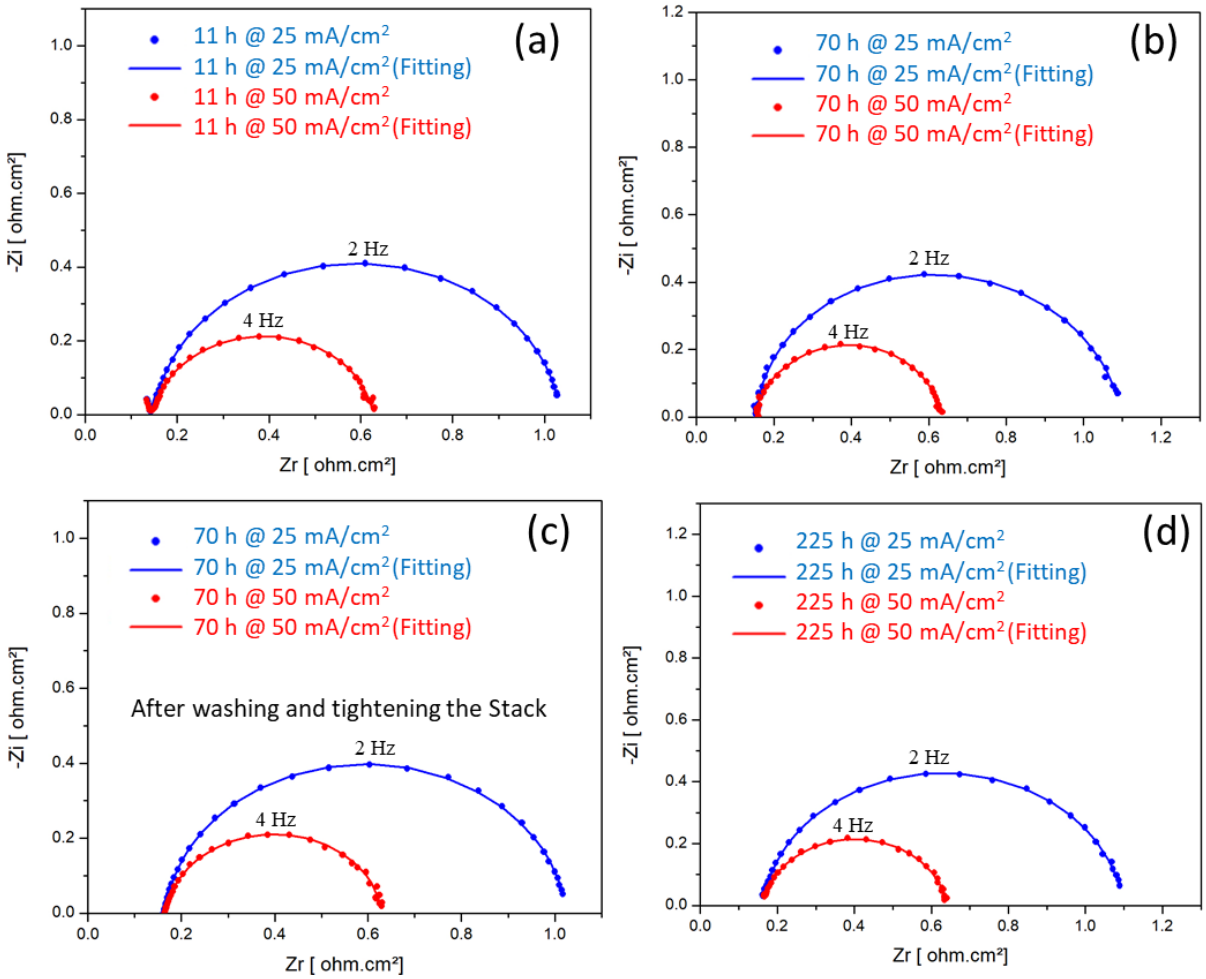


**Figure 6.22.** Experimental and best-fit EIS spectra measured on the commercial reference CCM at 25 and 50 mA/cm$^2$ during the stability test. EIS spectra and fitting after (a) 11h, (b) 70 h, (c) after washing and tightening, and (d) after 225hours of AST.

**Table 6.6.** Evolution of best-fit EIS parameters during the ASTs.

| Cell#1 | **Represent** | **11 h @ 25 mA/cm$^2$** | **11 h @ 50 mA/cm$^2$** | **70 h @ 25 mA/cm$^2$** | **70 h @ 50 mA/cm$^2$** | **Washing and tightening** | | **225h 25 mA/cm$^2$** | **225 h mA/cm$^2$** |
|---|---|---|---|---|---|---|---|---|---|
| | | | | | | **70 h @ 25 mA/cm$^2$** | **70 h @ 50 mA/cm$^2$** | | |
| $R_0$ (Ω.cm$^2$) | HFR | 0.145 | 0.145 | 0.154 | 0.153 | 0.157 | 0.157 | 0.162 | 0.162 |
| $R_1$ (Ω.cm$^2$) | $R_{ct}$ of HER | 0.005 | 0.0033 | 0.08 | 0.01 | 0.01 | 0.01 | 0.0006 | 0.002 |
| $CPE_1$-T (mF/cm$^2$) | HER | 0.3 | 0.006 | 0.4 | 0.15 | 0.19 | 0.075 | 0.13 | 0.03 |
| $CPE_1$-P (adim) | HER | 1 | 1 | 1 | 1 | 0.85 | 0.93 | 1 | 1 |
| $R_2$ (Ω.cm$^2$) | $R_{ct}$ of OER | 0.88 | 0.476 | 0.86 | 0.478 | 0.857 | 0.46 | 0.93 | 0.47 |
| $CPE_2$-T (mF/cm$^2$) | OER | 0.1 | 0.11 | 0.13 | 0.11 | 0.1 | 0.11 | 0.11 | 0.11 |
| $CPE_2$-P (adim) | OER | 0.95 | 0.92 | 0.92 | 0.93 | 0.95 | 0.94 | 0.94 | 0.93 |

A plot of HFR and $R_{ct}$ (HER and OER) during the test is shown in **Figure 6.23**. The resistances are almost constant, which is expected from such commercial reference CCM.

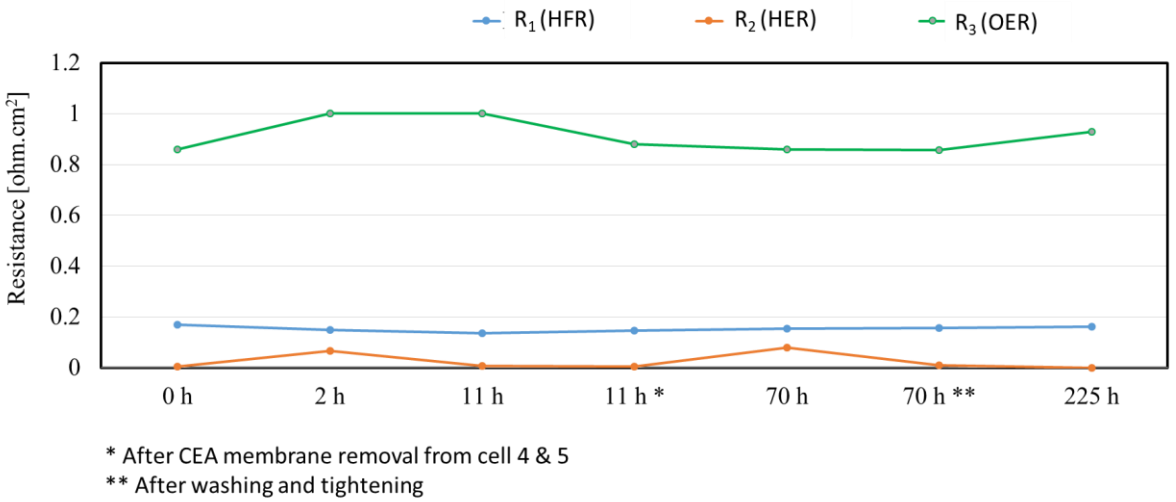


**Figure 6.23.** Variation of the fitted resistances by time for cell#3. EIS measured at 25 mA/cm$^2$.

### 6.4.2. Laboratory reference CCM (Cell#2)

We now present the results obtained with our own laboratory reference CCM. Cell#2 (laboratory reference CCM): Pt-C / Nafion 212 // Nafion 212 / $IrO_2$ with high catalyst loadings.

Chronopotentiometry

The stability of the laboratory reference CCM (cell#2) was also assessed by using a chronopotentiometry test at a constant current density of 25 mA/cm$^2$, as discussed and justified in the previous section. Results are shown in **Figure 6.24**. The cell voltage slightly increased by 35 mV (from 1.59 to 1.625 Volt) during the first 70 hours of the test. Once the stack was washed and re-tightened, the cell voltage decreased down to 1.58 V and increased by 26 mV up 1.606 V after 225 h. The conclusion is that our laboratory reference is less efficient but as stable as the commercial reference.

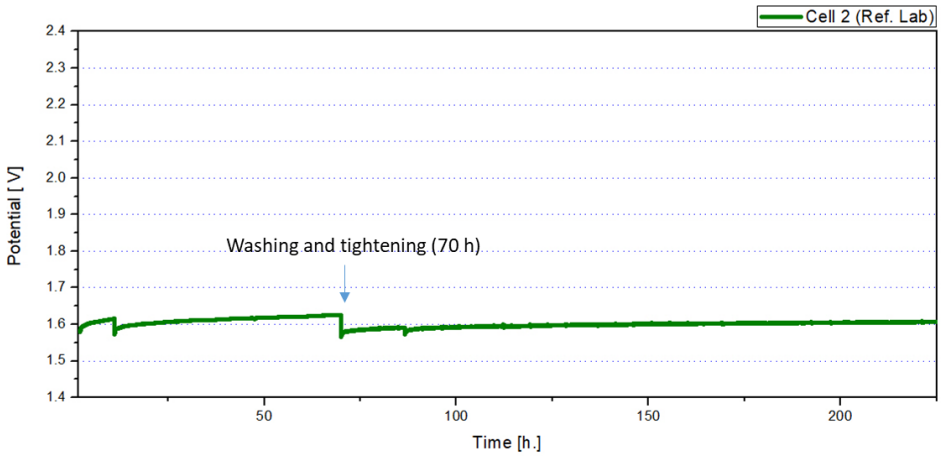


**Figure 6.24.** Chronopotentiometry of cell#2 at 25 mA/cm$^2$ for 225 h.

Cyclic Voltammograms (CV)

The cyclic voltammograms recorded during the stability test are shown in **Figure 6.25**. Specific capacitance values deduced from these graphs are compiled in **Table 6.7**.

Cs values are ranging from 11.0 to 36.9 mF/cm$^2$. A comparable Cs result was mentioned in the literature for CCM having equivalent catalyst loadings[92,93]. The value range is lower than the one of the commercial reference CCM (28.6 - 49.6 mF/cm$^2$) in similar test conditions. To some extent, this is an indication that less catalyst is in contact with the polymer electrolyte and explains why the iV curves are less efficient (see next paragraph): the coating process requires further improvement. However, the stability of the results during the test indicates that the catalyst layers are stable and adhere firmly to the Nafion membrane and are not easily prone to delamination during electrolysis.

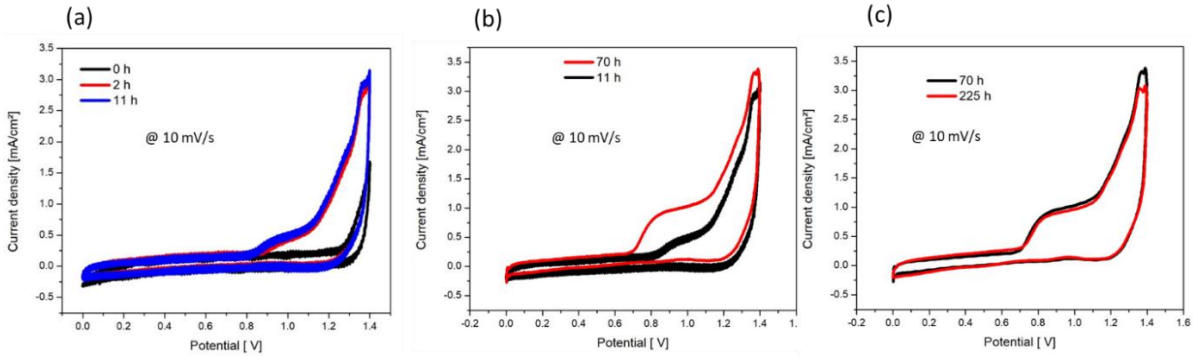


**Figure 6.25.** Cyclic voltammograms measured on a laboratory reference CCM at scan rates of 10 mV/s, after (a) 0, 2, 11 hours (b) 11, 70 hours and (c) 70, 225 hours.

**Table 6.7.** Specific areal capacitance values of the laboratory reference CCM measured at a scan rate of 10 mV/sec, at different times of the ASTs.

| **Cell#2** | **0 h** | **2 h** | **11 h** | **70 h** | **225 h** |
|---|---|---|---|---|---|
| $C_s$ (mF/cm$^2$) | 10.96 | 21.05 | 23.78 | 32.3 | 36.9 |

<u>iV curves</u>

The iV curves of Cell#2 measured in the low j range during the stability test are shown in **Figure 6.26**. They were measured before and after the stability test. A slight increase of the curve slope is observed after 70 h, possibly due to the rise of the internal cell resistance. After the stack was re-tightened at higher clamping pressure, the expected improvement was obtained.

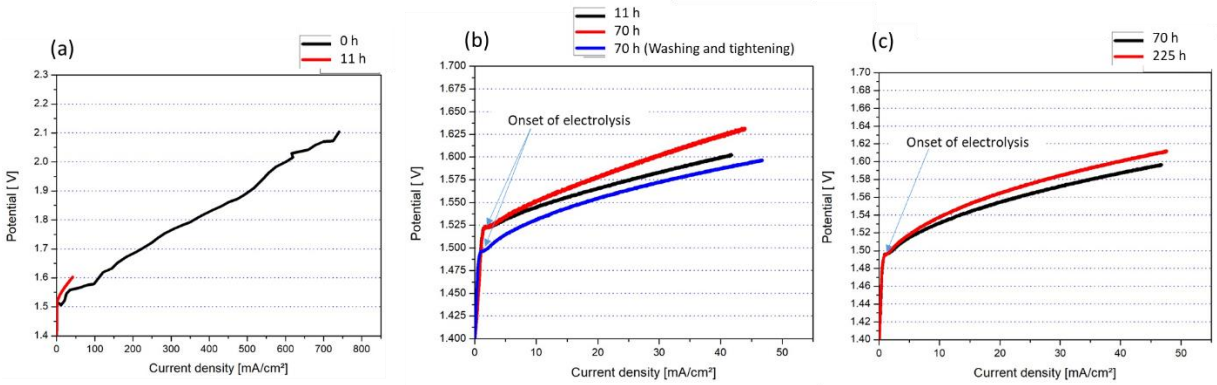


**Figure 6.26.** iV curves of the laboratory reference CCM measured after (a) 0, 11 hours (b) 11, 70 hours, 70 hours after washing and tightening, and (c) 70, 225 hours.

[92] Mandal M, Valls A, Gangnus N, Secanell M. *Analysis of Inkjet Printed Catalyst Coated Membranes for Polymer Electrolyte Electrolyzers*. J Electrochem Soc 2018;165:F543–52. https://doi.org/10.1149/2.1101807jes.
[93] Rasten E, Hagen G, Tunold R. *Electrocatalysis in water electrolysis with solid polymer electrolyte*. Electrochim Acta 2003;48:3945–52. https://doi.org/10.1016/j.electacta.2003.04.001.

EIS

The experimental EIS spectra of the PEM water electrolysis cell#2 (at 25 mA/cm$^2$) and their best-fits are displayed in **Figure 6.27**. and best-fit parameters are compiled in **Table 6.8**.

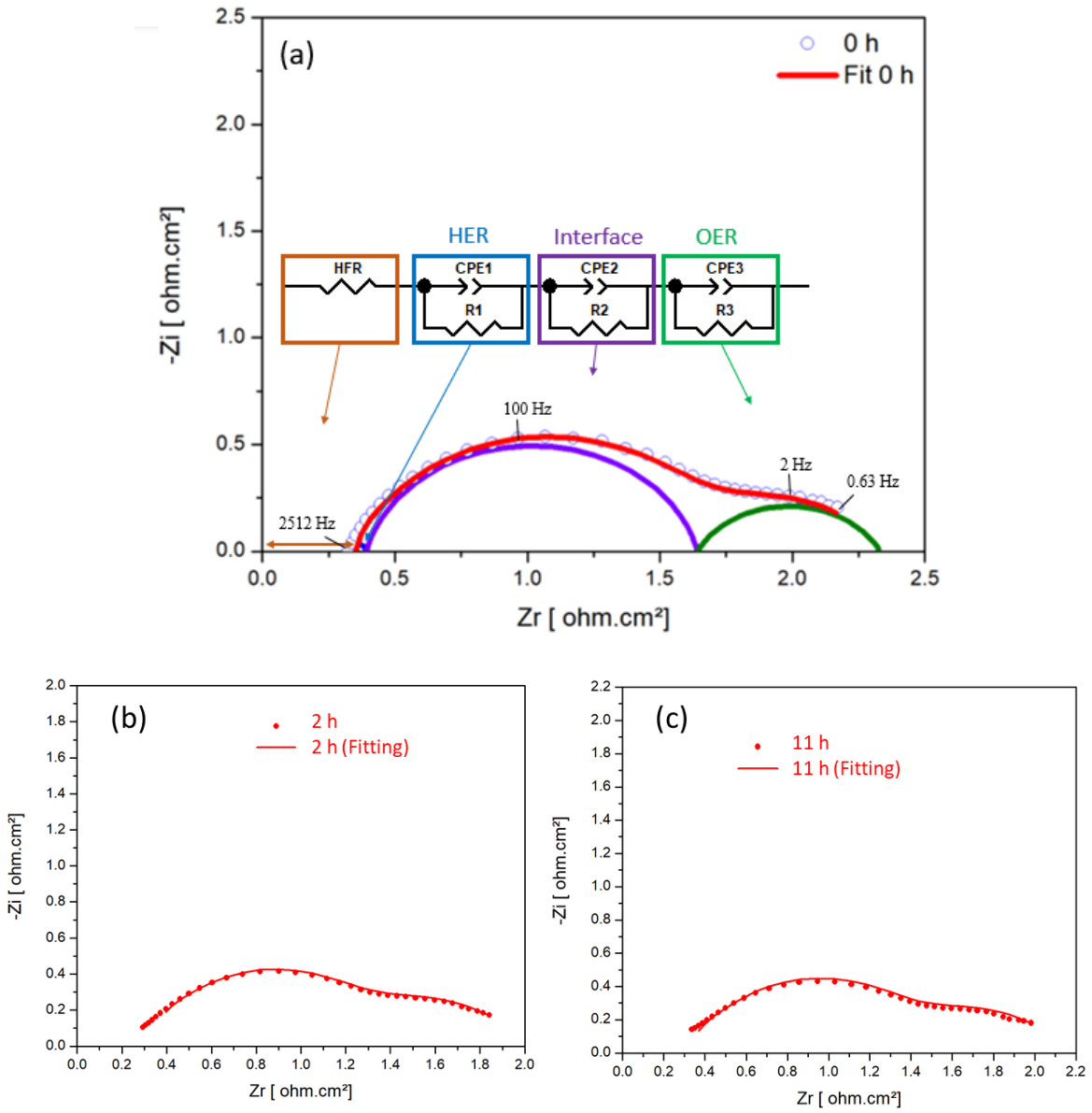


**Figure 6.27.** Experimental and best-fit EIS spectra of the laboratory reference CCM (a) electrical analogy used for the fit (Interface = Nafion112/Nafion112); EIS spectra at 25 mA/cm$^2$ after (a) 0 h, (b) 2 h and (c) 11 h of AST.

Compared to the commercial reference CCM, the shape of EIS spectra is different: on the high-frequency side, a 45° shape is sometimes observed (possibly linked to mass transport effect such as water transport to the anode layer, but this was disregarded in the fit) while on the low-frequency side, another overlapping semicircle appears. The HF semicircle is still flattened and contains two close time constants. A second semicircle is observed on the LF side of the spectrum. Therefore, experimental spectra were fitted using three different time constants (equivalent circuit of **Figure 6.27-a**). Compared to cell#3, the HFR was found to be slightly larger, even though the total membrane thickness is less: this may be attributed to a parasite contact resistance at the Nafion212/Nafion212 interface. The diameter of the HF and LF semicircles remained relatively constant with time during the stability test.

Best fit parameters are compiled in **Table 6.8**. The values of CPE-2 and CPE-3 are similar and differ from CPE-1. CPE-1 characterizes the HER, which is made of Pt nanoparticles dispersed onto carbon black and logically has a large electrochemical surface area. CPE-3 characterizes the OER, which is made of non-supported $IrO_2$ particles. Such a material which is usually synthesized by calcination of precursor Ir salts is known to be made of coarser particles and lower electrochemical surface area. CPE-2 is a characteristic of the membrane/membrane interface.

**Table 6.8.** List of best-fit EIS parameters extracted from the data of **Figure 6.27**.

| **Cell#2** | **Represent** | **0 h @25 mA/cm$^2$** | **2 h@ 25 mA/cm$^2$** | **11 h @25 mA/cm$^2$** |
|---|---|---|---|---|
| $R_0$ ($\Omega$.cm$^2$) | HFR | 0.325 | 0.325 | 0.325 |
| $R_1$ ($\Omega$.cm$^2$) | R of interface | 0.69 | 0.8 | 0.815 |
| $CPE_1$-T (mF/cm$^2$) | interface | 0.275 | 0.265 | 0.288 |
| $CPE_1$-P (adim) | interface | 0.7 | 0.65 | 0.65 |
| $R_2$ ($\Omega$.cm$^2$) | $R_{ct}$ of HER | 0.069 | 0.059 | 0.08 |
| $CPE_2$-T (mF/cm$^2$) | HER | 0.001 | 0.003 | 0.002 |
| $CPE_2$-P (adim) | HER | 1 | 1 | 1 |
| $R_3$ ($\Omega$.cm$^2$) | $R_{ct}$ of OER | 1.275 | 0.8 | 0.93 |
| $CPE_3$-T (mF/cm$^2$) | OER | 0.004 | 0.007 | 0.006 |
| $CPE_3$-P (adim) | OER | 0.85 | 0.9 | 0.87 |

EIS spectra measured at two different current densities are plotted in **Figure 6.28** for comparison. The equivalent electrical circuit used for fitting the EIS spectra of the Ref-Lab CCM is shown in (**Figure 6.28-a**). Three different time constants are used for fitting the experimental spectra. The diameter of the high-frequency and low-frequency semicircles decrease when the current density is increased. The membrane/membrane interface resistance ($R_{interface}$) and the charge transfer resistance of the HER ($R_{ct}$) both decrease when the current density increases. In the Lab-Ref CCM, the high-frequency semicircle contains two-overlapping semicircles, one due to the membrane/membrane interface and one due to the charge transfer resistance of the HER. The HER appears to significantly affect the high-frequency semicircle due to the poisoning of the cathode catalyst layer with the organic materials leached from the HNC membrane. Furthermore, this probably indicates that the resistance of the membrane/membrane interface requires activation energy to transport the protons. After tightening the stack at higher clamping pressure, the HFR was reduced due to a reduction of all contact resistances, but the HER and OER charge transfer resistances remained the same (**Table 6.9**).

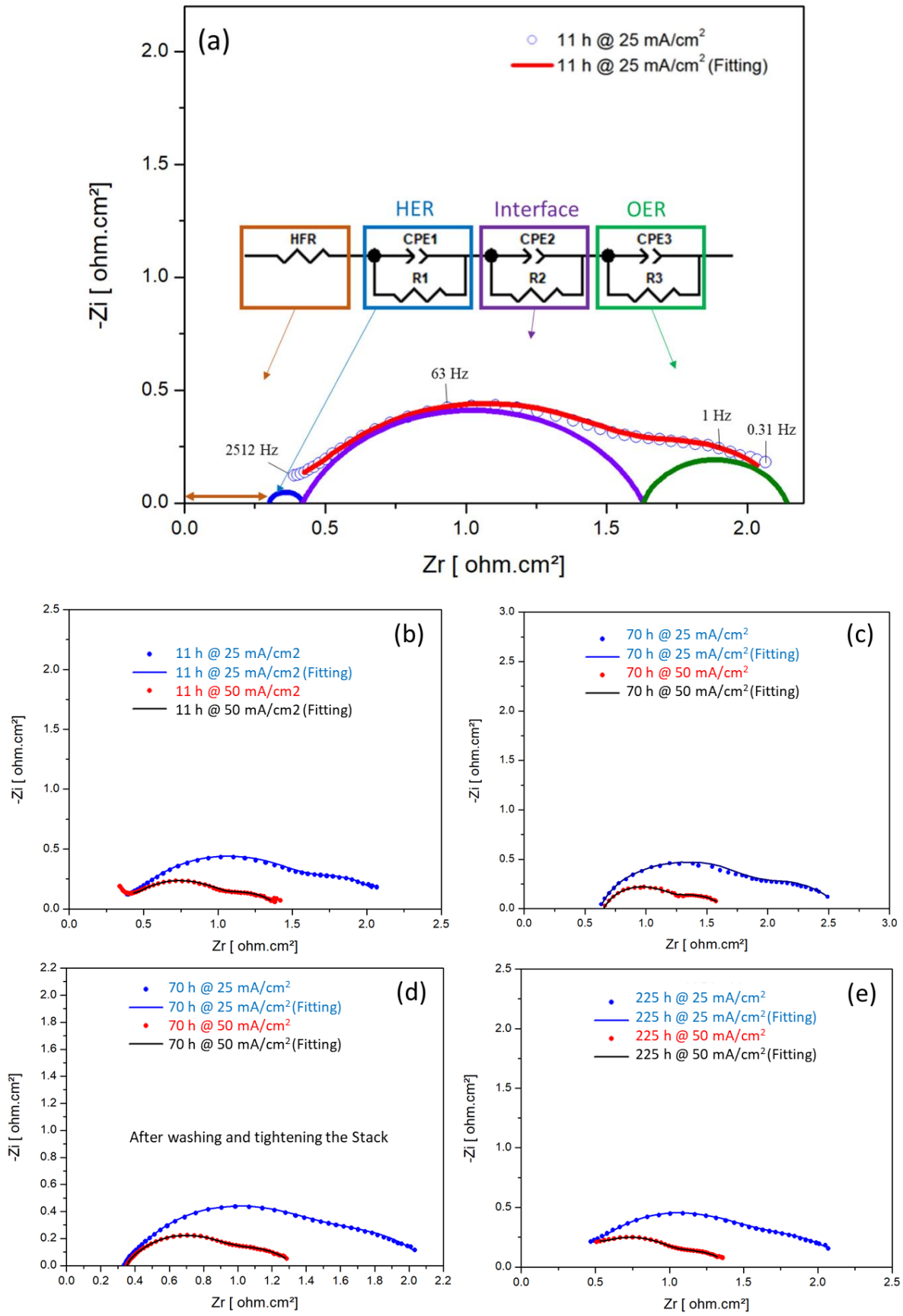


**Figure 6.28.** Experimental and best-fit EIS spectra of the laboratory reference CCM (a) electrical analogy used for the fit; EIS spectra after (b) 11h, (c) 70 h, (d) after washing and tightening, and (e) 225h of AST.

**Table 6.9.** List of best-fit EIS parameters extracted from the data of **Figure 6.28**.

| Cell#2 | Represent | 11 h @ 25 mA/cm$^2$ | 11 h @ 50 mA/cm$^2$ | 70 h @ 25 mA/cm$^2$ | 70 h @ 50 mA/cm$^2$ | Washing and tightening | | 225h 25 mA/cm$^2$ | 225 h mA/cm$^2$ |
|---|---|---|---|---|---|---|---|---|---|
| | | | | | | 70 h @ 25 mA/cm$^2$ | 70 h @ 50 mA/cm$^2$ | | |
| $R_0$ ($\Omega.cm^2$) | HFR | 0.3 | 0.296 | 0.49 | 0.49 | 0.33 | 0.33 | 0.33 | 0.33 |
| $R_1$ ($\Omega.cm^2$) | R of interface | 0.511 | 0.383 | 0.683 | 0.425 | 0.74 | 0.436 | 0.79 | 0.42 |
| $CPE_1$-T ($mF/cm^2$) | interface | 0.35 | 0.455 | 0.362 | 0.456 | 0.4 | 0.58 | 0.35 | 0.57 |
| $CPE_1$-P (adim) | interface | 0.82 | 0.666 | 0.693 | 0.633 | 0.63 | 0.58 | 0.62 | 0.6 |
| $R_2$ ($\Omega.cm^2$) | $R_{ct}$ of HER | 0.119 | 0.1 | 0.054 | 0.024 | 0.06 | 0.051 | 0.1 | 0.056 |
| $CPE_2$-T ($mF/cm^2$) | HER | 0.002 | 0.0002 | 0.02 | 0.0002 | 0.006 | 0.004 | 0.0009 | $7.5 \times 10^{-5}$ |
| $CPE_2$-P (adim) | HER | 0.87 | 1 | 1 | 1 | 0.964 | 0.95 | 1 | 1 |
| $R_3$ ($\Omega.cm^2$) | $R_{ct}$ of OER | 1.212 | 0.63 | 1.35 | 0.705 | 1 | 0.515 | 1 | 0.6 |
| $CPE_3$-T ($mF/cm^2$) | OER | 0.01 | 0.008 | 0.008 | 0.0059 | 0.014 | 0.013 | 0.01 | 0.01 |
| $CPE_3$-P (adim) | OER | 0.76 | 0.76 | 0.71 | 0.75 | 0.810 | 0.8 | 0.82 | 0.79 |

**Figure 6.29** shows a plot of HFR, $R_{ct}$ (HER and OER) and $R_{interface}$ during the test. The different resistances of the laboratory reference are mostly stable; some fluctuation can be seen in the OER $R_{ct}$ with has an average value of 1.07 ± 0.3.

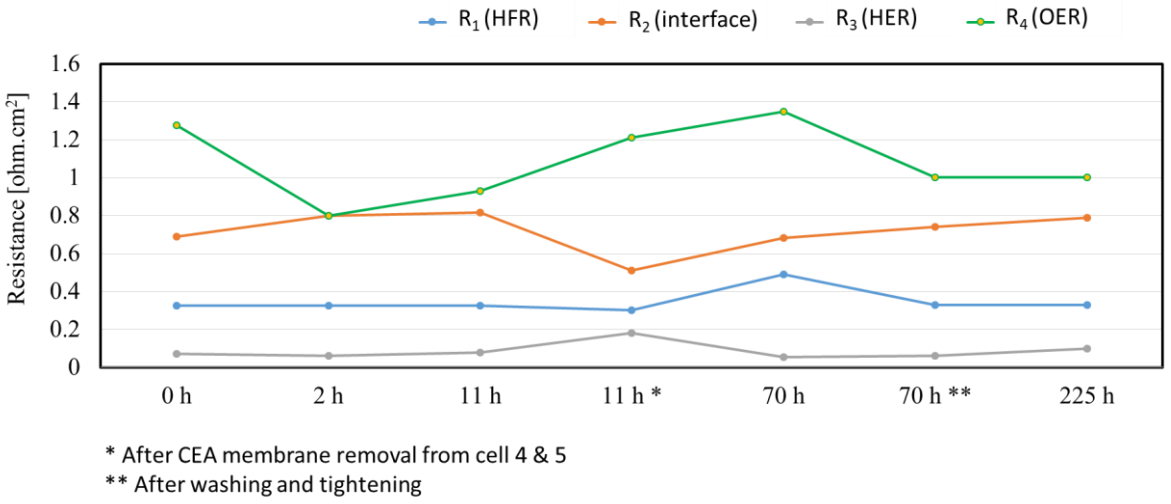


**Figure 6.29.** Variation of the fitted resistances by time for cell#2. EIS measured at 25 mA/cm$^2$.

Based on CV, iV and EIS results, we concluded that the laboratory reference CCM was stable during the electrochemical tests.

### 6.4.3. HNC CCM with moderate catalyst loading (Cell#1)

We now present the results obtained with cell#1 : Pt-C / Nafion 212 // HNC membrane // Nafion 212 / $IrO_2$ with medium catalyst loadings.

Chronopotentiometry

The behavior of cell#1 during the stability test performed by chronopotentiometry, a constant current of 25 mA/cm$^2$ is shown in **Figure 6.30**. The cell voltage dramatically increased by 650 mV (from 1.6 to 2.25) during the first 70 h. After cleaning and tightening, the cell voltage dropped to 1.7 V and then increased by 400 mV (up to 2.1 V) after 225 h of test.

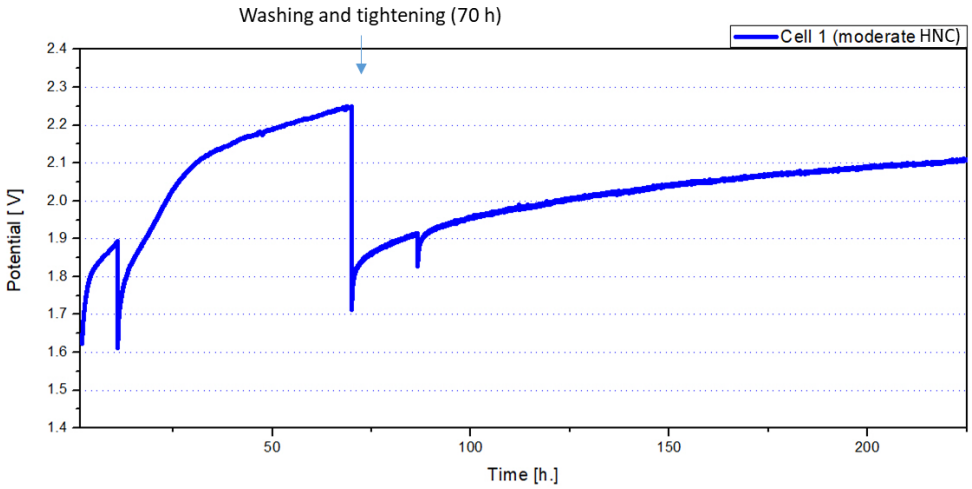


**Figure 6.30.** Chronopotentiometry of cell#1 at 25 mA/cm$^2$ for 225 h.

Cyclic Voltammograms (CV)

The voltage of cell#1 dramatically increased during the chronopotentiometry test (**Figure 6.30**), even though the CV shows a Cs increase after 70 h, which indicates no loss in catalytic surface area. The specific areal capacitance (Cs) increased from 13.5 to 14.4 mF/cm$^2$. The poisoning of the cathode by organic contamination leaking from the HNC membrane is a possible explanation for the voltage increase.

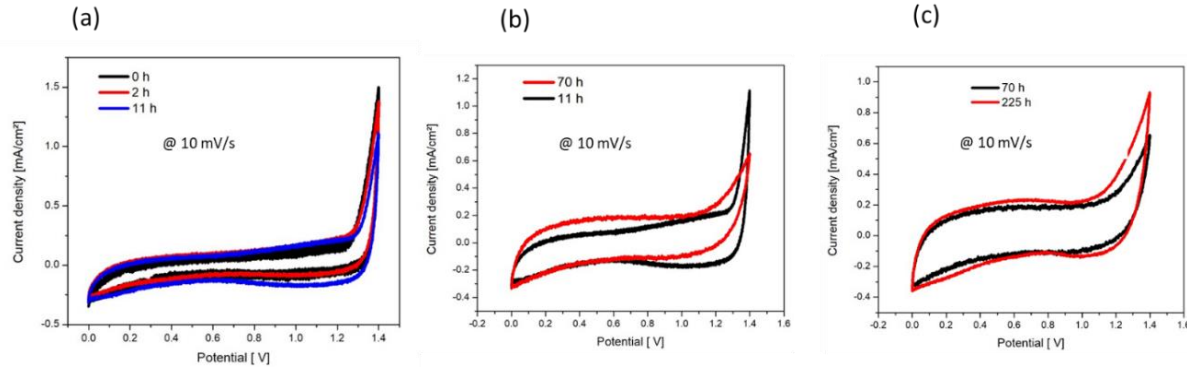


**Figure 6.31.** Cyclic voltammograms were measured on the HNC-CCM with moderate catalyst loadings at scan rates of 10 mV/s, after (a) 0, 2, 11 hours (b) 11, 70 hours and (c) 70, 225 hours.

**Table 6.10.** Specific areal capacitance values of the moderate-HNC CCM were measured at a scan rate of 10 mV/sec, at different times of the ASTs.

| **Cell 1** | **0 h** | **2 h** | **11 h** | **70 h** | **225 h** |
|---|---|---|---|---|---|
| Cs (mF/cm$^2$) | 9.5 | 11.32 | 13.48 | 14.42 | 18.57 |

iV curves

The iV curves measured after 70 h of test confirm the degradation observed during the chronopotentiometric test. The cell voltage at which the current starts to flow is the same, but the behavior in the activation domain indicates a loss of electro-active sites and the need for larger overvoltages.

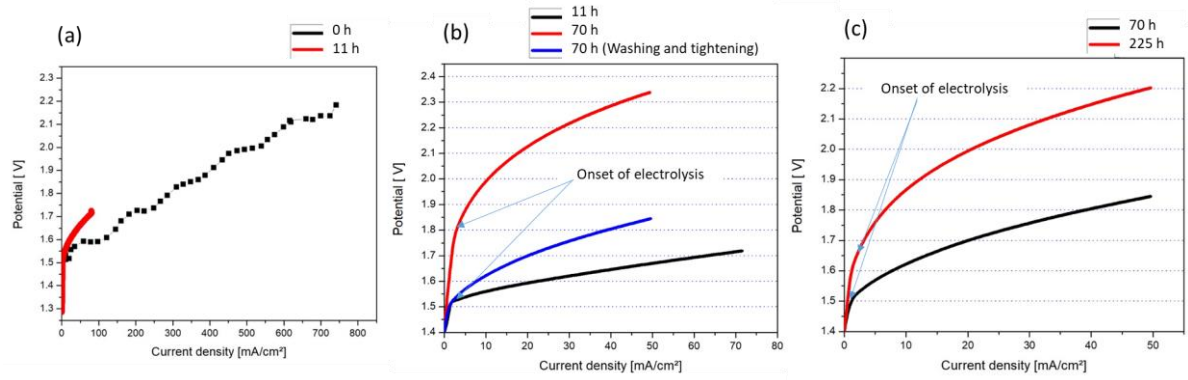


**Figure 6.32.** iV curves of the HNC-CCM with moderate catalyst loadings measured after (a) 0, 11 hours (b) 11, 70 hours, 70 hours after washing and tightening, and (c) 70, 225 hours.

EIS

The equivalent electrical circuit used for fitting the experimental EIS spectra measured on the HNC-moderate CCM (cell#1) is shown in **Figure 6.33**.

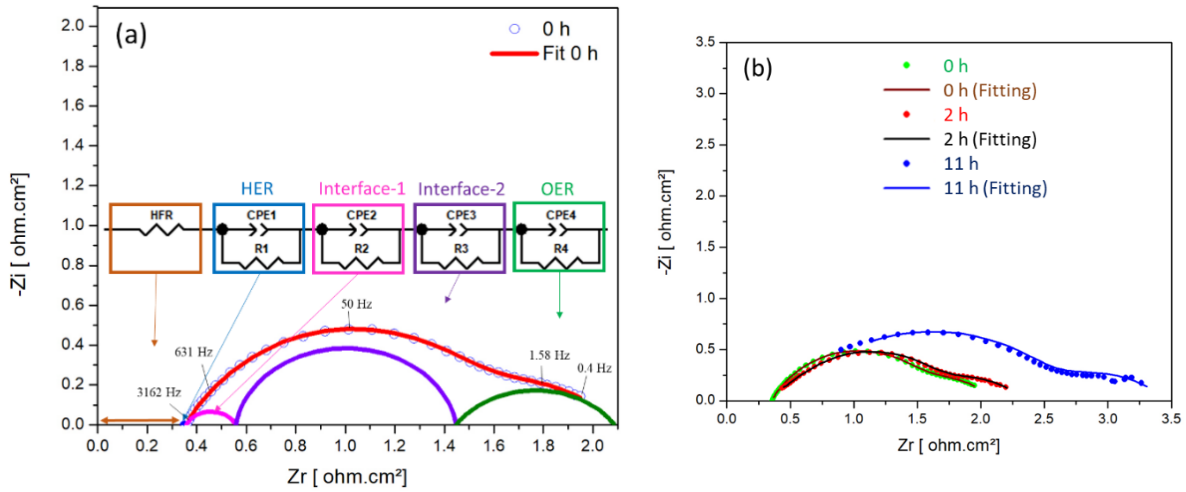


**Figure 6.33.** Experimental and best-fit EIS spectra of the HNC-CCM with moderate catalyst loadings (a) electrical analogy used for the fit; (b) EIS spectra at 25 mA/cm$^2$ after 0 h, 2 h and 11 h of AST.

There is one more membrane and, therefore, one more time constant. It consists of two membrane/membrane interface-resistances and two charge-transfer resistances, one for the HER and one for the OER. The two interface-resistances are those of the HNC/Nafion 212 interfaces. The first semicircle consists of two overlapped semicircles, (i) the Nafion/HNC interface; (ii) the HER CL. The situation prevailing at the beginning of the test is also shown in **Figure 6.33**. Best-fit parameters are compiled in **Table 6.11**. These two interface-resistances ($R_2$ and $R_3$) are not identical even if they are both made of the contact between a Nafion 212 and a HNC membrane.

**Table 6.11.**List of best-fit EIS parameters extracted from the data of **Figure 6.33**.

| **Cell#1** | **Represent** | **0 h 25 mA/cm$^2$** | **2 h 25 mA/cm$^2$** | **11 h 25 mA/cm$^2$** |
|---|---|---|---|---|
| $R_0$ ($\Omega$.cm$^2$) | HFR | 0.3 | 0.36 | 0.43 |
| $R_1$ ($\Omega$.cm$^2$) | R of interface 1 | 0.645 | 0.723 | 0.97 |
| $CPE_1$-T (mF/cm$^2$) | Interface 1 | 0.33 | 0.387 | 0.318 |
| $CPE_1$-P (adim) | Interface 1 | 0.63 | 0.604 | 0.57 |
| $R_2$ ($\Omega$.cm$^2$) | R of interface 2 | 0.147 | 0.187 | 0.73 |
| $CPE_2$-T (mF/cm$^2$) | Interface 2 | 0.028 | 0.007 | 0.001 |
| $CPE_2$-P (adim) | Interface 2 | 0.77 | 0.807 | 0.813 |
| $R_3$ ($\Omega$.cm$^2$) | $R_{ct}$ of HER | 0.126 | 0.035 | 0.142 |
| $CPE_3$-T (mF/cm$^2$) | HER | 0.083 | $3.5 \times 10^{-5}$ | $4 \times 10^{-7}$ |
| $CPE_3$-P (adim) | HER | 0.5 | 1 | 0.142 |
| $R_4$ ($\Omega$.cm$^2$) | $R_{ct}$ of OER | 0.88 | 1.026 | 1.18 |
| $CPE_4$-T (mF/cm$^2$) | OER | 0.006 | 0.006 | 0.004 |
| $CPE_4$-P (adim) | OER | 0.91 | 0.84 | 0.8 |

During the AST test, all resistances increase. The degraded sulfonic groups that form inside the HNC membrane during electrolysis bear negative charges and should therefore migrate to the positive electrode (anode) in reaction to the electric field. Therefore, the interface of the Nafion/HNC membranes on the anode side should be rich in sulfonic groups, while the other interface on the cathode side should be poor in sulfonic groups. Indeed, the EIS measurements show a significant increase of the diameter of the first semicircle. However, the electro-osmotic flow of water from anode to cathode may also contribute to the transport of degradation products towards the cathode and they can also be trapped at the HNC/Nafion interface. Therefore, it can be speculated that the degradation of the HNC membrane is the reason for the increase of the two interface-resistances.
Similar to the result obtained with the 4 cm$^2$ lab cell, there is an increase of the diameter of the first semicircle (corresponding to the interfacial membrane/membrane resistance) during the test. This effect was attributed to the poisoning by contaminants leaking from the HNC membrane.

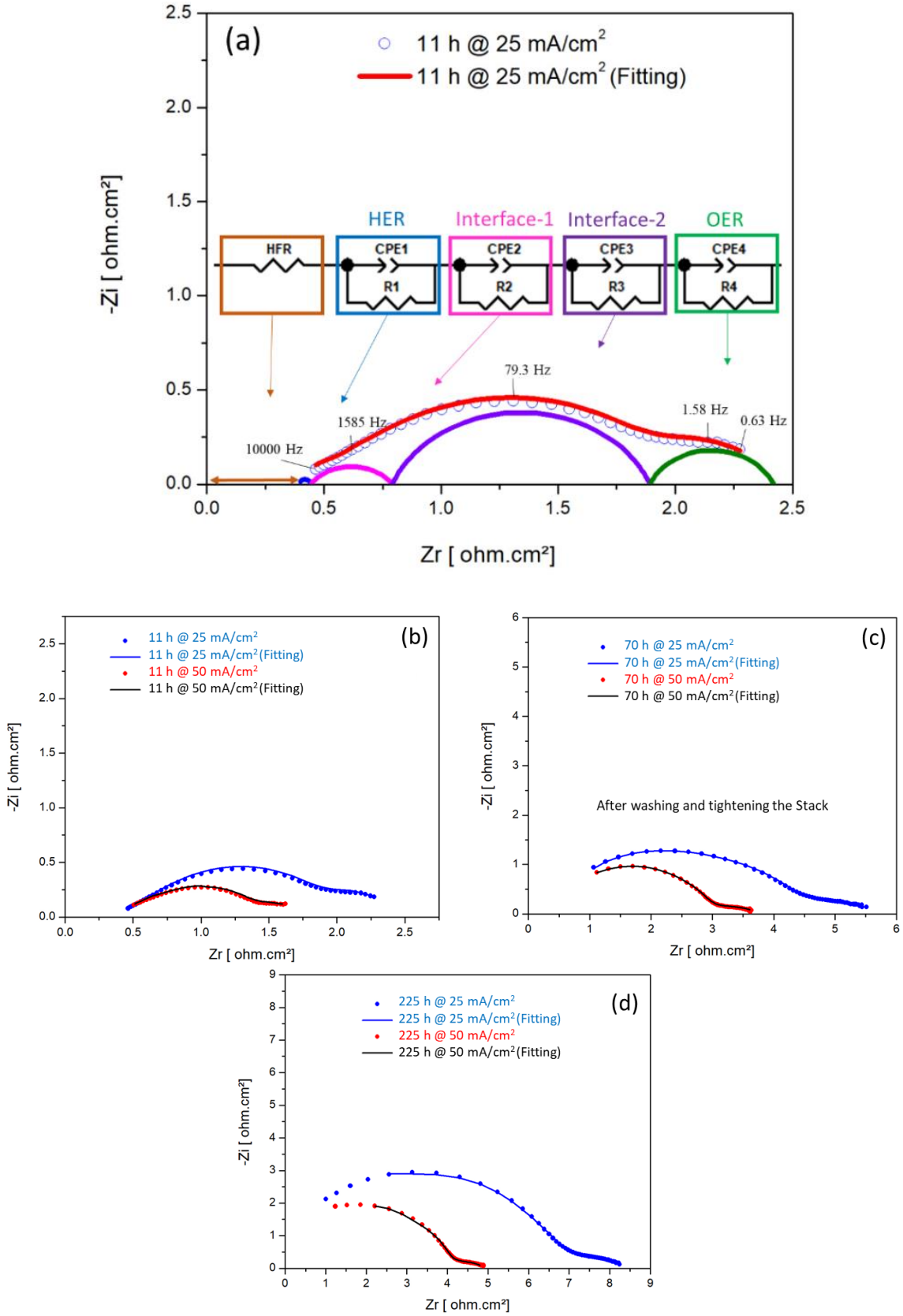


**Figure 6.34.** Experimental and best-fit EIS spectra of the HNC-CCM with moderate catalyst loadings (a) electrical analogy used for the fit; EIS spectra after (b) 11h, (c) 70h after washing and tightening, and (d) 225h of AST.

**Table 6.12.** List of best-fit EIS parameters extracted from the data of **Figure 6.34**.

| Cell#1 | Represent | 11 h @ 25 mA/cm$^2$ | 11 h @ 50 mA/cm$^2$ | Washing and tightening | | 225h 25 mA/cm$^2$ | 225 h mA/cm$^2$ |
|---|---|---|---|---|---|---|---|
| | | | | 70 h @ 25 mA/cm$^2$ | 70 h @ 50 mA/cm$^2$ | | |
| $R_1$ ($\Omega$.cm$^2$) | HFR | 0.395 | 0.395 | 0.678 | 0.678 | 0.7 | 0.7 |
| $R_2$ ($\Omega$.cm$^2$) | R of interface 1 | 0.5277 | 0.5465 | 1.567 | 1.08 | 2.039 | 1.275 |
| $CPE_1$-T (mF/cm$^2$) | Interface 1 | 0.33 | 0.4 | 0.141 | 0.224 | 0.07 | 0.1 |
| $CPE_1$-P (adim) | Interface 1 | 0.761 | 0.489 | 0.411 | 0.324 | 0.42 | 0.375 |
| $R_3$ ($\Omega$.cm$^2$) | R of interface 2 | 0.049 | 0.07 | 1.955 | 1.324 | 3.878 | 2.218 |
| $CPE_2$-T (mF/cm$^2$) | Interface 2 | 0.00001 | 0.001 | 0.0004 | 0.0001 | 0.0001 | 0.0001 |
| $CPE_2$-P (adim) | Interface 2 | 1 | 1 | 0.806 | 0.86 | 1 | 1 |
| $R_4$ ($\Omega$.cm$^2$) | $R_{ct}$ of HER | 0.348 | 0.185 | 0.203 | 0.129 | 0.678 | 0.23 |
| $CPE_3$-T (mF/cm$^2$) | HER | 0.012 | 0.006 | $1.6 \times 10^{-6}$ | $5.5 \times 10^{-7}$ | $1.4 \times 10^{-7}$ | $10^{-7}$ |
| $CPE_3$-P (adim) | HER | 0.63 | 1 | 1 | 1 | 1 | 1 |
| $R_5$ ($\Omega$.cm$^2$) | $R_{ct}$ of OER | 1.1 | 0.632 | 1.274 | 0.592 | 1.11 | 0.56 |
| $CPE_4$-T (mF/cm$^2$) | OER | 0.007 | 0.005 | $2.1 \times 10^{-5}$ | $8 \times 10^{-6}$ | 0.0005 | $10^{-6}$ |
| $CPE_4$-P (adim) | OER | 0.77 | 0.62 | 1 | 1 | 0.9 | 1 |

**Figure 6.35** shows a plot of the best-fit EIS resistances during the 225 hrs-long test. The increase of the two membrane/membrane interface resistances is the main contribution to the increase of the total cell impedance and to CCM performance degradation.

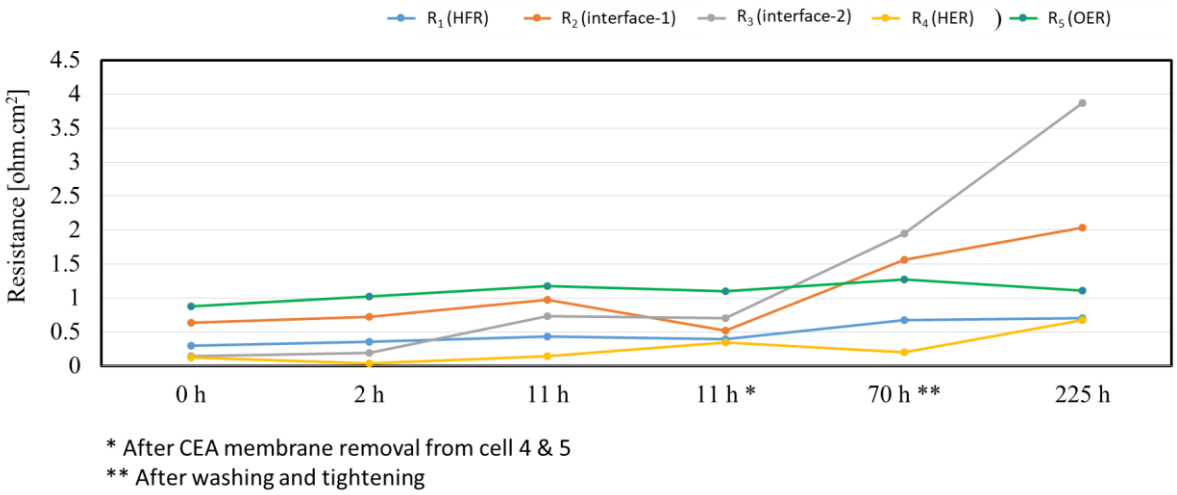


**Figure 6.35.** Variation of the fitted resistances by time for cell#1. EIS measured at 25 mA/cm$^2$.

From these results, we conclude that the reduction in cell performance is mainly due to problems with the HNC membrane (lack of chemical stability) and not to a loss of catalytic activity in the catalyst layers.

### 6.4.4. HNC CCM with low catalyst loading (Cell#4)

We now present the results obtained with cell#4 Pt-C / Nafion 212 // HNC membrane // Nafion 212 / $IrO_2$ with low catalyst loadings.

Chronopotentiometry

The response of cell#4 during the stability test performed by chronopotentiometry, a constant current density of 25 mA/cm$^2$ is plotted in **Figure 6.36**. When the HNC membrane was inside the CCM, the cell voltage hit the max value of 2.3 Volt after only 11h of test. Stability was obtained only after removing the HNC membrane from the CCM, cleaning and tightening the stack. The role of the HNC membrane in the observed fast degradation is clearly demonstrated.

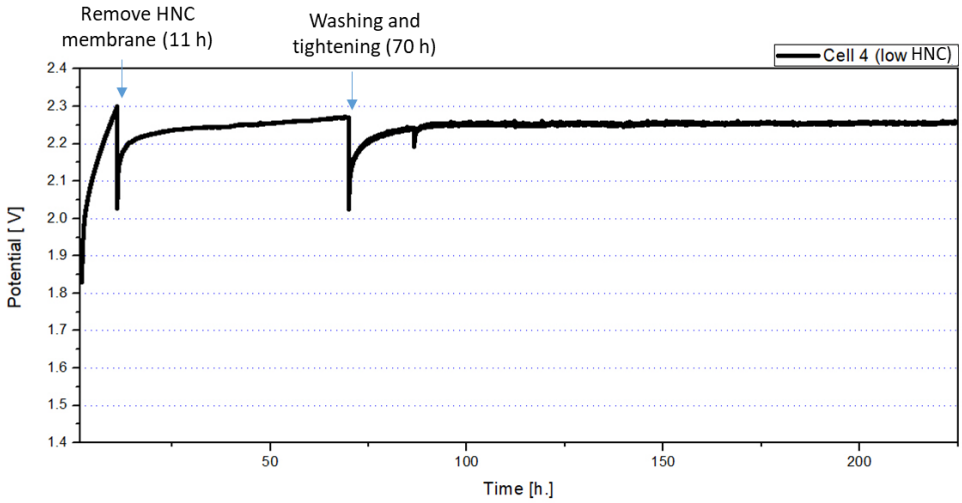


**Figure 6.36.** Chronopotentiometry of cell#4 at 25 mA/cm$^2$ for 225 h.

Cyclic Voltammograms (CV)

The cyclic voltammograms are plotted in **Figure 6.37**. The specific areal capacitance increases from 10.8 to 15.5 mF/cm$^2$, indicating an increase in the electrochemical surface area of the catalyst layer. The results suggest that the loss of efficiency does not come from the delamination of the CLs, but from the loss of HER activity on the cathode side, most probably by poising with impurities released from the HNC membrane.

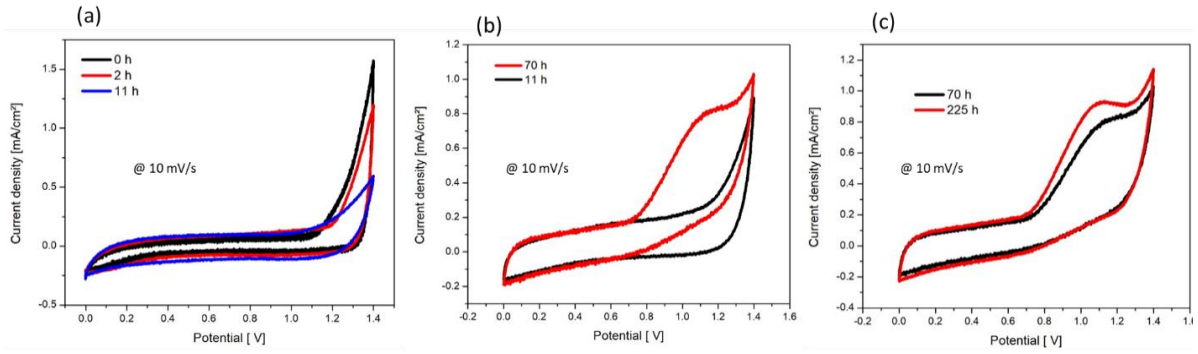


**Figure 6.37.** Cyclic voltammograms were measured on the HNC-CCM with low catalyst loadings at scan rates of 10 mV/s, after (a) 0, 2, 11 hours (b) 11, 70 hours and (c) 70, 225 hours.

**Table 6.13.** Specific areal capacitance values of the low-HNC CCM were measured at a scan rate of 10 mV/sec, at different times of the ASTs.

| **Cell#4** | **0 h** | **2 h** | **11 h** | **70 h** | **225 h** |
|---|---|---|---|---|---|
| Cs (mF/cm$^2$) | 9.5 | 11.32 | 13.48 | 14.42 | 18.57 |

iV curves

The iV curves measured before and after the stability test are shown in **Figure 6.38**. The iV curve is less efficient at the end of the test. The 200 mV cell voltage increase is close to the value measured during the chronopotentiometry test. The shapes of these curves provide some insights about what's taking place. The linear (ohmic) behavior observed at the onset of the cell current in the low current density range is attributed to the membrane/membrane interfaces. This is not to say that this resistance remains constant. Maybe there is a need to start the current flow before a good membrane/membrane interface is obtained. In addition to this linear behaviour, there is also a clear increase of overvoltage. Since, according to the CVs there is no significant loss of electrochemical sites, it can be speculated that this is due to an increase of the HER overvoltage due to the accumulation of HNC membrane residues in the HER catalyst layer.

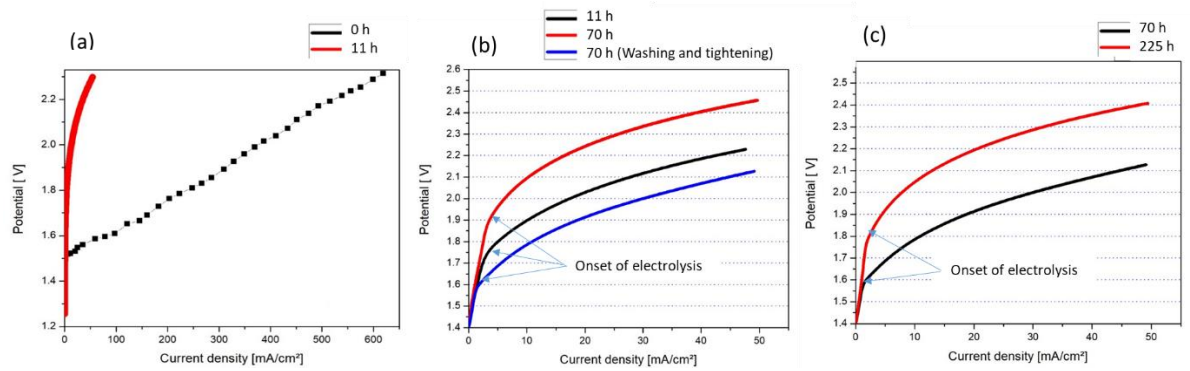


**Figure 6.38.** iV curves of the laboratory HNC-CCM with low catalyst loadings measured after (a) 0, 11 hours (b) 11, 70 hours, 70 hours after washing and tightening, and (c) 70, 225 hours.

EIS

Before removing the HNC membrane, there are two membrane/membrane interface resistances and two charge transfer resistances (HER and OER). The equivalent electrical circuit used for fitting experimental EIS spectra is shown in (**Figure 6.39-a**). The results are similar to those obtained on the Moderate-HNC CCM (cell#1), but the interface resistance and HER resistance are higher. After dismantling the stack, it was observed that the HNC membrane used for this CCM had more wrinkles. This is consistent with a higher contact resistance. Also, the low Pt/C loading is lower, and it gets thoroughly poisoned with contamination leaked from the HNC membrane. Thus, the diameter of the first semicircle is higher.

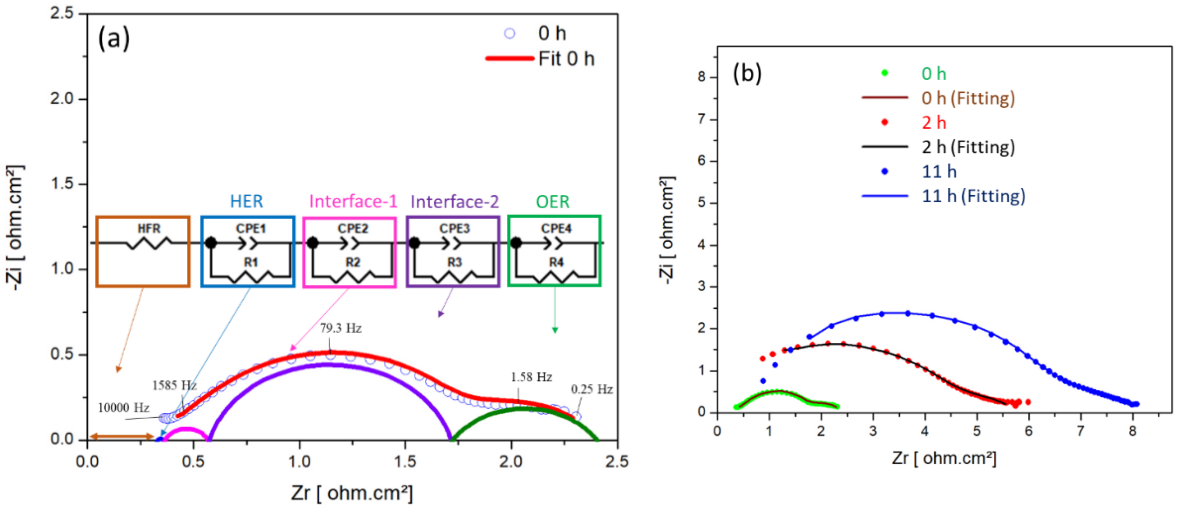


**Figure 6.39.** Experimental and best-fit EIS spectra of the HNC-CCM with low catalyst loadings (a) electrical analogy used for the fit; (b) EIS spectra at 25 mA/cm$^2$ after 0 h, 2 h and 11 h of AST.

**Table 6.14.** List of best-fit EIS parameters extracted from the data of **Figure 6.39**.

| **Cell#4** | **Represent** | **0 h 25 mA/cm$^2$** | **2 h 25 mA/cm$^2$** | **11 h 25 mA/cm$^2$** |
|---|---|---|---|---|
| $R_0$ (Ω.cm$^2$) | HFR | 0.33 | 0.33 | 0.55 |
| $R_1$ (Ω.cm$^2$) | R of interface 1 | 0.692 | 2.22 | 3.347 |
| $CPE_1$-T (mF/cm$^2$) | Interface 1 | 0.366 | 0.0001 | 0.0001 |
| $CPE_1$-P (adim) | Interface 1 | 0.649 | 0.867 | 0.98 |
| $R_2$ (Ω.cm$^2$) | R of interface 2 | 0.034 | 1.895 | 2.54 |
| $CPE_2$-T (mF/cm$^2$) | Interface 2 | 0.0001 | 0.0366 | 0.01 |
| $CPE_2$-P (adim) | Interface 2 | 1 | 0.455 | 0.51 |
| $R_3$ (Ω.cm$^2$) | $R_{ct}$ of HER | 0.21 | 0.254 | 0.56 |
| $CPE_3$-T (mF/cm$^2$) | HER | 0.005 | $10^{-7}$ | 0.0001 |
| $CPE_3$-P (adim) | HER | 0.79 | 0.85 | 0.0025 |
| $R_4$ (Ω.cm$^2$) | $R_{ct}$ of OER | 1.145 | 1.135 | 0.97 |
| $CPE_4$-T (mF/cm$^2$) | OER | 0.0036 | $9 \times 10^{-6}$ | $2.35 \times 10^{-6}$ |
| $CPE_4$-P (adim) | OER | 0.85 | 1 | 1 |

Once the HNC membrane was removed, the two membrane/membrane interface resistances merged into one, and the updated equivalent electrical circuit shown in **Figure 6.40-a** was used for the fits. The HFR decreased after tightening the stack at a higher clamping pressure (**Table 6.14**).

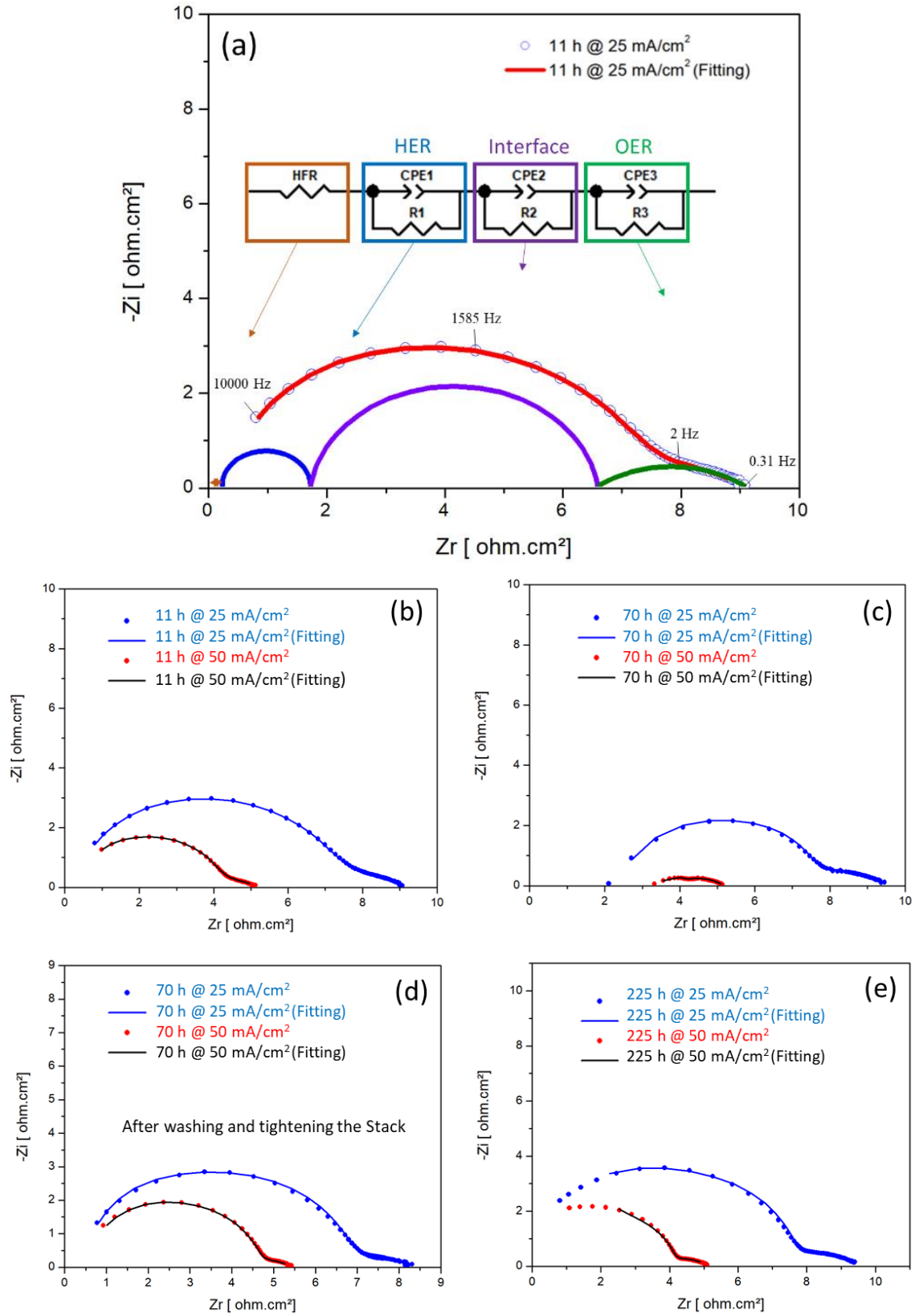


**Figure 6.40.** Experimental and best-fit EIS spectra of the HNC-CCM with low catalyst loadings (a) electrical analogy used for the fit; EIS spectra after (b) 11h, (c) 70 h, (d) after washing and tightening, and (e) 225h of AST.

**Table 6.15.** List of best-fit EIS parameters extracted from the data of **Figure 6.40**.

| Cell#4 | Represent | 11 h @ 25 mA/cm$^2$ | 11 h @ 50 mA/cm$^2$ | 70 h @ 25 mA/cm$^2$ | 70 h @ 50 mA/cm$^2$ | Washing and tightening | | 225h 25 mA/cm$^2$ | 225 h 50 mA/cm$^2$ |
|---|---|---|---|---|---|---|---|---|---|
| | | | | | | 70 h @ 25 mA/cm$^2$ | 70 h @ 50 mA/cm$^2$ | | |
| $R_0$ ($\Omega$.cm$^2$) | HFR | 0.247 | 0.247 | 2.05 | 3.25 | 0.55 | 0.6 | 0.6 | 0.6 |
| $R_1$ ($\Omega$.cm$^2$) | R of interface | 2.5 | 1.857 | 2.458 | 1.409 | 1.934 | 0.95 | 2.35 | 1.23 |
| $CPE_1$-T (mF/cm$^2$) | interface | 0.04 | 0.047 | 0.036 | 0.061 | 0.07 | 0.109 | 0.05 | 0.067 |
| $CPE_1$-P (adim) | interface | 0.4 | 0.333 | 0.46 | 0.422 | 0.426 | 0.435 | 0.45 | 0.466 |
| $R_2$ ($\Omega$.cm$^2$) | $R_{ct}$ of HER | 4.865 | 2.545 | 3.41 | 0.124 | 4.418 | 2.911 | 5.17 | 2.58 |
| $CPE_2$-T (mF/cm$^2$) | HER | $4.6 \times 10^{-5}$ | $2.6 \times 10^{-5}$ | $2.1 \times 10^{-5}$ | $10^{-6}$ | $2.7 \times 10^{-5}$ | $2.9 \times 10^{-5}$ | $1.7 \times 10^{-5}$ | $1.3 \times 10^{-5}$ |
| $CPE_2$-T (mF/cm$^2$) | HER | 0.91 | 0.97 | 1 | 1 | 0.97 | 0.96 | 1 | 1 |
| $R_3$ ($\Omega$.cm$^2$) | $R_{ct}$ of OER | 1.5 | 0.58 | 1.519 | 0.395 | 1.45 | 0.955 | 1.41 | 0.7 |
| $CPE_3$-T (mF/cm$^2$) | OER | $1.2 \times 10^{-5}$ | $2.8 \times 10^{-6}$ | $10^{-6}$ | $4.45\times 10^{-5}$ | $3.3 \times 10^{-6}$ | $4.4 \times 10^{-6}$ | $10^{-7}$ | $10^{-7}$ |
| $CPE_3$-T (mF/cm$^2$) | OER | 1 | 1 | 1 | 1 | 1 | 1 | 1 | 1 |

The best-fit resistance values measured during the test are plotted in **Figure 6.41**. The main cause for the increase in cell impedance until the removal of the HNC membrane was the increase in interface resistance. Then it was the increase in the HER charge transfer resistance that took over after the removal of the HNC membrane.

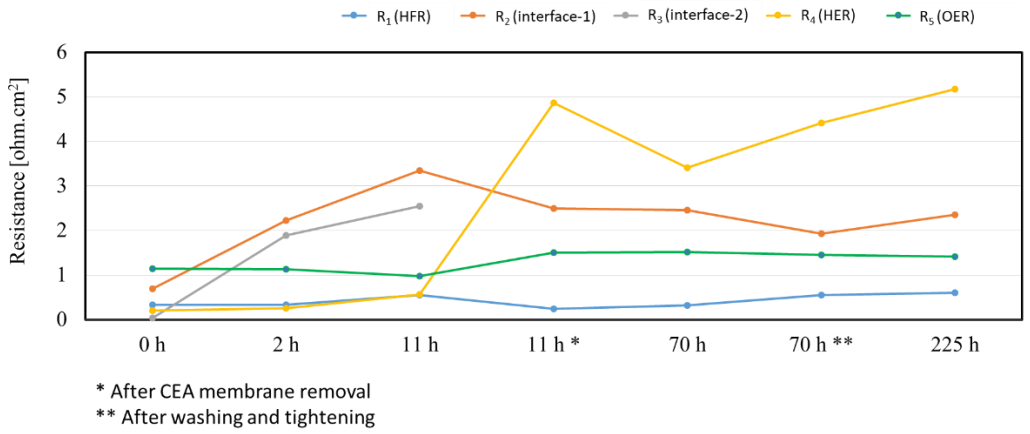


**Figure 6.41.** Variation of the fitted resistances by time for cell#4. EIS measured at 25 mA/cm$^2$.

### 6.4.5. HNC CCM with high catalyst loading (Cell#5)

We now present the results obtained with cell#5 : Pt-C / Nafion 212 // HNC membrane // Nafion 212 / $IrO_2$ with high catalyst loadings.

Chronopotentiometry

The behavior of cell#5 during the stability test performed by chronopotentiometry a constant current of 25 mA/cm$^2$ is shown in **Figure 6.42**. In the early phase of the test, the cell voltage rapidly increased (after 11 hours of test, a voltage increase of 420 mV was measured, the cell voltage jumping from 1.64 to 2.01 V), similar to cell#4. After 11 hours, the HNC membrane was removed from the sandwich CCM, and the test was continued.

The cell voltage continued to increase by 180 mV during the next phase from 11 h to 70h. After a logarithmic increase, the variation became linear (jumping from 1.67 V at 11h to 1.85 V at 70h). After the stack was cleaned and then tightened, a significant improvement in performance was obtained (cell voltage reduction down to 1.72 V) followed by a more classic behavior, leading to a stabilization of the cell voltage after ~ 4 h of operation at approximately 1.97 V after 225 hours. Such a cell voltage is very high but what is important here is its stabilization after extracting the HNC membrane and tightening the stack to try to compensate for the variations in the thickness of the CCM.

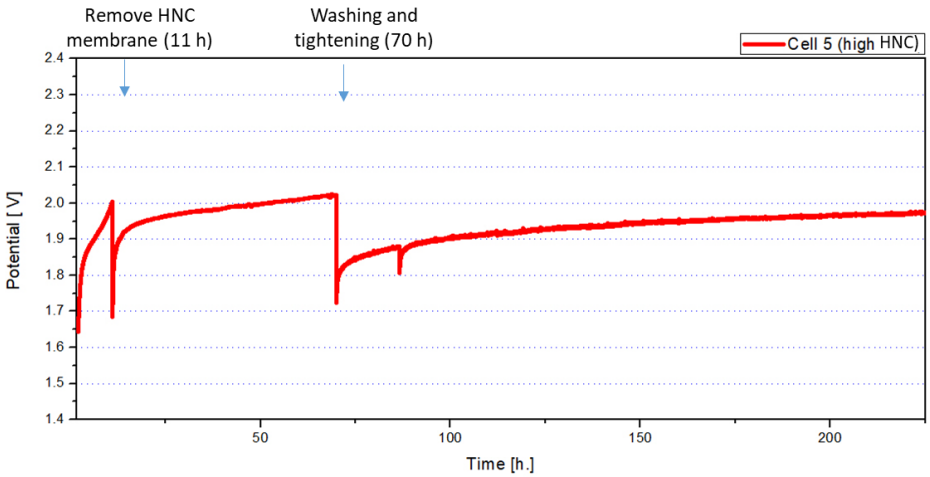


**Figure 6.42.** Chronopotentiometry of cell#5 at 25 mA/cm$^2$ for 225 h.

Cyclic Voltammograms (CV)

The CVs measured on cell#5 during the stability test are plotted in (**Figure 6.43**). The Cs (values are compiled in **Table 6.16**) was low (9.7 mF/cm$^2$) at the beginning of the test but, interestingly, increased to 25.7 after 225 hours. It is known that passing a current through the CCM induces activation of the catalyst layer and increases the catalyst's electrochemical surface area[94]. The fact that no significant Cs reduction was observed for any of the 5 cells between 70 h and 225 h indicates that no catalyst loss occurred, and that the CL firmly adheres to the membrane.

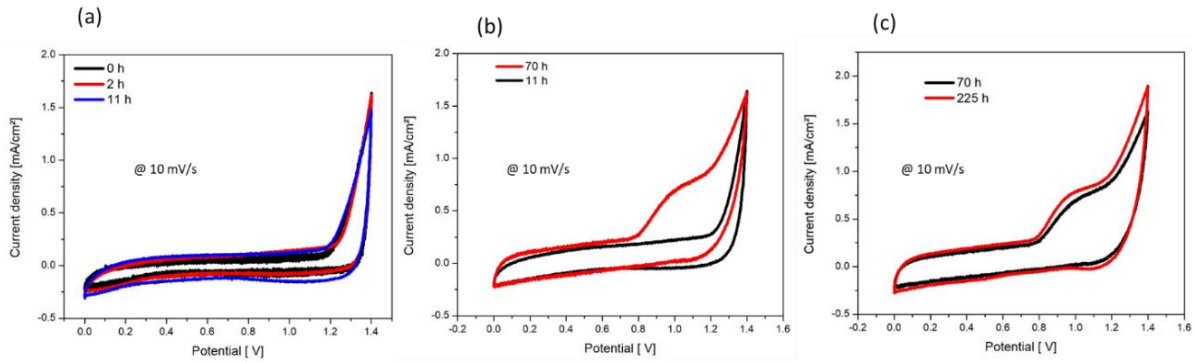


**Figure 6.43.** Cyclic voltammograms measured on the HNC-CCM with high catalyst loadings at scan rates of 10 mV/s, after (a) 0, 2, 11 hours (b) 11, 70 hours and (c) 70, 225 hours.

[94] Grigoriev SA, Dzhus KA, Bessarabov DG, Millet P. *Failure of PEM water electrolysis cells: Case study involving anode dissolution and membrane thinning*. Int J Hydrogen Energy 2014;39:20440–6. https://doi.org/10.1016/j.ijhydene.2014.05.043.

**Table 6.16.** Specific areal capacitance values of the high-HNC CCM measured at a scan rate of 10 mV/sec, at different times of the ASTs.

| **Cell#5** | 0 h | 2 h | 11 h | 70 h | 225 h |
|---|---|---|---|---|---|
| Cs (mF/cm$^2$) | 9.7 | 11.3 | 14.5 | 20.92 | 25.7 |

iV curves

The iV curves measured in the low current density range (electrochemical activation domain) on CCM#5 before and after the stability test are plotted in **Figure 6.44**. They are all similar in shape but differ by their position along the Y-axis. What is unusual is the linear behavior observed at the onset of the faradaic current: this was attributed to the two membrane/membrane interfaces. The worst curve is the one measured after 70 h of test, just before the HNC membrane was removed. After 225 hours of test, despite the fact that the HNC membrane has been removed from the CCM, the situation is not yet back to normal. This is evidence of reduced catalytic activity. Since the cyclic voltammograms show an increase of the specific areal capacitance from 14.5 to 20.9 mF/cm$^2$, indicating an increase in the electrochemical surface area of the catalyst layer., these results suggest that the loss of cell efficiency is not from catalyst delamination but from catalyst poisoning.

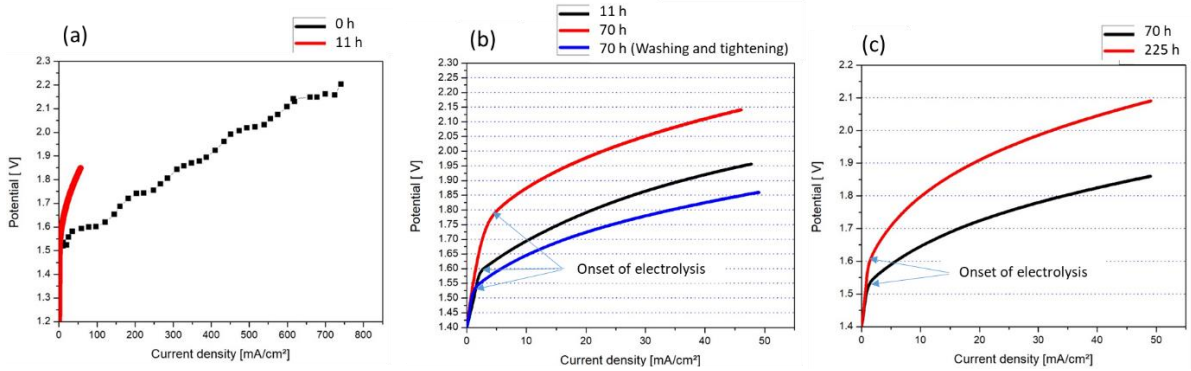


**Figure 6.44.** iV curves of the laboratory HNC-CCM with high catalyst loadings measured after (a) 0, 11 hours (b) 11, 70 hours, 70 hours after washing and tightening, and (c) 70, 225 hours.

EIS

Before removing the HNC membrane, there are two interface resistances and two charge transfer (HER and OER) resistances. The equivalent electrical circuit is shown in (**Figure 6.45-a**). The results are similar to cell#1 and cell#4, but the interface and HER resistance are higher than the Moderate HNC CCM. The HNC membrane used for this CCM had moderate wrinkles and, therefore, moderate contact resistances. Even if the Pt/C loading is high, it gets poisoned with contamination leaked from the HNC membrane, and the diameter of the first semicircle increases with time (**Figure 6.45-b**).

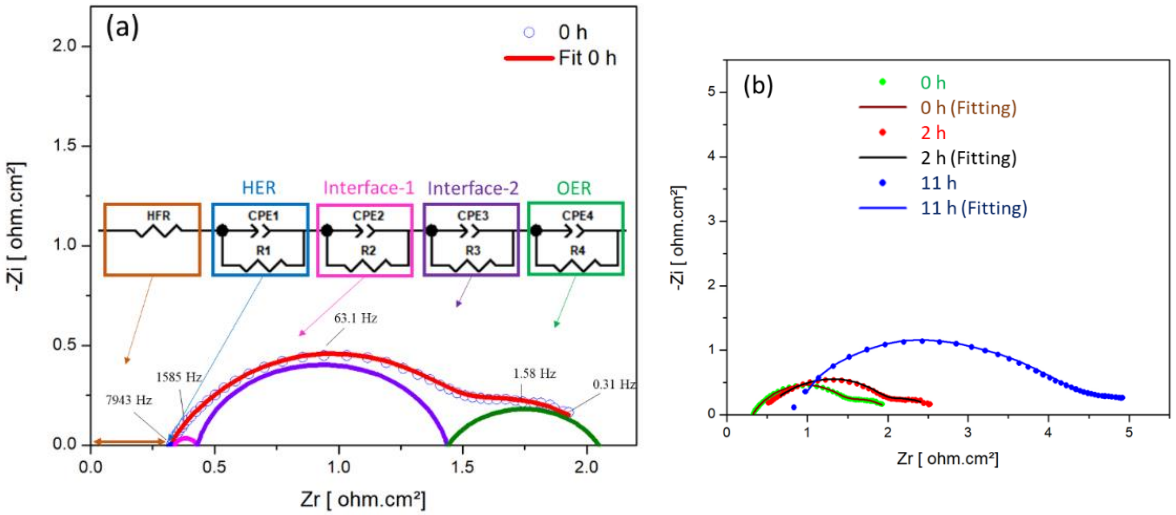


**Figure 6.45.** Experimental and best-fit EIS spectra of the HNC-CCM with high catalyst loadings (a) electrical analogy used for the fit; (b) EIS spectra at 25 mA/cm$^2$ after 0 h, 2 h and 11 h of AST.

**Table 6.17.** List of best-fit EIS parameters extracted from the data of **Figure 6.45**.

| **Cell#5** | **Represent** | **0 h 25 mA/cm$^2$** | **2 h 25 mA/cm$^2$** | **11 h 25 mA/cm$^2$** |
|---|---|---|---|---|
| $R_0$ (Ω.cm$^2$) | HFR | 0.32 | 0.459 | 0.76 |
| $R_1$ (Ω.cm$^2$) | R of interface 1 | 0.614 | 0.656 | 1.285 |
| $CPE_1$-T (mF/cm$^2$) | Interface 1 | 0.375 | 0.308 | 0.102 |
| $CPE_1$-P (adim) | Interface 1 | 0.614 | 0.7 | 0.494 |
| $R_2$ (Ω.cm$^2$) | R of interface 2 | 0.09 | 0.318 | 1.587 |
| $CPE_2$-T (mF/cm$^2$) | Interface 2 | 0.005 | 0.0032 | 0.001 |
| $CPE_2$-P (adim) | Interface 2 | 0.947 | 0.866 | 0.815 |
| $R_3$ (Ω.cm$^2$) | $R_{ct}$ of HER | 0.025 | 0.022 | 0.362 |
| $CPE_3$-T (mF/cm$^2$) | HER | 0.0007 | $1.9 \times 10^{-5}$ | $3.6 \times 10^{-6}$ |
| $CPE_3$-P (adim) | HER | 1 | 1 | 15 |
| $R_4$ (Ω.cm$^2$) | $R_{ct}$ of OER | 1.01 | 1.148 | 1.252 |
| $CPE_4$-T (mF/cm$^2$) | OER | 0.0055 | 0.0039 | $4.1 \times 10^{-5}$ |
| $CPE_4$-P (adim) | OER | 0.87 | 0.85 | 1 |

As for the Low-HNC CCM, the equivalent electrical circuit used for fitting experimental EIS spectra (**Figure 6.46-a**) consists of one interface resistance in addition to the HER and OER charge transfer resistances (three time constants). Furthermore, the HFR decreased after tightening the stack at a higher clamping pressure (**Table 6.17**).

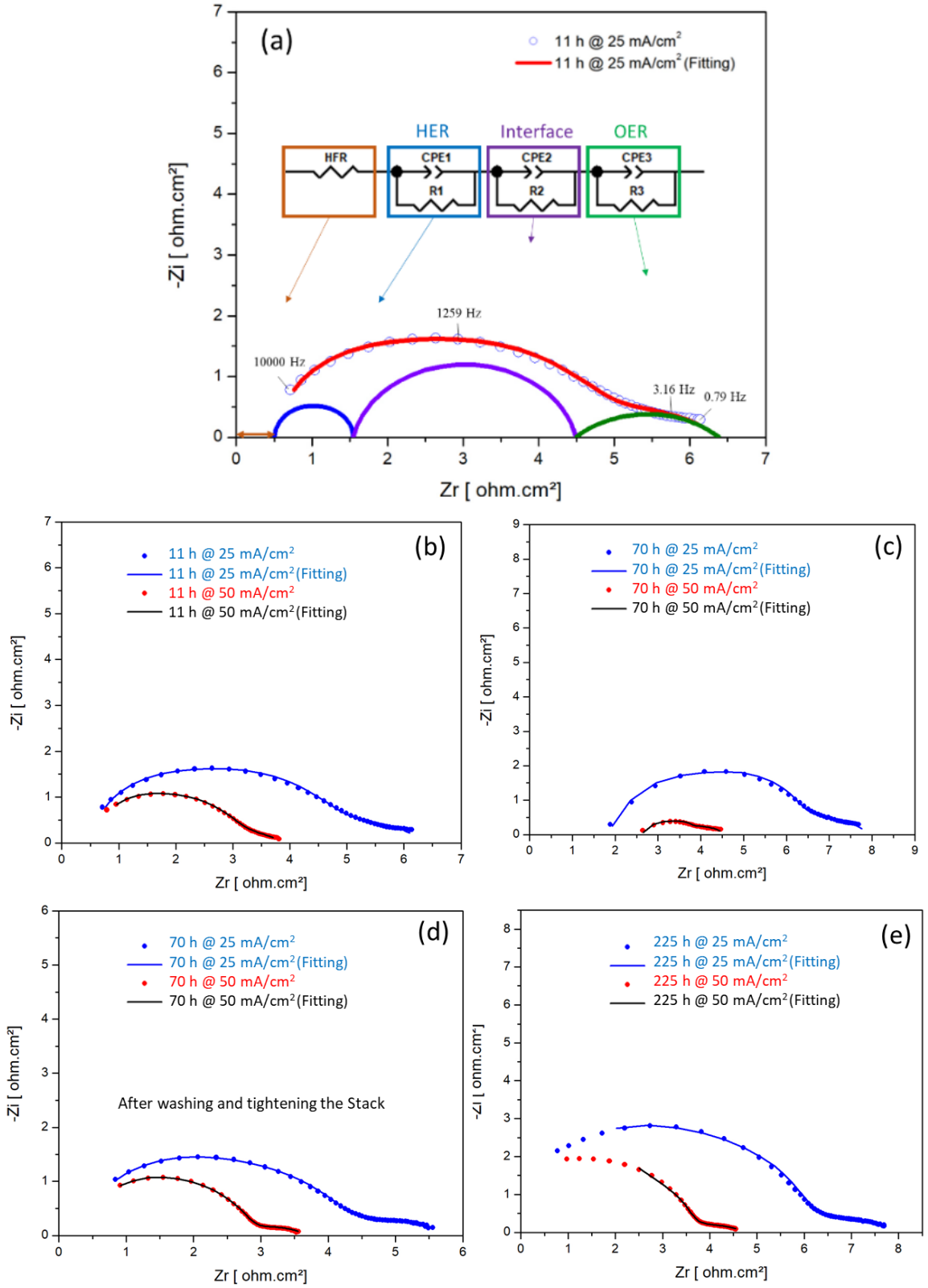


**Figure 6.46.** Experimental and best-fit EIS spectra of the HNC-CCM with high catalyst loadings (a) electrical analogy used for the fit; EIS spectra after (b) 11h, (c) 70 h, (d) after washing and tightening, and (e) 225h of AST.

**Table 6.18.** List of best-fit EIS parameters extracted from the data of **Figure 6.46**.

| **Cell#5** | **Represent** | **11 h @ 25 mA/cm²** | **11 h @ 50 mA/cm²** | **70 h @ 25 mA/cm²** | **70 h @ 50 mA/cm²** | **Washing and tightening** | | **225h 25 mA/cm²** | **225 h 50 mA/cm²** |
|---|---|---|---|---|---|---|---|---|---|
| | | | | | | **70 h @ 25 mA/cm²** | **70 h @ 50 mA/cm²** | | |
| $R_0$ ($\Omega.cm^2$) | HFR | 0.507 | 0.507 | 1.7 | 2.47 | 0.3 | 0.322 | 0.35 | 0.35 |
| $R_1$ ($\Omega.cm^2$) | R of interface | 1.896 | 1.2 | 2.047 | 1.055 | 1.785 | 1.013 | 2.4 | 1.616 |
| $CPE_1$-T ($mF/cm^2$) | interface | 0.053 | 0.055 | 0.024 | 0.05 | 0.152 | 0.232 | 0.07 | 0.125 |
| $CPE_1$-P (adim) | interface | 0.487 | 0.408 | 0.533 | 0.497 | 0.385 | 0.3547 | 0.37 | 0.3 |
| $R_2$ ($\Omega.cm^2$) | $R_{ct}$ of HER | 2.945 | 1.73 | 2.861 | 0.367 | 2.427 | 1.793 | 3.815 | 2.09 |
| $CPE_2$-T ($mF/cm^2$) | HER | 0.0001 | 0.0001 | $2 \times 10^{-5}$ | $1.39 \times 10^{-6}$ | 0.0002 | $9 \times 10^{-5}$ | $2.8\times10^{-5}$ | $2.8\times10^{-5}$ |
| $CPE_2$-P (adim) | HER | 0.87 | 0.9 | 1 | 1 | 0.81 | 0.86 | 0.97 | 1 |
| $R_3$ ($\Omega.cm^2$) | $R_{ct}$ of OER | 1.04 | 0.446 | 1.338 | 0.688 | 1.295 | 0.576 | 1.39 | 0.714 |
| $CPE_3$-T ($mF/cm^2$) | OER | $1.35 \times 10^{-5}$ | $5.1 \times 10^{-6}$ | $8.3 \times 10^{-7}$ | $8.9 \times 10^{-5}$ | $1.56 \times 10^{-5}$ | $8.5 \times 10^{-6}$ | $10^{-6}$ | $10^{-6}$ |
| $CPE_3$-P (adim) | OER | 1 | 1 | 1 | 1 | 1 | 1 | 1 | 1 |

**Figure 6.47** shows a plot of best-fit resistances during the test. The $R_{ct}$ (HER) increase is the main contributor to the cell impedance, as for the HNC-Low CCM (cell#4). This result is in agreement with iV curve measurements. The $R_{ct}$ (OER) was relatively constant during the test. The interface resistance was increasing before removing the HNC membranes and then became relatively stable. Washing and tightening the stack after 70 h significantly reduced the HFR, and slightly reduced the $R_{ct}$ (HER) and $R_{interface}$ resistances. However, after continuing electrolysis up to 225 h, both $R_{ct}$ (HER) and $R_{interface}$ have increased.

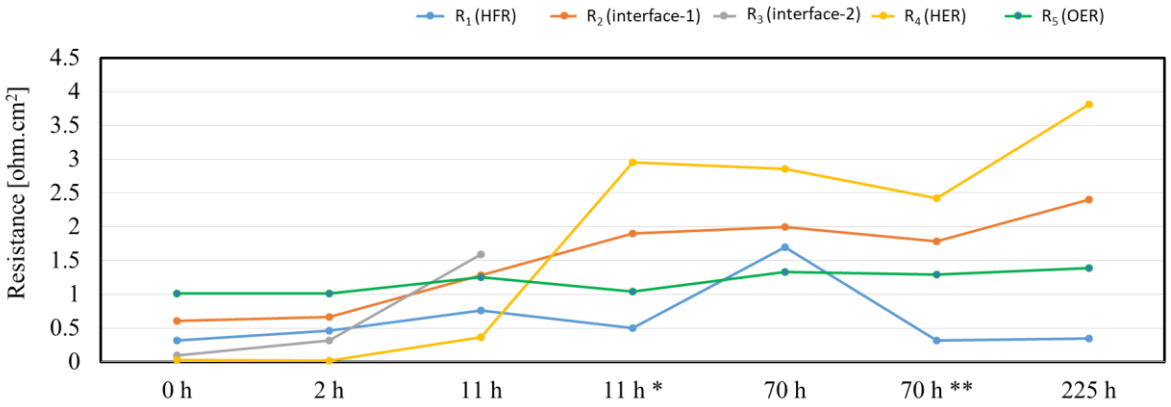


**Figure 6.47.** Variation of the fitted resistances by time for cell#5. EIS measured at 25 $mA/cm^2$

## 6.5. Conclusions

The CCM containing the HNC membranes show fast degradation rates. Several processes contribute to the degradation of performances:

1- Hydrolysis of PSS chains
2- Leaking of membrane components that poison the Pt/C cathode electrocatalyst.
3- Reduction of protonic conductivity (an increase of membrane ionic resistance) by loss of functional sulfonic groups.
4- Formation of wrinkles at membrane surface due to water swelling resulting in high contact resistances.
5- Loss of mechanical properties resulting from membrane swelling.

# Conclusions & perspectives

This doctoral thesis addresses the production of electrolytic hydrogen by water electrolysis using the so-called PEM (proton exchange membrane or polymer electrolyte membrane) technology. The main objective of the thesis was to evaluate the interest of replacing the existing PFSA polymers by a new type of hybrid nanocomposite (HNC) material developed by the French CEA. These proton-conducting membranes are called HNC materials because the two main functions required for the applications (proton conduction and the inert chemical skeleton, which provides mechanical strength and hydrophobicity) are synthesized separately and then chemically assembled in solution before forming the membrane by casting. Our thesis work did not focus on the synthesis of such materials but on their characterization as potential PFSA alternatives. They were used to manufacture CCMs (catalyst-coated membranes), the electrochemical behavior of which was analyzed in PEM water electrolysis cells. We first assessed the performances of two types of reference CCM: one is a commercial CCM, and the second is a laboratory CCM made and optimized to match as close as possible the performances of the commercial one. Despite the fact that there is still room for optimization, we were finally able to make CCM which compared well with the commercial one. The as-developed CCM manufacturing method was then adapted to manufacture CCMs integrating CEA's hybrid nanocomposite membranes. The catalyst layers were not made using a dispersion of hybrid nanocomposite material (not available for our studies) but a Nafion-dispersion instead for several reasons. First, using PFSA, the performances at the beginning-of-test are quite good. Then, degradation also occurs when the catalyst layers (CL) are coated on thin PFSA membranes and when sandwich CCMs (with the HNC membrane at the center) are made. Finally, all the results show that the bulk HNC membrane itself is not stable under the conditions of PEM water electrolysis. The membrane exhibits high chemical instability in the presence of liquid water (mainly the hydrolysis of the imine functional goups), even at rest conditions. During electrolysis, this leads to a rapid increase in the cell voltage, due in particular to the loss of proton conduction. By analyzing the degradation processes in more detail, we were able to show that the catalyst layers and the core of the membrane are mechanically and chemically weak. Various microscopic degradation phenomena have been highlighted. From a mechanical point of view, the HNC membrane brought into contact with liquid water is subject to swelling and strong dimensional changes. This weakens the CCM both at the level of the CLs (with loss of catalysts) and at the core of the membrane (this leads to a loss of mechanical properties, which can promote electrical short circuits during electrolysis). On the chemical side, the hydrolysis of the acid functions occurs as soon as the membrane is exposed to liquid water. Furthermore, styrene sulfonic groups exposed to the positive potential of the anode are also suspected to be unstable and to undergo electrochemical oxidation. These various weaknesses contribute to reduce operating times, which are incompatible with the target applications. An experimental trick has been used, in an attempt to indirectly increase the lifetime from a few hours to a few hundred hours. This was done by clamping the HNC membrane between two thin PFSA membranes (Nafion 212). Although this made it possible to increase the lifetime of the prepared samples, it did not prevent the degradation mechanisms. It can be thus concluded that the membrane, as it exists today, cannot be used in PEM water electrolysis applications. In terms of perspectives, some improvement paths are proposed for improving this type of HNC membrane. The first avenue for improvement would consist in increasing the percentage of crosslinking. Another would be to search for and test sulfonic links and cross-linking agents that are less sensitive to hydrolysis.

# Résumé étendu en français

Cette thèse de doctorat porte sur la production d'hydrogène électrolytique par électrolyse de l'eau en utilisant la technologie dite PEM (membrane échangeuse de protons ou membrane électrolyte polymère). L'objectif principal de la thèse était d'évaluer l'intérêt de remplacer les polymères PFSA existants par un nouveau type de matériau hybride nanocomposite (HNC) développé par le CEA. Ces membranes conductrices de protons sont appelées matériaux HNC car les deux principales fonctions nécessaires aux applications (la conduction protonique et le squelette chimique inerte, qui assure la résistance mécanique et l'hydrophobicité) sont synthétisées séparément puis assemblées chimiquement en solution avant de former la membrane par coulée. Notre travail de thèse ne s'est pas concentré sur la synthèse de tels matériaux mais sur leur caractérisation en tant qu'alternatives potentielles aux PFSA. Ils ont servi à fabriquer des CCM (catalyst-coated membranes) dont le comportement électrochimique a été analysé dans des cellules d'électrolyse de l'eau PEM. Nous avons d'abord évalué les performances de deux types de CCM de référence : l'un est un CCM commercial, et le second est un CCM de laboratoire conçu et optimisé pour correspondre le plus possible aux performances du CCM commercial. Malgré le fait qu'il y a encore de la place pour l'optimisation, nous avons finalement pu faire du CCM qui se comparait bien au commercial. La méthode de fabrication de CCM telle que développée a ensuite été adaptée pour fabriquer des CCM intégrant les membranes nanocomposites hybrides du CEA. Les couches de catalyseur n'ont pas été réalisées à l'aide d'une dispersion de matériau nanocomposite hybride (non disponible pour nos études) mais d'une dispersion de Nafion à la place pour plusieurs raisons. Tout d'abord, en utilisant PFSA, les performances en début de test sont assez bonnes. Ensuite, la dégradation se produit également lorsque les couches de catalyseur (CL) sont enduites sur de fines membranes PFSA et lorsque des CCM sandwich (avec la membrane HNC au centre) sont fabriqués. Enfin, tous les résultats montrent que la membrane HNC en vrac elle-même n'est pas stable dans les conditions d'électrolyse de l'eau PEM. La membrane présente une forte instabilité chimique en présence d'eau liquide (principalement l'hydrolyse des fonctions imines), même au repos. Lors de l'électrolyse, cela conduit à une augmentation rapide de la tension de la cellule, due notamment à la perte de la conduction protonique. En analysant plus en détail les processus de dégradation, nous avons pu montrer que les couches de catalyseur et le cœur de la membrane sont mécaniquement et chimiquement faibles. Différents phénomènes de dégradation microscopique ont été mis en évidence. D'un point de vue mécanique, la membrane HNC mise en contact avec de l'eau liquide est sujette à des gonflements et à de fortes variations dimensionnelles. Cela fragilise le CCM tant au niveau des CL (avec perte de catalyseurs) qu'au coeur de la membrane (cela conduit à une perte de propriétés mécaniques, ce qui peut favoriser les courts-circuits électriques lors de l'électrolyse). Du côté chimique, l'hydrolyse des fonctions acides se produit dès que la membrane est exposée à l'eau liquide. De plus, les groupements styrène sulfoniques exposés au potentiel positif de l'anode sont également suspectés d'être instables et de subir une oxydation électrochimique. Ces différentes faiblesses contribuent à réduire les temps de fonctionnement, incompatibles avec les applications visées. Une astuce expérimentale a été utilisée, pour tenter d'augmenter indirectement la durée de vie de quelques heures à quelques centaines d'heures. Cela a été fait en serrant la membrane HNC entre deux fines membranes PFSA (Nafion 212). Si cela a permis d'augmenter la durée de vie des échantillons préparés, cela n'a pas empêché les mécanismes de dégradation. On peut donc conclure que la membrane, telle qu'elle existe aujourd'hui, ne peut pas être utilisée dans des applications d'électrolyse d'eau PEM.

En termes de perspectives, quelques pistes d'amélioration sont proposées pour améliorer ce type de membrane HNC. La première piste d'amélioration consisterait à augmenter le pourcentage de réticulation. Une autre consisterait à rechercher et tester des liaisons sulfoniques et des agents de réticulation moins sensibles à l'hydrolyse.